sid.inpe.br/mtc-m21d/2021/12.09.17.38-TDI

ASSESSMENT OF THE DATA ASSIMILATION FRAMEWORK FOR THE PROTOTYPE RAPID REFRESH FORECAST SYSTEM TO REPRESENT CONVECTION OVER MID- AND TROPICAL LATITUDES

Ivette Hernández Baños

Doctorate Thesis of the Graduate Course in Meteorology, guided by Dr. Luiz Fernando Sapucci, approved in December 10, 2021.

URL of the original document:
<http://urlib.net/8JMKD3MGP3W34T/45U8KR5>

INPE
São José dos Campos
2021

PUBLISHED BY:

Instituto Nacional de Pesquisas Espaciais - INPE
Coordenação de Ensino, Pesquisa e Extensão (COEPE)
Divisão de Biblioteca (DIBIB)
CEP 12.227-010
São José dos Campos - SP - Brasil
Tel.:(012) 3208-6923/7348
E-mail: pubtc@inpe.br

sid.inpe.br/mtc-m21d/2021/12.09.17.38-TDI

ASSESSMENT OF THE DATA ASSIMILATION FRAMEWORK FOR THE PROTOTYPE RAPID REFRESH FORECAST SYSTEM TO REPRESENT CONVECTION OVER MID- AND TROPICAL LATITUDES

Ivette Hernández Baños

Doctorate Thesis of the Graduate Course in Meteorology, guided by Dr. Luiz Fernando Sapucci, approved in December 10, 2021.

URL of the original document:
<http://urlib.net/8JMKD3MGP3W34T/45U8KR5>

INPE
São José dos Campos
2021

Cataloging in Publication Data

Hernández Baños, Ivette.

He43a Assessment of the data assimilation framework for the prototype Rapid Refresh Forecast System to represent convection over mid- and tropical latitudes / Ivette Hernández Baños. – São José dos Campos : INPE, 2021.

xxvi + 163 p. ; (sid.inpe.br/mtc-m21d/2021/12.09.17.38-TDI)

Thesis (Doctorate in Meteorology) – Instituto Nacional de Pesquisas Espaciais, São José dos Campos, 2021.

Guiding : Dr. Luiz Fernando Sapucci.

1. Rapid Refresh Forecast System. 2. Convective scale data assimilation. 3. Convection. 4. Gridpoint statistical interpolation. 5. Amazon coastal squall lines. I.Title.

CDU 551.509.313.3

MINISTÉRIO DA CIÊNCIA, TECNOLOGIA E INOVAÇÕES

INSTITUTO NACIONAL DE PESQUISAS ESPACIAIS
Serviço de Pós-Graduação - SEPGR

DEFESA FINAL DE TESE DE IVETTE HERNÁNDEZ BAÑOS
BANCA Nº 330/2021, REG 133701/2017

No dia 10 de dezembro de 2021, as 14h00min, por teleconferência, o(a) aluno(a) mencionado(a) acima defendeu seu trabalho final (apresentação oral seguida de arguição) perante uma Banca Examinadora, cujos membros estão listados abaixo. O(A) aluno(a) foi APROVADO(A) pela Banca Examinadora, por unanimidade, em cumprimento ao requisito exigido para obtenção do Título de Doutora em Meteorologia. O trabalho precisa da incorporação das correções sugeridas pela Banca e revisão final pelo(s) orientador (es).

Título: "Assessment of the data assimilation framework for the prototype Rapid Refresh Forecast System to represent convection over mid- and tropical latitudes"

Membros da Banca:

Dr. José Antonio Aravéquia - Presidente - INPE
Dr. Luiz Fernando Sapucci - Orientador - INPE
Dr. Eder Paulo Vendrasco - Membro Interno - INPE
Dr. Pedro Leite da Silva Dias - Membro Externo - IAG/USP
Dra. Louisa Nance - Membro Externo - National Research for Atmospheric Research (NCAR) /Research Applications Lab (RAL)

Declaração de aprovação da Dra. Louisa Nance anexa ao processo (8924672)

Documento assinado eletronicamente por **Pedro Leite da silva dias (E)**, **Usuário Externo**, em 15/12/2021, às 11:38 (horário oficial de Brasília), com fundamento no § 3º do art. 4º do Decreto nº 10.543, de 13 de novembro de 2020.

Documento assinado eletronicamente por **José Antonio Aravéquia**, **Pesquisador**, em 20/12/2021, às 11:48 (horário oficial de Brasília), com fundamento no § 3º do art. 4º do Decreto nº 10.543, de 13 de novembro de 2020.

Documento assinado eletronicamente por **Eder Paulo Vendrasco**, **Tecnologista**, em 20/12/2021, às 13:27 (horário oficial de Brasília), com fundamento no § 3º do art. 4º do Decreto nº 10.543, de 13 de novembro de 2020.

Documento assinado eletronicamente por **Luiz Fernando Sapucci**, **Pesquisador**, em 28/12/2021, às 14:45 (horário oficial de Brasília), com fundamento no § 3º do art. 4º do Decreto nº 10.543, de 13 de novembro de 2020.

A autenticidade deste documento pode ser conferida no site http://sei.mctic.gov.br/verifica.html, informando o código verificador **8823253** e o código CRC **7F3D2124**.

Referência: Processo nº 01340.008804/2021-00 SEI nº 8823253

To my family

ACKNOWLEDGEMENTS

This study was financed in part by the Coordenação de Aperfeiçoamento de Pessoal de Nível Superior - Brasil (CAPES) - Finance Code 001. Support for this research was also provided by the Developmental Testbed Center (DTC) through the DTC Visitor Program. The DTC Visitor Program is funded by NOAA, National Center for Atmospheric Research (NCAR), and the National Science Foundation.

I am grateful to the National Institute of Space Research, National Oceanic and Atmospheric Administration (NOAA) and NCAR for providing the computing resources and data for the development of this research. The Protection System of the Amazon (SIPAM; acronym in Portuguese for Sistema de Proteção da Amazônia) is also acknowledged for making available radar data for part of this study.

I would like to thank my advisor Luiz Fernando Sapucci for his guidance, support, and encouragement during all this time. I am grateful to the DTC for the opportunity of being a Graduate Visitor and support my visitor project. It has been enriching professionally and personally. It gave me the opportunity to work more closely with experts in the area, especially with my DTC hosts Ming Hu, Guoqing Ge, and Will Mayfield. I would also like to thank Louisa Nance and Eric Gilleland for their support during my visit. I am grateful to Daryl Kleist and Jacob Carley for their guidance to this research since the time of writing the proposal.

Additionally, I would like to express my gratitude to the Evaluation Committee members Pedro Leite Dias, José Antonio Aravéquia, Eder Vendrasco, and Louisa Nance for accepting to be a part of the committee and the comments, questions, and suggestions which helped to improve the quality of the final document.

Last, but not least, I am deeply grateful to my family and friends for their endless support and love.

ABSTRACT

The NOAA next generation rapidly-updated, convection-allowing ensemble forecast system, or Rapid Refresh Forecast System (RRFS), is under development and aims to replace the current operational suite of convection-allowing models of the NCEP in the next operational upgrade. In this study, the data assimilation framework for the prototype RRFS is investigated through the simulation of a typical spring squall line over central US and an Amazon coastal squall line case during the 2020 Amazon dry season. The hybrid three dimensional ensemble–variational data assimilation (3DEnVar) algorithm and various configurations in the Gridpoint Statistical Interpolation (GSI), which is the current data assimilation component of RRFS, are assessed for their impacts on RRFS analyses and forecasts of the two squall line cases. A domain of 3 km horizontal grid-spacing is configured for each case study and rapid update analysis cycles are performed. Conventional and unconventional observations from the Global Data Assimilation System (GDAS) are assimilated and GDAS 80 member ensemble forecasts are used for the ensemble-based background error covariance (BEC). Results from the case study over central US show that a baseline RRFS run without data assimilation is able to represent the observed convection, but with stronger cells and large location errors. With data assimilation, these errors are reduced, especially in the 4 and 6 h forecasts using 75 % of the ensemble BEC and with the supersaturation removal function activated in GSI. Convection is greatly improved when using planetary boundary layer pseudo-observations, especially at 4 h forecast, and the bias of the 2 h forecast of temperature is reduced below 800 hPa. Lighter hourly accumulated precipitation is predicted better when using 100 % ensemble BEC in the first 4 h forecast, but heavier hourly accumulated precipitation is better predicted with 75 % ensemble BEC. On the other hand, over northern South America, a methodology is firstly applied for the case selection using ForTraCC, which showed to be appropriate for the identification of main convective systems associated with these squall lines. Results from the numerical simulations show that RRFS is able to capture the main large scale patterns with a correct positioning of the precipitating systems as analyzed using the CMORPH precipitation estimates. When using data assimilation, the precipitation coverage along the coast is improved and lower RMSE and bias values of the 3 h forecast of 2 m temperature and 2 m dew point temperature are shown during the night hours. Increasing the localization radius in the ensemble-based BEC shows analysis increments with more flow dependent characteristics, however the impact on the forecasts of surface observations is neutral to negative. Overall, the results provide insight into current capabilities of the RRFS data assimilation system and identify configurations that should be considered as candidates for the first version of RRFS. Although further testing and evaluation are warranted in addition to the options tested here, data assimilation proves to be crucial to improve short term forecasts of storms and precipitation in RRFS over both regions.

Keywords: Rapid Refresh Forecast System. Convective scale data assimilation. Convection. Gridpoint Statistical Interpolation. Amazon coastal squall lines.

AVALIAÇÃO DA ESTRUTURA DE ASSIMILAÇÃO DE DADOS PARA O PROTÓTIPO DO SISTEMA DE PREVISÃO DE ATUALIZAÇÃO RÁPIDA PARA REPRESENTAR CONVECÇÃO SOBRE LATITUDES MÉDIAS E TROPICAIS

RESUMO

A próxima geração do Sistema de Previsão de Atualização Rápida (RRFS) por conjunto e convecção permitida da NOAA, está em desenvolvimento e visa substituir o conjunto operacional atual de modelos com convecção permitida do NCEP na próxima atualização operacional. Neste estudo, a estrutura de assimilação de dados para o protótipo RRFS é investigada através da simulação de uma linha de instabilidade típica da primavera sobre o centro dos EUA e um caso de linha de instabilidade costeira da Amazônia durante a estação seca de 2020 na Amazônia. O algoritmo de assimilação de dados híbrido em três dimensões por conjunto-variacional e varias configurações no GSI, que é a componente de assimilação de dados atual do RRFS, são avaliados nas análises e previsões do RRFS nos dois casos de linhas de instabilidade. Um domínio com 3 km de espaciamento de grade horizontal é configurado para caso de estudo e ciclos de análise com atualização rápida são realizados. Dados convencionais e não convencionais do Sistema de Assimilação de Dados Global (GDAS) são assimilados bem como as previsões do conjunto de 80 membros do GDAS são usados para a BEC baseada no conjunto. Os resultados do estudo sobre o centro dos EUA mostram que o experimento sem assimilação de dados usado como controle é capaz de representar a convecção observada, mas com células mais fortes e grandes erros de localização. Com a assimilação de dados, esses erros são reduzidos, especialmente nas previsões de 4 e 6 h usando 75 % da matriz de covariância dos erros do background advinda do conjunto (BEC) e com a função de remoção de supersaturação ativada no GSI. A representação da convecção é melhorada ao usar pseudo-observações da camada limite planetária, especialmente às 4 h de previsão, e o viés da previsão de 2 h da temperatura a 2 m é reduzido abaixo de 800 hPa. A previsão de precipitação acumulada em 1 h mais fraca apresenta melhor resultado ao usar o 100 % da BEC nas primeiras 4 h de previsão, mas a previsão da precipitação acumulada horária mais intensa apresenta melhor resultado com 75 % da BEC. Por outro lado, no norte da América do Sul, inicialmente é aplicada uma metodologia para a seleção de casos utilizando o ForTraCC, que se mostrou adequado para a identificação dos principais sistemas convectivos associados a essas linhas de instabilidade. Os resultados das simulações numéricas mostram que o RRFS é capaz de capturar os principais padrões de grande escala com um correto posicionamento dos sistemas de precipitação, conforme estimativas de precipitação CMORPH. Ao usar a assimilação de dados, a cobertura de precipitação ao longo da costa é melhorada e menores valores RMSE e viés na previsão de 3 h de temperatura e temperatura de ponto de orvalho a 2 m são mostrados durante a noite e madrugada. O aumento do raio de localização da BEC mostra incrementos de análise com características mais dependentes do fluxo, no entanto, o impacto nas previsões de observações de superfície resultou ser de neutro para negativo. No geral, os resultados fornecem uma visão sobre a presente habilidade do sistema de assimilação de dados no RRFS e identifica configurações que devem ser consideradas como candidatas para a primeira versão

do RRFS. Embora mais testes e avaliações sejam necessários, além das opções testadas aqui, a assimilação de dados prova ser crucial para melhorar as previsões de curto prazo de tempestades e precipitação no RRFS em ambas as regiões.

Palavras-chave: Sistema de Previsão de Atualização Rápida. Assimilação de dados em escala convectiva. Convecção. Sistema the Interpolação em Ponto de grade. Linhas de instabilidade costeiras da Amazônia.

LIST OF FIGURES

Page

sh

LIST OF TABLES

Page

LIST OF ABBREVIATIONS

1D/3D/4D	–	one/three/four dimensional
ACARS	–	Aircraft Communications Addressing and Reporting System
AIREP	–	Aircraft Weather Report
AMDAR	–	Aircraft Meteorological Data Relay
AMV	–	Atmospheric Motion Vectors
ATLAS	–	Autonomous Temperature Line Acquisition System
BUFR	–	Binary Universal Form for data Representation
CCPP	–	Common Community Physics Package
CMORPH	–	Climate Prediction Center morphing technique
CONUS	–	Contiguous United States
COSMIC	–	Constellation Observing System for Meteorology, Ionosphere,
	–	and Climate
CPC	–	Climate Prediction Center
CPTEC	–	Center for Weather Forecast and Climatic Studies
DTC	–	Developmental Testbed Center
ECMWF	–	European Centre for Medium-RangeWeather Forecasts
EMC	–	Environmental Modeling Center
EnBEC	–	Ensemble Background Error Covariance
EnKF	–	Ensemble Kalman Filter
EnSRF	–	Ensemble Square Root Filter
EnVar	–	Ensemble Variational
FV3	–	Finite Volume cubed-sphere
FV3LAM	–	Finite Volume cubed-sphere Limited Area Model
GDAS	–	Global Data Assimilation System
GFDL	–	Geophysical Fluid Dynamics Laboratory
GFS	–	Global Forecast System
GPCP	–	Global Precipitation Climatology Project
GNSS	–	Global Navigation Satellite System
GPS	–	Global Positioning System
GSI	–	Gridpoint Statistical Interpolation
GSL	–	Global Systems Laboratory
HAFS	–	Hurricane Analysis and Forecast System
HPC	–	High Performance Computing
HPC	–	Hydro-meteorological Prediction Center
HPSS	–	High Performance Storage System
HRRR	–	High-Resolution Rapid Refresh
ICs	–	Initial conditions
INPE	–	National Institute for Space Research
ITCZ	–	Intertropical Convergence Zone
IWV	–	Precipitable Water Vapor

KOMPSat5	–	Korea Multi-Purpose Satellite-5
LBCs	–	Lateral Boundary Conditions
MDCRS	–	Meteorological Data Collection and Reporting Service
MET	–	Model Evaluation Tools
METAR	–	Surface Weather Observations and Reports (translated from French)
MetOp	–	Meteorological Operational satellites
MESONET	–	Mesoscale Network
MLCAPE	–	Mixed Layer Convective Available Potential Energy
MMI	–	Median of Maximum Interest
MODE	–	Method for Object-Based Diagnostic Evaluation
MSMR	–	Multi-Sensor Multi-Radar
MYNN-EDMF	–	Mellor-Yamada-Nakanishi-Niino - Eddy diffusivity-mass flux
NCAR	–	National Center for Atmospheric Research
NCEP	–	National Centers for Environmental Prediction
NOAA	–	National Oceanic and Atmospheric Administration
NRL	–	Navy Research Laboratory
NSST	–	Near-Surface Sea Temperature
NWP	–	Numerical Weather Prediction
OmA	–	Observation minus Analysis
OmF	–	Observation minus Forecast
OSE	–	Observation System Experiment
PBL	–	Planetary Boundary Layer
PIBAL	–	Pilot Balloon observation
PIREP	–	Pilot Report
PMW	–	passive microwave
prepBUFR	–	prepared Binary Universal Form for data Representation
PSAS	–	Physical-space Statistical Analysis System
RAP	–	Rapid Refresh
RASS	–	Radio Acoustic Sounding System
RMSE	–	Root Mean Square Error
RO	–	Radio Occultation
RRFS	–	Rapid Refresh Forecast System
RRTMG	–	Rapid Radiative Transfer Model
RUC	–	Rapid Update Cycle
SRW	–	Short-Range Weather
SODAR	–	Sonic Detection And Ranging
TAMDAR	–	Tropospheric Airborne Meteorological Data Reporting
TDWRs	–	Terminal Doppler Weather Radars
UFS	–	Unified Forecast System
UPP	–	Unified Post Processor
WRF	–	Weather Research and Forecasting
WSR88D	–	Weather Surveillance Radar-1988 Doppler

CONTENTS

Page

1 INTRODUCTION

The increase in computational resources over the last several decades has allowed a considerable increase in horizontal resolution in numerical weather prediction (NWP) (BAUER et al., 2015; YANO et al., 2018). Currently, many NWP centers have developed and use high resolution models operationally for short range weather forecast guidance (BANNISTER et al., 2019). These models have provided more realistic forecasts of hazardous weather events where deep convection is explicitly resolved (LEAN et al., 2008). Typically, in models with grid spacing less than 4 km, the deep cumulus parameterization is turned off and convection is treated explicitly, though not necessary completely resolved. Such configurations are therefore often called convection-allowing models (SCHWARTZ; SOBASH, 2019).

More powerful computer resources have also allowed to leverage advanced developments in weather and climate models under a unified modeling approach. Improvements in the weather forecast skill and climate prediction biases have demonstrated the importance of a unified system in operational numerical weather centers, such as the Met Office, the Météo-France, and the European Centre for Medium-Range Weather Forecasts (ECMWF), which are pioneers in adopting this modeling strategy (HAZELEGER et al., 2010; NATIONAL RESEARCH COUNCIL, 2012). Accordingly, the United States operational NWP enterprise has recognized these advantages which is now captured under the Unified Forecast System effort (UFS[1]). UFS is a unique community-based system that uses the same dynamical core for all spatiotemporal scales with unified physics and data assimilation frameworks, post-processing, verification tools, and software infrastructure (LINK et al., 2017). The UFS application for convection-allowing forecasts is the Rapid Refresh Forecast System (RRFS). RRFS is under development and aims to facilitate the unification of the regional convection-allowing suite of models by subsuming the present suite of multi-dynamic core modeling applications at the National Centers for Environmental Prediction (NCEP) in the next operational upgrade (ALEXANDER; CARLEY, 2020).

The Finite Volume Cubed-Sphere (FV3) dynamical core developed at the Geophysical Fluid Dynamics Laboratory (GFDL) (LIN, 2004; HARRIS; LIN, 2013) was selected for UFS applications, after a thorough evaluation process (JI; TOEPFER, 2016). In the past several years, multiple studies have been conducted using the FV3 dynamical core for convective scale NWP where it has demonstrated skill. For example,

[1] https://ufscommunity.org/

based on the FV3 dynamical core, the System for High-resolution prediction on Earth-to-Local Domains (SHiELD) was also developed at the GFDL, showing a good representation of different phenomena on various time scales, such as hurricanes and the Madden Julian Oscillation (HARRIS et al., 2020b). The grid stretching capability of a FV3-based global model was evaluated in Zhou et al. (2019). Small scale structures of the convective activity in a squall line case were correctly resolved, although an overprediction of the precipitation and radar reflectivity values was observed. The importance of the initials conditions was highlighted, which could have led to better results. In the framework of the 2018 Spring Forecasting Experiment of the National Oceanic and Atmospheric Administration (NOAA) Hazardous Weather Testbed, Gallo et al. (2021) discussed the strengths as well as elements that need improvement in FV3-based convection-allowing models when compared to the High Resolution Rapid Refresh (HRRR) model. An overproduction of high reflectivity values (45 dBZ) in the storms was one of the findings pointed out by the authors. A limited area model capability based on the FV3 dynamical core (FV3LAM) has also been developed, which reduces required computational resources associated with having to run a global model to accommodate a nest. Month long tests at convection-allowing resolution with FV3LAM show comparable performance relative to a two-way nested domain at forecast lead less than 24 hours (BLACK et al., 2021). Additionally, developments on the UFS hurricane application using the FV3LAM, the Hurricane Analysis and Forecast System (HAFS), have shown improvements of track and intensity forecasts compared to the Global Forecast System (GFS) (DONG et al., 2020).

Since its origins, NWP has strongly relied on the accuracy of the "current" state of the atmosphere given to the forecast model as initial conditions for the integration of the primitive equations. Limited and imperfect observations are combined with past estimates of the state of the atmosphere, taking into consideration the uncertainty of both, to produce a more optimal analysis (KALNAY, 2003). Convection-allowing forecasts are no different. At convective scales, forecasts strongly depend on the quality of the initial conditions and the ability of the analysis algorithm to provide accurate state estimates of fine-scale spatiotemporal structures that are of inherent interest in convection-allowing NWP, such as ongoing convection, complex circulations associated with subtle boundaries (e.g. dry lines), etc. To achieve such analyses with reasonable fidelity, dense and accurate observations are needed in the data assimilation window. However, implementing observation operators for the most dense observation types is often complex, such as radar reflectivity, as they are often indirectly related to state variables. In addition, nonlinear model processes along with

nonGaussian error characteristics are commonplace at the convective-scale, both of which encumber the accurate specification of error covariance matrices and, to varying degrees, violate some of the underlying parametric assumptions that are at the foundation of most state-of-the-art analysis algorithms (POTERJOY et al., 2017; GUSTAFSSON et al., 2018). Nevertheless, many studies have shown the benefits of using data assimilation in improving convection-allowing forecasts (DIXON et al., 2009; BROUSSEAU et al., 2012; GAO et al., 2021). Dixon et al. (2009) used the three-dimensional variational algorithm (3DVar) and nudging methods to assimilate moisture and precipitation observations, showing a great performance of convective precipitation forecasts in the first 7 hours. Shen et al. (2017) explored the benefits of using a flow-dependent ensemble covariance from the hybrid ensemble transform Kalman filter based ensemble 3DVar (3DEnVar) and found that hybrid analyses lead to more skillful 12 h precipitation forecasts compared to pure 3DVar.

The NOAA next generation rapidly-updated, convection-allowing ensemble forecast system, the RRFS, is presently being built upon the UFS Short Range Weather Application (SRW) (ALEXANDER; CARLEY, 2020). The first version (v1.0.0) of the SRW (UFS DEVELOPMENT TEAM, 2021) was released in March 2021 and it includes the FV3LAM with pre-processing utilities, the Common Community Physics Package (CCPP), the Unified Post Processing System (UPP), and a workflow to run the system. However, the publicly available SRW does not include a data assimilation capability and thus initial conditions in recent studies (HARROLD et al., 2021; KALINA et al., 2021) are purely from external models. The first and only high resolution convection-allowing data assimilation study using the FV3 dynamical core, although not based on the SRW, is Tong et al. (2020) which studied the impact of the assimilation of radar radial velocity and reflectivity using different data assimilation algorithms with the Gridpoint Statistical Interpolation (GSI) (WU et al., 2002; KLEIST et al., 2009). Since SRW will underpin the RRFS, it is imperative that the data assimilation component behave as good or better than current operational state-of-the-art, which is HRRR version 4. But in order to achieve comparable forecast skill, each component of RRFS needs to be exhaustively tested. Recently, the GSI system has been added as the analysis component of the SRW application to improve initial conditions for the FV3LAM in development of the RRFS at NOAA's Global Systems Laboratory (GSL). This provides a suitable research framework with the necessary components to answer the following question: will current prototype RRFS be capable to better place squall lines over mid-latitudes when using its own initial conditions?

HRRR covers the contiguous United States (CONUS) with 3 km grid resolution (SMITH et al., 2008) and uses the Rapid Refresh (RAP[2]) (BENJAMIN et al., 2016; HU et al., 2017) analyses and forecasts to initiate its hourly updated analyses. RAP performs hourly updated cycles using the GSI hybrid 3DEnVar over the CONUS, Alaska, and the Caribbean Sea with 13 km of horizontal resolution. RRFS is intended to cover a similar domain as the operational RAP which also includes part of the Atlantic Ocean and northern South America. This region is also covered by the HAFS domain, and therefore, it is crucial to evaluate the RRFS ability to represent convection on the tropical region. Known issues still present in large scale models are highly related to the misrepresentation of tropical phenomena (GRIMM; DIAS, 1995). For example, the inadequate representation of the diurnal variability of tropical deep convection that leads to too early peaks of precipitation (BETTS; JAKOB, 2002; ITTERLY et al., 2018) and the double Intertropical Convergence Zone (ITCZ) problem, which is not a feature of the mean tropical circulation as shown by Hubert et al. (1969) but is observed in most of global climate models (HWANG; FRIERSON, 2013), remotely affecting climate projections of the winter precipitation over southwest US and the Mediterranean basin (DONG et al., 2021). Such deficiencies are closely related to the deep cumulus parameterization in global models and subgrid processes that are not well captured by the model resolution. Underrepresented subgrid processes are also a known deficiency in convection-allowing models, along with the size, grid resolution, lateral boundary conditions, among others (KHAIROUTDINOV; RANDALL, 2006). However, the improved realism of mesoscale convective systems and local circulations (GERMANO; OYAMA, 2020), especially when using data assimilation, makes them the state-of-the-art numerical models that can currently be used to better understand the phenomena at convective scales.

Over northern South America is located the Amazon, which is the largest tropical rainforest in the world with ∼40% of the global tropical forest area (ARAGÃO et al., 2014). Its key role in the hydrological water cycle it is well known as it provides humidity which is transported to other regions (DURáN-QUESADA et al., 2012) and water storage in the forest is a critical aspect. Clusters of convective clouds organized in the form of bands originate along the coast of northern South America and propagate across the Amazon basin are known as Amazon coastal squall lines (GARSTANG et al., 1994). These systems are responsible for a considerable portion of the precipitation that falls in that region during the dry season (COHEN et al., 1995). Amazon coastal squall lines have been studied in numerous researches,

[2] https://rapidrefresh.noaa.gov/

mostly using the data collected during field campaigns, reanalyses, satellite-derived data, and numerical modeling (GRECO et al., 1990; SILVA-DIAS; FERREIRA, 1992a; ALCÂNTARA et al., 2011; BIAZETO; DIAS, 2012; OLIVEIRA; OYAMA, 2015). However, the only study found in the literature using data assimilation over the Amazon is Campos (2018), in which precipitable water vapor (IWV) measurements derived from a Global Positioning System (GPS) network were assimilated using GSI coupled to the Weather Research and Forecasting (WRF) model. The GPS network used was the one installed during the field campaign in Belem, Para, as part of the CHUVA project (MACHADO et al., 2014). The lack of dense and routinely available data in near real-time over Amazon makes it difficult for operational NWP applications using data assimilation. This has a direct impact in the adequate representation of these systems and its associated precipitation in operational regional and global forecasts. At convective scales, this is more challenging because of the need of dense observations to ingest in rapid updated data assimilation cycles, such as in HRRR and future operational RRFS. At this scale, an important data source are radars(VENDRASCO et al., 2016). However, despite the existence of a radar network covering parts of northern Brazil, sometimes is hard to find several radars working at the same time mainly due to data transmission errors, maintenance, data storage, among others. Therefore, in this framework the next question arises: will current prototype RRFS coupled with data assimilation and a low data density represent the initiation and development of convection over northern South America?

In this study, the data assimilation infrastructure of the prototype RRFS system using GSI is described and assessed in terms of its ability to improve forecast convection when compared to not using data assimilation. The simulation of frequent weather systems over mid- and tropical latitudes, such as a case of a typical spring squall line over central US and an Amazon coastal squall line case during the 2020 Amazon dry season, gives a deeper understanding about the RRFS data assimilation capability to adequately represent the structure of the observed convection over both of regions. Also, this study gives guidance on the convective scale data assimilation over regions of the globe with low density of data, as in the Amazon region. Operational convective scale data assimilation at the Brazilian Center for Weather Forecasts and Climate Studies of the National Institute for Space Research (CPTEC-INPE[3]) is still an incipient approach. However, in research mode, multiple efforts are underway focusing on testing and evaluating different models, methods, cycling strategies, and datasets. This study seeks to improve our knowledge on this

[3] https://www.cptec.inpe.br/

subject and give indications to the development of the future operational convective scale data assimilation at CPTEC-INPE. It also shows the performance of an FV3-based system, which is relevant to the CPTEC since it envisions unifying its modeling suite and is in the first steps towards selecting a new dynamical core.

1.1 Hypothesis and objectives

The hypothesis of this research is that the RRFS is capable of capturing convection initiation and evolution over mid-latitudes and the tropical region, with good guidance in areas with low data density. To confirm this hypothesis, this study investigates the data assimilation framework for the prototype RRFS to improve convection forecasts over central US and northern South America. This is explored through the assessment of multiple configurations in GSI and physics suites using two cases study. Forecasts are assessed using the Model Evaluation Tools (MET), which is the unified verification package that will be used by UFS applications (BROWN et al., 2021). To fulfill this main objective, the following specific objectives are necessary:

- Explore the initial data assimilation infrastructure of a prototype RRFS system;
- Assess different physics suites on forecasts of convective storms;
- Evaluate various configurations and algorithms available in GSI;
- Investigate the impact of a cycling strategy on the cycled analyses in RRFS;
- Investigate the impact of using data assimilation on forecasts of convective storms.

A theoretical background on the main study subjects is presented in the Chapter 2. A description of RRFS and its components can be found in Chapter 3, with details of the configurations tested. The case study overview over US with the corresponding methods and results are presented in Chapter 4. Chapter 5 is dedicated to the case study over northern South America, which is divided into two main section: the first describes the methodology applied for the selection of the case to be studied and the overview of the case selected and the second section presents the configuration of the numerical experiments performed along with the results and discussions. The conclusions, final remarks, and future work are presented in Chapter 6. The code and data used for this study is detailed in the Appendix A.

2 THEORETICAL BACKGROUND

The theoretical framework on which this research is built is presented in this chapter. The objective is to organize the research carried out and respective results obtained in some aspects (techniques, methods, and phenomenons) that this thesis explores to develop the experiments and analyze the obtained results. It should be mentioned that the literature currently available on some topics is very copious, and a selection of more relevant material for the objective of this study was necessary. The author recognizes that there are many other papers related to the theme of this thesis that are not mentioned in this revision, which can be accessed in the reference section of the referred papers. The intention of this chapter is not to exhaust the subject, but to provide a mainline for readers to start in the theme of this research. The topics covered in this chapter are directly associated with experiments carried out in this study, which can be useful to organize the ideas and give support to the discussion developed in the analysis of results. A background on data assimilation is presented in Section 2.1 which emphasizes the different methods used in this study, such as Variational, Ensemble, and Hybrid data assimilation methods. Section 2.2 gives the basis for an overview of previous studies on convective scale data assimilation. Section 2.3 summarizes the data assimilation activities at CPTEC with a focus on ongoing studies. Emphasis is given to the studies carried out at the center, since the present study, developed at the Graduate Program of INPE, forms part of these efforts and contributes to the mission of the center. Finally, a brief overview of squall lines and specifically on Amazon squall lines is presented in Section 2.4.

2.1 Data assimilation methods

NWP is an initial value problem. This was firstly stated by the Norwegian scientist Vilhelm Bjerknes in 1904 when referring to the "*problems of the meteorological prediction*". According to Bjerknes, one of the "*rational solutions*" was that "*the condition of the atmosphere must be known at a specific time with sufficient accuracy*" (BJERKNES, 1904). Years later, in 1914, the scientist Henri Poincaré postulated that "*if we knew exactly the laws of nature and the situation of the universe at the initial moment, we could predict exactly the situation of that same universe at a succeeding moment*", however, "*we could still only know the initial situation approximately. [...] It may happen that small differences in the initial conditions produce very great ones in the final phenomena.*" (POINCARÉ; MAITLAND, 1914). Decades later it was proved by Edward Lorenz that even with perfect models and perfect observations, the chaotic nature of the atmosphere would impose a finite limit of

predictability in the weather forecast (LORENZ, 1963).

The first NWP attempt was made by Richardson in 1922 by numerically integrating (by hand) the equations of motion to predict the surface pressure tendency over Germany; the result found was 145 hPa in 6 hours. Richardson's work served to highlight the fact that the initial condition must be in balance to perform the numerical prediction in an adequate way, as well as the need for a computer to perform the calculations. His effort was recognized by Jules Charney, who along with other colleagues, pioneered the use of modern computers in weather forecasting and witnessed the beginning of the operational NWP in the 1950s (PALMER; HAGEDORN, 2006).

Initially, a subjective analysis was used to create the initial condition for the numerical model. Observed values were subjectively interpolated to the model grid points and the experience of a synoptic meteorologist was essential for the preparation of the analysis (GILCHRIST; CRESSMAN, 1954). However, in order to create initial conditions without human interference using a computing machine and with more robust interpolation methods, the objective analysis emerged in which the available observations were interpolated on the model grid by means of an interpolation polynomial. This method was firstly proposed by Panofsky (1949) and revisited by Gilchrist and Cressman (1954) using a local quadratic fitting to the observations by the method of least squares. However, because there were far fewer observations than degrees of freedom in the forecast model, and the observations were spatially incomplete, the objective analysis could not be satisfactorily solved by only using observational values. It is worth to mention that, generally speaking, the number of degrees of freedom of the model will be given by the amount of meteorological variables to be analyzed in all grid points (including the vertical) of the model. Gilchrist and Cressman (1954) suggested the use of an earlier forecast for the analysis over areas with poor coverage. A better estimate of the state of the atmosphere was then made by combining the observations with some previous estimate (first guess or climatology) and the use of computers for the automation and operationalization, as proposed by Bergthörsson and Döös (1955). This approach was improved and made operational in the US by Cressman (1959) with the method of successive corrections to the initial guess. Despite the success and simplicity of the Cressman method and its variants (BARNES, 1964), it did not account for the errors in the observations which led to the need to represent mathematically the uncertainties.

Statistical information on the errors in the observations and the model can guide

the weight given to each one during the analysis preparation. Methods of optimal interpolation were therefore introduced for the objective analysis of meteorological variables (GANDIN, 1965). The purpose of this procedure is to calculate an optimal correction (weight matrix) for the background state that minimizes the analysis error covariance by using observations and estimates of the uncertainty associated with the background state and observations. The weight matrix is given by a ratio between the errors of observation and prediction, but given in terms of their respective covariances. The correction can also be thought as an update in the sense that current weather observations are used to update/correct a past weather forecast. In the optimal interpolation method, the analysis equation can be derived using the the least squares estimation. In the literature this method is also called statistical interpolation, because it is not optimal in practice (DALEY, 1991; KALNAY, 2003).

Another approach to objective analysis is the variational assimilation technique. The variational approach can also be derived using the least squares estimation and is equivalent to optimal interpolation as shown in Lorenc (1986) and Kalnay (2003). The main difference between these methods is given by how the weight matrix is specified. This also applies for the Kalman filter. These methods are discussed in the next subsections.

2.1.1 Variational data assimilation

In the variational approach, a cost function (J) is minimized which represents the weighted distance between an $\mathbf{x}$ field and the background, and the weighted distance between that analysis and the observations. The minimum of this function is found for the vector $\mathbf{x} = \mathbf{x}_a$, which is called the optimal analysis and corresponds to the state with the maximum probability, and therefore, the "best estimate" (KALNAY, 2003). For the 3DVar case J has the form:

$$\begin{aligned} J(\mathbf{x}) &= \frac{1}{2}(\mathbf{x}-\mathbf{x}_b)^T B^{-1}(\mathbf{x}-\mathbf{x}_b) + \frac{1}{2}(\mathbf{y}-H(\mathbf{x}))^T R^{-1}(\mathbf{y}-H(\mathbf{x})) \\ &= J_b(\mathbf{x}) + J_o(\mathbf{x}) \end{aligned} \tag{2.1}$$

J_b and J_o are the background and observations terms of the cost function, respectively. The minimum of J for $\mathbf{x} = \mathbf{x}_a$ is found when the gradient of J is zero at $\mathbf{x}_a$ by making the assumptions that the observation operator is linear ($H = \mathbf{H}$), $\mathbf{x} = \mathbf{x}_b$,

$\mathbf{B}$, $\mathbf{R}$, and all the inverse matrices are positive definite[1], such that:

$$\begin{aligned}
\nabla J(\mathbf{x}_a) = 0 &= 2\mathbf{B}^{-1}(\mathbf{x}_a - \mathbf{x}_b) - 2\mathbf{H}^T\mathbf{R}^{-1}(\mathbf{y} - H(\mathbf{x}_a)) \\
0 &= \mathbf{B}^{-1}(\mathbf{x}_a - \mathbf{x}_b) - \mathbf{H}^T\mathbf{R}^{-1}(\mathbf{y} - H(\mathbf{x}_b)) - \mathbf{H}^T\mathbf{R}^{-1}\mathbf{H}(\mathbf{x}_a - \mathbf{x}_b) \\
\mathbf{x}_a - \mathbf{x}_b &= (\mathbf{B}^{-1} + \mathbf{H}^T\mathbf{R}^{-1}\mathbf{H})^{-1}\mathbf{H}^T\mathbf{R}^{-1}(\mathbf{y} - H(\mathbf{x}_a))
\end{aligned} \tag{2.2}$$

therefore, the analysis using the variational approach has the form:

$$\mathbf{x}_a = \mathbf{x}_b + (\mathbf{B}^{-1} + \mathbf{H}^T\mathbf{R}^{-1}\mathbf{H})^{-1}\mathbf{H}^T\mathbf{R}^{-1}(\mathbf{y} - H(\mathbf{x}_b)) \tag{2.3}$$

or, the incremental form:

$$\begin{aligned}
\delta\mathbf{x}_a &= (\mathbf{B}^{-1} + \mathbf{H}^T\mathbf{R}^{-1}\mathbf{H})^{-1}\mathbf{H}^T\mathbf{R}^{-1}\delta\mathbf{x}_b \\
\delta\mathbf{x}_a &= \mathbf{x}_a - \mathbf{x}_b, \delta\mathbf{x}_b = \mathbf{y} - H(\mathbf{x}_b)
\end{aligned} \tag{2.4}$$

where $\mathbf{x}_a$ is the analysis model state vector, $\mathbf{x}_b$ is the background model state vector, $\mathbf{y}$ is the vector containing the observations, $\mathbf{B}$ and $\mathbf{R}$ are the covariance matrices containing the background and observations errors, respectively. The combination of these covariance matrices will determine the amount of correction to be applied to the background fields. In theoretical terms these matrices are obtained by applying the Mathematical Expectation in the multiplication of the corresponding vector error by its transpose ($\boldsymbol{\epsilon}\boldsymbol{\epsilon}^T$). The observation error covariance matrix includes contributions from the instruments, representativeness errors and from the observation operator H. H represents the observation operator, or *forward model*, that performs the interpolation and transformation of the model variables into the space and time of the observations through the product $H(\mathbf{x}_b)$. The comparison between observations and their counterpart from the model, $(\mathbf{y} - H(\mathbf{x}_b))$, is known as observational increment or innovation vector, and when compared against the analysis is known as analysis residuals. The H and $\mathbf{H}$ in Equation 2.3 differ in the fact that the later is called the Tangent Linear Forward Model operator and results from the linearization of the observation operator in the vicinity of the background state (see Equation 2.5) as shown by Bouttier and Courtier (2002). The authors remark that this hypothesis has limitations in the presence of discontinuities where higher-order variations of H cannot be neglected. This is a particularly important point in convection-allowing models. Clouds represent discontinuities in the atmospheric liquid water field. The liquid water discontinuity leads to sharp temperature and wind gradients (vertical and horizontal). These gradients are fundamental for computing the moisture, heat

[1]For any vector $\mathbf{x}$, $\mathbf{x}^{-T}\mathbf{A}\mathbf{x} > 0$ unless $\mathbf{x} = 0$. The eigenvalues of the matrix are the variances in the direction of the eigenvectors (BOUTTIER; COURTIER, 2002)

and momentum exchanges between the clouds and the environment.

$$H(\mathbf{x}) - H(\mathbf{x}_b) \approx \mathbf{H}(\mathbf{x} - \mathbf{x}_b) \tag{2.5}$$

In comparison with the optimal interpolation, the variational approach provides greater flexibility in terms of, for example, the data selected for the analysis. The background error covariance matrix does not need to be defined through local approximations. An approach that has been widely used to determine the background error covariance matrix in variational systems is the National Meteorological Center method (NMC) (PARRISH; DERBER, 1992). In this method, the differences between pairs of forecast valid at the same time but with different length (e.g., 24 and 48 hours) are considered to be representative of the background error. This method is easy to implement and provides an estimate for the entire domain. Another advantage of the variational approach is the addition of constraints as a term in J (J_c) which helps to control nonphysical solutions in the analysis. Furthermore, more robust observation operators can be developed allowing for more nonlinear relationships between observed and model variables as well as the direct assimilation of quantities such as radiances instead of retrievals (KALNAY, 2003).

In practical situations, the cost function J is minimized using iterative methods such as the conjugate gradient (DERBER; ROSATI, 1989). This is because the high computational cost required for the inversion of the matrices in Equation 2.3. Iterative methods can still be very computationally expensive and therefore some approaches, such as the incremental technique and the use a preconditioner (a change of minimization space) to decrease the number of iterations (LORENC, 1997), are followed in order to reduce that cost, in addition to code optimization. Another approach to reduce the computational cost, which increases with the model resolution, and reduce the complexity of the data assimilation system, is to calculate the analysis in a control variable space. Advantage is taken from relationship between variables, such as the stream function and velocity potential and u and v components of the wind. Thus, in many cases, the control variables are those used in the minimization.

As 3DVar, the 4DVar algorithm seeks to find the optimal analysis that minimizes J. However, it includes the time dimension which allows the use of observations distributed within the assimilation window. Thus, differently than 3DVar which considers that observations in the assimilation window are all valid at the same time, 4DVar takes into account the time that the measurement was taken. In order to obtain the model states at a given time i ($\mathbf{x}_i$), this method depends on a model

forecast operator that will be integrated from the initial time to i. In 4DVar, the minimization of J by finding the analysis state when $\nabla J = 0$, will require not only the model integration from times 0 to n but also the integration of the adjoint model operator (M_i^T) and transposes of the tangent linear model operators at each time ($\mathbf{H}_i^T$). Therefore, this method is more computationally expensive than 3DVar and the implementation of the adjoint model is complex. Nevertheless, by using the forecast model in the assimilation procedure, it is ensured the consistency between the analysis and the model equations. Kalnay (2003) highlights the equivalence between the 4DVar analysis at the final time step and the Kalman filter analysis.

It is important to point out that in addition to the assumptions mentioned before, the variational approach (3D/4DVar), as well as optimal interpolation, assumes that $\mathbf{x}_a$ will be the best estimator of the true state ($\mathbf{x}_t$) when the background and observations are unbiased (i.e., $\mathbf{x}_b - \mathbf{x}_t = \mathbf{y} - H(\mathbf{x}_t) = 0$) and their error covariance matrices $\mathbf{B}$ and $\mathbf{R}$ are assumed to be known. From the Bayesian point of view this means that the probability density functions are Gaussian (the expected value of the mean of the innovation is zero). Additionally, it is assumed that their errors are uncorrelated, meaning that their covariance is equal to zero (i.e., $(\mathbf{x}_b - \mathbf{x}_t)(\mathbf{y} - H(\mathbf{x}_t))^T = 0$). Nevertheless, the variational approach (e.g., pure 3DVar) was successfully used for many years in operational data assimilation activities at the NCEP (PARRISH; DERBER, 1992) and the Met Office (LORENC et al., 2000). As data assimilation methods evolved, operational centers also transitioned to use more sophisticated methods (BAUER et al., 2015; GUSTAFSSON et al., 2018).

2.1.2 Kalman filter

The Kalman filter was introduced in Kalman (1960) to address issues in the area of communication and control related to signals and noise for a linear dynamic system. In Kalman and Bucy (1961), this study was extended to a continuous-time case. With this method, the analysis obtained is equivalent to the optimal interpolation and variational approaches, using the least square estimation. The time distribution of the observations is taken into account and the forecast error covariance matrix is found at every time step and over the entire interval over which data are provided. The observations are assimilated sequentially and discarded once the information was used for the analysis (GHIL; MALANOTTE-RIZZOLI, 1991). A forecast model M is used for the propagation in time, such that $\mathbf{x}_{t+1} = \mathbf{M}(\mathbf{x}_t) + \eta$, $\langle \eta \eta_t^T \rangle = \mathbf{Q}$, where $\mathbf{M}$ is the linearized forecast operator and $\mathbf{Q}$ is the model error covariance matrix (LORENC, 1986). The analysis equation derived using the Kalman filter is as

follows:

$$\mathbf{x}_a(i) = \mathbf{x}_f(i) + \mathbf{K}(i)(\mathbf{y}(i) - H(i)\mathbf{x}_f(i)) \tag{2.6}$$

where

$$\mathbf{x}_f(i+1) = M_{i\rightarrow i+1}\mathbf{x}_a(i) \tag{2.7}$$

$$\mathbf{P}_f(i+1) = M_{i\rightarrow i+1}\mathbf{P}_a\mathbf{M}^T_{i\rightarrow i+1} + \mathbf{Q}(i) \tag{2.8}$$

$$\mathbf{K}(i) = \mathbf{P}_f(i)\mathbf{H}^T(i)(\mathbf{H}(i)\mathbf{P}_f(i)\mathbf{H}^T(i) + \mathbf{R}(i))^{-1} \tag{2.9}$$

$$\mathbf{P}_a(i) = (\mathbf{I} - \mathbf{K}(i)\mathbf{H}(i))\mathbf{P}(i) \tag{2.10}$$

All variables follow the definitions as in 3DVar but at time i and using a forecast model M. Some differences in the notations correspond to the background and analysis error covariances, denoted by $\mathbf{P}_f$ and $\mathbf{P}_a$, respectively, as well as the background state $\mathbf{x}_b$ which is now a forecast denoted by $\mathbf{x}_f$. $\mathbf{I}$ is the identity matrix. $\mathbf{K}$ is the so-called Kalman gain matrix and is equivalent to the weight matrix in the optimal interpolation method. The Kalman filter assumes a linearized forecast model and observation operator (i.e., $M = \mathbf{M}$ and $H = \mathbf{H}$), meaning that the computations are done in the vicinity of the model state and forecast model, respectively, similar to the concept in Equation 2.5. For the case in which the forecast model and observation operator are nonlinear, an Extended version of the Kalman filter (EKF) was developed. However, since in EKF the linear tangent and adjoints of the nonlinear model are needed to compute the error covariances, this method is more complex and requires a high computational cost (DALEY, 1991; BOUTTIER; COURTIER, 2002).

2.1.3 Ensemble data assimilation

Results from Lorenz's twin experiments led scientists to realize that perfect forecasts would never be achievable. Instead, it could be possible to quantify the uncertainties by the means of an ensemble of forecasts (PALMER; HAGEDORN, 2006). The use of ensemble methods has been key for the prediction of highly variable parameters such as precipitation, where the spread of the ensemble have been used to quantify the uncertainty of the rain location and intensity forecasts (SCHUMACHER; DAVIS, 2010).

In the context of data assimilation, one of the greatest advantages of ensemble forecasts is the estimation of the statistics of the background errors, giving a flow dependent estimate of the uncertainties. The flow dependent characteristic allows to account for time varying and more spatial anisotropic contributions in the covariances statistics typical of systems with discontinuities or sharp horizontal gradients.

This approach was firstly explored by Evensen (1994) with the Ensemble Kalman Filter (EnKF) method for an oceanographic application. In EnKF, an ensemble of perturbations is created which is added, for example, to the observations dataset that is assimilated by each member of the initial state. Thereafter, each of the initial states is used to integrate the model and create a subsequent ensemble forecast that will be used as background or first guess for the next ensemble analysis. The EnKF method and its variants, for example the Ensemble Square Root Filter (EnSRF) (WHITAKER; HAMILL, 2002), have been widely used by the research community as well as operational activities. Ensemble-based systems require lower computational cost than EKF and better results have been found when compared to pure 3D or 4DVar (HAMILL; SNYDER, 2000; HAMILL et al., 2001).

Nevertheless, ensemble-based systems need a large number of ensemble forecasts in order to estimate a full rank covariance matrix. Even with the latest increase in computational resources, this is still computationally impractical for operational and research activities. Hamill et al. (2001) compared the signal and noise estimates from an ensemble with 400 members versus an ensemble with 25 members and showed that the ensemble-based covariances are very noisy when using the smaller ensemble size, which resulted in inaccurate analyses. In addition, the authors found out that for a small size ensemble there is a distance-dependent noise in the magnitude of the background error covariance estimates. This means that distant observations could contribute for more noise than closer observations. That happens basically due to bad specification of the errors resulting in a wrong weight given to the observation or the background for the analysis, which grows with the cycles. This can make the filter inefficient and is known as filter divergence. This issue can be addressed by localizing the covariances. Houtekamer and Mitchell (2001) used a Schur product (i.e., element by element multiplication) to spatially localize the covariances. The distance-dependent correlation matrix of Gaspari and Cohn (1999) was used for every grid point, in which the correlation is close to 1.0 near the observation location and decreases to 0.0 as the distance increases. A length scale needs to be specified in the correlation matrix which determines how the ensemble covariance varies with distance. For small (large) ensemble size it was pointed out that the localization function should also be small (large). As confirmed by Hamill and Snyder (2000) and Whitaker et al. (2004), this approach is particularly important in areas of low data density such as over the Antartica and the Southern Hemisphere.

Furthermore, other approaches such as the covariance (or multiplicative) inflation, the additive inflation, and the relaxation-to-prior have been developed in order to

mitigate the filter divergence problem and are referred in the literature as parameterizing the model error. The relaxation-to-prior is performed after the analysis is obtained by modifying the analysis perturbations back toward the prior perturbations (WHITAKER et al., 2008). In the inflation methods, the covariances are either multiplied by a factor or random noise is added, respectively. Using both inflation approaches, Hamill and Whitaker (2005) have proved their effectiveness with better results when using the additive inflation. The inflation can be defined in several ways. For example, in Hamill et al. (2001) the covariances were inflated by 1% each cycle. However, finding the adequate values for the inflation can be computationally expensive which have motivated the development of adaptive methods for the parameters estimation (KOTSUKI et al., 2017).

Using the EnSRF, Whitaker et al. (2008) explored the three model errors parameterization methods in comparison with an experiment using 3DVar. In this study, the authors used the Blackman window distant-dependent function of Oppenheim and Schafer (1989) for the localization of the covariances instead of the function of Gaspari and Cohn (1999). The additive inflation was set to vary with latitude and in the vertical, and it was found to produce better results than multiplicative inflation and relaxation-to-prior. The geopotential height forecast skill was greatly improved over Southern Hemisphere extratropics and modest improvements were also found in the Northern Hemisphere extratropics.

2.1.4 Hybrid data assimilation

An alternative method for the objective analysis was proposed by Hamill and Snyder (2000) which combines the background error covariance from the 3DVar system (static or climatological statistics) with the ensemble background error covariance of the EnKF. This method takes the advantages of both methods and therefore is called hybrid. It allows the use of flow dependent background error covariance while helping the rank deficiency by combining it with the static matrix. It also avoids the development and maintenance of a tangent linear and adjoint model. Thus, its implementation is more straightforward with a reduction of the computational cost involved. In this method the most probable optimal analysis state is found as in 3DVar by minimizing the cost function J. The analysis formulation follows the incremental form of Equation 2.4 and uses an iterative conjugate residual descent algorithm to find the analysis increment. In the study, the $\mathbf{B}$ matrix from the 3DVar has the following form:

$$\mathbf{B}_{static} = \mathbf{SCS}^T \tag{2.11}$$

where $\mathbf{C}$ is the diagonal matrix of variances of the spectral coefficients and $\mathbf{S}$ is a transform from spectral coefficients to grid points. The study ofHamill and Snyder (2000) was conducted using a quasegeostrophic spectral forecast model. On the other hand, the sample covariance matrix estimated for each member using the EnKF ($\mathbf{P}_i^b$) follows the suggestion of Houtekamer and Mitchell (1998) of excluding the last forecast from the estimation of the covariance in order to avoid an underestimate of the variance of the forecast errors, and is defined as:

$$\mathbf{P}_i^b = \frac{1}{n-2} \sum_{j=1, j\neq i} (\mathbf{x}_j^b - \overline{\mathbf{x}}_i^b)(\mathbf{x}_j^b - \overline{\mathbf{x}}_i^b)^T \tag{2.12}$$

where the overbars represent the ensemble mean, n is the number of members and subscripts refer to ensemble members. Finally, the $\mathbf{B}$ matrix of the hybrid EnKF–3DVar scheme proposed has the form:

$$\mathbf{B}_{hybrid} = (1-\alpha)\mathbf{P}^b + \alpha \mathbf{S}\mathbf{C}\mathbf{S}^T \tag{2.13}$$

where the parameter α controls the relative weight that is given to each covariance matrix and can have values up to 1. The difference $1-\alpha$ indicates the weight given to the ensemble background error covariance. The case of $\alpha = 0$ indicates the use of pure ensemble-based background error covariance and $\alpha = 1$ for pure static background error covariance. Different values of α were tested in Hamill and Snyder (2000), such as 0.1, 0.4, 0.7, and 1.0, along with various size of the ensemble (25, 50, and 100). Compared with 3DVar, the hybrid system proved to be superior with encouraging results for sparse observation networks, especially for small ensemble sizes. The analysis errors were more reduced when using a $\alpha = 0.1$ and 50 members, and slightly better when using 100 members. It also showed potential for higher resolution forecasts.

Thereafter, this method was explored in many researches using a combination of variational and ensemble methods variants. Etherton and Bishop (2004) explored a hybrid data assimilation scheme based on the ensemble transform Kalman filter (ETKF) and 3DVar. This study was inspired by the fact the many of the studies at the time were conducted under perfect model assumptions. Thus, the performance of these systems was examined in the presence of model errors, such as resolution and parameterization errors, using a two-dimensional turbulence model. A relaxation method was applied for the model errors parameterization. Different ensemble generation schemes were also tested. In this sense, the authors found that a perturbed observations hybrid and a singular vector hybrid showed a better

performance among the schemes tested. Overall, the hybrid ETKF/3DVar system outperforms the purely isotropic correlation model in 3DVar. Smaller errors in the average 24 h forecast were found for any combination of the ensemble-based data assimilation tested when compared to 3DVar and for both model errors. The results demonstrated that the data assimilation performance can be significantly improved even in cases of very small relative weight of ensemble-based error correlations to the hybrid error correlation model.

A hybrid system also based on the ETKF was investigated by Wang et al. (2007). In this case instead of 3DVar, the optimal interpolation analysis scheme gave the framework to find the mean analysis state. This hybrid system was then compared with an EnSRF analysis using a two-layer primitive equation model and perfect model assumptions. As expected, the hybrid and EnSRF systems outperformed the pure optimal interpolation. For α values between 0.2 and 0.6, the hybrid ETKF–Optimal interpolation scheme using 50 member ensemble showed lower root mean square analysis error when spatially localizing the covariances than when not. The results using the EnSRF showed similar performance to the hybrid when using those α values. Larger errors were found when reducing the size of the ensemble to 20 members and filter divergence was experienced in EnSRF when reducing the ensemble size to 10 and 5 members. The authors pointed out that the better results found for the hybrid system for small ensemble sizes was due to the static background error covariance, which helped to keep the EnKF stable.

A further study of Wang et al. (2009) focused on the case of the imperfect model case, this is including model errors. The hybrid system used was also based on the ETKF and compared with an EnSRF analysis. In addition, the same two-layer primitive equation model was used. Additive noise was used to parameterize model errors in the background ensemble for both schemes. As in the previous study, the EnSRF showed to be more sensitive to the ensemble size than the hybrid system, experiencing filter divergence for small sizes. The authors pointed out that this was due to sampling errors in parameterizing the model errors and the additional covariance localization in EnSRF (only one in EnKF) which could have led to unbalance in the analysis.

A variation of the hybrid method was proposed by Penny (2014) using a hybrid gain data assimilation. In this new method the philosophy is inverse, it seeks to explore the impacts that a 3DVar system has on an EnKF. The variational approach is used to stabilize the EnKF within the model space. In this study the hybrid gain

system uses the local ensemble transform Kalman filter (LETKF) (HUNT et al., 2007) and the 3DVar. The goal is to calculate a hybrid Kalman gain matrix that will be used to obtain a hybrid analysis by using the LETKF. The hybrid gain matrix is composed of the Kalman matrix as in Equation 2.9 and the correction applied to the background fields in the variational algorithm as in Equation 2.3. Although, the Lorenz-96 model was used, the results showed better results when using this new method over pure 3DVar and LETKF. Nevertheless, the filter diverge issue was faced for a 5 members ensemble. Additionally, this method relies on the tuning of the parameter α. To avoid the definition of the relative weight necessary in the hybrid gain approach, Chang et al. (2020) developed a method in which the correction from the variational is restricted to the subspace orthogonal to the linear basis defined by the analysis ensemble perturbations. This study uses a quasigeostrophic model and the EnKF for the hybrid analysis. In the recent work of Azevedo et al. (2020), a geographically varying weighting factor alpha is defined and the ensemble spread is used for the assignment of the weights.

Since hybrid systems give better results even for small ensemble size (depending on the approach applied), the attractiveness of the hybrid ensemble variational (3D/4DEnVar) data assimilation method for operational activities was quickly recognized by the scientific community (LORENC, 2003; BUEHNER, 2005). Nowadays, it has gained mainstream practice and is widely used by the research community as well as operational NWP centers (KLEIST; IDE, 2015a; BANNISTER, 2017), in particular for convective scale applications (GUSTAFSSON et al., 2018).

2.2 Convective scale data assimilation

A better understanding of atmospheric processes related to convective clouds and storms was possible with the development of nonhydrostatic cloud-scale numerical models in the late 1970s (LILLY, 1990). As NWP models increased their spatial resolution and more dense and frequent observations were available, the need for initial conditions with a more realistic representation of the phenomena occurring in a high spatiotemporal scale along with the favorable dynamical and thermodynamical environments for those phenomena to occur became crucial. Typically, atmospheric phenomena lasting few minutes to several hours and with horizontal scale of about 2 m to 2000 km are between the microscale and mesoscale. For example, cumulus cloud convection has a characteristic scale of 1 km, deep convection of 10 km, and mesoscale processes of 100 km (COLEMAN; LAW, 2015). Particularly, the scale at which the moist-convective processes occur is known as convective scale. NWP at

convective scales aims to accurately predict local weather such as a preconvective environment, convection initiation, cloud, precipitation, etc. (CLARK et al., 2016).

Currently, that is achieved using convection-allowing models with small grid lengths, typically 1–4 km. At such grid lengths, a more detailed representation of the topography is possible as well as the surface fluxes and local circulations. Using the WRF model with three nested domains, Germano and Oyama (2020) identified local circulation features over eastern Amazon. Within the smaller domain (0.3 km grid spacing), a river-breeze circulation was detected and confirmed in the anomaly of the zonal and meridional wind fields for Belem, Para, Brazil. The river breeze is a very important mechanism controlling convection initiation in the Amazon. However, it should be mentioned that the sensitivity to horizontal grid spacing in convection-allowing models is subject of active research and development (SCHWARTZ; SOBASH, 2019). Lean et al. (2008) using the Met Office's Unified Model showed that the 4 and 1 km grid length models generally give precipitation fields more realistic than with 12 km grid spacing because convection processes are explicitly resolved on this scale, primarily the time evolution of the convection. It results in better forecasts than when the processes are parameterized in the larger scale. However, the showers in the simulations were too small and overall too intense. As mentioned previously and as the name indicates, convection-allowing models do not require to active a convective parameterization in order to adequately represent deep convection. A problem with convective parameterizations is the fact that the parameterization is called every so many time steps. Thus, convective forcing is not continuous in time. Clark et al. (2016) pointed out that these models are able to represent with a good degree of realism the formation of daughter cells and back-building of storms, advect showers realistically with the flow, organize convection, and improve the location of showers. In these models, the microphysical and turbulence parameterization pass then to play a very important role. However, accurate estimates of the model forecast uncertainty are necessary for realistic predictions at this spatial and temporal scale. The errors in the initial conditions can grow more rapidly in a short period. Therefore, the use of ensemble-based data assimilation systems can be essential.

Initially, much of the developments successfully used for the data assimilation at synoptic scales, such as those described previously, were applied or adapted for convective scales. Brousseau et al. (2011) using differences between forecasts from an AROME (Applications of Research to Operations at Mesoscale) ensemble assimilation, introduced spatial localization to the climatological background error covariances used in the operational 3DVar system at Météo-France. In a follow up

study, Brousseau et al. (2012) generalized the covariance calculation in order to account for flow dependency in the background error covariances in the AROME-France (2.5 km resolution) 3DVar operational system. Although a small number of members was used (6 members), the authors affirmed that the flow dependent covariance estimates were statistically robust. A clear improvement was found in terms of the Brier Skill Score for the 6 h rainfall totals forecasts when compared to an experiment using the 3DVar with static background error covariance. Ballard et al. (2012) showed that using pure variational methods there was an improvement of 18 hours gain in the skill of the Limited Area Forecasting as measured by the UK Index during the period of 2001 to 2007. Moreover, between 2006 and end of 2010, there was a 24 hours increase in skill of forecasts of cloud fraction $> .325$. A multi-incremental 4DVar scheme for the HIgh Resolution Limited Area Model (HIRLAM) forecasting system was introduced in Gustafsson et al. (2012). During the tangent linear model integrations as part of the 4DVar minimization, a weak digital filter constraint was applied in order to damp high-frequency oscillations. It removed the need for explicit initialization for the HIRLAM integration. The multi-incremental 4DVar system designed was superior to the 3DVar, showing improvements on the baroclinicity of the initial state which led to an adjustment in the intensity of the storm development.

Hybrid systems have also proved to be beneficial for convective scales, as it allows a greater ability to deal with errors. At NOAA, HRRR was made operational in September 2014 using a 3DEnVar approach and GSI as the analysis system (BENJAMIN et al., 2016). HRRR uses lateral boundary conditions from the 13 km RAP forecasts and performs 18 hour forecasts every cycle and 48 hour forecasts at 00:00 and 12:00 UTC. Similar to RAP, HRRR performs hourly updated cycles using a digital-filter initialization, pseudo-innovations from near surface observations within the planetary boundary layer (PBL), radar reflectivity assimilation using a latent heating approach, and a cloud and hydrometeor assimilation techniques using a combination of information from METAR (METeorological Aerodrome Reports), Geostationary Operational Environmental Satellite (GOES) and the background state (BENJAMIN et al., 2016). The recent study of Benjamin et al. (2021) describes the updated version of the stratiform cloud and hydrometeor assimilation technique (HU et al., 2006a; HU et al., 2006b). The latent heat approach in HRRR aims to update the temperature tendency during the beginning of the model integration with a reflectivity-based temperature tendency. It allows to introduce observed deep convection into the model. At grid points without radar coverage, the tendency calculated by the model is then used. The PBL pseudo-observation function was initially

developed to further leverage the information provided by METAR observations, extending their representativeness through the PBL depth and then obtaining a better representation of the PBL in the Rapid Update Cycle (RUC) analyses. Using this function, Benjamin et al. (2004) found improvements in the temperature, dew point, and CAPE forecasts when spreading the innovations from temperature, moisture, and wind in the layers above surface and below the top of the PBL. Smith et al. (2007) also found a positive impact in the 3 h forecast of CAPE by using the PBL pseudo-observations, and the impact was greatly increased when additionally assimilating GPS-IPW. Benjamin et al. (2010) found higher positive impact during the summer, when the PBL is deeper. This is an important point that needs to be carefully analyzed in the Amazon convective system. Precipitation by warm clouds is quite important in the Amazon. The Large-Scale Biosphere-Atmosphere Experiment research shows that warm cloud precipitation may be responsible for about 50% of the precipitation during the wet season in southwest Amazon (KELLER et al., 2004). However, most models do not appropriately account for the warm cloud precipitation. The vertical distribution of latent heating in shallow warm precipitation cloud is much shallower than the convective diabatic heating of deep clouds. Therefore, the vertical structure of the response circulation to the convective forcing is not like the response to deep convection forcing (upper tropospheric divergence and low level convergence) and is therefore an important issue for future research.

A new data assimilation method for the convective scale using a local particle filter is presented in Poterjoy et al. (2017). Although the potential of the method was explored in an idealized framework.

High resolution and dense observations from different sources are core in convective scale data assimilation. For example, polarimetric radars provide a high and frequent volume of information on the types, shapes, and size distributions of hydrometeors which are used to identify and characterize the convection as well as estimate the precipitation occurring in the radar range. However, to introduce these data into the assimilation system an observation operator is needed as well as control variables related to hydrometeoros. For the radar-derived radial wind velocities the observation operator needs contribution from the prognostic continuity equation for radial velocity in order to estimate the entire velocity field. Radar-derived reflectivities, on the other hand, are more difficult to assimilate and therefore are basically used to retrieve hydrometeors information (TONG et al., 2020). Several studies have been carried out exploring the use of these data using different approaches. For instance, the 3DVar has been used, however the addition of radar data leads to unbalance in

the initial condition and therefore the impact of assimilating these data is mainly in the first forecast hours, up to 3 h forecast in Sun et al. (2012) and up to 7 h forecast in Wang et al. (2013a) using the WRF model. The 4DVar approach can implicitly alleviate part of this issue (WANG et al., 2013b), but despite of the success the method, at the beginning of the assimilation window a static background error covariance is used (GAO et al., 2021). Snyder and Zhang (2003) introduced the use of the EnKF method to provide cross covariances between the predicted radar reflectivity and the other model state variables with satisfactory results. However, this method is still affected by sampling and model errors. Alternatively, more promising results have been found when using hybrid systems, such as the hybrid 3DEnVar (SHEN et al., 2017) and 4DEnVar within the WRF model (GAO et al., 2021). Gao et al. (2021) used 75% weighting value for the ensemble covariance with a 50 member ensemble. In this study, the velocity components were used as new control variables and an indirect scheme was used to assimilate radar reflectivity. The results outperformed those obtained with pure 3DVar and hybrid 3DEnVar, in terms of the neighborhood-based fraction skill score and bias.

In the Netherlands, other data that have been explored are wind and temperature observations retrieved using the tracking and ranging radar from the air traffic control facility at Schiphol Airport, Amsterdam (HAAN; STOFFELEN, 2012). A range of 270 km from the surveillance radar is considered to extract the observations. Hourly cycles assimilating these new data into the HIRLAM (version 7.0) model with 11 km horizontal resolution and using a 3DVar technique improved wind and temperature forecasts up to 2–3 hours. This is of particular importance for nowcasting applications. Upper air observations are not available from many sources, usually radiosondes and aircraft. Thus, as a new data source for upper air wind and temperature profiles, it should be more explored and considered in other NWP centers.

Other sources of dense and high temporal resolution data are radiances derived from GOES satellites, especially those from microwave and infrared channels sensitive to humidity, cloud, and precipitation. For many years operational activities in NWP centers only included the assimilation of clear sky radiances (i.e., not cloud and precipitation-affected). However, many efforts in the last years have been focused on the development of a forward operator (radiative transfer model) that calculates the model counterpart that account for these effects, and therefore that is currently a reality in some centers. However, several issues arise. For example, the undetermined problem in the absence of background and viceversa, nongaussianity in the error

statistics, observation operator with scattering capabilities, the tangent linear and adjoint moist physics models, among others (GEER et al., 2017). Despite those known issues, results have proved the positive impact of assimilating those data, and thus, work is underway in most of NWP centers toward their assimilation (GEER et al., 2018).

Although observations with higher spatiotemporal availability are desired for convective data assimilation, observation error correlations can break the assumption of uncorrelated errors that is usually made in data assimilation algorithms (as explained previously). A common practice in NWP is thinning and/or superobbing observations, such as satellite-derived radiances and radar-derived radial winds. Thinning is applied in order to reduce redundant data and thereby reduce the error correlation between observations very close to each other. Meanwhile, superobbing reduces the density of the data by averaging the innovations in a region and assigning this average (plus the background value) as a single superobservation value. This method intends to reduce representativeness errors when comparing simulated against observed ones due to, for example, the model discretization (HOFFMAN, 2018).

Simulation and sensitivity experiments with convective scale models can provide more details on the relative importance of different meteorological variables as initial conditions. Weissmann et al. (2017) used the information from the ensemble to estimate the impact of different observations. The authors concluded that attention need to be paid to possible systematic errors in the verification metric, especially if it is correlated with the analysis. A large beneficial impact in the surface pressure observations was found, but the authors presume that, at some extent, it could be related to the model bias correction. Therefore, the objective would be to remove the cause of the model bias and not the symptom. For the ensemble approach, the authors stated that a better understanding of where to place our priorities in relation to regional observation networks and the inclusion of new observations in the regional assimilation of data is needed.

Currently, there is a wide variety of available observations that have not yet been exploited in convective scale data assimilation systems, such as Global Navigation Satellite System (GNSS) radio occultation (GNSSRO) observations. Obviously, that is due to its current distribution in space and time. Ladstädter et al. (2015) pointed out the urgent need to continue GNSSRO missions with a sufficient number of GNSSRO observations, considering that at least 20.000 events per day are a required number for climate and other applications, including at regional scale. Other studies

such as VILLANUEA-BIRREL et al. (2008), have addressed the assimilation of GNSSRO data in a limited area to study mesoscale convective systems. The impact of assimilating GNSSRO data on cases of severe weather has also shown encouraging results (HA et al., 2014; HUANG et al., 2009). With the Constellation Observing System for Meteorology, Ionosphere, and Climate (COSMIC-2) launched in June 2019, new horizons for GNSSRO applications have been opened, especially for the tropical latitudes.

As shown here, convective scale data assimilation is a research area with great challenges. Continued efforts are being made to develop new methodologies that address the current demand for initial conditions for high resolution forecast models. Some review studies, such as Bannister (2017), Gustafsson et al. (2018), Yano et al. (2018), Bannister et al. (2019), offer a broad spectrum of information on what is being done in terms of both, research and operations, as well as discuss several of the challenges of these activities. Furthermore, these studies provide new ideas on observations that could be used and methodologies that could be followed, opening a path for further research.

2.3 Data assimilation at CPTEC

Operational data assimilation activities at CPTEC started in 1998 with the Physical-space Statistical Analysis System (PSAS) using the regional Eta model. But it was not until 2004 that data assimilation in both regional and global scales became operational (HERDIES et al., 2008). Between 2006 and 2013, several efforts were dedicated to implement the LETKF with the the General Atmospheric Circulation Model (MCGA; acronym in Portuguese for Modelo de Circulação Geral Atmosférico)) (FERTIG et al., 2009). However, in practice, in January 2013, the PSAS was replaced with the 3DVar algorithm of the GSI analysis system. The new system was called G3DVar integrating the 3DVar method with the MCGA. The difference between PSAS and the algorithms presented in Section 2.1 is that, as the name indicates, the minimization is performed in the observations space instead of the model space. A greater number of observations was possible to ingest into the assimilation window mainly due to the capability to directly assimilate satellite radiances in GSI, with the greatest positive impacts on the Southern Hemisphere and South America (AZEVEDO et al., 2017). Using the G3DVar, Penna et al. (2015) assessed the impact of the brightness temperature from channels sensitive to the surface from the series of NOAA satellites 15, 18, and 19. The results indicated that the radiative transfer model in GSI, the Community Radiative Transfer Model, overestimates

the brightness temperature from the channels sensitive to the earth surface for all the three satellites included and over South America during the austral summer. G3DVar was operational until December 2015 (BASTARZ, 2017).

At present, all operational models are cold started using the GFS analyses. Also, GFS forecasts are used to provide lateral boundary conditions for the operational regional models. Meanwhile, in research mode, multiple efforts are underway focusing on testing and evaluating different models, methods, cycling strategies, data, and configurations that can guide future applications for global and regional scales. Sapucci et al. (2016), for example, investigated the impact of GNSSRO-derived refractivities using the LETKF coupled with the MCGA. The Radio Occultation Processing Package (ROPP) observation operator from the Radio Occultation Meteorology Satellite Applications Facilities/European Organization for the Exploration of Meteorological Satellites (ROM SAF/EUMETSAT) was used to calculate the model counterpart. The authors found significantly positive impacts over South America, for all variables evaluated and during the entire time of integration of the model. Silveira (2017) focused on the contribution of the soil and vegetation characteristics used to simulate the microwave land surface emissivity and their impacts on the analysis. It was found that the soil moisture and temperature are the parameters that contribute more to the emissivity simulations, consequently, have a higher contribution to the simulated brightness temperature in the data assimilation. The system used was the BAM/GSI resulting from the coupling between the Brazilian global Atmospheric Model (BAM) (FIGUEROA et al., 2016) and the GSI version 3.3 utilizing the background error covariance matrix from the GFS. Bastarz (2017) computed a new background error covariance matrix using the NMC method with forecasts pairs from the BAM model. This represented significant progress compared to G3DVar. Using the G3DVar, Banos et al. (2018) explored the assimilation of GNSSRO refractivities from the European Meteorological Operational (MetOp) B satellite. The inclusion of these data allowed for more data from other included low Earth orbit (LEO) satellites to be assimilated. The zonal and meridional wind components at 250 hPa were indirectly benefited as indicated by an increase in the anomaly correlation coefficient values. Later, using the BAM/GSI, Banos et al. (2019) studied the impacts of using GNSSRO-derived bending angle instead of refractivity using the NCEP's Bending Angle Method (NBAM) (CUCURULL et al., 2013) available in GSI. A higher amount of data was possible to assimilate with positive impact in the upper levels, specifically a reduction in the root mean square error (RMSE) values was observed for the zonal and meridional wind components and geopotential height at 250 hPa.

Some studies have advanced to regional and convective scales. For example, Vendrasco et al. (2016) investigated the impact of adding a large scale analysis constraint on the problem of unbalanced initial conditions when assimilating radar data using a 3DVar approach. The constraint consisted on adding the departures of a high resolution 3DVar analysis from a coarser GFS analysis for the variables horizontal velocity components, temperature, and humidity to the 3DVar cost function. As mentioned in Section 2.1.1, constraints can be added as a new term J_c to the variational cost function (see Equation 2.1). Radar radial wind and reflectivity data were from the Paraiba Valley Experiment of the CHUVA project. The WRF Variational Data Assimilation (WRFDA) system was used. The results indicated that when using the proposed constraint, a closer fit to the radar observations is achieved, with a distribution of the analysis increments in areas outside the radar range. The verification against radar-derived precipitation showed improvements for all the statistics analyzed. Ferreira et al. (2017) also explored the assimilation of radar radial wind and reflectivity from the radars Cascavel e Assunção which cover part of southern Brazil and Paraguay as well as a close region from Argentina. The 3DVar algorithm within the WRFDA was also used with a cold start using the GFS analysis. Assimilating the radar data indirectly impacted the variables throughout the entire atmosphere and showed improvements on the forecast of intense precipitation cores. Overall, results showed the potential of radar data assimilation for nowcasting in Brazil. Campos (2018) also used the WRF model but with the 3DVar application in GSI to investigate the impact of assimilating PWV from the GPS network installed in Belem, Para during the CHUVA project. The assimilation of these data allowed to better represent the initiation and evolution of the different types of squall lines analyzed in the study.

Moreover, the potential use of lightning density rates from the Geostationary Lighting Mapper (GLM), onboard the GOES-16 satellite, as a proxy for data assimilation was investigated in Vendrasco et al. (2020). This study was inspired by the fact that previous investigations had showed the existence of correlations between lightning frequency and microphysics using radar reflectivity. From these correlations, relations between reflectivity thresholds and the lightning occurrence can be extracted. Therefore, the GLM lightning density rates can be indirectly assimilated through mean reflectivity profiles using the WRFDA 3DVar system. Substantial improvements were found in the forecasts of reflectivity patterns and storm motion. This work indicates the possible use of GLM data over areas with low data density, as in regions of South America. It also show the potential of these data for nowcasting applications. Recently, Nobre et al. (2021) explored the hybrid 3DEnVar, EnSRF,

and 3DVar methods available in GSI version 3.3 integrated with the WRF model into the Regional Modeling System in development at CPTEC. The 21 members from the Global Ensemble Forecast System (GEFS) with 1° of resolution were used to cold start the systems at 00:00 UTC and for the computation of the statistics for the ensemble-based covariance matrix. For the two cases study, the analysis systems showed different results with 3DEnVar outperforming the pure variational and ensemble for one case. For the other case study, the EnSRF showed better results in terms of the RMSE values.

2.4 Mesoscale convective systems: squall lines

Over tropical and mid-latitudes, mesoscale convective systems (MCS) are among the weather systems that most contribute to annual precipitation totals. MCS result from the grouping of individual convective clouds extending over areas with horizontal scale of about 20 to 200 km (COLEMAN; LAW, 2015). According to Schumacher and Rasmussen (2020), in the Great Plains of the US these systems account for ∼40% of the annual and >60% of the warm season rainfall. Meanwhile in the tropics, for instance over Amazon, Rehbein et al. (2019) analyzed the MCS contribution to rainfall occurrence during the Green Ocean Amazon experiment from January 2014 to December 2015 (GoAmazon2014/5[4]) (MARTIN et al., 2016), which accounted for ∼70% of the total registered in that period.

When MCS are organized in the form of bands (lines) of convective storms, they are called instability lines or squall lines. Squall lines occur with a high frequency in the central US, especially over the Great Plains, causing severe weather events, such as hail, tornadoes, high wind, flash floods as well as much of the precipitation that falls in that region particularly during spring and summer. Using a 10-year period (1994–2003) of radar data, Hocker and Basara (2008) found that squall line storms are one of the most significant storm modes observed in Oklahoma, as shown in previous studies such as Bluestein and Jain (1985). Due to its associated severe weather and contribution to the hydrological cycle, squall lines have been subject of many studies (BLUESTEIN; JAIN, 1985; ROTUNNO et al., 1988; WEISMAN et al., 1988; TAO et al., 1993; LOEHRER; JOHNSON, 1995; PARKER; JOHNSON, 2000; TRAPP et al., 2005).

Over the years, squall lines have been categorized considering different criteria. They can be classified as broken line, back-building, broken areal, and embedded areal

[4] http://chuvaproject.cptec.inpe.br/portal/goamazon/

according to their morphology (BLUESTEIN; JAIN, 1985), symmetric and asymmetric considering the position of mesolows and mesohighs (LOEHRER; JOHNSON, 1995), and leading stratiform, parallel stratiform, and trailing stratiform by taking into account the position of the stratiform area (PARKER; JOHNSON, 2000). Additionally, they can also be distinguished by the associated precipitation, as heavy convective precipitation. One of the most well known references on squall lines is the study of Rotunno et al. (1988), in which the authors show that the vertical low level wind shear and the cold pool intensity are the main ingredients for long-lived and intense squall lines. Although these studies have been conducted for squall lines over the US, their concepts have been investigated and extended for other regions, such as the southern Brazil (RIBEIRO; SELUCHI, 2019) and the Amazon basin (GRECO et al., 1994; COHEN et al., 1995; ALCÂNTARA et al., 2011).

2.4.1 Amazon coastal squall lines

In the Amazon basin, coastal squall lines are among the main rain-producing systems, as defined by Greco et al. (1990). Using GOES infrared imagery, the authors identified three major rain-producing systems: Coastal Occurring Systems (COS), Basin Occurring Systems (BAS), and Locally Occurring Systems (LOS). In particular, COS can attain a spatial length of 3500 km and last 20 to 24 hours, or more, reaching dimensions between the mesoscale and synoptic scale. These systems form along the northern coast of South America and propagate inland at an average speed of 50–60 km h^{-1}, reaching sometimes the central Amazon. The maximum rainfall amounts were found to occur between 16:00 UTC and 18:00 UTC, with peaks of surface convergence coinciding with the onset of rainfall and maximum divergence afterwards. This study was conducted during the second phase of the Amazon Boundary Layer Experiment (ABLE 2B) field campaign conducted in the central Amazon basin during April and May of 1987 (GARSTANG et al., 1990). The precipitation associated with the COS occurrence, represented 40% of the experiment rainfall. Nevertheless, these systems had already been explored in previous works, such as Kousky (1980), in which it was identified that these COS systems result from the convection induced by the sea-breeze during the afternoon and that propagate inland along the sea-breeze front, reaching as far as the Andes 48 hours after their initiation. Later, using a linear model Sun and Orlanski (1981) found that the propagation inland could be associated with the trapeze instability, which is triggered by the sea-breeze circulation. Cavalcanti and Kousky (1982) identified that these systems occur all year round following the meridional displacement of the ITCZ.

In order to understand the dynamics of these squall lines, Silva-Dias and Ferreira (1992b) used a linear nonhydrostatic spectral model with the wave-conditional instability of the second kind (CISK) theory to parameterize the heating induced by the cumulus scale and vertical profiles of temperature and wind observed during the ABLE 2B field campaign. With this model configuration the authors were able to analyze the group velocity for the most unstable modes, which are related to the squall lines propagation. The results indicated that, even though it was used a linear model, it was possible to satisfactorily simulate cases with no squall line propagation as well as to produce reasonably realistic unstable modes (speeds comparable to those observed in propagating squall lines). More importantly, this study showed the importance of a deep low level jet in order to obtain results closer to the observed propagating squall lines (i.e., a 700 mb jet of 13 m s^{-1}, with a wind speed greater or equal to 10 m s^{-1} at 600 mb).

The data collected during the ABLE 2B field campaign was also used by Garstang et al. (1994) to study the structure, kinematic, and life cycle of these squall lines. In this study the authors introduced the term "Amazon coastal squall lines" to refer to the COS of Greco et al. (1990). Thereafter, this term has been widely used in the literature. Besides data from the ABLE 2B campaign, the authors explored other sources, such as GOES infrared imagery, radar, upper air rawinsonde, and surface Portable Automated Mesonet. One of the main findings of this study is the life cycle of Amazon coastal squall lines: coastal genesis, intensification, maturity, weakening, reintensification, and dissipation. The coastal genesis refers to the initiation of the first convective cells during the afternoon in the sea-breeze convergence zone along the coast. During this stage, the cells continue to develop increasing in number and size. Later, during the late afternoon and evening, larger clusters are developed and organized in a quaselinear pattern parallel to the coast. During the night the system moves inland and by early morning it has increased its length, but the strongest convection has weakened because the absence of solar heating. Midlevel clouds have spread horizontally and some clusters of the system have reached maturity. These characteristics define the intensification stage. The maturation stage follows afterwards, in which the system is the strongest and has reached its maximum length and width. The authors stated that, at this stage it is possible to identify the squall line in the synoptic scale as a discontinuous or arc of discrete clusters of cells, organized on the mesoscale. The system starts to decay in the weakening phase. The cloud tops become warmer, the width decreases, and the speed of propagation decreases as well. However, after the weakening, the authors observed that in many cases, the system can regenerate due to the diurnal heating and therefore the convective

clusters intensify and grow. At some point, it starts to dissipate again until it disappears, enclosing the last phase of dissipation. Additionally, three different cloud components were identified: a prestorm region, leading edge convection, and a trailing stratiform region. These results are in agreement with the model of Gamache and Jr (1982), in which two circulation features are identified: a convective squall line region and a stratiform anvil region. Another important result from this study is the model of the flow structure for a mature Amazon coastal squall line. This model describes the major updrafts and downdrafts that maintain the structure of the system and indicates the convergence in the midlevels where can be found the trailing stratiform region (the anvil region).

In a follow up study, Greco et al. (1994) investigated the convective and stratiform contribution to the total budgets of heat and moisture transport. The authors found a peak heating in the midlevels at around 550–500 mb and a peak drying around 450–650 mb in a mature squall line case. This was attributed to strong detrainment processes in the convective region of the system. Consistently, a peak in the vertical eddy flux of total heat in the trailing stratiform region between 550 to 700 mb was found. In addition, it was found a substantial amount of heat being transported within the leading edge convection and the trailing stratiform, but that only 2 to 3 % reaches the upper levels between 300 to 100 mb. The authors suggested that this occurs because the use of the low level energy to maintain the deep convection in the leading edge and to support the stratiform development.

Through an observational case study, Cohen et al. (1995) confirmed the role of the magnitude and thickness of the low level jet in days with squall line occurrence, as had been previously suggested by Silva-Dias and Ferreira (1992b). During the ABLE 2B period, it was observed an easterly low level jet at around 800 hPa that was stronger and parallel to the coast during the days with squall lines than the days without them. The layer of maximum winds was located between 900 and 650 hPa in cases of squall lines. Easterly waves over the Atlantic Ocean were observed during the squall line case study which could have contributed to the intensification of the low level jet, however, this was not conclusive since the presence of a localized heat source in the western Amazon was also favoring the convergence toward that region. The authors pointed out the interaction among system of different scales that were present during that case study, this is, the presence of easterly waves over the Atlantic Ocean and tropical heat sources in the western Amazon in the larger scale, the sea-breeze formation in the mesoscale, and the interaction within the convective leading edge and the stratiform region in the cloud circulation scale. Furthermore,

some climatological aspects of these squall lines were discussed, following the study of Cohen et al. (1989) in which squall lines were classified according to the displacement inland. Cohen et al. (1995) pointed out that these systems have a higher frequency between April and August with those that propagate more than 400 km inland occurring more frequently during July.

The role of low level jets in Amazon squall lines was investigated by Alcântara et al. (2011). GOES imagery were used to identify squall lines along with ECMWF reanalyses to identify the low level jet occurrence and characteristics. Low level jets were identified as areas of maximum velocity of the zonal wind between the 900 and 600 hPa levels. The presence of a low level jet was found in each type of squall line analyzed and as in Cohen et al. (1995), a higher the number of low level jets was found as the number of squall lines were also identified. In addition, it was found that propagating squall lines occur under the presence of more intense and deeper low level jets. In this study a climatology of Amazon squall lines is obtained in which cases with low level jet are distinguished. Overall, the results corroborate that July is the month with the most occurrence. Thereafter, several studies have been conducted for the dry season and specifically for July, such as the studies of Oliveira and Oyama (2015) and Ghate and Kollias (2016). Oliveira and Oyama (2015) investigated the atmospheric conditions prior to a squall line occurrence. The month of July was selected for the analysis and an objective method was developed using Forecasting and Tracking the Evolution of Cloud Clusters (ForTraCC) (VILA et al., 2008). Once the squall line cases were filtered, a subjective analysis was conducted in order to find the atmospheric conditions occurring in each case. A moister layer between 850 and 350 hPa, and a northeasterly flow at 350 hPa were the main conditions found during the midmorning, given that the squall lines form during the afternoon.

3 RAPID REFRESH FORECAST SYSTEM COMPONENTS

Since RRFS is the convection-allowing forecast system explored in this research, a brief description of each of the components of the current prototype is provided in this chapter. As mentioned previously, the prototype RRFS includes the FV3LAM model with pre-processing utilities, the CCPP, a unified post-processing system, and data assimilation capability using GSI analysis system. Each of these components are briefly described, especially the main capabilities of GSI are presented. The workflow used to streamline all components of the system and the cycling configuration is also presented. The MET tools are covered here since MET will be the verification package for UFS. The use of MET was relevant in this research as many of its tools were explored.

3.1 Atmospheric model

The FV3 dynamical core was implemented in GFS replacing the spectral dynamical core for an operational upgrade in June 2019. The FV3 is a fully compressible, nonhydrostatic core featuring a Lagrangian vertical coordinate and cubed sphere grid (LIN; ROOD, 1996; LIN; ROOD, 1997; LIN, 1997; LIN, 2004; PUTMAN; LIN, 2007; HARRIS et al., 2020a). The Lagrangian vertical coordinate allows for a unique, straightforward representation of vertical motions directly through the relative deformation of the vertical layers. This is in contrast to the Eulerian framework presently featured in operational nonhydrostatic dynamical cores in use at the convective-scale, such as the Advanced Research Weather Research and Forecasting model (WRF-ARW) (SKAMAROCK et al., 2008)) and Non-hydrostatic Multiscale Model on the B-grid (JANJIć et al., 2001).

The FV3, originally a global model, features three types of local refinement capabilities: stretching of the global grid using the Schmidt refinement technique (HARRIS et al., 2016), one- and two-way nesting within the global grid (HARRIS; LIN, 2013), and recently a LAM capability (BLACK et al., 2021). The LAM capability underpins the future RRFS and thus is the focus in this study. It requires fewer computing resources to achieve similar forecast performance as compared to a two-way nesting method at lead times less than 24 hours (BLACK et al., 2021). For the FV3LAM, a parent domain is not needed to provide the initial and lateral boundary conditions (ICs and LBCs). Instead, an external model can be used. A linear interpolation is performed in space and time between the external model fields and the grid points of the regional domain. However, the grid needs to be carefully configured allowing for at least four extra rows and columns beyond the area of interest. These addi-

tional grid points compose what is called the halo region and are used to ensure the correct integration of the model. ICs must also be provided at least once to initiate the forecast sequence for subsequent data assimilation cycling. A more complete description of the FV3LAM and additional justification for limited area modeling in the context of operational, convection-allowing numerical weather prediction can be found in Black et al. (2021).

The pre-processing is done by the utilities (UFS_UTILS[1]) developed by NCEP's Environmental Modeling Center (EMC) and other collaborators. UFS_UTILS can be used to generate the model grid, orography, and surface climatology (e.g. maximum snow albedo, soil, vegetation type, vegetation greenness, etc.). UFS_UTILS can also read from external models and prepare ICs and LBCs for a FV3LAM model run.

3.2 Physics

The CCPP[2] is a collaborative effort between scientists at NOAA and the National Center for Atmospheric Research (NCAR). The goal is to assemble parameterizations developed by different groups into a common framework to be used interchangeably for numerical prediction at any scale (HEINZELLER et al., 2019). Hence, the CCPP contains a set of physical schemes and a common framework that facilitates the interaction between the physics and a numerical model (BERNARDET et al., 2020). The current common framework was developed by the Developmental Testbed Center (DTC). A number of physics suites are available allowing great flexibility for a wide range of users. A single-column model (CCPP SCM) option has also been developed, which is available in the latest CCPP release (version 5.0, CCPPv5[3]). The CCPPv5 supports the RRFSv1a and GFS version 15 (GFS_v15p2, GFSv15 for simplicity) physics suites for the SRW.

The RRFSv1a physics suite in CCPPv5 is under active development for its use in operational RRFS. It is based on physical schemes implemented in the operational RAP and HRRR systems. This suite is composed by a subgrid-scale cloud pre-radiation interstitial following (XU; RANDALL, 1996), the Mellor-Yamada-Nakanishi-Niino–eddy diffusivity-mass flux (MYNN-EDMF) (NAKANISHI; NIINO, 2009; OLSON et al., 2019) boundary layer and shallow cloud scheme, the unified gravity wave physics scheme version 0 (ALPERT et al., 2019), the Thompson Aerosol-Aware microphysics

[1] https://github.com/NOAA-EMC/UFS_UTILS
[2] https://dtcenter.org/community-code/common-community-physics-package-ccpp
[3] https://dtcenter.ucar.edu/GMTB/v5.0.0/sci_doc/index.html

scheme (THOMPSON; EIDHAMMER, 2014), the Rapid Radiative Transfer Model for Global Circulation Models (RRTMG) for longwave and shortwave radiation processes (MLAWER et al., 1997; IACONO et al., 2008), the surface layer scheme of Long (1986), the near-surface sea temperature (NSST) scheme of Li et al. (2015), the NoahMP (Noah Multi-Physics) land surface model (NIU et al., 2011), and the Navy Research Laboratory (NRL) ozone photochemistry (2015) and stratospheric water vapor schemes (MCCORMACK et al., 2008). Table 3.1 summarizes the RRFSv1a physics as well as GFSv15, which are tested in this study. The default configuration for each CCPP suite is used.

Table 3.1 - Common Community Physics Package (CCPP) suites tested.

Physical process	**Physics suites**	
	RRFSv1	**GFSv15**
Deep Cu	*off*	GFS sa-SAS for deepcnv
Shallow Cu	MYNN-EDMF	GFS sa-MF for shalcnv
Microphysics	Thompson	GFDL
PBL/TURB	MYNN-EDMF	Hybrid EDMF
Radiation	RRTMG and SGSCLOUD	RRTMG
Surface layer	GFS	GFS
Land	Noah-MP	Noah
Gravity wave drag	uGWP	uGWP
Ocean	NSST	NSST
Ozone	NRL 2015	NRL 2015
Water vapor	NRL 2015	NRL 2015

SOURCE: Author's production.

3.3 Data assimilation system

GSI is a variational data assimilation system featuring 3DVar (WU et al., 2002; KLEIST et al., 2009), hybrid 3DEnVar (WANG, 2010; WANG et al., 2013; WU et al., 2017), and hybrid 4DEnVar methods (KLEIST; IDE, 2015a). It also includes an optional nonvariational, complex cloud analysis capability that executes after the variational analysis as a method to specify cloud and hydrometeor variables, as mentioned previously. GSI features the following standard control (analysis) variables: streamfunction, velocity potential, temperature, surface pressure, and normalized relative humidity following Holm et al. (2002). However the choice of control variable is flex-

ible and one may extend or modify the standard set to include other fields, such as hydrometeors or radar reflectivity (WANG; WANG, 2017). In 3DVar and the associated hybrid variants, the static background error covariance is approximated through the application of a recursive filter which models the autocorrelations (PURSER et al., 2003) while cross-covariances are handled in the standard context through statistical balance relationships obtained via regression (PARRISH; DERBER, 1992; WU et al., 2002). The analysis is obtained by minimizing the incremental form cost function through the preconditioned conjugate gradient method (BATHMANN, 2021).

The extension of GSI from traditional 3DVar to hybrid 3DEnVar and to hybrid 4DEnVar is accomplished through the extended control variable approach (LORENC, 2003; WANG, 2010; KLEIST; IDE, 2015a; KLEIST; IDE, 2015b). In this configuration, one is able to incorporate flow-dependent covariance information obtained from a complementary suite of ensemble forecasts. Typically this ensemble is obtained from a companion ensemble-based data assimilation system, such as the EnKF. However one may use any suitably available ensemble. In fact, the regional operational data assimilation systems at NCEP have used the ensemble members from the GFS Data Assimilation System directly in the hybrid 3DEnVar framework with considerable benefit to the resulting forecast (WU et al., 2017). Although the use of lower-resolution global ensemble members may not be ideal for the representation of the error characteristics at finer scales, Wu et al. (2017) showed that considerable forecast improvement can be obtained even if the ensemble provided is from a different system, which is consistent with findings in other studies such as (HU et al., 2017). This study focuses on the 3DVar and hybrid 3DEnVar frameworks and uses the global ensembles as described in (WU et al., 2017). The localization function in GSI is implemented as a single application of an isotropic recursive filter (PURSER et al., 2003) and the radius is specified as a Gaussian half-width, either in scale height ($\ln p$) or in terms of number of vertical layers. Future work on RRFS involves the extension to a convective-scale ensemble in the EnKF, which will improve the representativeness associated with the forecast error covariance at finer scales. However, such a change is not a panacea. Aside from increased computational expense, the problem of rank deficiency of the ensemble-derived error covariance becomes more apparent with the expanded degrees of freedom associated with the finer spatial resolution. While localization helps somewhat, a computationally affordable ensemble is one that is often insufficiently sized. Therefore future work also includes efforts to introduce multi-scale data assimilation capabilities, such as scale dependent localization (HUANG et al., 2021).

GSI is capable of assimilating a large suite of observations. This includes, but is not limited to, satellite radiances, derived GNSSRO observations, radar radial velocity and reflectivity, GLM lightning flash rates, web-camera derived estimates of horizontal visibility (CARLEY et al., 2021), and conventional observations. After 2014 it became a community system, maintained and supported by the EMC and the DTC (SHAO et al., 2016). Recently, it has been added as the analysis component to improve initial conditions for the RRFS (HU et al., 2021).

Presently, GSI is the data assimilation system used at NCEP for all operational atmospheric data assimilation applications (KLEIST; IDE, 2015a; HU et al., 2017). It was initially developed by the EMC (WU et al., 2002) and implemented as the analysis component in the operational GFS in May 2007 (KLEIST et al., 2009) and in the operational RAP in May 2012 (BENJAMIN et al., 2016).

3.4 Post-processing

UPP is used at NCEP in all operational models. A community version is currently supported and maintained by the DTC. UPP takes native output from the model grid points/cells and creates post-processed outputs including numerous diagnostic quantities in the same model output grid and model-native or isobaric vertical coordinate (UPP, 2021). Post-processed outputs include diagnostics fields that are not part of the model computation that have been developed for different applications. These include, for example, precipitation type, composite reflectivity, simulated satellite brightness temperatures, updraft helicity, storm motion, ceiling or cloud-base height, vertically integrated liquid water, and lightning, among several others. More details on the diagnostic fields developed for hourly updated NOAA weather models such as RAP and HRRR, and how they are calculated, can be found in Benjamin et al. (2020). These products are critical for users in their forecast processes. UPP was selected as the unified post-processing system for UFS and modifications have been made to work with FV3-based models. Currently, it can be used in the UFS medium range weather and SRW applications.

3.5 Workflow

The workflow ties all RRFS components together and handles all system interdependencies. In essence, it manages the cycling configuration taking into account each task dependency and specification. It oversees that tasks to generate ICs and LBCs only start if all needed information was obtained from the previous step. It manages how the data assimilation cycle advances, i.e. by running the forecast to generate

the first guess and running the analysis once the first guess is completed. It handles the model execution by supervising availability of ICs and LBCs for the specific hour, and controls that model outputs only be postprocessed if they exist in the model run directory. It also manages crucial information on computational resource requirements to run each task.

A schematic diagram of major tasks and the general pipeline of the RRFS system is provided in Figure 3.1. The task "Make Fixed Files" generates the model grid, orography, and climatological information needed for the model execution. The tasks "Make ICs" and "Make BCs" read data from external models (such as GFS and HRRR), perform the necessary calculation, interpolation, conversion, and then generate appropriate ICs and LBCs for a FV3LAM model run. The task "Run analysis" (the gray shaded area in Figure 3.1) executes the data assimilation system for a FV3LAM run. It ingests various types of observations and combines them with a first guess (or background) to generate a best possible atmospheric analysis for the initialization of the FV3LAM model integration. The first guess can be either an IC from an external model (after the task "Make ICs") or a short term forecast (1 – 6 h forecast, configurable by users) from a previous FV3LAM model run. The first scenario is referred to as a "cold start" (the blue box in Figure 3.1) while the latter is called a "warm start" (the red box in Figure 3.1). In practice, for a FV3LAM "warm start," the first guess comes from "restart" forecast files generated by the FV3LAM model. The task "Run model" is to run the FV3LAM model with ICs and LBCs prepared from the previous steps. It is worth mentioning that besides the "cold start" and "warm start," a FV3LAM model run can also start from an IC made directly from an external model without the data assimilation step. This is also referred as a "cold start." The task "Run post" is to post-process the FV3LAM forecasts and generate all target model fields for downstream plotting and/or examination.

Figure 3.1 - Schematic diagram of the RRFS tasks and workflow.

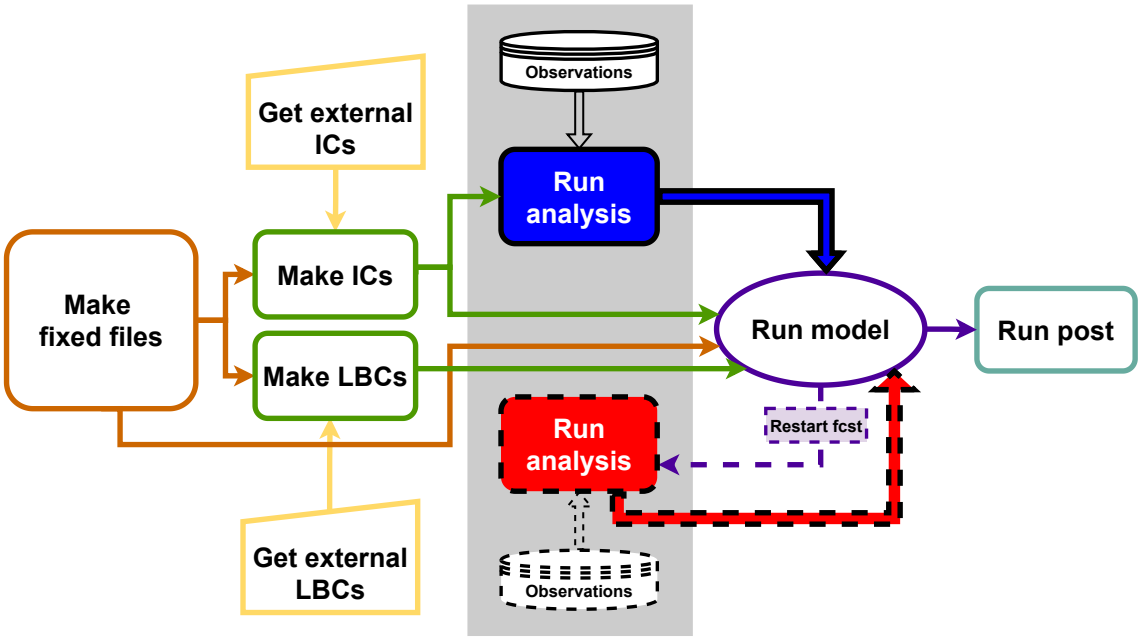

SOURCE: Author's production.

3.6 Verification tools for RRFS forecasts

The community MET is the unified verification package that will be used for UFS applications (BROWN et al., 2021). MET was developed at the DTC and has been widely used by the NWP community. It includes several tools from re-formatting, re-gridding, masking the input observations to the computation of traditional metrics, wavelet, neighborhood, and object-based verification as well as analysis tools to process the outputs. Specifically, the PB2NC, Point-Stat, Grid-Stat, Stat-Analysis, Method for Object-Based Diagnostic Evaluation (MODE), and MODE-analysis tools were used in this study.

The PB2NC tool converts observations from prepBUFR (prepared Binary Universal Form for data Representation) files to NetCDF, the format used by MET tools. Information on the observation quality provided in the prepBURF files (WMO, 2002) is taken into account by the PB2NC tool. A maximum quality mark setting in PB2NC allows only observations with this quality flag or below to be used in the verification. The Point-Stat tool computes traditional metrics, such as the mean, RMSE, bias, and standard deviation of the difference between the point observations

and forecasts. The calculation of statistics is based on the matched pairs. Various methods to interpolate model values to the observation locations are available. For example, nearest neighbors, bilinear interpolation, minimum and maximum value, distance-weighted mean, among others. The Grid-Stat tool is similar to Point-Stat, but using gridded reference data. It can be an analysis, gridded precipitation and reflectivity from different sources, etc. Similar interpolation methods can be applied. Thresholds can be applied to compute the statistics. MODE in MET follows the work of Davis et al. (2009). This method mimics what a human specialist would do in order to find a region of rain in the forecast and decide if it has analogous characteristics in the observation. Different metrics can be computed, for example the median of maximum interest (MMI (F+O)). This metric results from the median between the maximum interest from each observed object with all predicted objects (MIF), and the maximum interest from each predicted object with all observed objects (MIO). It takes into account all attributes used in the total interest calculation, summarizing them into a single value. The forecast with the best quality or in greater agreement with the observations will give MMI (F+O) values close to one. Otherwise, the value will close to zero. MET version 9.0 (JENSEN et al., 2020) is used for forecast verification. At this moment, it is part of the RRFS workflow.

4 RRFS OVER CENTRAL NORTH AMERICA

This chapter gives more information on the motivation of this work using the RRFS with data assimilation. An overview of the case study selected over central US is presented along with the data, methods, the results obtained, and subsequent discussions.

4.1 Introduction

The current suite of operational convection-allowing models at the NCEP consists of multiple dynamical cores and physics schemes, none of which have shared much in the components with their global counterpart (i.e. the GFS). At present, convection-allowing forecasts at the NCEP are produced by the North American Mesoscale Forecast System (NAM) 3 km nests, the HRRR model, and the High Resolution Window (HIRESW) systems. These systems are then combined into a convection-allowing ensemble known as the High Resolution Ensemble Forecast system (HREF) (ROBERTS et al., 2020). The global modeling suite is based on the FV3 dynamical core with a physics suite developed and tuned for global applications, while the regional operational models are based on unique physics suites and dynamical cores, such as the Advanced Research WRF model (WRF-ARW) (SKAMAROCK et al., 2008) and Nonhydrostatic Multiscale Model on the B-grid (JANJIć et al., 2001).

Considerable human and computing resources and efforts are required to maintain and improve such a variety of models in order to continuously provide successful numerical guidance for different sectors of society (LINK et al., 2017). Therefore, NOAA is currently transitioning toward the UFS (EMC, 2018). This transition forms part of the Research to Operations Initiative aiming to build the Next Generation Global Prediction System (NGGPS) for the US. A unified forecasting system brings together advanced developments in weather and climate models, maximizing collective efforts and resources, while also connecting expertise across the scientific community (NATIONAL RESEARCH COUNCIL, 2012). Within the UFS framework, the GFS was coupled with the Wavewatch III wave model in the operational upgrade of March 2021, improving the low-level cold bias seen in the previous GFS version during the cool season (NWS, 2021). The UFS encompasses medium and short range weather, hurricane, subseasonal to seasonal, air quality, coastal, marine and cryosphere as well as space weather applications (UFS, 2019). The UFS and its components are currently under development, but early versions are available allowing contributions from the research community to become available for operational activities.

As previously mentioned, RRFS is the future operational convection-allowing ensemble prediction system of the US, and is built upon the SRW. Harrold et al. (2021) investigated how the SRW represents the convective gray zone for varied model grid spacing in two physics suites: GFS version 16 and the RRFS (RRFSv1a). It was found that for both physics suites a 3 km resolution yields a more realistic representation of convection but with a cool 2 m temperature bias and an underforecast of lower reflectivity values. Kalina et al. (2021) also examined these two SRW physics suites and demonstrated that they failed to depict trailing stratiform precipitation in simulations of a squall line and Hurricane Barry (July 2019). Preliminary results indicate that this issue could be related to a smaller amount of ice crystals in the model runs than in the radar-derived data. Moreover, the same experimental configuration was used by Newman et al. (2021) to investigate the land-atmosphere interactions using a heatwave case and a winter cold air outbreak case. A cooler PBL with increased cloudiness and less surface downward shortwave were found in the heatwave case simulations, while an increase is seen in the 10 m wind speed in the cold air outbreak case. All recent studies using SWR v1.0.0 are cold started using an external model, since the application does not have integrated a data assimilation system. Tong et al. (2020) filled that gap using an earlier version of the FV3LAM and the GSI to generate the analyses. However, this is the only work found in the literature using data assimilation with the FV3LAM. Although results were for a single case study, positive impacts of assimilating radar data were found in all analyses and forecasts. Using hybrid 3DEnVar with 75 % of the ensemble-based and 25 % of the static background error covariance showed storm structures in the 2 h forecast comparable to when using EnKF, although EnKF outperformed 3DEnVar in the first hour forecast. Both methods, hybrid En3DVar and EnKF, showed higher equitable threat scores (ETS) when compared to 3DVar and pure 3DEnVar during the 4 h forecast analyzed.

As the GSI analysis system has been recently added as the analysis component of prototype RRFS, it provides a suitable research framework to assess the current ability of this forecast system to represent convection. This research seeks to describe the initial data assimilation infrastructure and performance of a prototype RRFS system. The focus is on extensive testing within the context of a case study to establish an understanding of baseline sensitivities, and an evaluation of various configurations and algorithms available in GSI is performed in order to investigate the impact of using data assimilation on forecasts of convective storms. The 3DVar and hybrid 3DEnVar data assimilation algorithms, supersaturation removal, PBL pseudo-observations, and various weights of the ensemble background error covari-

ance in the hybrid EnVar analyses are assessed. A cycling strategy is configured and its effect on the cycled analyses is evaluated. A case study that focuses on a severe convective weather event is used to demonstrate sensitivities. Experiment results were verified using MET. Results obtained provide developers insight into the capabilities of current prototype RRFS developments in predicting convection as well as suggestions for the RRFS data assimilation system framework.

4.2 Methods

In order to achieve skillful forecasts comparable to the current operational convection-allowing suite, each component of the RRFS needs to be exhaustively tested to determine the best configuration. This study focuses on the initial configuration of the data assimilation framework. In this section, the case study, general setup of the experiments, description of the experiments conducted, and verification methodology are presented.

4.2.1 Case overview

A line of convective storms developed over northeastern Oklahoma ahead of a southward moving cold front during the afternoon of 4 May 2020. At 18:00 UTC on 4 May 2020, a surface low pressure was observed across western Oklahoma with a dry line extended over western Texas, favoring an environment with low-level convergence, high temperatures, and humidity over these areas. Between 19:00 UTC and 20:00 UTC, high values of mixed layer convective available potential energy (MLCAPE) (3694 J kg^{-1}) and effective bulk shear (48 kt for the surface to 3 km layers and 36 kt for the surface to 6 km shear) were observed over northeastern Oklahoma. This environment provided favorable conditions for severe convective storms with potential for strong updrafts and development of supercells (WEISMAN; KLEMP, 1982; MCCAUL; WEISMAN, 2001). At 20:00 UTC, the convective cells were first seen in the radar reflectivity observations over that region (Figure 4.1a), and at around 22:00 UTC (Figure 4.1c) a line of storms extended across central Oklahoma along the pre-frontal wind shift. The system evolved while slowly moving southeastward. A supercell developed over far southwestern Missouri at 00:00 UTC on 5 May (Figure 4.1e), producing hail of 1.25 inches and 1.5 inches in diameter according to hail reports from the Storm Prediction Center (SPC). Clusters of severe storms developed across south-central Oklahoma along the intersection of the cold front with the dry line. The convection associated with the squall line evolution resulted in several instances of large hail and high wind, mostly over northeastern and south-central Oklahoma, southeastern Kansas, southwestern Missouri, and northwestern

Arkansas.

Figure 4.1 - Hourly Multi-Radar Multi-Sensor (MRMS) composite reflectivity and hourly hail (black stars), high wind (black squares), and tornado (red circles) reports from the SPC, from 20:00 UTC on 4 May 2020 through 01:00 UTC on 5 May 2020.

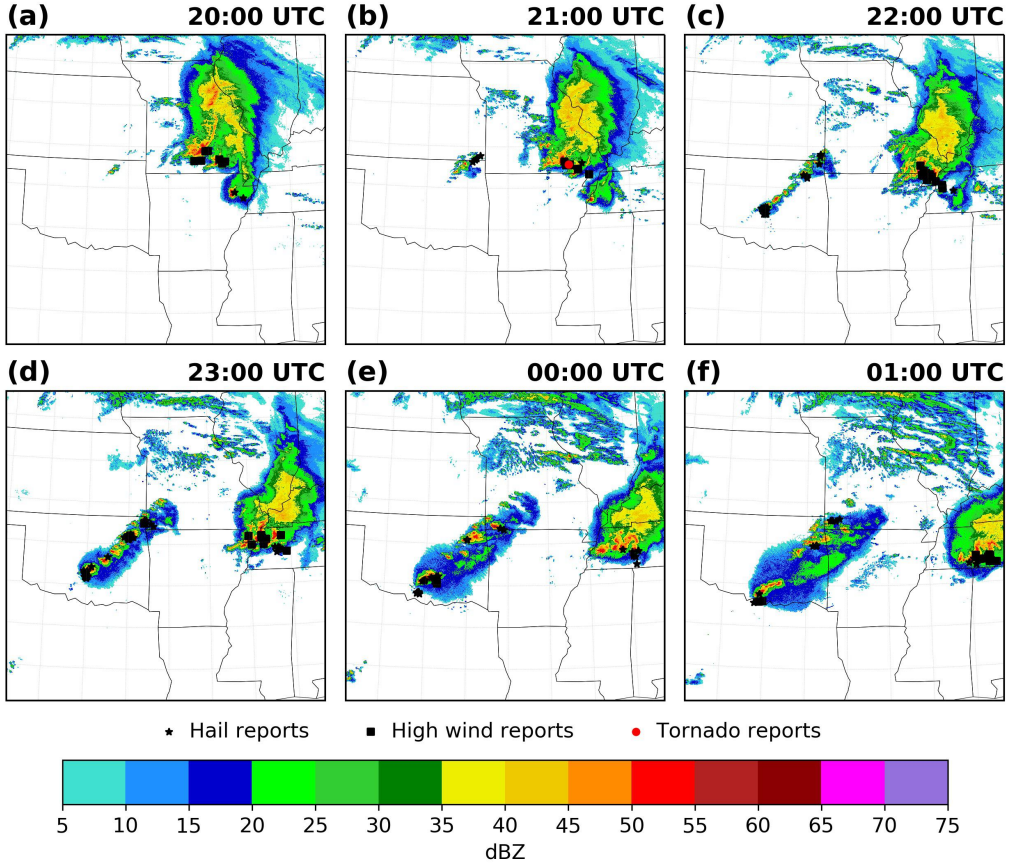

SOURCE: Author's production.

4.2.2 Setup of experiments

For the simulation of this case, a domain is configured consisting of 460 × 460 grid cells centered on Fort Smith, Arkansas with a 3 km horizontal grid-spacing and 64 vertical layers. The Extended Schmidt Gnomonic method developed by Purser et al. (2020) and implemented in the SRW was used for grid generation. Figure 4.2 shows the domain coverage and orography created by the pre-processing utilities, where the black star indicates the central point.

Figure 4.2 - Domain with the orography created for numerical experiments of case study over central North America. The black star indicates the central latitude and longitude on Forth Smith, Arkansas.

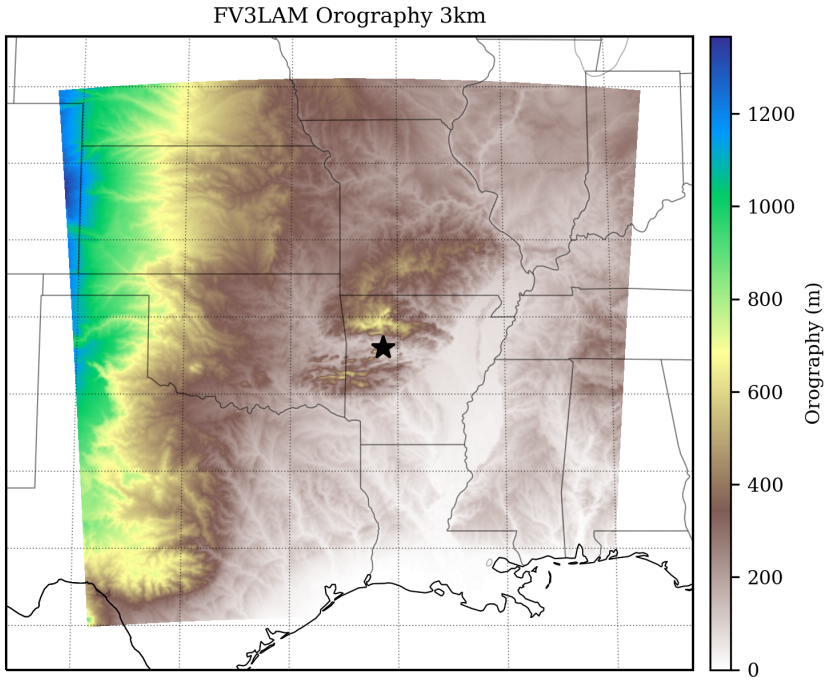

SOURCE: Author's production.

4.2.2.1 Data

All simulations start at 00:00 UTC on 4 May 2020 and run hourly cycles until 06:00 UTC on 5 May 2020. Hourly 3 km HRRR analyses and forecasts are used to generate the ICs and LBCs for the FV3LAM. The observation data assimilated in each experiment are the same as those used in the operational RAP system. Hourly RAP observations are generated at NCEP for the hourly updated data assimilation component in RAP and typically include all available data from 30 minutes before to 30 minutes after the analysis hour (HU et al., 2017). Historic data were obtained from NOAA's High Performance Storage System (HPSS) archives. RAP observations include upper air observations from rawindsondes, dropsondes, pilot balloons, aircraft, and wind profilers; surface data from synoptic stations, METAR, and the Mesoscale Network (MESONET); radar radial velocity and the vertical azimuth display derived from radar radial velocity; Atmospheric Motion Vectors (AMV) wind derived from satellite observations; and the GPS-IPW. Table 4.1 provides detailed

information on the observation types as well as their sources, where ps stands for station (surface) pressure; t for virtual temperature and/or sensible (dry bulb) temperature; q for specific humidity; and uv for u- and v-components of wind. The time window used is 1 hour, allowing for observations within 30 minutes before to 30 minutes after the central analysis time to be assimilated.

Table 4.1 - Sources of assimilated observations.

Observation Type	**Description**	**Observation variable**				
		ps	t	q	pw	uv
ADPUPA	Rawindsonde	√	√	√		√
RASSDA	RASS virtual temperature		√			
AIRCFT	AIREP and PIREP aircraft		√			√
AIRCFT	AMDAR aircraft		√			√
ADPUPA	Dropsonde		√	√		
AIRCAR	MDCRS ACARS aircraft		√	√		√
AIRCFT	TAMDAR aircraft		√	√		√
AIRCFT	Canadian AMDAR aircraft		√	√		√
GPSIPW	GPS Integrated Precipitable Water				√	
SFCSHP	Ship, Buoy, C-MAN, and Tide Gauge reports	√	√	√		√
ADPSFC	SYNOPTIC and METAR	√	√	√		√
SFCSHP	Splash-level Dropsonde over ocean	√	√	√		
ADPSFC	METAR	√	√	√		√
MESONET	Surface MESONET	√	√	√		
SATWND	Cloud drifts, cloud top, and deep layer from different satellite imagery					√
ADPUPA	PIBAL					√
PROFLR	Wind Profiler					√
VADWND	Vertical Azimuth Display from WSR88D radars					√
PROFLR	Multi-Agency Profiler and SODAR					√
PROFLR	Wind Profiler from PIBAL					√
SFCSHP	ATLAS Buoy					√
WDSATR	Scatterometer winds over ocean					√

SOURCE: Author's production.

In addition, BUFR observation files from the Global Data Assimilation System (GDAS) are used to assimilate bending angles derived from GNSSRO observations. GDAS is the operational global data assimilation system used to create the initial conditions for GFS, and its observation files are available daily at synoptic hours.

GDAS observation files include all valid data from 3 hours before to 3 hours after the analysis time (KLEIST et al., 2009). In order to use GDAS observation data in the hourly cycles configured in this study (see Section 4.2.3, the same observation file is reused for each of the 3 hours before and 3 hours after its analysis time, and two files are used at overlapping times (Figure 4.3). For example, the file for synoptic hour 12:00 UTC was used to run the cycles 09:00 UTC through 15:00 UTC. However, since observations before 09:00 UTC are also included in the 06:00 UTC GDAS observation files, both 06:00 UTC and 12:00 UTC GDAS observation files are used in GSI at 09:00 UTC, as the purple boxes indicate in Figure 4.3.

Figure 4.3 - Strategy used to assimilate GNSSRO bending angles from GDAS observations each hour.

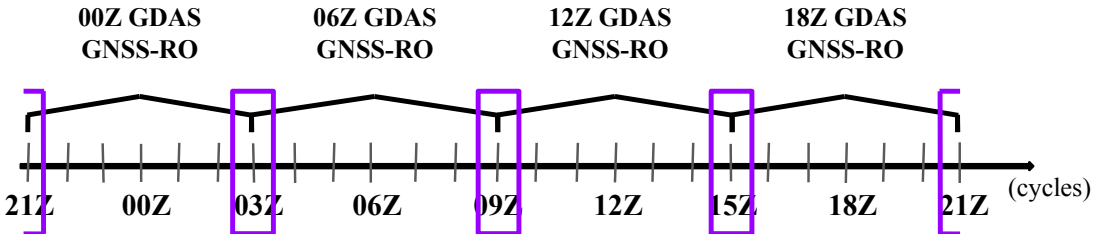

SOURCE: Author's production.

Available LEO satellites during 4 to 5 May 2020 include the second mission of the COSMIC-2, the MetOp A, B, and C satellites, the Korea Multi-Purpose Satellite-5 (KOMPSat5), the Spanish mission PAZ, and the German Tandemx and TerraSARX satellites. COSMIC-2 and MetOp C were not among the satellites that were currently assimilated in the GSI version used in this study. Because GNSSRO observations are not well distributed in the limited domain, these satellites were therefore added to the code in order to increase the number of available bending angle observations during the execution period. Quality control procedures were maintained similar to those applied on COSMIC-1 and MetOp A and B observations, respectively. Bending angles from all LEO satellites were assimilated up to 50 km.

Experiments are conducted testing the GSI 3DVar and 3DEnVar systems. For the hybrid 3DEnVar analysis, the Global Data Assimilation System (GDAS) 80 member ensemble forecasts (9 h forecasts) are used to provide the ensemble background

error covariance (WU et al., 2017). These forecasts have a horizontal resolution of approximately 25 km and are available four times per day, therefore the same 9 h GDAS ensemble forecasts are used for the 2 hours before and 3 hours after its valid hour as indicated in Figure 4.4. For example, the 9 h GDAS ensemble forecasts initialized at 00:00 UTC (valid at 09:00 UTC) are used for the cycles from 07:00 UTC to 12:00 UTC. Similarly, the 9 h forecast GDAS ensemble initialized at 06:00 UTC (valid at 15:00 UTC) is used for the cycles from 13:00 UTC to 18:00 UTC. This follows the same strategy in the RAP system (HU et al., 2017). As shown in Hu et al. (2017), using off-time global and fixed ensemble based BEC still produces better results than just using the static BEC. In all experiments with data assimilation, two outer loops with 50 iterations each loop are performed to minimize the cost function and find each analysis. In each outer loop a re-linearization is performed (KLEIST et al., 2009). The increment is zero for the first outer loop while for the second it is updated with the solution found after the 50 iterations of the first outer loop. In this study, 50 iterations were enough to achieve convergence. The grid ratio of the analysis and the ensemble to the background was 1, yielding a spatial resolution of the analysis of 3 km.

Figure 4.4 - Strategy to reuse 9 h forecast GDAS ensembles in GSI every hour.

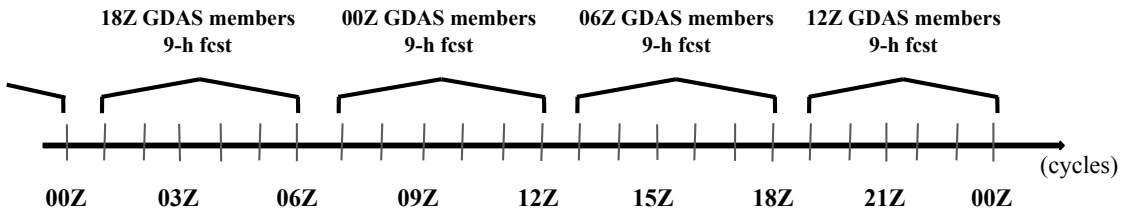

SOURCE: Author's production.

4.2.3 Cycling configuration

The current cycling configuration of the prototype RRFS is similar to the one used in RAP, i.e. cold starts are performed every 12 hours and warm starts are performed at all other cycles using the 1 h forecast from the previous cycle as background for the analysis. RAP performs hourly-updated continuous cycles with cold starts at 09:00 UTC and 21:00 UTC using the 1 h forecast from cycles initialized at 08:00 UTC and 20:00 UTC in 6 h parallel hourly spin-up cycles. The parallel spin-up cycles are

cold started from GFS atmosphere analyses and RAP surface fields at 03:00 UTC and 15:00 UTC. Cold starts in RAP introduce the atmospheric conditions while RAP land surface fields are fully cycled in the continuous cycle (BENJAMIN et al., 2016; HU et al., 2017). Periodic updates of the large scale atmospheric conditions are needed in regional modeling systems in order to account for corrections made by global observations over land and ocean and to avoid model drift from those conditions (BENJAMIN et al., 2016). At the time of execution of this research not many RAP functionalities were available for use in the RRFS data assimilation framework, therefore a more simplified configuration with partial cycling is used. Development currently underway includes establishing a partial cycling capability for the inaugural operational implementation, RRFS version 1, with subsequent plans to consider a fully cycled version in later versions leveraging recent advances discussed in Schwartz et al. (2022). Figure 4.5 illustrates the RRFS cycling configuration from cycles initialized between 00:00 UTC through 06:00 UTC. In each cycle, an 18 h free forecast is launched following the analysis, with hourly outputs. A cold start is performed at 00:00 UTC and warm starts between 01:00 UTC to 06:00 UTC using the FV3LAM 1 h forecast from the previous cycle as background for the analysis.

Figure 4.5 - Diagram of the hourly cycling configuration for RRFS.

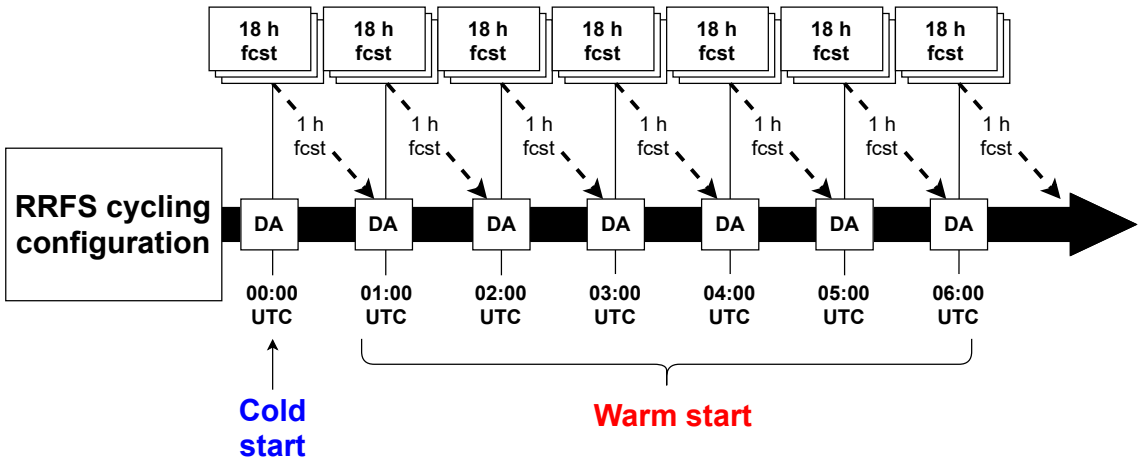

SOURCE: Author's production.

4.2.4 Sensitivity experiments

GSI provides many functionalities and parameters, enabling users to make the best data assimilation configurations for different applications. A series of experiments were designed to examine the impact of different configurations on the analyses and forecasts. Some RAP configurations were tested in the experiments following Hu et al. (2017). An experiment with no data assimilation is provided, acting as the baseline for all other experiments. This baseline experiment is called NoDA and uses the same cycling configuration as experiments with data assimilation in terms of the cold and warm start ICs. The 3 km ICs from the HRRR are consistent with the 3 km grid-spacing of the RRFS, such that fine scale features found in the HRRR are present in the RRFS ICs. Table 4.2 lists all experiments in this research.

However, before performing the experiments with data assimilation, two experiments were conducted testing the RRFSv1a and GFSv15 CCPP suites available in the SWR. This was in order to choose the appropriate physics suite for this study over central US. Results testing other suites in CCPPv4 are available in Banos et al. (2021a). These experiments used the same NoDA baseline configuration. Figure 4.6 presents the 2, 4, and 6 h composite reflectivity forecasts from the 19:00 UTC cycle on 4 May 2020, with 5 dBZ (solid lines) and 35 dBZ (dash lines) reflectivity observation contours overlaid for NoDA experiments ccpp_RRFS and ccpp_GFS using RRFSv1a and GFSv15 suites, respectively. The ccpp_RRFS experiment shows stronger convective cells but a better coverage of the convection occurring in different parts of the domain at all forecast lengths. Meanwhile, the ccpp_GFS shows weaker and smoother cells with overall less convection coverage. At 2 h forecast, the convection initiation over northeastern Oklahoma is misplaced when using RRFSv1 and at 4 and 6 h forecast there are noticeable misplacement errors in both experiments. Nevertheless, the experiment with RRFSv1a presents a slightly better representation of the convection than the experiment with the GFSv15 suite. Therefore, the RRFSv1a suite is used in the baseline configuration of all experiments presented in this study.

Figure 4.6 - 2, 4, and 6 h composite reflectivity forecasts from experiments ccpp_RRFS (a, b, and c) and ccpp_GFS (d, e, and f), initialized at 19:00 UTC 4 May 2020. Solid and dashed black lines are the 5 and 35 dBZ MRMS observation contours, respectively.

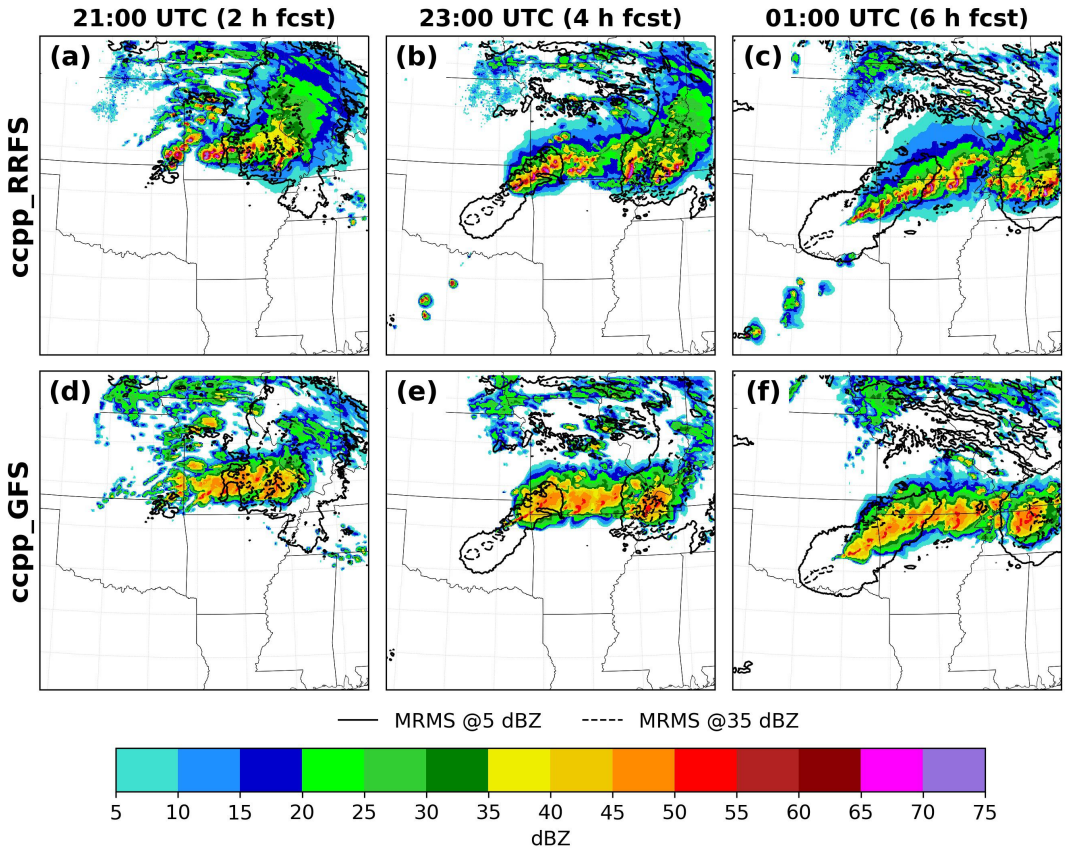

SOURCE: Author's production.

Additionally, comparison experiments were executed to investigate the impact of different analysis resolution for this squall line case. GSI has the flexibility to perform data analysis at the same or at different resolutions from the first guess. In this research, the FV3LAM model runs at a 3 km resolution. Thus, the data can be analyzed either at 3 km or, for example, 9 km to save computation time. It was found that in this case study, a 3 km analysis resolution allows for more convective scale details in the analysis increments and a slightly better representation of the composite reflectivity forecasts (see Figure 4.7). Therefore, all the subsequent experiments are performed at the 3 km resolution.

Figure 4.7 - As in Figure 4.6, but for experiments using 3DVar data assimilation with analysis grid ratio of 3 (GR3 (9 km)) (a, b, and c) and 1 (GR1 (3 km)) (d, e, and f).

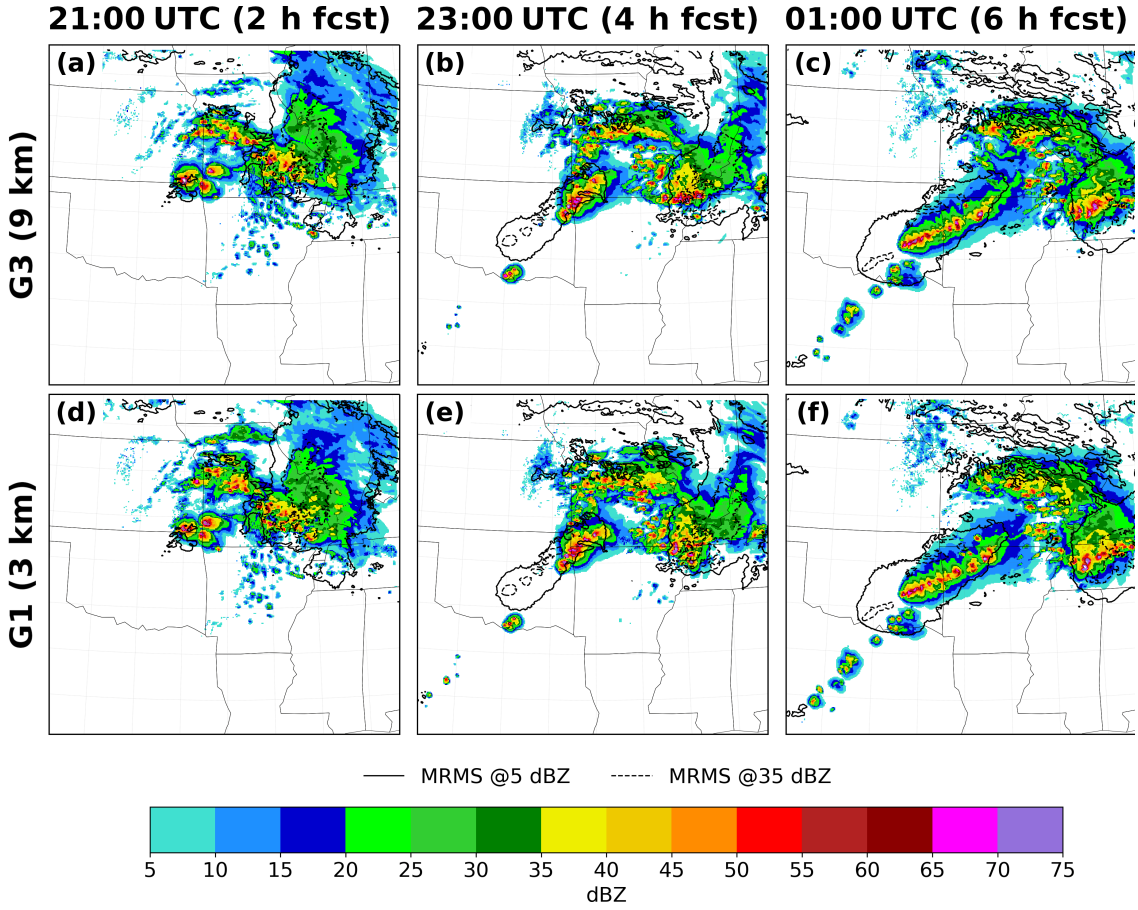

SOURCE: Author's production.

In order to examine how different weights of the ensemble background error covariance affect the results and what would be the best choice for the RRFS analysis, experiments with different ensemble weights were conducted. Only results from three experiments are presented here, i.e. 3DVar, 100EnBEC, 75EnBEC. The experiment with 3DVar does not include the ensemble background error covariance part, 100EnBEC uses pure ensemble background error covariance and does not include the static part, and 75EnBEC uses a combination of 75 % ensemble and 25 % static background error covariance. The static background error covariance for the 3DVar is the same as currently used in RAP and HRRR (BENJAMIN et al., 2016)

Previously, it was shown that ensemble localization length scales play an important role in ensemble-based data assimilation algorithms, such as hybrid EnVar analyses, as an effective way to mitigate sampling errors due to the relatively small ensemble size available for hybrid EnVar and ensemble analyses (HOUTEKAMER; MITCHELL, 2001; HAMILL et al., 2001), especially at convective scales (GUSTAFSSON et al., 2018). At this stage, it is important to determine how large the localization radius needs to be for RRFS analyses. Hu et al. (2017) tested a vertical localization radius of 9 layers in RAP, but using this larger localization radius degraded the forecast when compared to 3 layers. Knowing the expected results for a relatively larger vertical localization value using an 80 member ensemble, this study looked at the impact of reducing the vertical localization radius from 3 grid points to 1 in the lowest 10 vertical model levels in the experiment VLOC. VLOC was designed to examine the vertical localization radius that yields more realistic forecasts in RRFS. A separate study is underway in which the optimal horizontal localization for RRFS is also investigated and therefore it is not examined here. The localization function in GSI is implemented as a single application of an isotropic recursive filter (PURSER et al., 2003) and the radius is specified as a Gaussian half-width, either in scale height ($\ln p$) or in terms of number of vertical layers. In this study, the radius is specified in terms of layers. In VLOC, the vertical ensemble localization radius is changed from 3 vertical layers for the whole atmosphere (used in all other experiments) to a height-dependent localization setting: 1 vertical layer in the lowest 10 model layers and 3 layers for other model layers. A comparison experiment (not shown) was conducted reducing the vertical localization to 2 layers in the first 10 model layers, but results showed neutral impacts over VLOC.

The PBL pseudo-observation function mentioned in Chapter 2 has been used operationally since RAP version 3 (BENJAMIN et al., 2016). In practice, it first identifies the PBL height using the background forecast. It then computes the 2 m temperature and 2 m moisture observation innovations (OmB) such that they are inserted at multiple vertical levels, from the surface to the level corresponding to 75 % of the PBL height and spaced every 20 hPa (BENJAMIN et al., 2016). This technique works as if additional PBL observations are available at those levels and thus more observation innovations can be computed. Therefore, they are called “PBL pseudo-observations”. Many studies have reported the benefits of using it. Therefore, it needs to be tested and tuned for its potential use in RRFS analyses. To test whether and how this function works for a prototype RRFS system, experiment PSEUDO is designed and results are presented in Section 4.3.3.

The study of Tong et al. (2020) showed that regardless of the data assimilation method used, the storm coverage was overestimated and reflectivity values were much higher than the observed, which is likely to be linked to the physics suite used. However, it is also well known that nonphysical solutions (nonrealistic updraft/downdraft, negative humidity, supersaturation, etc.) can arise as a result from the data assimilation procedure (JANJIĆ et al., 2014) and can be tackled using constraints. Tong et al. (2016) used a divergence constraint in an hourly update 3DVar data assimilation system and found more skillful forecasts 1than when the constraint was not applied. In this study, experiment CLIPSAT is conducted to analyze how the supersaturation removal procedure available in GSI affects the storm forecasts of RRFS. This function constitutes a simple adjustment in the background supersaturation during the cost function minimization. More details on this function are presented in Section 4.3.4.

Experiments VLOC, PSEUDO, and CLIPSAT are performed using the hybrid 3DEnVar algorithm with 75 % of the ensemble background error covariance and compared against 75EnBEC results. Considering the good results obtained for experiment 75EnBEC (see Section 4.3.2) and that RAP uses operationally 75 % of the ensemble background error covariance (HU et al., 2017), this percentage was then used for these other experiments.

Table 4.2 - List of experiments presented in this study.

Experiments	**BEC weights**	**Supersat. removal**	**PBL pseudo-obs.**	**Vertical scale**
NoDA	**No data assimilation**			
3DVar	**0 % ensemble** 100 % static	false	false	3 layers
100EnBEC	**100 % ensemble** 0 % static	false	false	3 layers
75EnBEC	**75 % ensemble** 25 % static	false	false	3 layers
CLIPSAT	**75 % ensemble** 25 % static	**true**	false	3 layers
PSEUDO	**75 % ensemble** 25 % static	false	**true**	3 layers
VLOC	**75 % ensemble** 25 % static	false	false	**1 layer in first 10 3 layers above**

SOURCE: Author's production.

4.2.5 Forecast verification

After executing the experiments, MET is used for the forecast verification. Specifically, the PB2NC, Point-Stat, Grid-Stat, and Stat-Analysis tools were used in this study. Upper air (ADPUPA) and surface (ADPSFC) RAP observations were used to verify the forecasts. First, the PB2NC tool was used to convert RAP observations to the format used by MET tools. For upper air observations, the time window used was from 1 hour and 30 minutes before to 1 hour and 30 minutes after the verification time, and it was narrowed to 15 minutes before to 15 minutes after the verification time for surface observations. This was because upper air data, such as soundings, are available twice a day while surface data are available with a higher frequency. Information on the observation quality provided in the prepBURF files (WMO, 2002) was also taken into account by the PB2NC tool. The maximum quality mark setting in PB2NC allowed only observations with this quality flag or below to be used in the verification. Here, the maximum quality mark used for the observations was 2.

Next, the Point-Stat tool was used to compute the mean, RMSE, bias, and standard deviation of the difference between the point observations and forecasts. Various methods to interpolate model values to the observation locations were tested. Figure 4.8 shows the bias results for 6 h forecast of 2 m temperature at each cycle when using bilinear and nearest neighbors interpolation methods. Since the difference between the bias calculated with these two methods was very small, the bilinear method was selected for the rest of the calculations.

Figure 4.8 - Bias for 6 h forecast of 2 m temperature against METAR and SYNOP reports using bilinear and nearest neighbors interpolation methods.

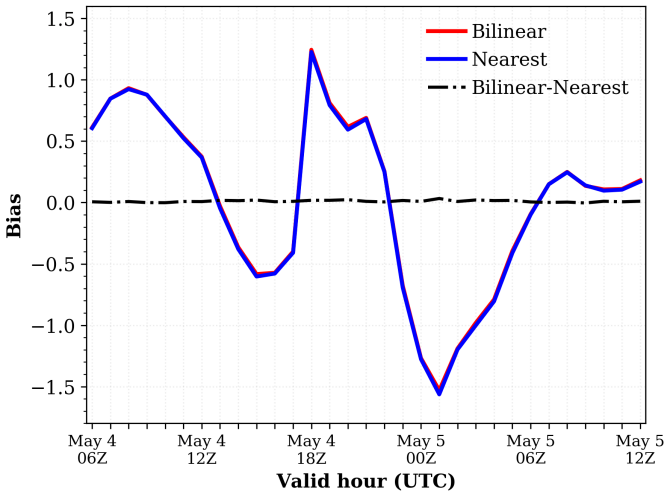

SOURCE: Author's production.

The analysis of matched pairs found that some stations had observation values diverging significantly from surrounding stations. Thus, a quality control procedure was applied to flag those stations and filter them from the verification. A quality control similar to the gross check in GSI was applied using the GSI observation error table (HU et al., 2018). The 2 m temperature and 2 m dew point temperature use the METAR observation errors. The temperature and wind vertical profiles use the observation errors from the radiosonde observations.

Figure 4.9 shows the spatial distribution of the matched pair errors (forecast minus observation) for 2 m dew point temperature in Kelvin at valid hour 17:00 UTC on 4 May 2020 (0 h forecast), before (Figure 4.9A.) and after (Figure 4.9C.) applying the quality control. The purple point in Figure 4.9B. indicates that an extremely divergent station was correctly identified. The color bar in Figure 4.9A. indicates the large magnitude of the errors before implementing the quality control. After the quality control application, this magnitude decreased considerably (see the color bar in Figure 4.9C.).

Figure 4.9 - Matched pairs for 2 m dew point temperature (K) forecasts against SYNOP and METAR stations valid at 17:00 UTC on 4 May 2020 (0 h forecast), before (A) and after (C) applying quality control. Panel B. shows the spatial distribution of METAR observations at this valid hour.

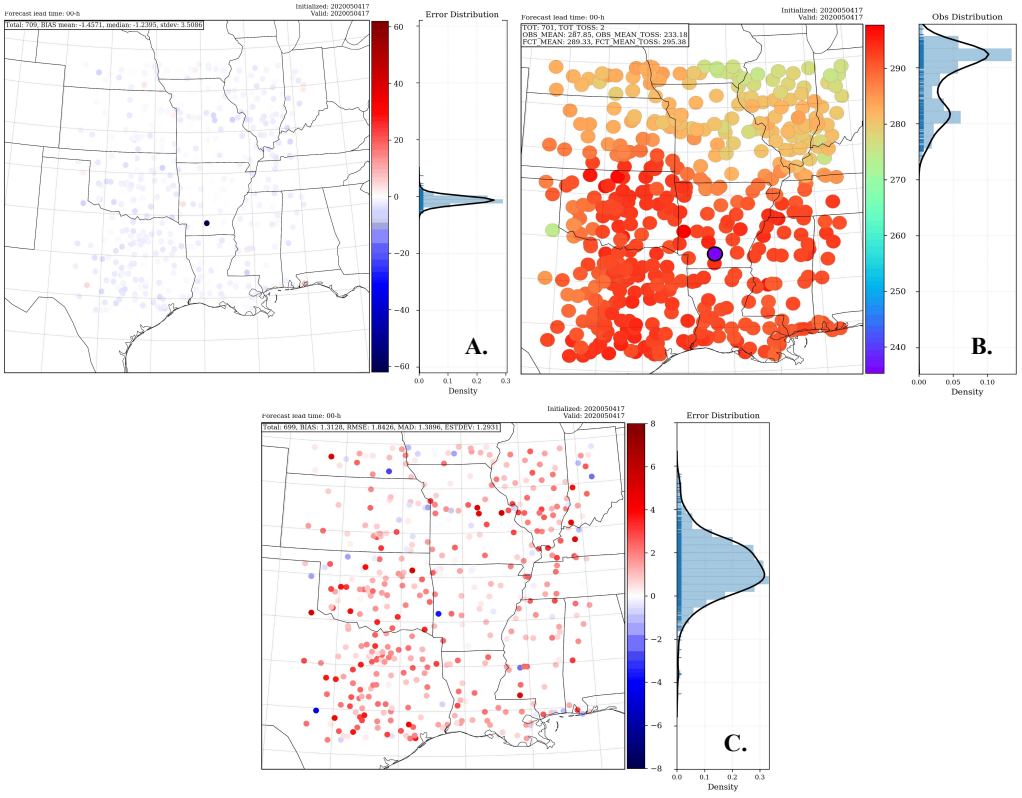

SOURCE: Author's production.

The RMSE and bias are computed, displayed with 95 % confidence intervals that were derived using a bootstrap resampling technique of 1000 replications with replacement at each forecast lead hour in every cycle, and with bias-corrected percentiles (WILKS, 2006). Upper air statistics are further analyzed at 00:00 UTC and 12:00 UTC valid times.

Precipitation forecasts are verified against the hourly Stage IV precipitation product (LIN; MITCHELL, 2005) in terms of the ETS and frequency bias (FBIAS) for different thresholds, but only >0.01 inches h^{-1} (0.254 mm h^{-1}) for lighter precipitation and >0.25 inches h^{-1} (6.35 mm h^{-1}) for heavier precipitation are presented here. The grid-to-grid approach in MET is used.

Hourly MRMS composite reflectivity mosaics (optimal method) observa-

tions (ZHANG et al., 2016) are used to verify the composite reflectivity forecasts using the MODE in MET. In order to quantitatively identify the experiment configuration that yielded better forecasts, the MMI (F+O) metric explained in Section 3.6 is analyzed.

4.3 Results and discussions

4.3.1 Examination of analyses

Observation availability and coverage play an important role in the data assimilation process. Therefore, how many and what type of observations are available for this squall line case are examined. Figure 4.10 shows the spatial distribution of assimilated temperature observations at the 19:00 UTC cycle on 4 May 2020 for experiment 3DVar (other cycles and experiments have similar distributions and are not shown here). The analysis residuals (OmA) are also depicted in Figure 4.10 using red and blue color depth for positive and negative values, respectively. In this analysis, assimilated temperature observations include those from aircraft, surface marine synoptic stations, METAR, and MESONET observations. There are a total of 3307 observations, which are well distributed across the limited model domain. Among these observations, 1545 are from aircraft, which concentrate around a few major airports as the flight descends or ascends, and spread along flight paths during the cruising portion of the flight. Moreover, a substantial amount of MESONET surface observations are also assimilated. There are far fewer METAR observations, but they are distributed evenly in the domain. A very limited number of surface marine synoptic stations are found near the coast on the Gulf of Mexico. The analysis residuals for temperature are generally small for aircraft and METAR observations, mostly less than $\pm$ 1° K in magnitude, while some MESONET observations have large analysis residuals. As pointed out in Morris et al. (2020), while some MESONET stations are well maintained, the majority do not meet siting standards and maintenance protocols and therefore are assigned a higher observation error via a station blacklist. As expected, larger residuals are found from these observations when compared to other observation networks.

Figure 4.10 - Spatial distribution of temperature observations and analysis residuals (OmA) for the analysis at 19:00 UTC on 4 May 2020 from experiment 3DVar. The color scale to the right indicates the magnitude of analysis residuals. The legend of observation type markers is shown at the top along with brackets listing associated counts and RMS error for the OmA.

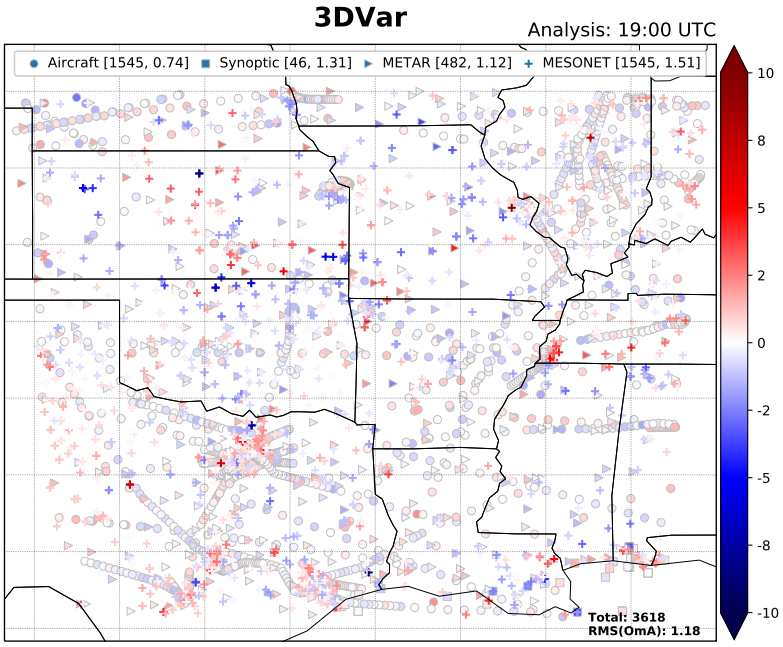

SOURCE: Author's production.

In order to check how results of the RRFS analysis behave at different cycles and whether it executes correctly, Figure 4.11 presents time series of the RMS error and bias for the backgrounds (1 h forecasts) as well as the analyses, verified against temperature observations (including all surface and upper air data as mentioned in Section 4.2.2). Results presented are for experiments 75EnBEC (Figure 4.11a) and 3DVar (Figure 4.11b). Verification is conducted by utilizing the observation innovations (OmB) and the analysis residuals (OmA) generated by GSI for each assimilated observation. Based on these OmB and OmA data, the RMS error and bias for the background and analysis are computed. It can be seen from Figure 4.11 that the analyses have smaller RMS errors and biases compared to the background in both experiments. This means the analyses fit the observations more closely, though owing to observation error not perfectly, which is expected from a correctly executed data assimilation procedure. There is a noticeable jump in the RMS error values of the OmB from 00:00 UTC (12:00 UTC) to 01:00 UTC (13:00 UTC) on 4 May 2020. This is because 00:00 UTC and 12:00 UTC are cold started from HRRR analyses. On

the contrary, at 01:00 UTC (13:00 UTC) on 4 May, the background used is from the FV3LAM 1 h forecast. Therefore, forecasts used to initialize cycles at 01:00 UTC and 13:00 UTC undergo a spin-up process. The FV3LAM 1 h forecasts are still in this spin-up process and hence yield larger RMS errors. In Figure 4.11a, the background RMS error increases steadily from 14:00 UTC to 23:00 UTC, compared to the relatively gentle increase between 02:00 UTC to 11:00 UTC on 4 May. This may be due to the fact that there is active convection during the afternoon hours and, hence, it is harder to obtain good forecast skill. Figure 4.11b has a much larger increase in the RMS error of OmB than that in Figure 4.11a during the same time period (from 14:00 UTC to 23:00 UTC), indicating that 75EnBEC performs better than 3DVar. Results from 100EnBEC are similar to 75EnBEC and not shown here.

Figure 4.11 - RMS and bias of the temperature background (OmB) and analysis (OmA) against all observation types for analyses in all cycles performed for experiments (a) 75EnBEC and (b) 3DVar. Black arrows highlight the time period from 14:00 UTC to 23:00 UTC.

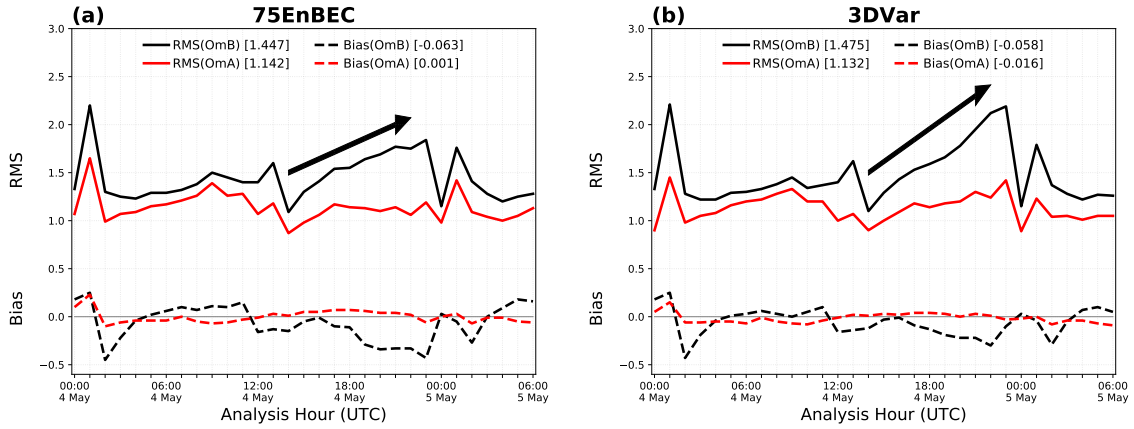

SOURCE: Author's production.

4.3.2 The impact of hybrid ensemble weights and ensemble localization radius

4.3.2.1 The impact of hybrid ensemble weights

In this hourly updated RRFS system, the hybrid 3DEnVar method is tested. One of the major concerns is how to obtain the optimal weight for the ensemble background

error covariance in the hybrid 3DEnVar analysis. A series of weighting sensitivity experiments were conducted in order to find the best option for this study.

Figure 4.12 shows the specific humidity and temperature analysis increments for the 19:00 UTC cycle on 4 May 2020 for experiments 100EnBEC, 75EnBEC and 3DVar. The analysis conducted at 19:00 UTC is during a cycling period using warm starts and is close in time to the initiation of convection in the afternoon hours. Forecasts initialized by this analysis cover the squall line evolution from its initiation to decay stages. Therefore, this cycle was selected to show the analysis increments and storm forecasts in the following sections. The analysis increments from experiment 3DVAR (Figure 4.12c and f) are smoother as compared to those from 75EnBEC (Figure 4.12b and e), which exhibits some flow-dependent features. As it goes into pure ensemble background error covariance (Figure 4.12c and d), more flow-dependent increments are obtained.

Figure 4.12 - Analysis increment for temperature (K) (a, b, and c) and specific humidity (g kg^{-1}) (d, e, and f) at the first level above the surface for 19:00 UTC on 4 May 2020, using 100 % ensemble background error covariance (a and d), 75 % ensemble background error covariance (b and e), and 3DVar (c and f).

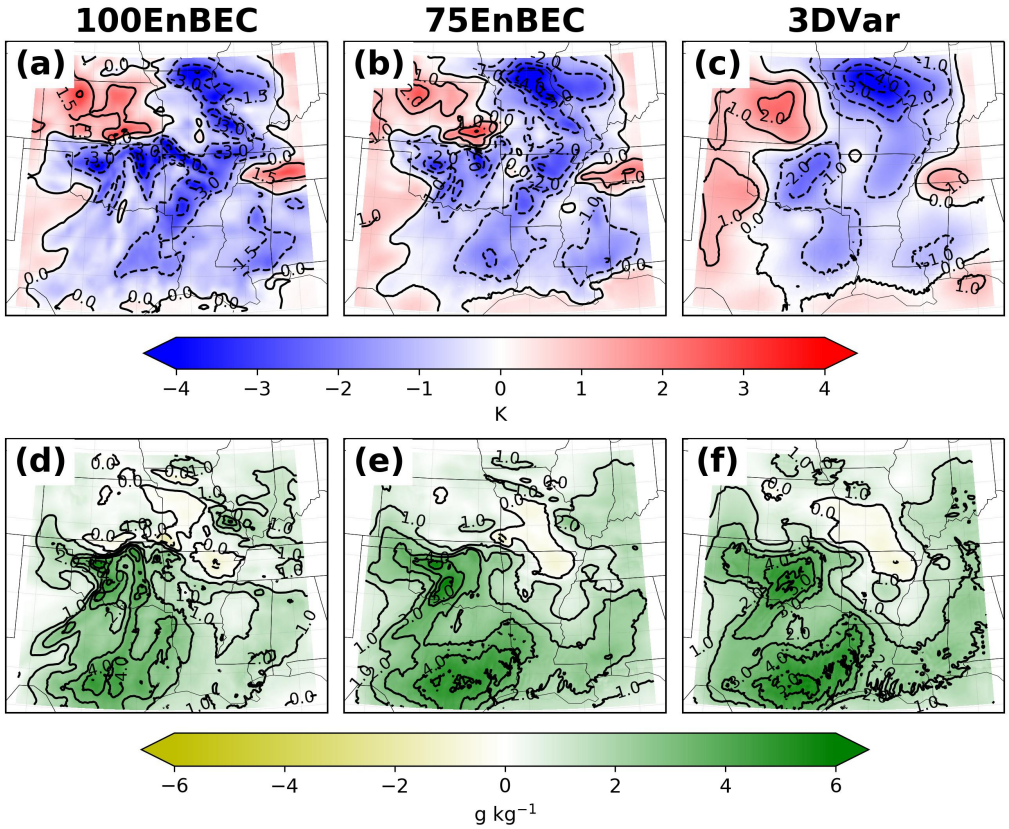

SOURCE: Author's production.

Figure 4.13 shows the 2, 4, and 6 h forecasts of composite reflectivity from the 19:00 UTC cycle on 4 May 2020, with 5 dBZ (solid lines) and 35 dBZ (dash lines) reflectivity observation contours overlaid for experiments 100EnBEC, 75EnBEC, 3DVar, and NoDA. The regridding tool in MET is used to interpolate the MRMS composite reflectivity observations to the same grid as the model forecasts. Additionally, MMI (F+O) results for reflectivity values larger than 35 dBZ for each experiment are shown in the lower right corner of each panel. All experiments predict the general evolution of the squall line, from the initial stage to maturity, with overforecasting of high reflectivity values and underforecasting of spatial coverage. At the 2 h forecast, the experiments capture the convective initiation around northeastern Oklahoma, but the extent and intensity of the cells are overpredicted (Fig-

ure 4.13a, d, g, and j). The initial cells are represented and located more accurately in the experiments with data assimilation, especially 75EnBEC with a MMI (F+O) value of 0.540 (Figure 4.13d). In the 4 h forecast, the squall line enters its mature stage and a line of storms are ranged from southwest Missouri to central Oklahoma (Figure 4.13b, e, h, and k). Every experiment predicts a squall line, but there is substantial location and coverage error in the NoDA experiment. 3DVAR improves a little over NoDA, but due to coverage predicted a decrease in the MMI (F+O) value from 0.632 to 0.556 is observed. 75EnBEC does well to predict the squall line at the correct location with the larger MMI (F+O) value of 0.698, although the storm near the southwest tip of the observed squall line is still missing as in all other experiments (Figure 4.13e). 100EnBEC overproduces the convection associated with the squall line, but still improves over 3DVar and NoDA at this forecast hour. In the 6 h forecast, the squall line moves eastward and covers from southern Missouri and northwestern Arkansas to southeastern Oklahoma. At this time, 3DVAR again performs better than NoDA with very close MMI (F+O) results, and 75EnBEC still makes the best forecast among all experiments (Figure 4.13c, f, i, and l). However, in terms of the MMI (F+O) values, the experiment 75EnBEC shows a slightly degradation for the forecast of reflectivity values larger than 35 dBZ and the experiment 100EnBEC shows the best MMI (F+O) value of 0.555. Overall, data assimilation introduces evident, positive impacts to the storm forecasts in terms of the squall line location, orientation and coverage, though different assimilation strategies yield different impacts. The improvement from 3DVar is somewhat limited while hybrid 3DEnVar is seen to perform much better. Among the experiments, 75% ensemble BEC gives the overall best forecasts.

Figure 4.13 - 2, 4, and 6 h forecasts of composite reflectivity from experiments 100EnBEC (a, b, and c), 75EnBEC (d, e, and f), 3DVar (g, h, and i), and NoDA (j, k, and l), initialized at 19:00 UTC on 4 May 2020. Solid and dashed black lines are the 5 and 35 dBZ reflectivity observation contours, valid at the forecast time, respectively.

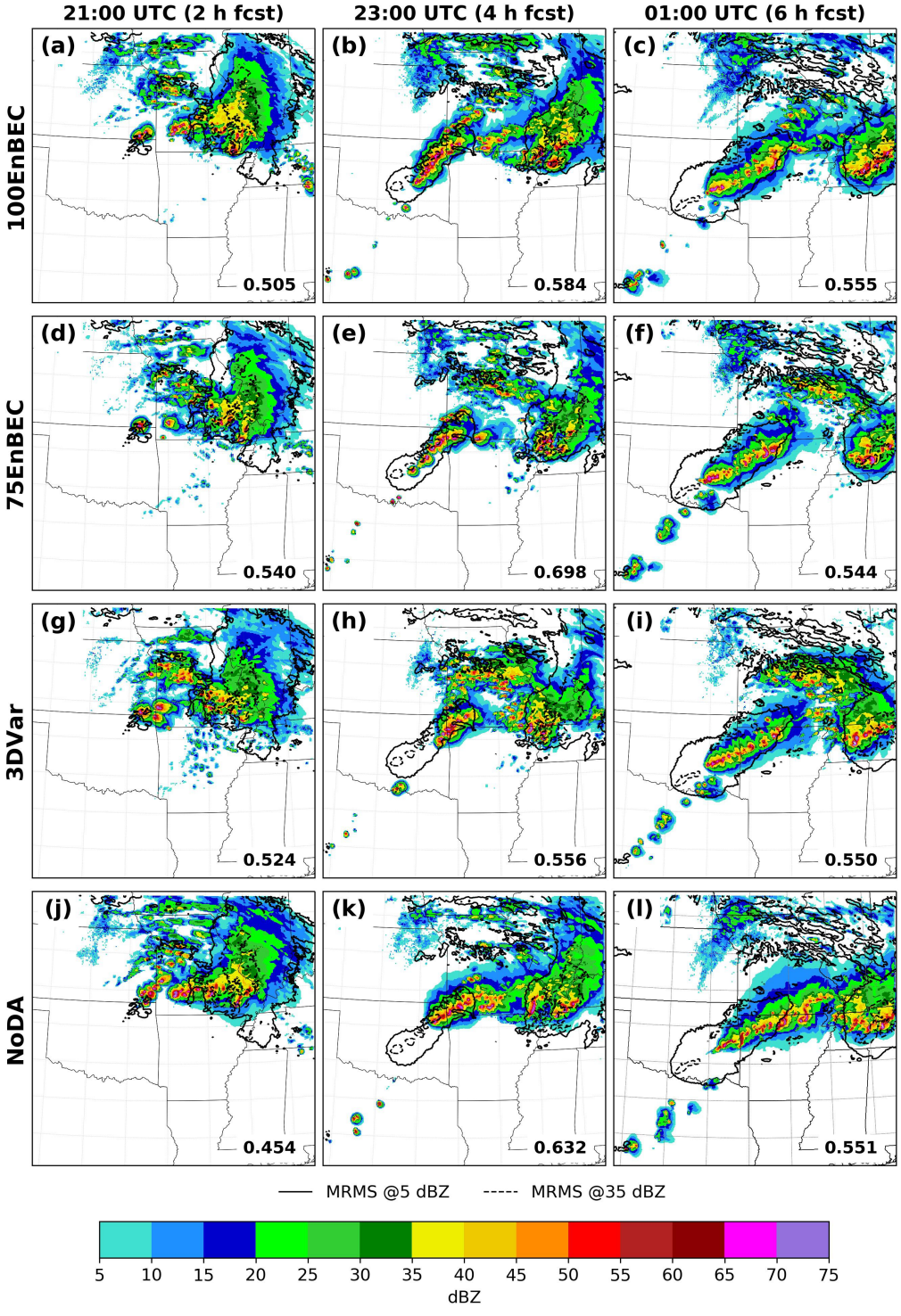

SOURCE: Author's production.

In order to examine the convective environment a few hours before the convection developed over central Oklahoma (Figure 4.1c), Figure 4.14 shows the temperature, dew point temperature, and wind vertical profiles in a Skew-T log-P diagram for the experiments 100EnBEC, 75EnBEC, 3DVar, and NoDA. The observed sounding is from the KOUN, Norman, Oklahoma station and forecast values are from the nearest grid point to the station latitude and longitude [35.18;-97.44] at 19:00 UTC on 4 May 2020. As indicators of the thermodynamic instability, the CAPE and convective inhibition (CIN) for different lifted parcel, such as surface-based (SB-CAPE), most unstable (MUCAPE), and mixed layer (MLCAPE) are also shown in this figure. The temperature and dew point temperature profile forecasts show a dryer and colder environment than the observations especially in the lower levels. Temperature forecasts are similar among the experiments and colder than observations below 600 hPa and between 275 and 225 hPa. Otherwise, the temperature forecasts are slightly warmer. Dew point temperature forecasts are also colder than observations through almost the entire atmosphere, except at the layers between 325 and 300 hPa, where the experiments predict warmer values. A very pronounced inversion is predicted at 300 hPa, which was not observed. The inversion around 875 hPa is sharper in the forecasts than that in the observations, with the 3DVar and 75EnBEC showing the coldest values in this level. Moreover, the wind is weaker than observed at all layers, mainly at middle levels. The turn of winds direction from the south closer to the surface to the west at around 400 hPa, is smoother in the forecasts than in the observations. The observed strong southwesterly low-level jet was not present in the forecasts of any experiments. All of the lift parcel CAPE values are much lower in the forecast than observed, while the predicted inhibition indices more than double the value of those observed in most of the experiments. Additionally, the pressure of level from which parcels were lifted (LPL) in the experiments are lower than the observed LPL. These environment characteristics are not favorable for convective initiation, which may be the reason of the lack of convection over central and south-central Oklahoma in all of the forecasts.

Figure 4.14 - Observed skew-T log-P diagram for KOUN, Norman, Oklahoma station at 19:00 UTC on 4 May 2020 and the 2 h forecast counterparts from experiments 100EnBEC, 75EnBEC, 3DVar, and NoDA initialized at 17:00 UTC on 4 May 2020. The observed and predicted SBCAPE, MUCAPE, and MLCAPE are shown in J kg^{-1}.

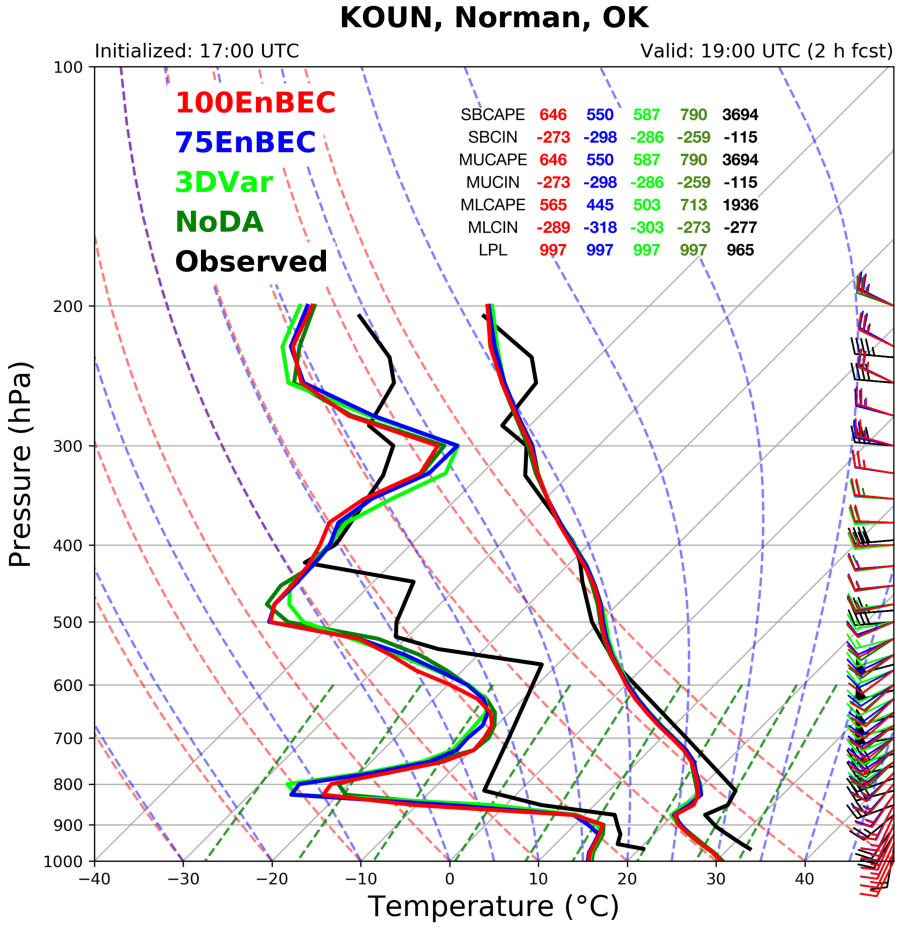

SOURCE: Author's production.

Vertical profiles of RMSE and bias with 95 % confidence intervals for the 2 h forecast of temperature, specific humidity, and wind at 00:00 UTC and 12:00 UTC valid hours (from cycles initialized at 22:00 UTC and 10:00 UTC on 4 May, respectively) are shown in Figure 4.15. The confidence intervals help to highlight where the differences between the experiments are statistically significant. Experiments show a consistent warm bias at both 00:00 UTC and 12:00 UTC in most vertical levels (Figure 4.15a and d). A cold temperature bias is present in the layers between 850 and 650 hPa at 00:00 UTC and at 1000 hPa and 150 hPa at 12:00 UTC in all experiments. Experiment 75EnBEC has smaller temperature RMSE values between 400 and 250 hPa

at 00:00 UTC and between 550 and 400 hPa at 12:00 UTC. The improvements for the temperature bias at 00:00 UTC are statistically significant between 500 and 400 hPa. Experiment 100EnBEC shows smaller RMSE at 850 hPa at both valid hours. All experiments with data assimilation have smaller temperature RMSE and bias below 850 hPa for 00:00 UTC, which are statistically significant as shown by the confidence intervals indicating the positive impact from data assimilation, but the impact of the analysis on the 2 h temperature forecast valid at 12:00 UTC is less clear. Similarly, the specific humidity forecasts show improved RMSE and bias from data assimilation below 900 hPa at 00:00 UTC and varied results among the experiments at 12:00 UTC (Figure 4.15b and e). The 2 h forecast of wind profiles has a positive bias in the lower levels at both valid hours, but mostly negative above 850 hPa (Figure 4.15c and f). The wind RMSE results do not clearly indicate which experiment is best, but in general 100EnBEC shows the lowest values when considering all vertical levels. These results may indicate that the static BEC matrix used may not be optimal for RRFS v0.1 and efforts are underway in order to obtain a better BEC matrix. Moreover, an online estimation approach may be explored for the specification of the hybrid weighting parameter, such as the method proposed by Azevedo et al. (2020) in which a geographically varying weighting factor alpha is defined and the ensemble spread is used for the assignment of the weights.

Figure 4.15 - Vertical profiles of RMSE (left), bias (right), and upper (95 %) and lower (5 %) limits of the confidence interval (shading) for the 2 h forecast of temperature (a and d), specific humidity (b and e), and wind (c and f) against rawindsonde, dropsonde, and pilot balloon observations at 00:00 UTC (a, b, and c) and 12:00 UTC (d, e, and f) valid hours on 4 May 2020 for experiments 100EnBEC, 75EnBEC, 3DVar, and NoDA. Matched pair counts used for RMSE and bias computation at each level are shown on the right vertical axis. Each experiment's mean RMSE and bias across all vertical levels are shown in the upper corner of each panel.

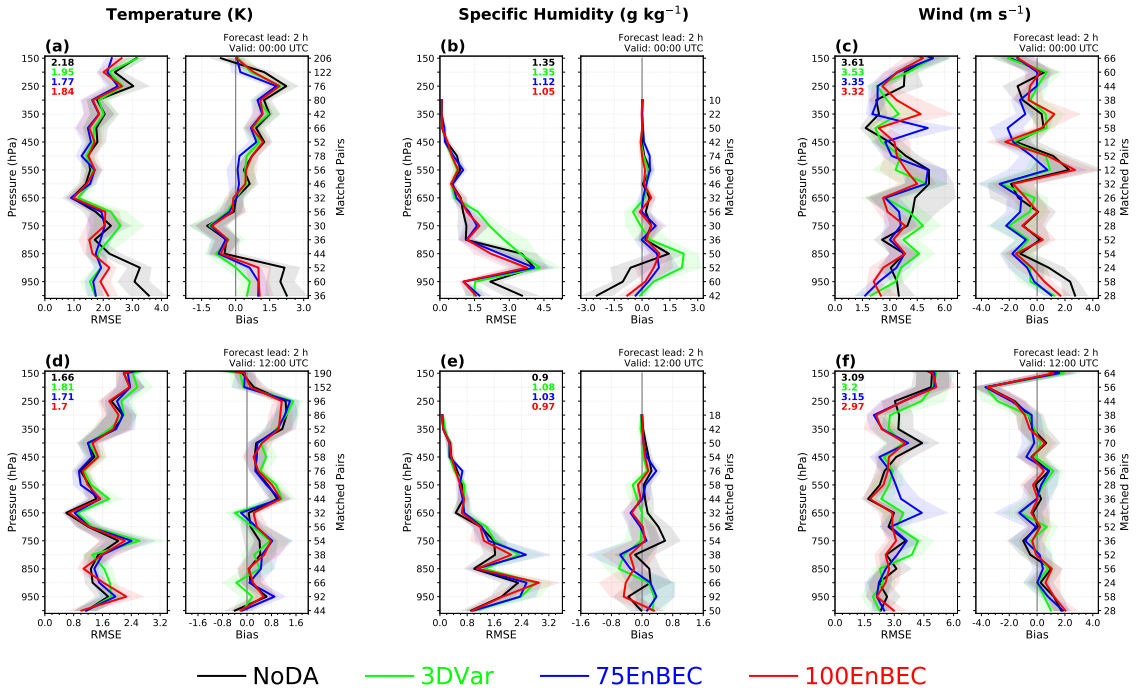

SOURCE: Author's production.

Figure 4.16 presents the RMSE and bias for the 2 h forecast of 2 m temperature (Figure 4.16a and c) and 2 m dew point temperature (Figure 4.16b and d) for experiments 100EnBEC, 75EnBEC, 3DVar and NoDA. 2 m temperature and 2 m dew point RMSE are evidently larger between cycles initialized at 16:00 UTC and 23:00 UTC in all experiments. This may be related to the initiation and development of convection in many areas of the domain. During this period, all data assimilation experiments have smaller 2 m temperature and 2 m dew point RMS errors compared to the NoDA experiment, demonstrating the positive impact from data assimilation. Further, experiments 75EnBEC and 3DVar perform better than 100EnBEC between cycles initialized at 16:00 UTC and 20:00 UTC (18:00 UTC and 22:00 UTC valid

hour) (Figure 4.16a). Among them, 75EnBEC produces the smallest 2 m temperature and 2 m dew point RMSE. From 16:00 UTC to 23:00 UTC valid hour, the 2 h forecasts from all experiments show a warm and dry bias. Data assimilation experiments helped to reduce this warm and dry bias to some extent.

Figure 4.16 - RMSE and bias for the 2 h forecast of 2 m temperature (a and c) and 2 m dew point temperature (b and d) against synoptic station and METAR observations for experiments 100EnBEC, 75EnBEC, 3DVar, and NoDA. On average 600 observations between these two sources were used each analysis cycle for the statistics computation. The legend for each experiment is shown at the bottom of each panel along with brackets listing the associated RMSE averaged over all cycles in panels (a) and (b).

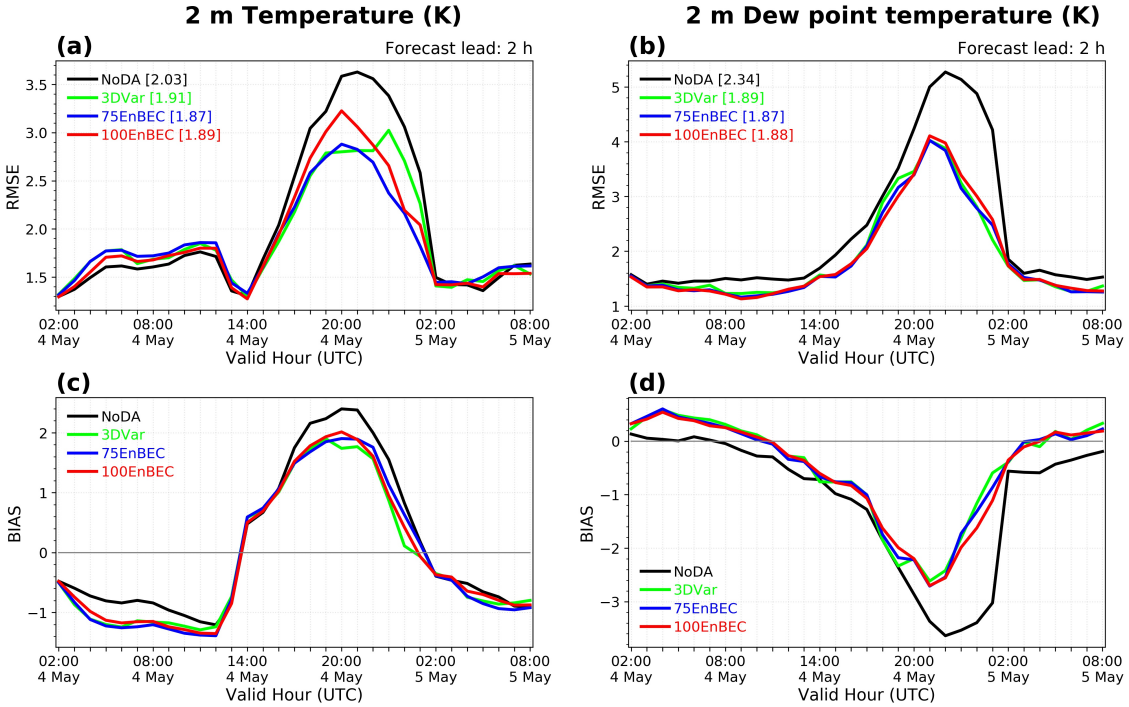

SOURCE: Author's production.

To summarize, experiment 75EnBEC performs the reasonably better among all experiments discussed in this section. It gives the smallest 2 m temperature and 2 m dew point RMSE during the afternoon storm hours and a better representation of the storm in all forecasts lengths. Therefore, all subsequent experiments use the 75 % ensemble background error covariance.

4.3.2.2 The impact of vertical ensemble localization radius

As discussed in Chapter 2, a function is applied to the ensemble-based covariances in order to spatially localize their variation with distance. Gustafsson et al. (2018) pointed out that the localization needs to be large enough to not disrupt the large scale balance but small enough to represent fluctuations at the convective scale. Thus, unlike at global scales, the operational RAP and HRRR systems use a horizontal localization radius of 110 km in combination with a vertical localization radius of 3 layers, which give optimal forecast skill in RAP applications (HU et al., 2017). In the experiment VLOC, a reduction in the vertical localization radius from 3 to 1 is adopted to capture finer vertical features of low atmosphere from the observations close to the surface and below the PBL.

Figure 4.17 presents the RMSE and bias with 95 % confidence intervals for vertical profiles of the 2 h forecast of temperature, specific humidity, and wind valid at 00:00 UTC and 12:00 UTC for experiments VLOC and 75EnBEC. For the temperature forecasts, VLOC has a lower RMSE between 800 and 550 hPa and smaller bias in the lower atmosphere between 1000 to 900 hPa and 800 to 700 hPa during the late afternoon (valid hour 00:00 UTC) (Figure 4.17a). At valid hour 12:00 UTC, VLOC gives a lower RMSE between 950 and 900 hPa and 350 and 300 hPa, and lower bias in the upper atmosphere between 450 and 250 hPa (Figure 4.17d). For specific humidity, the RMSE and bias are improved at all levels above 650 hPa at 00:00 UTC with VLOC. However, a degradation is observed in the RMSE in the lower levels below 700 hPa. Degradation is also seen in the bias between 950 and 800 hPa (Figure 4.17b). At valid 12:00 UTC, not much improvement is shown in either the RMSE or bias from VLOC (Figure 4.17e). Most of the differences between these experiments are not statistical significant as indicated by the confidence intervals. Meanwhile, a general positive impact is observed in the RMSE and bias for the winds above 650 hPa but negative impact in lower levels at 00:00 UTC valid hour. At 12:00 UTC valid hour, slight improvements are shown for VLOC in the RMSE between 650 and 500 hPa and at 400 hPa, and in the bias at 550 hPa and 350 hPa (Figure 4.17f).

Figure 4.17 - As in Figure 4.15, but for experiments 75EnBEC and VLOC.

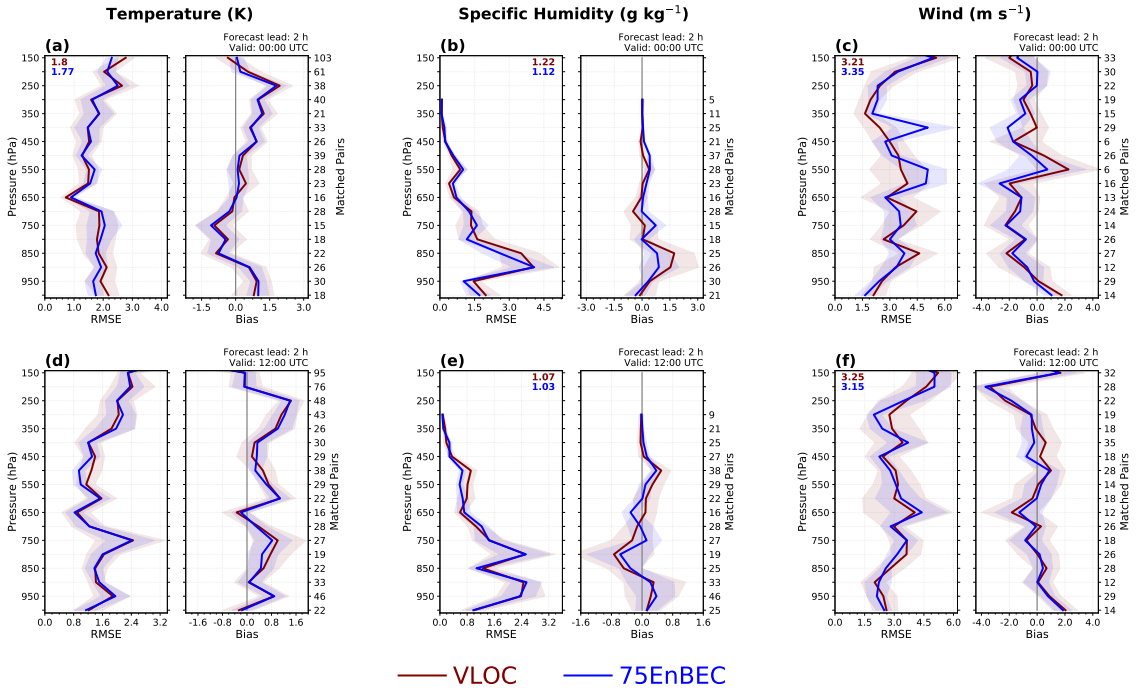

SOURCE: Author's production.

The change in vertical localization slightly improves the extent and intensity of convection over northeastern Oklahoma in the 2 h forecast, however MMI (F+O) values indicate that the experiment 75EnBEC is still more skillful representing the reflectivity larger than 35 dBZ with a decrease from 0.540 in 75EnBEC to 0.528 in VLOC. An underforecast of the convection over central and eastern Oklahoma is observed in VLOC in the 4 h forecast with a smaller MMI (F+O) value of 0.587 and an overforecast over north-central Arkansas and south-central Missouri is observed in the 6 h forecast with a slight improvement in the MMI (F+O) value from 0.544 in 75EnBEC to 0.563 in VLOC (Figure 4.18). While reducing the vertical localization scale did produce small improvement at some vertical levels and larger forecast lengths, degradation dominated the overall signature, indicating this variation of localization scale produces overall less skillful storm forecasts. The analysis cycling technique and multivariate relationships in the background error covariance spread the observations impact throughout different levels and locations, which could have led to the slight positive impact above 650 hPa instead of the lower atmosphere where the modification in the vertical localization is made. It suggests a vertical

ensemble localization radius of 3 layers is already a good choice if not the best.

Figure 4.18 - As in Figure 4.13, but for experiments VLOC (a, b, and c) and 75EnBEC (d, e, and f).

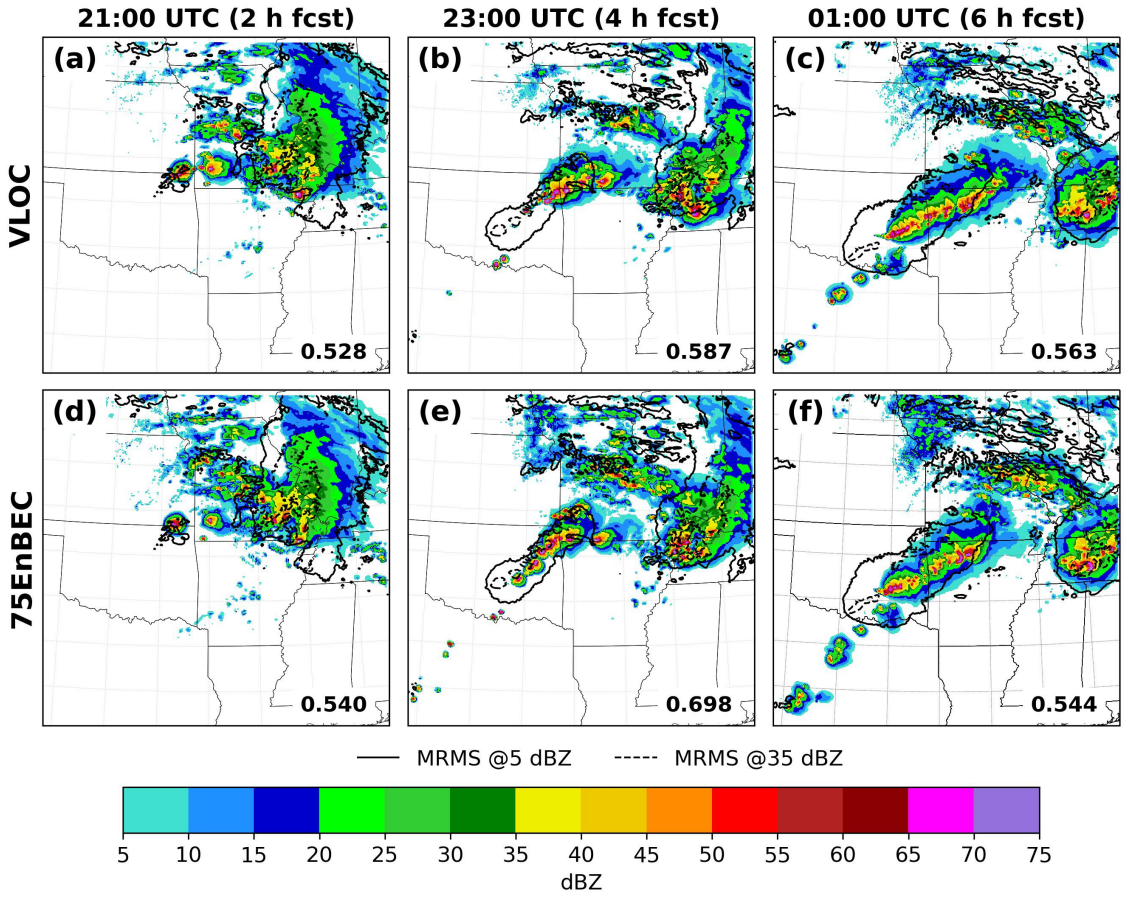

SOURCE: Author's production.

4.3.3 The impact of PBL pseudo-observations

The impact of adding PBL pseudo-observations to the analysis based on surface temperature and moisture observations is evaluated in experiment PSEUDO. This function is tested with the PBL pseudo-observation configuration used in the operational RAP system.

The 2, 4, and 6 h composite reflectivity forecasts from experiments PSEUDO and 75EnBEC are presented in Figure 4.19. PSEUDO clearly predicted more convection

than 75EnBEC in the 2 h forecast, with a smaller MMI (F+O) value of 0.533 in comparison to 0.540 in the experiment 75EnBEC (Figure 4.19a). However, noticeable improvements in the coverage and positioning of the storm are found in 4 and 6 h forecasts, with a corresponding increase in the MMI (F+O) values when compared to 75EnBEC (Figure 4.19b and c). Especially at 4 h, the representation of the squall line over Oklahoma is greatly improved after adding PBL pseudo-observations with a better coverage of the squall line, although an increase in the intensity of the convective cores is also noted (Figure 4.19b). Spurious convection also appeared over northwest Oklahoma and Texas in the 4 h forecast and over Texas in the 6 h forecast. These results indicate the potential of using PBL pseudo-observations in RRFS to improve the representation of convection.

Figure 4.19 - As in Figure 4.13, but for experiments PSEUDO (a, b, and c) and 75EnBEC (d, e, and f).

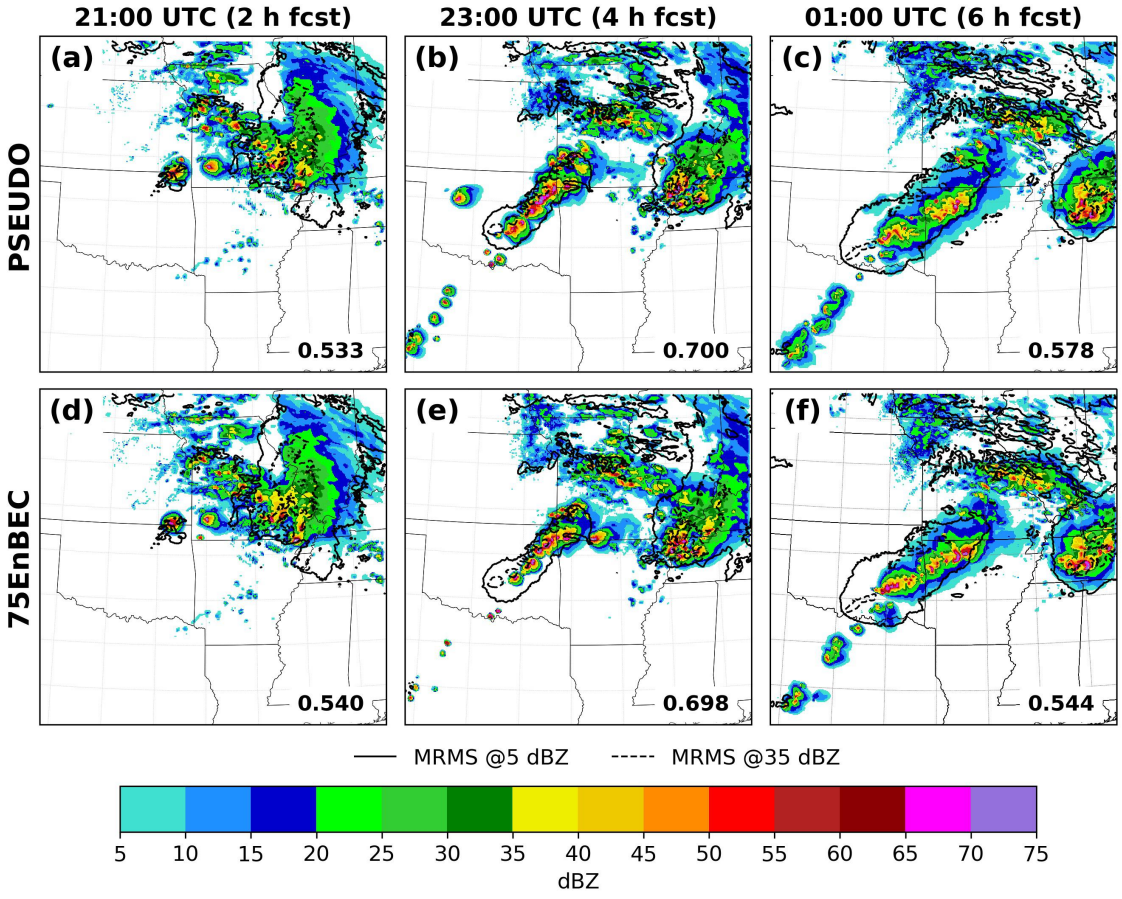

SOURCE: Author's production.

The RMSE and bias vertical profiles for the 2 h forecast of temperature, specific humidity, and wind against sounding observations at the 00:00 UTC and 12:00 UTC valid hours are presented in Figure 4.20. The use of PBL pseudo-observations gives subtle positive impacts at both valid hours and most vertical levels for the RMSE and bias of temperature and specific humidity (Figure 4.20a, b, d, and e). Improvements in the RMSE and bias of temperature are observed below 900 hPa at valid hour 00:00 UTC. The positive impact in the bias extends to 800 hPa, indicating the better representation of the lower atmosphere in the experiment PSEUDO (Figure 4.20a). A slight degradation is observed in the middle levels at the same valid hour. For wind, the RMSE shows more promising results with a positive and statistically significant impact between 500 and 550 hPa at 00:00 UTC and 12:00 UTC valid hours. This positive impact is also significant at 300 hPa in the RMSE and bias results at 00:00 UTC (Figure 4.20c). At 12:00 UTC, the bias shows more subtle improvements in 750 hPa and 300 hPa (Figure 4.20f).

Figure 4.20 - As in Figure 4.15, but for experiments 75EnBEC and PSEUDO.

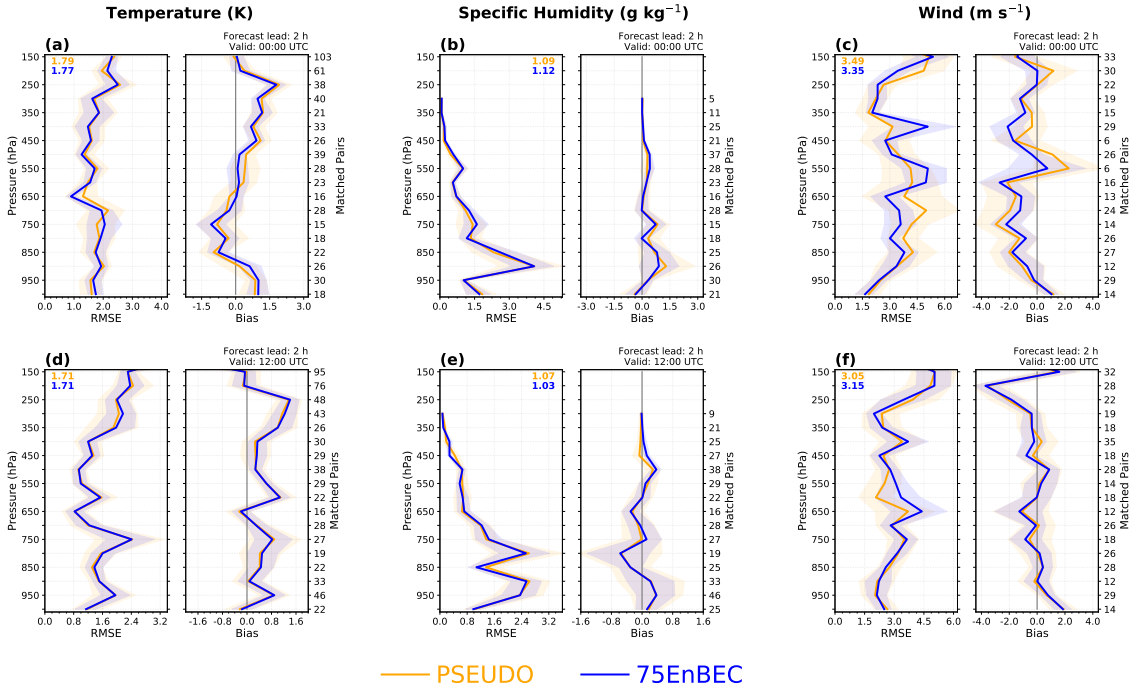

SOURCE: Author's production.

Similar to the upper air verification, the RMSE and bias of 2 m temperature and 2 m dew point temperature for the 2 h forecast in PSEUDO show overall neutral impact. A degradation in the RMSE of 2 m temperature is observed between cycles initialized at 21:00 UTC and 00:00 UTC (Figure 4.21a) and in the bias between cycles initialized at 17:00 UTC and 21:00 UTC. A subtle improvement in the bias of 2 m temperature between cycles initialized at 21:00 UTC and 23:00 UTC. Slight improvements are observed in the RMSE and bias of 2 m dew point temperature between cycles initialized at 19:00 UTC and 23:00 UTC. Adding PBL pseudo-observations helps to mitigate near surface dry bias during afternoon hours, makes upper air forecasts better in some levels of middle and upper atmosphere, and clearly improves the storm forecast in the 4 h and 6 h forecasts. Nevertheless, more tuning and testing of this function are needed before applying this technique in the RRFS.

Figure 4.21 - As in Figure 4.16, but for experiments 75EnBEC and PSEUDO.

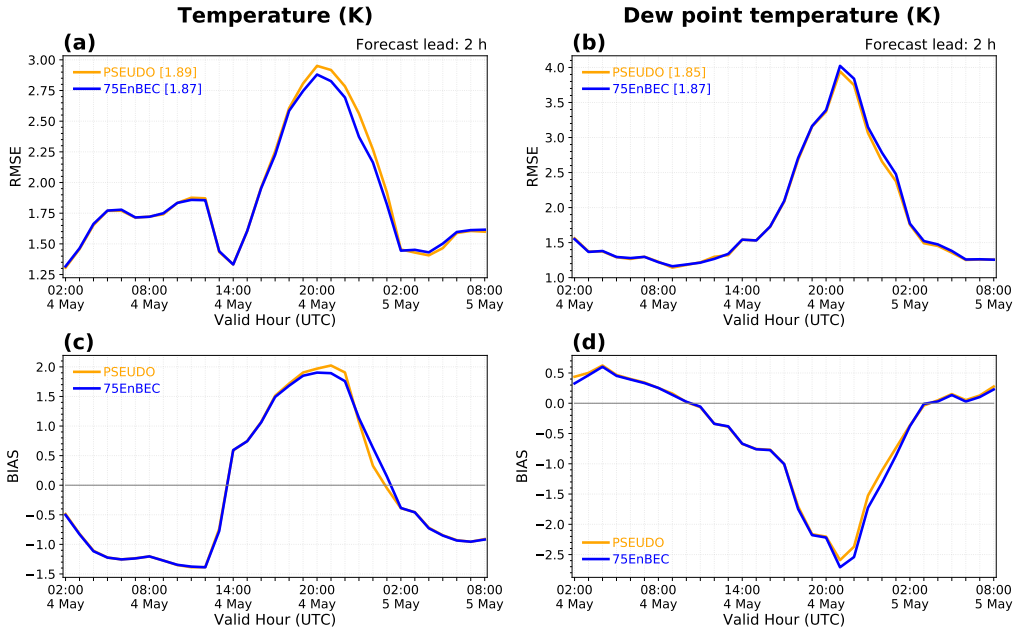

SOURCE: Author's production.

4.3.4 The impact of supersaturation removal

GSI has a function to remove supersaturation in the background by capping specific humidity to its saturation value in each outer loop during the minimization of the cost function, as calculated using the background fields (CIMSS, 2014). Figure 4.22

shows the difference in the specific humidity (g kg^{-1}) analyses between the 75EnBEC analysis and the 75EnBEC analysis with the supersaturation clipping function activated (75EnBEC vs. CLIPSAT) for the 19:00 UTC cycle on 4 May 2020. Since more moisture is present in the lower atmosphere, model hybrid level 50 (located in the lower atmosphere at around 850 hPa) was selected to show this result. Positive (negative) differences in Figure 4.22 indicate that more (less) specific humidity is found in the 75EnBEC analysis than in CLIPSAT. The figure suggests that supersaturation is removed in the CLIPSAT analysis mostly over southwestern and northwestern Missouri, southeastern Kansas, northern Arkansas and Oklahoma. It is worth mentioning that the computational run time of the analyses in CLIPSAT was quite similar to 75EnBEC (not shown).

Figure 4.22 - Difference in specific humidity (g kg^{-1}) fields for the 19:00 UTC cycle on 4 May 2020 between analyses without and with supersaturation clipping activated (75EnBEC - CS), at model hybrid level 50.

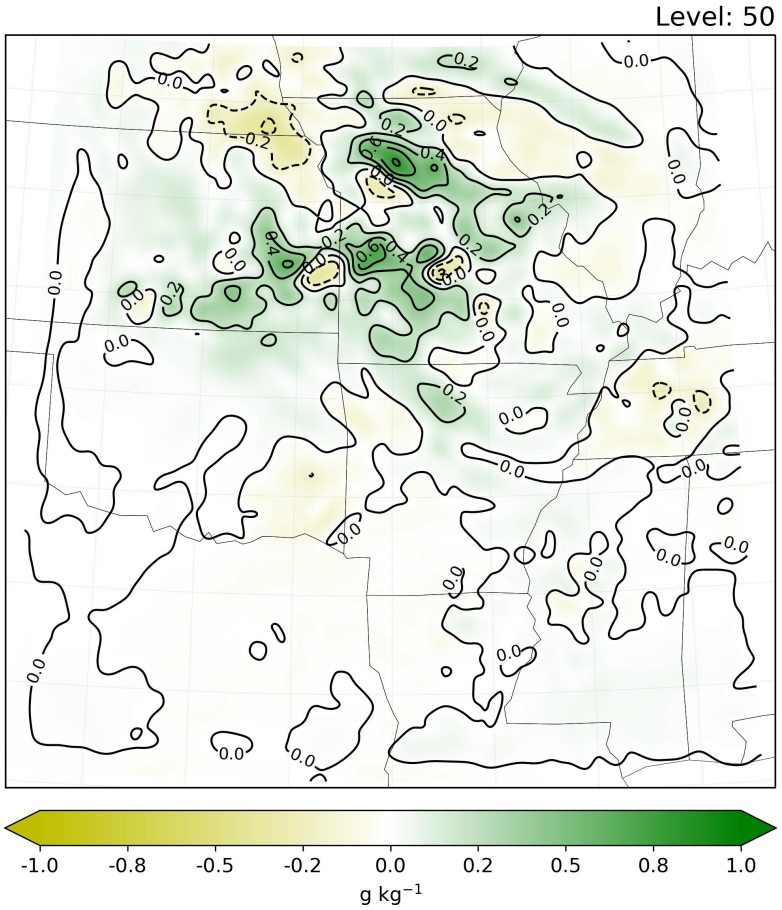

SOURCE: Author's production.

The 2, 4, and 6 h composite reflectivity forecasts are shown in Figure 4.23 for experiments CLIPSAT and 75EnBEC. When the supersaturation removal function is activated in the analyses, a better evolution of the squall line is observed in the 4 and 6 h forecasts (Figure 4.23b and c). The displacement errors are reduced and less spurious convection is seen over southern Missouri and northern Arkansas at these forecast hours (Figure 4.23b, c, e, and f). As seen in Figure 4.22, over these areas the CLIPSAT analysis showed less specific humidity content than in 75EnBEC. However, less spatial coverage of the convection is forecast over eastern Missouri, and the spurious convection is increased over southwestern Missouri at the 2 h forecast in CLIPSAT when compared to 75EnBEC (Figure 4.23a and d). The MMI (F+O) values show more skillful forecast of reflectivity larger than 35 dBZ for all forecast lengths in the experiment CLIPSAT. These values are greatly increased at 2 h forecast from 0.540 in 75EnBEC to 0.811 in CLIPSAT, and from 0.698 to 0.793 at 4 h forecast. Results from CLIPSAT indicate the presence of longer-term bias that is being corrected to some extent in this experiment. However, because the atmospheric state is periodically refreshed with the large scale conditions as part of the partial cycling procedure, the model bias cannot be fully examined. Further investigation involves adapting the approach employed by Wong et al. (2020) in which forecast tendencies are used to investigate systematic model biases in a continuously cycled experiment.

Figure 4.23 - As in Figure 4.13, but for experiments CLIPSAT (a, b, and c) and 75EnBEC (d, e, and f).

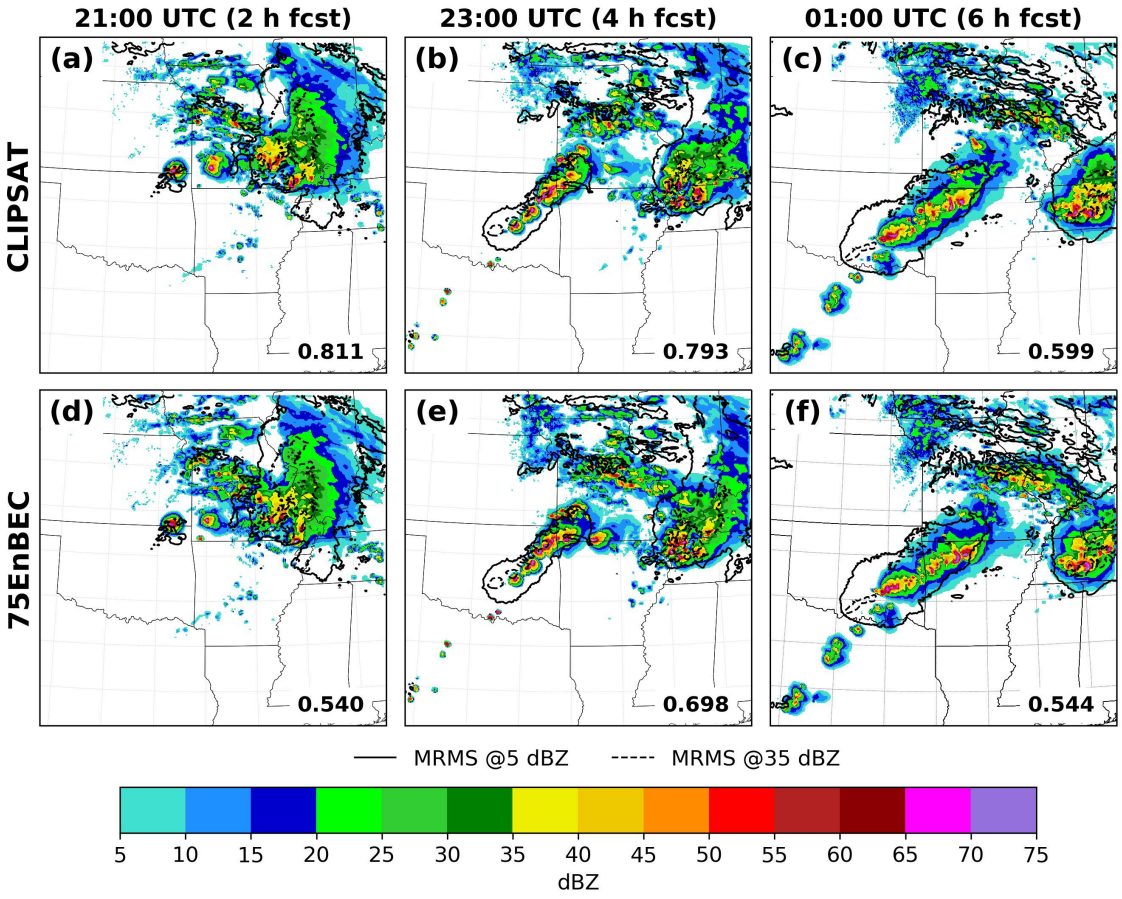

SOURCE: Author's production.

Although this function imposes a nonphysical constraint to remove the supersaturation from the background when minimizing the cost function, it leads to overall more skillful forecasts without an increase in the computational cost. These results agree with what is found in previous studies, in which the use of constrains in the analyses led to more skillful forecasts (VENDRASCO et al., 2016; TONG et al., 2016) using a divergence constraint). This is a common practice in order to preserve nonnegativity in the analyses but also comes at the cost of violating mass conservation (JANJIĆ et al., 2014; JANJIĆ et al., 2021).

4.3.5 Quantitative precipitation forecast verification

To further evaluate the experiments conducted, the FV3LAM 1 h accumulated precipitation is also analyzed. Precipitation forecasts remain a challenge for NWP models at various spatial and temporal scales. Because of their complexity, precipitation forecasts are frequently used to evaluate model performance.

As mentioned in Section 4.2.5, precipitation forecasts are verified against Stage IV precipitation observations at various thresholds. Figure 4.24 shows the ETS and FBIAS for 1 h accumulated precipitation greater than 0.01 inches h^{-1} (Figure 4.24a and c) and 0.25 inches h^{-1} (Figure 4.24b and d) for all experiments at each forecast lead hour. These verification measures are based on the two-by-two contingency table used for categorical (dichotomous) variables (JENSEN et al., 2020). ETS is based on the threat score or critical success index and is commonly used to examine the performance of precipitation forecasts. Perfect forecasts have ETS values close to 1, while forecasts without skill have ETS values close to 0. Meanwhile, FBIAS indicates when an event is forecast more or less often than it is observed. FBIAS greater than 1 indicates an event is overforecast, while less than 1 suggests an event is underforecast. An FBIAS equal to 1 indicates that the event is predicted as frequently as it is observed (WILKS, 2006).

For this case study, ETS values decrease as the precipitation threshold increases in all of the experiments assessed (Figure 4.24a and b), indicating the difficulty in predicting heavier precipitation events. Most of the experiments with data assimilation have higher ETS scores for precipitation greater than 0.01 inches h^{-1} than NoDA during almost the entire 18 hour forecast (Figure 4.24a). This shows the positive impact of data assimilation in the analyses and subsequent lighter precipitation forecasts. Experiments 100EnBEC, CLIPSAT, 75EnBEC, and PSEUDO show higher ETS values in the first 4 hours of the forecast. Between 4 h and 16 h forecast, experiment CLIPSAT shows the best performance among all experiments, followed by 100EnBEC, 75EnBEC, and PSEUDO which shows very close results to 75EnBEC. In terms of FBIAS, 100EnBEC shows better scores until the 11 h forecast lead (Figure4.24c). Between 2 and 8 h forecast, experiment VLOC shows the largest underforecast among all experiments. The verification of 1 h accumulated precipitation greater than 0.25 inches consistently shows that using hybrid and pure ensemble BEC in data assimilation improves the precipitation forecasts in the first 13 hours forecast, with 75EnBEC outperforming 100EnBEC within the first four hours (Figure 4.24b). After the 13 h forecast, experiment NoDA performs better, which shows

data assimilation mainly improves the short term forecast and the major factor for a good long term forecast is the quality of the background from the outside model as well as the FV3 LAM model itself. For the 0.25 inches h^{-1} threshold, precipitation is overforecast in experiments 100EnBEC and NoDA in the first 3 hours, underforecast in experiments 3DVar, 75EnBEC, PSEUDO, VLOC, and CLIPSAT. All experiments underforecast accumulated precipitation greater than 0.25 inches h^{-1} after the 9 h forecast (Figure 4.24d).

Figure 4.24 - ETS (a and b) and FBIAS (c and d) for 1 h accumulated precipitation forecasts greater than 0.01 inches (a and c) and 0.25 inches (b and d) from experiments CLIPSAT, PSEUDO, VLOC, 100EnBEC, 75EnBEC, 3DVar, and NoDA for 18 hour forecasts.

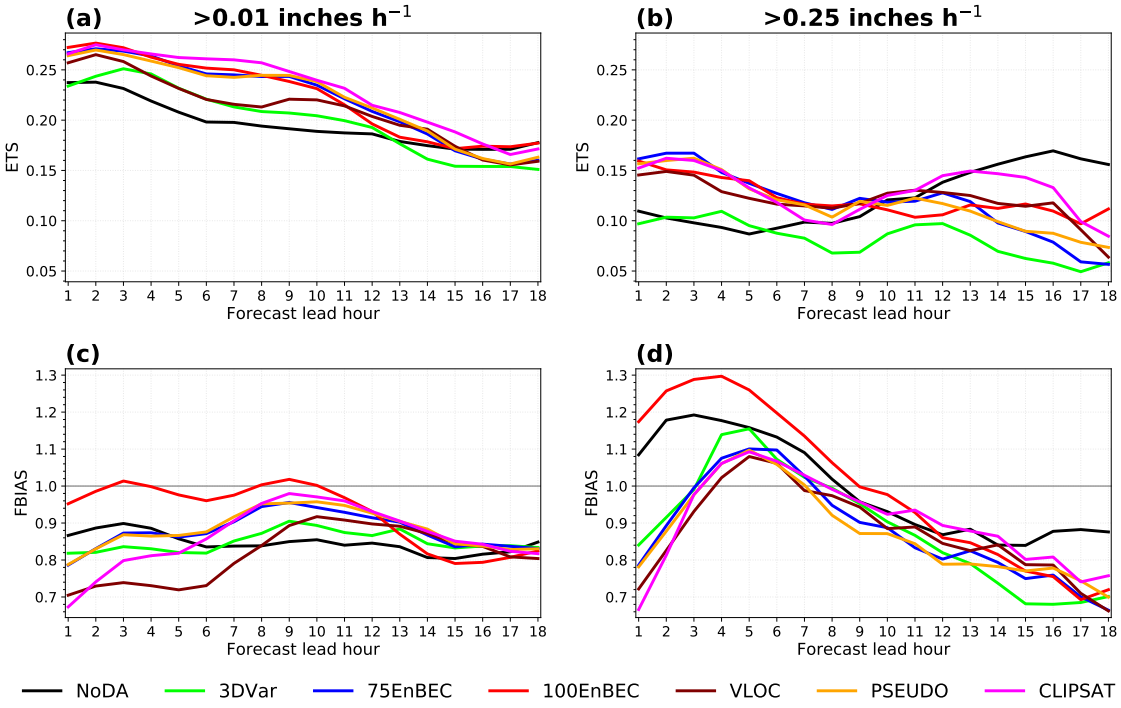

SOURCE: Author's production.

5 RRFS OVER NORTHERN SOUTH AMERICA

This chapter is divided into two main parts: the first is dedicated to the case study selection (see Section 5.2) and a second part focuses on the configuration and execution of numerical simulations of the selected case (see Section 5.3). An overview of the data and methods employed is presented in each section along with the results and discussions of the impacts on the analyses and forecasts.

5.1 Introduction

The Amazon offers favorable conditions for the development of deep convection that is organized in MCS. In northern South America, MCS occurrence is related to Amazon coastal squall lines and to the incursion of cold outbreaks, mostly in southwest Amazon. Amazon coastal squall lines are observed in satellite imagery as discontinuous clusters of convective cells along the northern coast of South America, developed on the sea-breeze circulation, organized on the mesoscale, and considered one of the main rain-producing systems in the region (GARSTANG et al., 1994; COHEN et al., 1995). Because of the role the Amazon plays on the regional weather and climate, numerous studies have been conducted using observations derived from field campaigns held in the Amazon, meteorological satellites, *in situ* sources, reanalyses, and numerical models providing the scientific community with a better understanding of processes at various scales. In particular, the data collected during field campaigns, such as the ABLE field campaign (GARSTANG et al., 1990), the Large-Scale Biosphere-Atmosphere Experiment (KELLER et al., 2004) and more recently the GoAmazon2014/5 experiment (MARTIN et al., 2016), have been invaluable in providing large amounts of data that otherwise would not be possible to obtain. The results from these field campaigns have greatly improved the knowledge and understanding of the atmospheric chemistry of the Amazon as well as the dynamics, environmental conditions, structure, rainfall characteristics, and life cycle of convective systems that occur in the Amazon basin. However, despite all these efforts, the deep convection and diurnal cycles of precipitation and convection in the Amazon region are not satisfactorily simulated by the models.

As global numerical models increase the horizontal resolution and more NWP centers are concentrating their efforts on unified models, it is important to examine what is the current capability of regional and convection-allowing models representing a wide variety of phenomena. As mentioned previously, NOAA is transitioning toward a unified model in which the same dynamical core is used for all applications, from global to convective scale through the UFS. RRFS, as the UFS application for

regional and convective scales, is intended to cover a similar domain as the operational RAP, which imposes the need to investigate the capability of the prototype RRFS to represent convection over part of northern South America and the Atlantic Ocean. In particular, the initiation and development of Amazon coastal squall lines can give an insight in the capabilities of RRFS over areas with low data density. Another important issue is the role of the tropical waves in establishing the dynamical and thermodynamical conditions for triggering the intense coastal lines that eventually develop into long lasting lines. Therefore, the data assimilation system should be able to capture the wave structure over the ocean and not just over the continent.

In this study, the data assimilation framework for the prototype RRFS is assessed and impacts on forecasts of an Amazon coastal squall line case study are investigated. Overall, this study examines to what extent the assimilation of few and sparse data can still have a positive impact in the RRFS analyses over this region. Due to the data availability issues along with a lack of severe weather reports in this region, a methodology is determined for the selection a case study. This methodology follows Oliveira and Oyama (2015) in an attempt to create an objective algorithm to identify squall lines in the outputs of the tracking system ForTraCC (VILA et al., 2008). It is worth mentioning that ForTraCC outputs give information on individual tracked convective systems where one or more can be part of a squall line. Therefore, identifying squall lines in ForTraCC outputs in an objective manner is still a challenge. Here, the goal is to test available methodologies and provide a list of steps to follow to select case studies in this area with data availability issues, especially for modeling purposes. Once the case is selected, sensitivity tests using RRFS are performed similar to the experiments conducted in Chapter 4. Different configurations in GSI are tested, such as various ensemble background error covariance weights in hybrid analyses, supersaturation removal, the PBL pseudo-observations function as well as varied observation types. Two physics suites are tested: one based on the GFS version 15 physics and a suite based on the HRRR physics. As in the previous chapter, MET is used for forecast verification. Although the area studied has a low density data coverage, results show that large scale patterns are well captured in all experiments and the forecasts are improved when using data assimilation.

5.2 Case study selection

Differently from the mid-latitudes, seasons in the tropics are defined following the rainfall frequency rather than temperature. Thus, precipitation distribution along

the year determines the rainy and dry periods as the main seasons. This has been attributed to the South American monsoon system (SAMS) (MARENGO et al., 2001). Determining the onset (end) and end (onset) of the dry (rainy) season has been the subject of many studies (LIEBMANN; SMITH, 1996). Various methodologies have been applied and there are climatological dates in which these periods are expected to occur. However, due to the interannual variability in rainfall occurrence (ZENG, 1999), the first step for the case study selection is to determine the onset and end of the dry season for the Amazon in 2020. The dry season was chosen in order to better identify the convection associated to the Amazon squall line from the diurnal convection which occurs everywhere during the rainy season. The methodology proposed in Marengo et al. (2001) based on the computation of pentads (5-days average) of accumulated precipitation is applied in this research. The second step is to execute ForTraCC for the period corresponding to the dry season using GOES-16 imagery from channel 13. Finally, an algorithm for the identification of squall lines using ForTraCC outputs is developed based on the objective method of Oliveira and Oyama (2015). The objective method is complemented with a visual analysis of the corresponding satellite imagery.

5.2.1 Data

For the pentads computation, the MERGE product from CPTEC (ROZANTE, 2017) is used. This product combines observed data from SYNOP observations, data collection platforms (DCPs) and data from regional meteorological centers with satellite-derived precipitation estimates from the Global Precipitation Measurement (GPM) Integrated Multi-satellitE Retrievals for GPM (IMERG-Early) (HUFFMAN et al., 2015a; HUFFMAN et al., 2015bb; HUFFMAN et al., 2015ba). The goal is to correct precipitation estimates from satellites with surface observations by minimizing the uncertainties, especially over regions with a low density of rain gauges, such as the Amazon. The product became available in 2010 (ROZANTE et al., 2010), and since then, various updates with new data have been made available. A recent comparison between MERGE and the product Combined Scheme (CoSch) (VILA et al., 2009) also developed at CPTEC, showed that MERGE outperforms CoSch in terms of the magnitude of the bias and in the analysis of rain/no rain and light to moderate rainfall (0.5 to 20.0 mm) (ROZANTE et al., 2020). MERGE data are in a grid point with a spatial resolution of 10 km and cover 87% of the globe between the latitudes of 60 ^{o}N and 60 ^{o}S. The daily product is the one used in the computations.

Images from the GOES-16 infrared channel 13 with spatial resolution of 2 $\times$ 2 km

and temporal resolution of 10 minutes are used for the tracking of the convective systems. This channel is a clean infrared longwave band being less sensitive to atmospheric moisture than other infrared channels. These images are processed at the Satellite Division and Environmental Systems of CPTEC and are available in rectangular projection and NetCDF format.

5.2.2 Onset and end of the dry season

The methodology proposed by Marengo et al. (2001) focuses on determining the onset of the rainy (dry) season as the pentad with daily average precipitation greater (less) than 4.5 mm day^{-1} and this value remains above (below) 4.5 mm day^{-1} in the 6 to 8 subsequent pentads. Prior to pentads indicating the initial (ending) date, the values of pentads with daily average precipitation must be more (less) than 3.5 mm day^{-1} in the subsequent 6 to 8 pentads. This computation is performed for the area in the mouth of the Amazon River as defined in Marengo et al. (2001). This area is representative of the precipitation regime for the convection initiated over the northern coast of South America. Figure 5.1 presents the reference area (grey circle). This area is centered at the mouth of the Amazon River with coordinate point at Ecuador and 49°W and the accumulated precipitation data inside a 3.5° radius is considered for the pentad computation. The solid black line in Figure 5.1 indicates the bio-geographic limits of Amazon basin according to RAISG (acronym in Portuguese for Rede Amazônica de Informação Socioambiental Georreferenciada). This georeferenced data is publicly available and can be found at: `https://www.amazoniasocioambiental.org/en/maps/#download`

Figure 5.1 - Reference area considered in the computation of rainfall pentads.

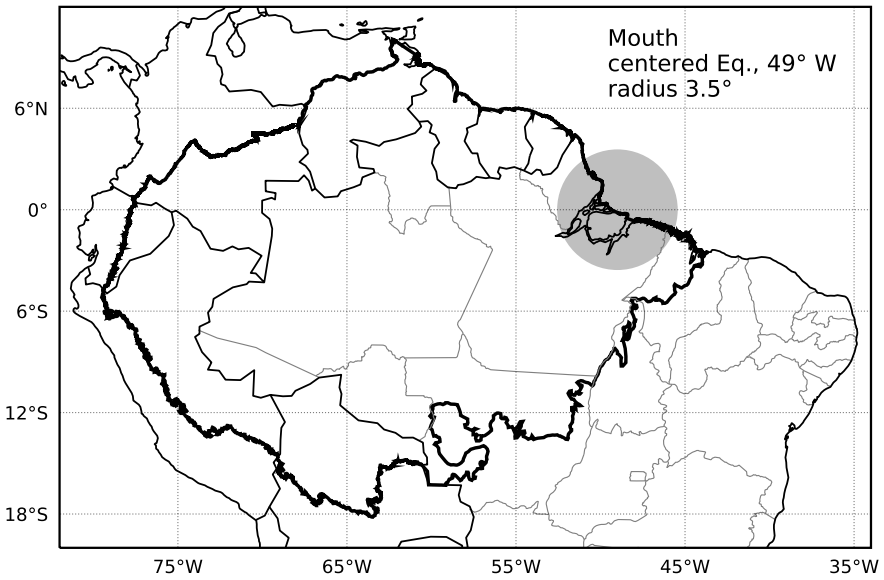

SOURCE: Author's production.

The onset (end) of the dry (rainy) season in the Amazon varies regionally. According to Marengo et al. (2001), the rainy season ends first in the southeast and progresses toward the north. However, the authors pointed out that the withdrawal is slower than onset. In that study, it was found that near the mouth of the Amazon, the onset of the rainy season occurs in December with the earliest pentad of the onset centered on 4 November and the latest centered on 24 December. On the other hand, the end of the rainy season was found for the pentad centered on 17 July with the earliest recorded withdrawal date in the pentad centered on 22 June.

Figure 5.2 shows the time series of the 73 pentads of rainfall, in which can be observed that the dry season of 2020 near the mouth of the Amazon began in the pentad centered on 21 June and ended in the pentad centered on 29 October. In this figure, the pentads where the values did not exceeded 4.5 mm day^{-1} are highlighted in orange. This means that the onset of the 2020 dry season occurred inside the earliest limits suggested by Marengo et al. (2001) while the end occurred slightly earlier than the range considered in the climatological values. ForTraCC is then executed for the period between 21 June and 29 October 2020.

Figure 5.2 - Time series of average precipitation over 5 consecutive days (pentads) during the period from 1 January to 31 December 2020 over the area near the mouth of the Amazon river.

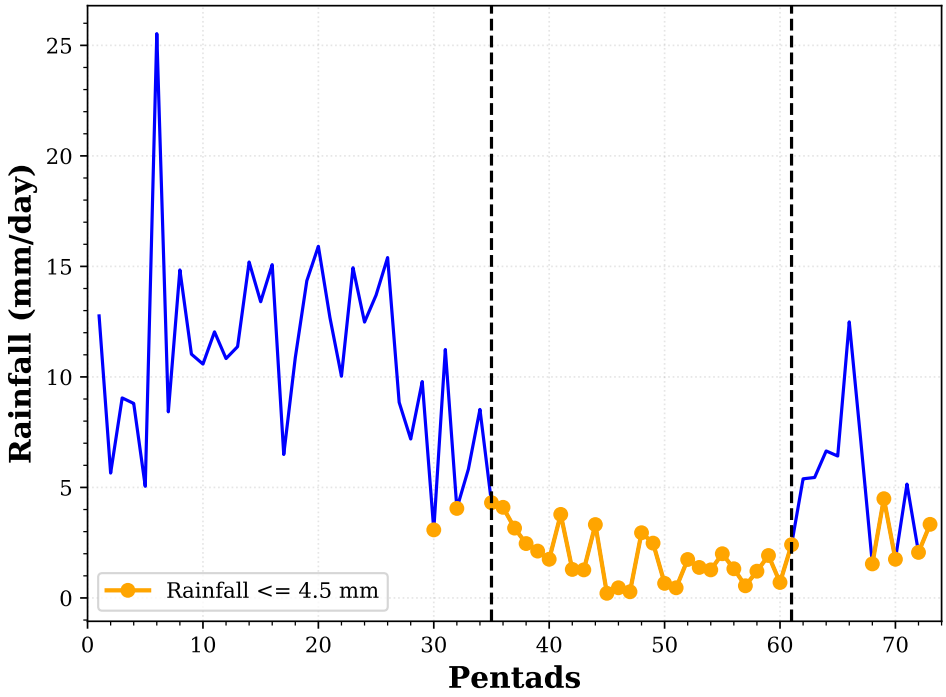

SOURCE: Author's production.

5.2.3 Tracking of convective systems

ForTraCC is an algorithm for tracking and predicting the morphological and radiative characteristics of convective systems using infrared channel images from GOES satellites (VILA et al., 2008). In this work, only the tracking module is used because predicting the system displacement is not part of the objective of this work. ForTraCC performs the convective system detection using a brightness temperature threshold, considering that temperatures below this threshold adequately represent convective systems. Following several works and the study of Vila et al. (2008), a threshold of 235 K is used to detect the systems. Once the systems in an image are identified, a method of superposition of at least 25 % of the system between one image and the next at time $t + dt$ is observed. In terms of number of pixels, the overlay must be found in 150 pixels in order to consider that the system is a continuation of the previous one. From the application of the superposition criterion, it is possible to identify whether the system is new or spontaneously generated; a con-

tinuity (Conti) of the previous system, a split (Split) if two systems with the same characteristics as in the previous time are found in the image in time $t + dt$, or a merge (Merge) when at time t there are several systems and at the next time $t + dt$ only one is found. Statistics of the size, system duration, minimum temperature, average and maximum speed, direction of displacement, are among the parameters derived from ForTraCC for each detected system. The ForTraCC tracking system is currently operational at CPTEC/INPE.

Prior to the execution of ForTraCC, a quality control procedure is applied to the GOES imagery. Figure 5.3 presents an example of an image in which bad pixels (see the black band on the bottom of the figure) are observed. This can be related to failures in the transmission systems among other reasons. This control consisted of determining the images with temperatures below 180 K and removing them.

Figure 5.3 - Example of an image with bad pixels.

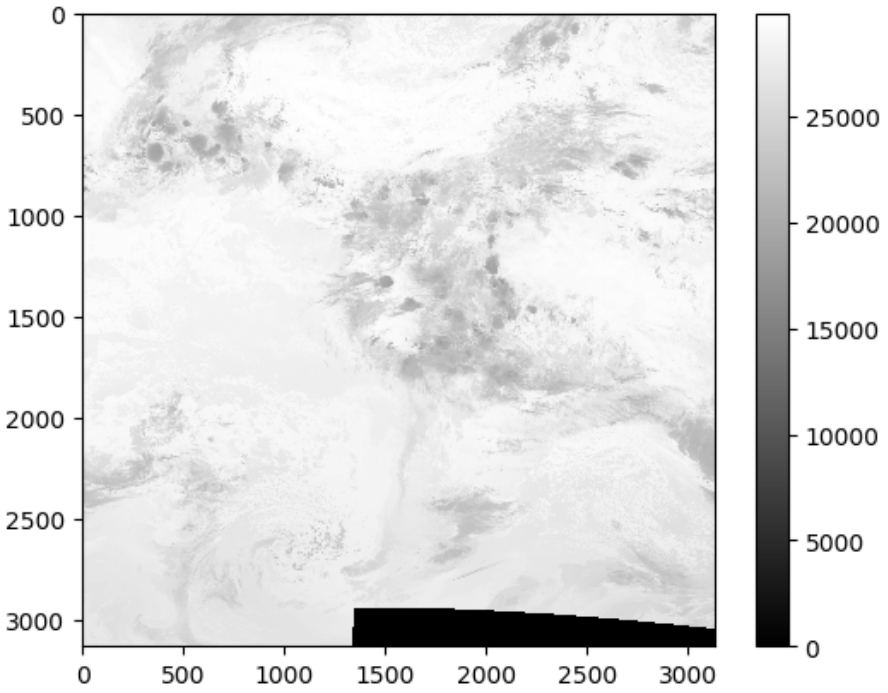

SOURCE: Author's production.

Convective systems with initiation inside the limits of the Amazon basin are selected for further analyses (Figure 5.4). Figure 5.4c shows a 2D spatial histogram with the

distribution of pairs of latitude/longitude at which convective systems were initiated during the entire period. Figure 5.4a and b show the latitudinal and longitudinal distributions, respectively. During this period, the area where most convective systems were formed is centered on the northwestern Amazon, extending through parts of the west and central west Amazon. This area coincides with higher terrain elevation indicating the influence of high topography (lifting mechanism) to the genesis of convection. This result is similar to what is found in Rehbein et al. (2018), also using ForTraCC but for the period between 2000 and 2013 using a composite of infrared imagery from GOES west and east, Meteosat, and the Japanese Geostationary Meteorological Satellite (GMS). Over northern Amazon can be identified the source region for the Amazon coastal squall lines.

Figure 5.4 - (a) Latitudinal, (b) longitudinal, and (c) spatial distribution for convective system genesis inside the limits of the Amazon basin during the 2020 dry season.

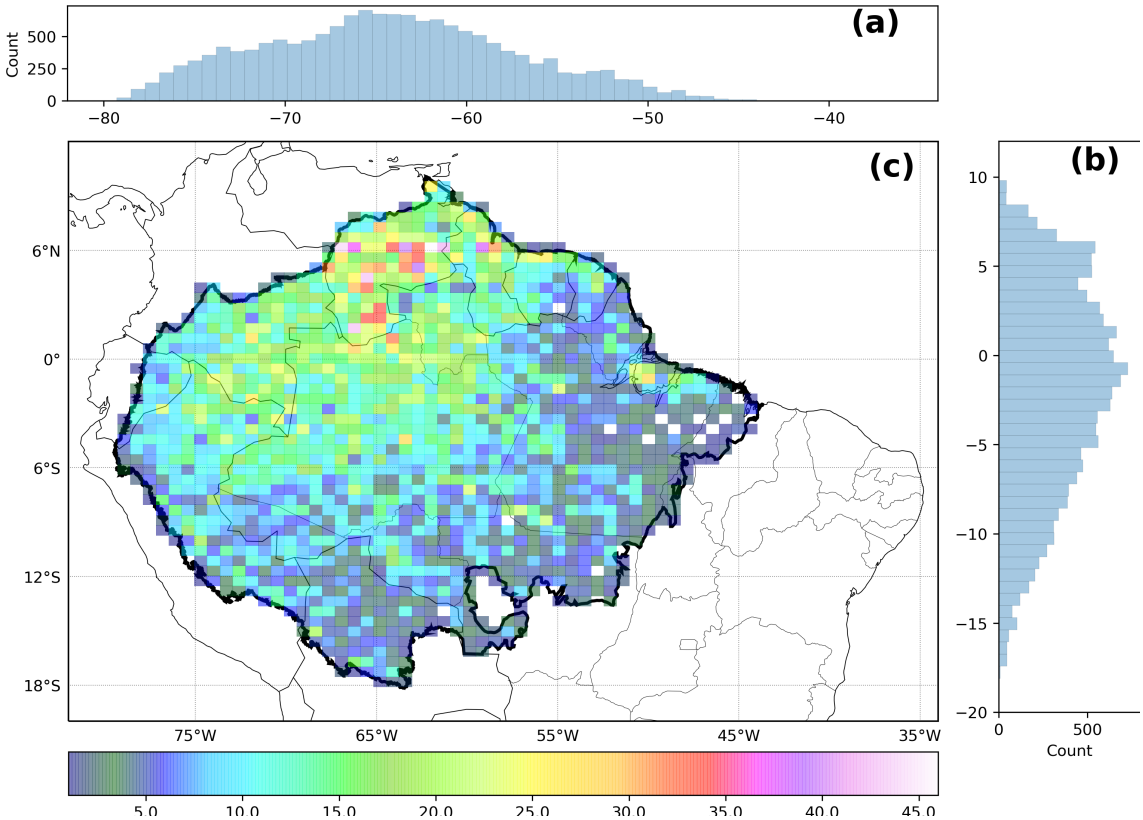

SOURCE: Author's production.

The monthly spatial distribution for July, August, September, and October is presented in Figure 5.5. The few days from June that are inside the dry season range are not considered in this monthly analysis. During the four months analyzed, the preferred region of initiation varies slightly from the north and northwest in July, to be more concentrated on the northwest in September, to spread toward the west and slightly to the central and southern region, to then completely spread toward the central and eastern Amazon with some spread over the south. These results are in agreement with previous studies such as Rehbein et al. (2018). Over the northern Amazon, there are convective systems initiating throughout the four months, however, July is the month with the most convective genesis. The results for July corroborate what is found in many studies that this is the most of preferred initiation for Amazon squall lines (COHEN et al., 1995; ALCÂNTARA et al., 2011).

Figure 5.5 - Spatial distribution of the preferred regions of genesis of convective systems for (a) July, (b) August, (c) September, and (d) October.

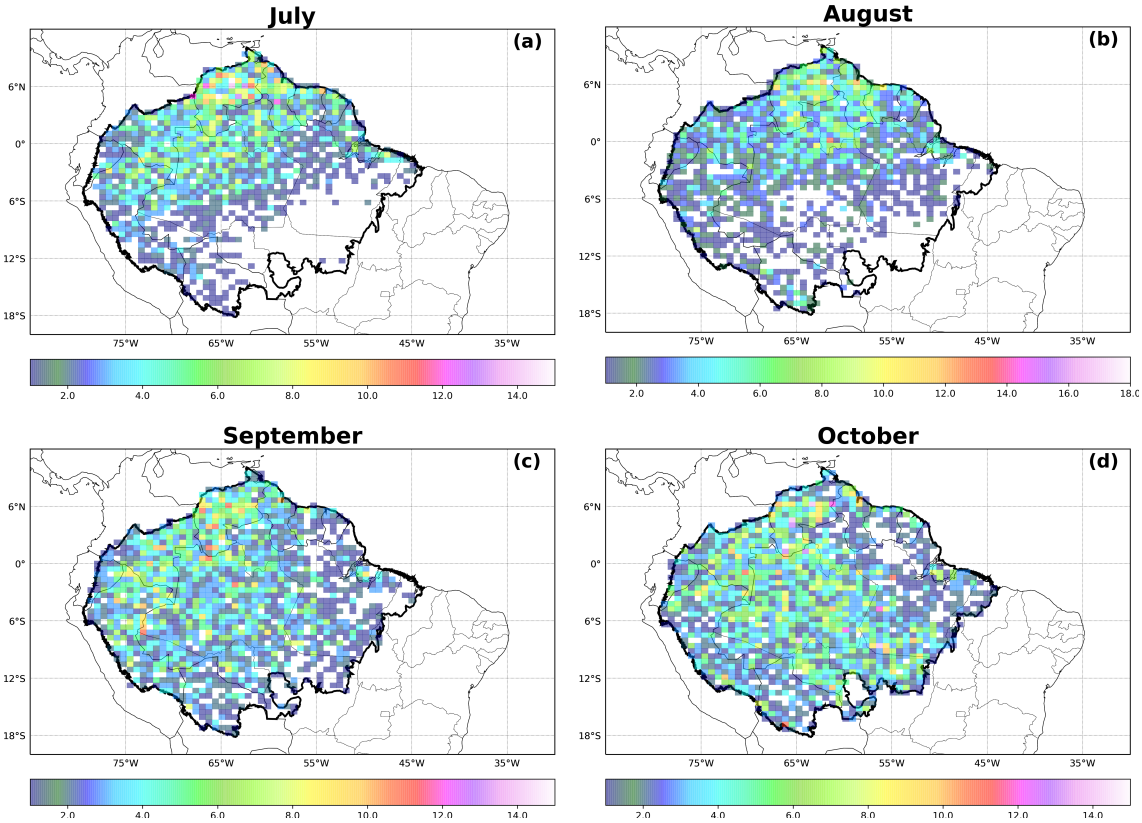

SOURCE: Author's production.

The number of systems is computed for each month and they are classified as short-lived and long-lived following Rehbein et al. (2018) (Figure 5.6). For this analysis, only systems that lasted more than 3 hours are considered. Short-lived systems are those that lived more than 3 hours but less than 6 hours, whereas long-lived systems consider those that lasted more than 6 hours. Not surprisingly, among the months analyzed, a larger amount of convective systems are initiated in October, which agrees with what is observed in Figure 5.5. The amount of short- and long-lived systems between these months do not show a significant variation, but it is noted that October is the month with the largest amount of short-lived system, followed by September and July. Similarity between the months for the long-lived systems is also found in Rehbein et al. (2018). However, slightly more long-lived systems were initiated in July.

Figure 5.6 - Number of systems with genesis inside the Amazon basin during the months July, August, September, and October (green bars) as well as the monthly variation of short- (blue bars) and long-lived (red) convective systems. The difference between green bar and the total of blue and red bars corresponds to systems with span-life < 3 h.

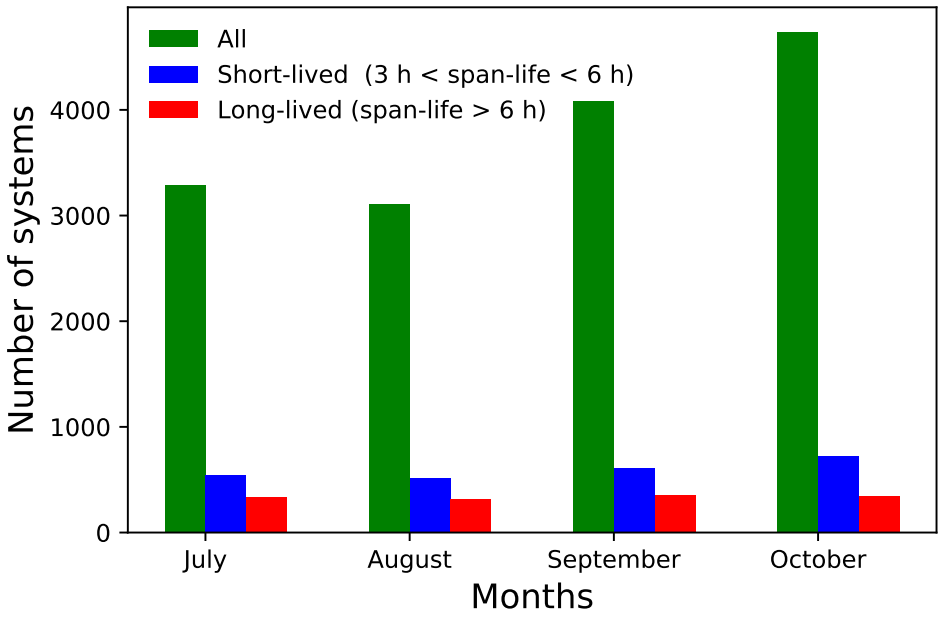

SOURCE: Author's production.

Following the squall lines classification of Cohen et al. (1995), convective systems are

categorized according to their propagation. This classification is used in an attempt to find a squall line case that propagates inland. Table 5.1 presents the classification details.

Table 5.1 - Classification of squall lines according to their propagation inside the continent.

Coastal line Convection (CLC, *Coastal line Convection*)	$\geq$ 170 km
Squall Lines Type 1 (SL1, *Squall lines type 1*)	170 km $<$ SL1 $\geq$ 400 km
Squall Lines Type 2 (SL2, *Squall lines type 2*)	SL2 $>$ 400 km

SOURCE: Author's production.

According to Cohen et al. (1995), the formation region for Amazon coastal squall lines is between the latitudes 10°N and 5°S, south of the ITCZ during the dry season. The results shown in Figure 5.5 confirm that. The source region considered in this study corresponds to the shaded blue polygon in Figure 5.7.

Figure 5.7 - Source region considered for coastal convection.

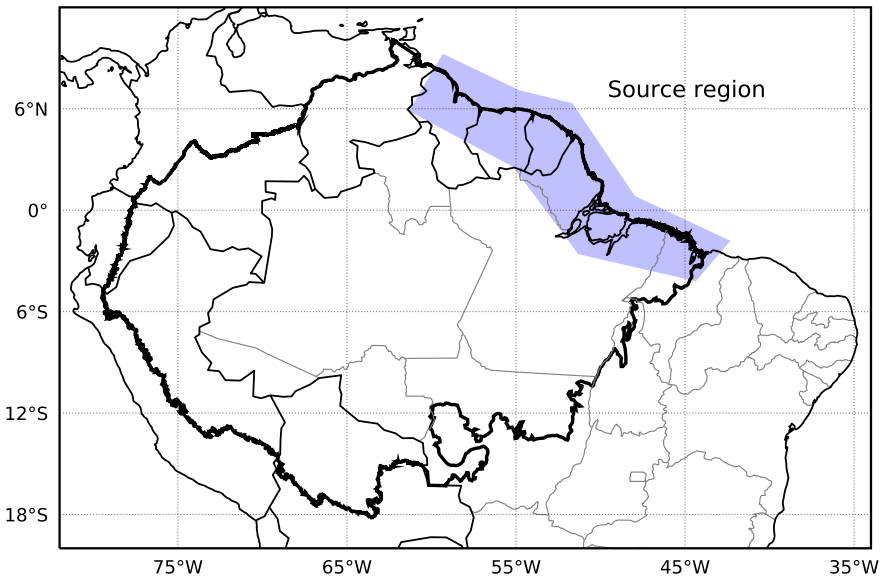

SOURCE: Author's production.

The number of systems with genesis in the blue area of Figure 5.7 is presented in Figure 5.8. In this figure, the orange bars correspond with all systems that had initiation along the coast, the cyan, yellow, and fuchsia bars correspond with the number of systems classified as CLC, SL1, and SL2, respectively. On the secondary axis of this figure is also plotted the maximum duration in hours of the systems in each classification, indicated by the small squares with the colors matching each classification. As expected, most of the convective systems in all categories have genesis in July, followed by August, October, and September. On average, the maximum duration of all systems is around 12 hours which corresponds with the mean maximum duration of SL2. This agrees with results of Rehbein et al. (2018) for oceanic systems. Nevertheless, those classified as SL1 always show the longer duration. This can indicate that SL1 systems were slower than SL2, although SL2 traveled a greater distance.

Figure 5.8 - Number of all systems with genesis inside the Amazon basin (orange bars) classified as CLC (cyan bars), SL1 (yellow bars), and SL2 (fuchsia bars) and the corresponding maximum duration during July, August, September, and October.

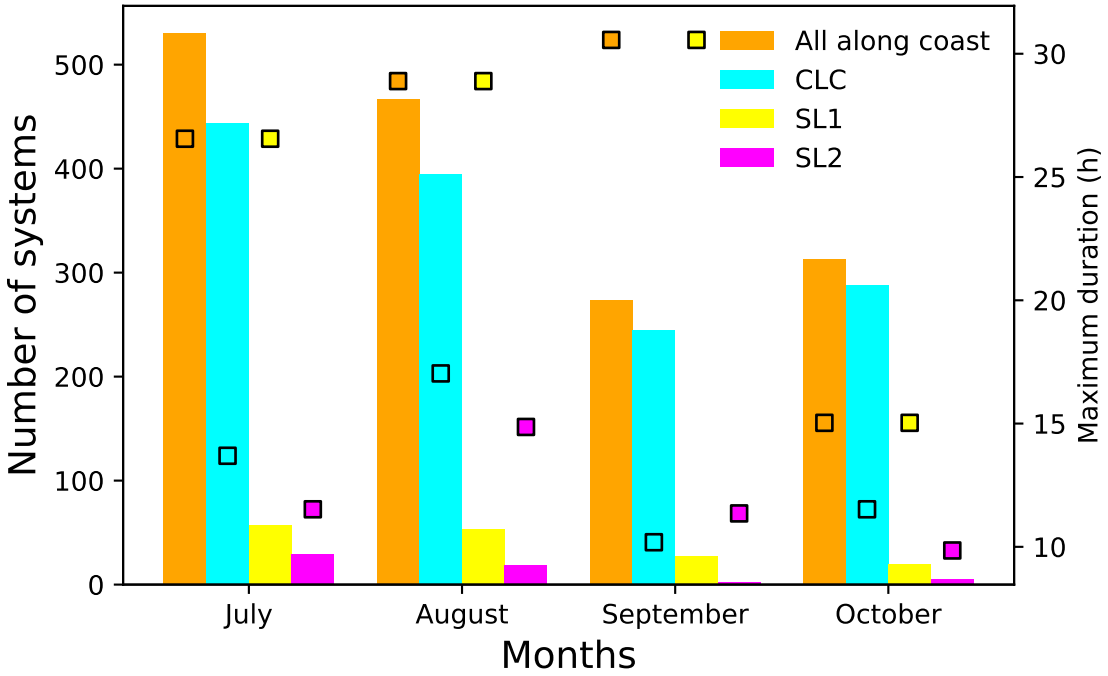

SOURCE: Author's production.

The last step for the case selection is to analyze the morphological characteristics of the tracked convective systems (called families in ForTraCC) following part of the algorithm proposed by Oliveira and Oyama (2015). The method applied in this thesis consists of filtering convective systems according to their morphological characteristics after it is verified that the convective system had genesis inside the shaded blue area in Figure 5.7. The area, tilting, and eccentricity are examined in order to find tracked convective systems that are more linear and tilted. The initial criteria is to check whether one convective system of the families with coastal genesis had an area >100 and tilting $<2.5°$. If this condition is satisfied, then search if at least one cluster of the convective systems had an area >1750 pixels and eccentricity ≤ 0.7. If this condition is met, the algorithm will also check if at least two clusters had an area >1300 pixels and eccentricity ≤ 0.75. Finally, if this condition is also satisfied, the algorithm will check if three clusters had eccentricity ≤ 0.75. The identification numbers of convective systems that meet all the conditions are saved along with their morphological and radiative characteristics.

Figure 5.9a shows that this methodology is able to identify the main tracked convective system associated with cases of Amazon squall lines. The linear organization along the coast line as the system evolved is well identified by the algorithm. However, there are two points that need to be considered. The first is that Amazon coastal squall lines can reach the synoptic scale with the form of a discontinuous or arc of discrete clusters of cells (GARSTANG et al., 1994), and second is that new cells can be developed as part of the squall line circulation (interaction between the updrafts and downdrafts), and be identified by ForTraCC as a separate system rather than as part of the whole system. Two examples are shown in Figure 5.9b–c of convective systems tracked in ForTraCC for which hour and longitude genesis are very close to the main system in Figure 5.9a. With a visual analysis of the satellite imagery, it is possible to identify that these other systems are part of the same Amazon coastal squall line that reached synoptic dimensions with new convection being developed at different times. Therefore, with this current methodology, a subjective analysis is still needed to complement the information obtained with ForTraCC.

Figure 5.9 - Tracked convective systems associated with an Amazon coastal squall line from ForTracc outputs using the modified objective method. The blue clusters represent the positioning and extent of the tracked system during its evolution. Panels present the evolution of (a) the convective system identified with number 4596, (b) the convective system identified with number 4630, and (c) the convective system identified with number 4915.

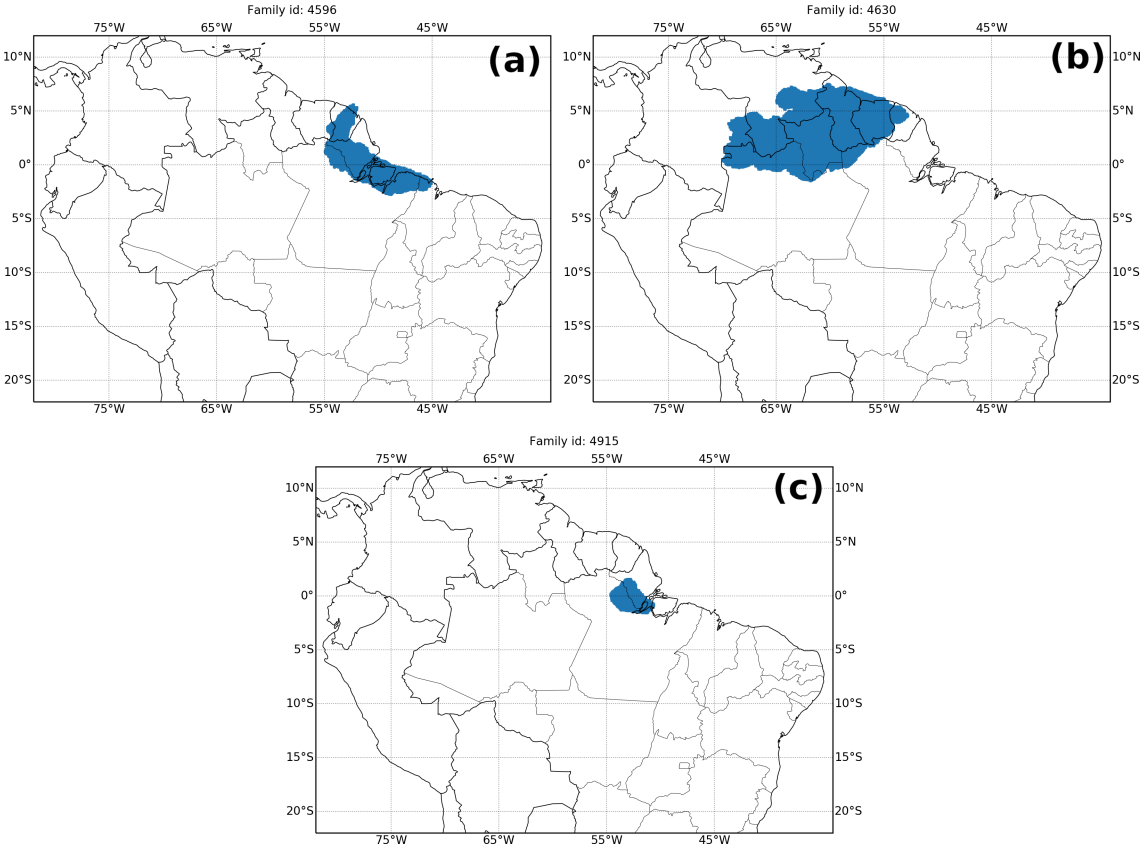

SOURCE: Author's production.

The morphological and radiative characteristics of three tracked convective systems are summarized in Table 5.2. The systems with identification numbers (Ids) 4596 and 4630 were identified with only 40 minutes of difference where 4630 seems to be one of the clusters initially developed at the edge of the system. Meanwhile the system with Id: 4915 was identified 6 hours and 10 minutes later, when the main system seems to be between the intensification and maturation stage. The three systems show a consistent wind propagation direction, from the northeast to southwest (third quadrant: 180 to 270°). System 4596 shows more of a linear shape with mean eccentricity of 0.35. In general, systems 4596, 4630, and 4519 propagated 256, 1657, and 144 km inland toward the southwest with a mean velocity

of 41.4, 49.56, and 34.12 km h^{-1}, and a span-life of 7.348, 26.553, and 4.509 hours respectively. According to the traveled distance inland, these systems are classified as SL1, SL2, and CLC, respectively. Considering that the three systems are part of a larger scale squall line, after several continuous, split, and merge stages, the whole system had an average span-life of 12.8 h, similar to what is found in other studies (REHBEIN et al., 2018).

Table 5.2 - Morphological and radiative characteristics of tracked convective systems associated with an Amazon coastal squall line from ForTracc outputs, where: Lat_ini and Lon_ini are the initial latitude and longitude where the system was detected; Dir is the direction of movement of the system; Dista is the distance traveled; Siz_max, Siz_me, Tilt_max, Tilt_me, Ecc_max, Ecc_me, Vel_max, and Vel_me are the mean and maximum size, tilt, eccentricity, velocity achieved by the convective system along its trajectory; Tmin_min and Tmin_me are the mean and minimum of the minimum temperature achieved by the system; New, Conti, Split, and Merge are the different classifications according to the superposition criterion explained in Section 5.2.3; and Class corresponds to the classification received according to Cohen et al. (1995) and presented in Table 5.1. The date format is yyyymmddhhmm.

Ids	4596	4630	4915
Date	202007051720	202007051800	202007052330
Lat_ini	-0.758	4.71	0.001
Lon_ini	-47.912	-53.748	-52.487
Dir	245.081	265.611	246.285
Dista	256	1657	144
Dura	7.348	26.553	4.509
Siz_max	13906	20975	2837
Siz_me	5674.93	10424.19	1770
Tilt_max	-2.21	42.9	6.64
Tilt_me	-16.25	0.06	-28.57
Ecc_max	0.64	1	0.92
Ecc_me	0.35	0.72	0.6
Vel_max	63.23	68.55	62.48
Vel_me	41.4	49.56	34.12
Tmin_min	187.2	184.38	193.96
Tmin_me	198.02	197.71	202.87
New	1	1	0
Conti	35	124	25
Split	5	16	3
Merge	4	19	0
Class	SL1	SL2	CLC

SOURCE: Author's production.

5.2.4 Case overview

The Amazon coastal squall line case previously presented is selected for the numerical simulations. Figure 5.10 shows the initiation and evolution of the convection associated with this system. Some of the initial cells are observed between French Guiana, the state of Amapá and northern Para in Brazil. Between 19:00 UTC and 21:00 UTC, more cells develop and a line of discontinuous convective storms is observed along the coast in the satellite images. The strongest convection occurs at 23:00 UTC, and it is also observed that the stratiform part has widened. This cloud band, with a northwest-southeast orientation, slowly propagates inland from northeast to southwest. Some inner clusters have very cold cloud tops (white shade indicates temperatures lower than -75°) indicating possible overshootings and that deep convection is occurring. At 01:00 UTC the line has propagated more inland and some clusters have decreased their intensity while some are still very deep. 4 hours later, at 05:00 UTC, the squall line is further into the continent and afterwards it seems to merge with other convective systems in the area. The convection associated with the squall line continues to propagate toward the southwest Amazon, but it loses its linear characteristics. Over the Atlantic ocean, strong convection is occurring associated with the ITCZ.

Figure 5.10 - Brightness temperature from the GOES-16 infrared 13 channel from 17:00 UTC on 5 July 2020 through 01:00 UTC on 6 July 2020 every 2 hours (a, b, c, d, and e) and at 05:00 UTC on 6 July 2020 (f).

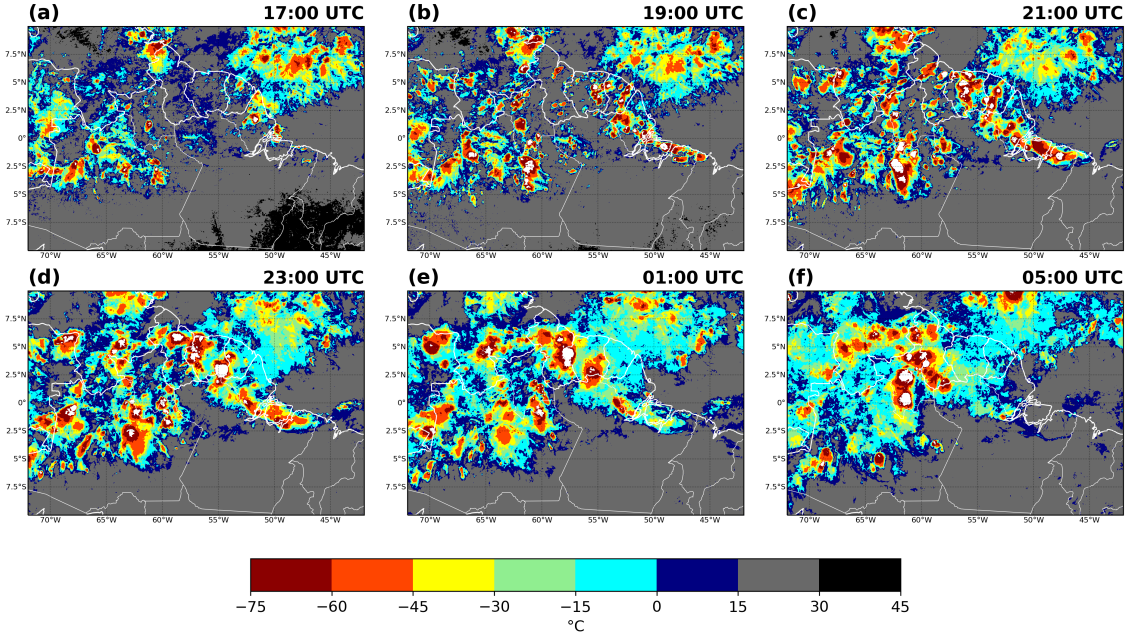

SOURCE: Author's production.

In order to explore the large scale conditions on 5 and 6 July 2020, the wind speed is examined. Figure 5.11 presents the mean of the wind speed at 250 hPa and at 850 hPa for both days from the ECMWF Reanalysis v5 (ERA5) (EUROPEAN CENTRE FOR MEDIUM-RANGE WEATHER FORECASTS, 2019). The presence of a low level jet is clear at 850 hPa, which can also be observed through 900 hPa to 600 hPa (figures not shown) as indicated in previous studies (COHEN et al., 1995). Level 850 hPa shows the average characteristics among those vertical levels. The easterly low level jet with maximum winds between 20 to 25 kts (10 to 12.86 m s^{-1}) is observed parallel to the coast, from French Guiana to the north of Ceara, Brazil and extending into the continent. At 23:00 UTC, maximum winds reach 30 to 35 kts (15.43 to 18 m s^{-1}) on the area over the ocean and northern Amapá. This indicates the support of the low level jet to the propagation of the squall line toward the continent. At higher levels, an anticyclonic circulation is observed over the southwest Amazon as a response to heat sources supporting the divergence in altitude and convergence in the lower levels. The ITCZ is observed at around 5°, as expected for

this month. Part of the subtropical jet is observed on the Pacific Ocean at around 20°S.

Figure 5.11 - Mean of the wind speed at 250 hPa (a) and at 850 hPa (b) on 5 and 6 July 2020 from the ECMWF Reanalysis v5 (ERA5).

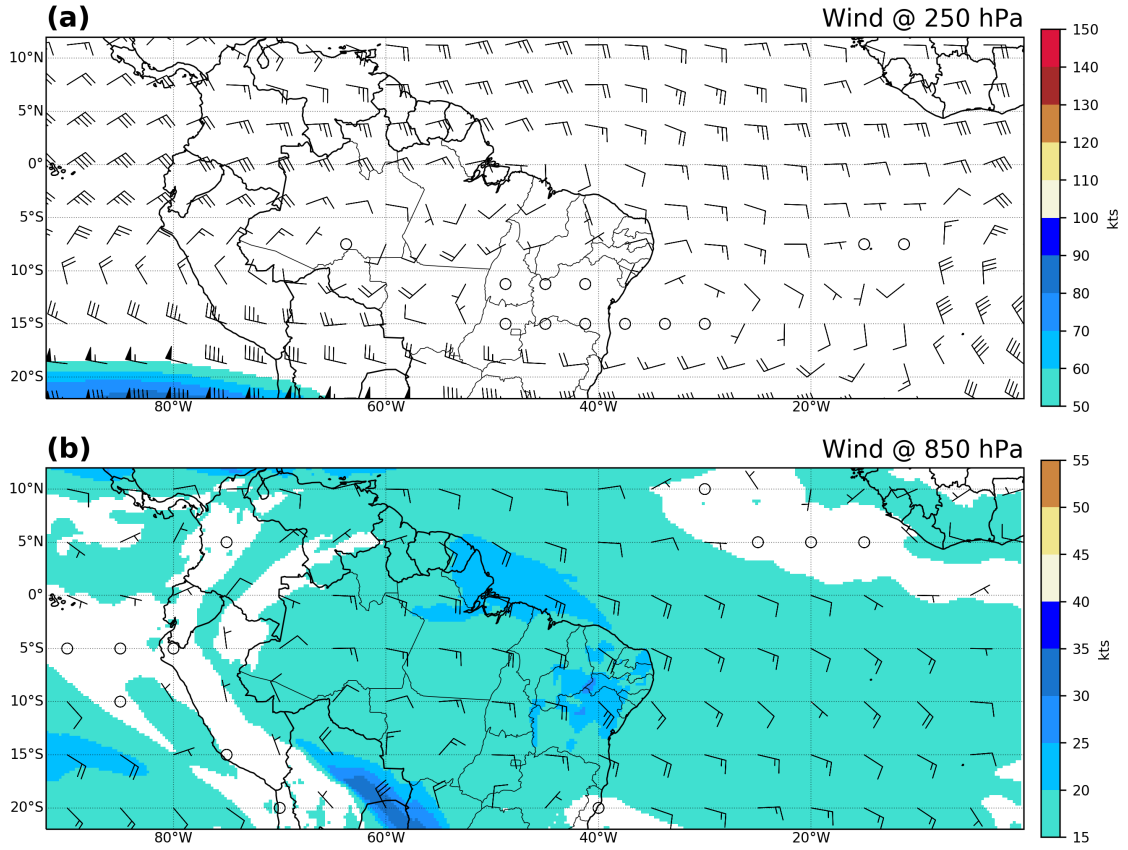

SOURCE: Author's production.

5.3 Numerical experiments

The focus of this section is to extend the testing and evaluation of RRFS to the context of the case study over northern South America. Many of the options tested for the case study in the central US are also tested for this domain over South America. In this section, the general setup of the experiments, cycling configuration, description of the experiments conducted, verification methodology, and results and subsequent discussions are presented.

5.3.1 Setup of the experiments

For the simulation of this case, a domain is configured using 1200 × 700 grid cells centered on the coordinate point at 1°N and 57°W with 3 km horizontal grid spacing and 64 vertical layers. The domain covers the area of formation and propagation of the squall line through the western Amazon. It is configured to also include part of the Atlantic Ocean in order to provide the model adequate boundary conditions with information on the larger scale systems, such as part of the ITCZ that can be observed in Figure 5.10. Similar to the case over the central US, the Extended Schmidt Gnomonic method developed by Purser et al. (2020) and implemented in the SRW application is used for grid generation. Figure 5.12 shows the domain coverage and orography created by the pre-processing utilities.

Figure 5.12 - Domain with the orography created for numerical experiments of the case study over northern South America. The black star indicates the central latitude and longitude of the domain.

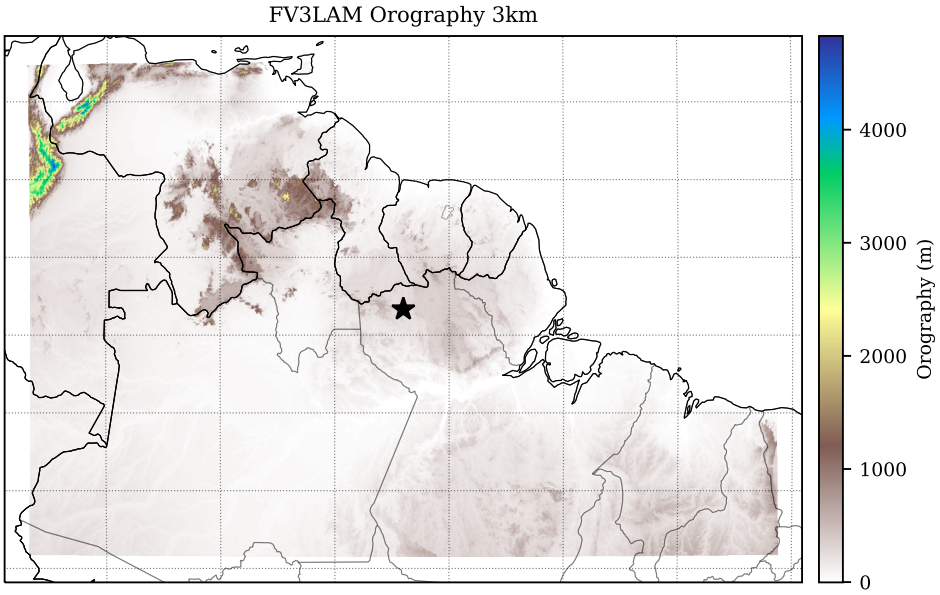

SOURCE: Author's production.

5.3.1.1 Data

A survey of available data sources in the area was carried out for data assimilation purposes. Some of the available sources for meteorological weather applications on

the Amazon have been discussed in Wohl et al. (2012). In this region, some meteorological stations are available, both conventional and automatic, from the Brazilian Institute of Meteorology[1] (INMET; acronym in Portuguese for Instituto Nacional de Meteorologia). Although there are very few locations, radiosondes are launched providing vertical profiles of pressure, temperature, wind, and humidity. Airports and conventional weather stations provide METAR reports and aircrafts also provide atmospheric information in the different phases of flights. In this region, there is radar coverage, mainly from the Protection System of the Amazon (SIPAM[2]; acronym in Portuguese for Sistema de Proteção da Amazônia). Another data source is the Brazilian Network for Continuous Monitoring of the GNSS Systems (RBMC[3]; acronym in Portuguese for Rede Brasileira de Monitoramento Contínuo dos Sistemas GNSS em tempo real) which provides GPS-IWV measurements. The availability of these data sources was verified for the period of occurrence of the squall line. Among all sources listed, there was no coverage over the interest area from RBMC stations and SIPAM radars. Therefore, most of the available data are from conventional sources which already go into the GTS. Hence, observations from GDAS prepBUFR are used for the data assimilation which includes sondes, marine, synotic and METAR reports.

All simulations start at 00:00 UTC on 4 July 2020 and run 3-hourly cycles until 21:00 UTC on 6 July 2020. Analyses and forecasts from the GFS with 0.25° of resolution are used to generate the ICs and LBCs for the FV3LAM. GDAS prepBUFR observations are assimilated in each experiment along with BURF GNSSRO bending angles and satellite-derived winds and radiances. Available LEO satellites during 4 to 6 July 2020 include the same missions as for the case over the central US (see Section 4.2.2.1), that is, COSMIC-2, MetOp A, B, and C satellites, KOMPSat5, PAZ, and Tandemx and TerraSARX satellites. Assimilated radiances included the Microwave Humidity Sounder (MHS), the Infrared Atmospheric Sounding Interferometer (IASI), the High resolution Infrared Radiation Sounder (HIRS/4), the Atmospheric Infrared Sounder (AIRS), and the Advanced Microwave Sounding Unit-A (AMSU-A) sensors. Table 5.3 shows the sensors and satellites from which radiance observations are assimilated, using the symbol $\surd$. The strategy followed in Section 4.2.2.1 to assimilate GNSSRO observations from GDAS observations is followed for this case study for all the data assimilated. At overlapping hours, such as 03:00 UTC, 09:00 UTC, 15:00 UTC, and 21:00 UTC, observation files from the

[1] https://portal.inmet.gov.br/

[2] https://ipam.org.br/glossario/sipam-2/

[3] https://www.ibge.gov.br/en/geosciences/geodetic-positioning/services-for-geodetic-positioning.html

adjacent synoptic hours are reused, as shown in Figure 4.3. The time window used is 3 hours, allowing for observations within 1 hour and 30 minutes before to 1 hour and 30 minutes after the analysis time to be assimilated. Furthermore, the hybrid 3DEnVar analysis uses the GDAS 80 member ensemble forecasts (9 h forecasts), following the same strategy in the RAP system as in the case study over the US (see Figure 4.4).

Table 5.3 - Assimilated radiances observations from each sensor and satellite.

	Satellites				
Sensors	NOAA-18	NOAA-19	MetOp A	MetOp B	AQUA
MHS		√	√	√	
AMSU-A	√	√	√	√	√
HIRS/4		√	√		
IASI			√	√	
AIRS					√

SOURCE: Author's production.

5.3.2 Cycling configuration

For this case study, the cycling configuration of Section 4.2.3 was modified due to the lack of hourly resources (observations, analyses, and forecasts) to provide model initial and boundary conditions. Therefore, a 3 hourly updated cycling strategy is configured using GFS ICs and LBCs and GDAS observations. Cold starts are similarly performed every 12 hours at 00:00 and 12:00 UTC and warm starts are performed at all other cycles using the FV3LAM 3 h forecast from the previous cycle as background for the analysis. In each cycle, a 24 h free forecast is launched following the analysis, with hourly outputs. Figure 5.13 illustrates the RRFS cycling configuration from cycles initialized between 00:00 UTC through 18:00 UTC.

Figure 5.13 - Diagram of the 3-hourly cycling configuration for RRFS for the case study over northern South America (SA).

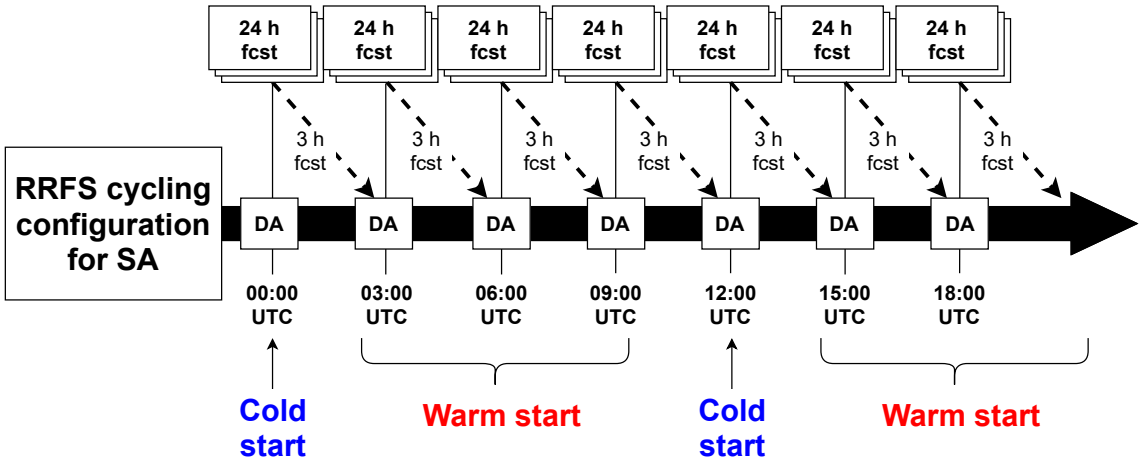

SOURCE: Author's production.

5.3.2.1 Sensitivity experiments

Various configurations and algorithms available in GSI that were tested over the US are also tested in this chapter in order to understand sensitivities of the system in this different environment with low data density and to what extend the low data density assimilation can positively impact the analyses. Table 5.4 lists all experiments in which GSI options are tested.

As in Chapter 4, an experiment with no data assimilation called NoDAsa is provided, which is used as the baseline for all other experiments. Similar to NoDA, NoDAsa uses the cycling configuration of Section 5.3.2 but without data assimilation in any cycle. Two physics suite were also tested in order to choose the most appropriate one for this case study: the GFSv15 physics suite and a suite based on the HRRR physics, which is an updated version of the physics suite used in Chapter 4 and is called FV3_HRRR. As the physics suite RRFSv1a, FV3_HRRR is based on the Thompson Aerosol-Aware microphysics scheme (THOMPSON; EIDHAMMER, 2014) and keeps the other physical parameterizations mentioned in Section 3.2. On the other hand, the GFSv15 is based on the GFDL six-category cloud microphysics scheme. Figure 5.14 shows precipitation forecasts from these experiments which were run without data assimilation. 1 h accumulated precipitation estimations from the Climate Prediction Center (CPC) morphing technique (CMORPH)

satellite precipitation estimates are used for comparison. The ccpp_HRRR shows smaller coverage than ccpp_GFSv15, but it captures the main precipitating patterns shown in the observations and with intensity closer and scattered patterns as in the precipitation estimations. The ccpp_GFSv15 overestimates the accumulated precipitation in terms of coverage and the intensity, which is greatly overestimated at 6 h forecasts. Therefore, the suite based on HRRR physics was the selected suite in all experiments.

Figure 5.14 - 2, 4, and 6 h forecasts of 1 h accumulated precipitation from experiments ccpp_HRRR (d, e, and f) and ccpp_GFSv15 (g, h, and i), initialized at 19:00 UTC on 4 July 2020 and the precipitation estimates from CMORPH at valid hours 17:00, 19:00, and 21:00 UTC (a, b, and c), respectively.

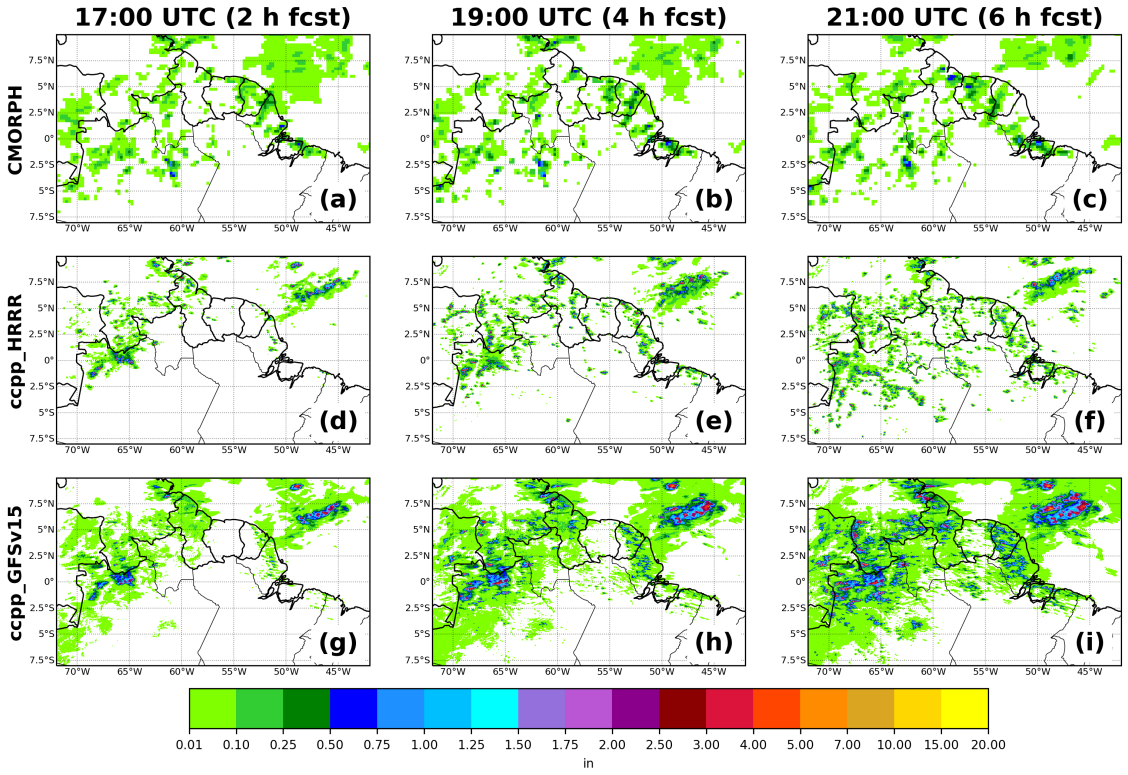

SOURCE: Author's production.

In previous chapters, the importance of using hybrid methods for areas with sparse data was discussed. Thus, a series of experiments were conducted testing different relative weights of the ensemble background error covariance. These experiments

explore what is the best weight of the ensemble background error covariance for this region. For this case, pure ensemble background error covariance, a combination of 85 % ensemble and 15 % static background error covariance, and 3DVar are examined in experiments 100EnBECsa, 85EnBECsa, and 3DVarsa, respectively. An experiment using a combination of 75 % ensemble and 25 % static background error covariance (75EnBECsa) was also conducted, but since differences were subtle in comparison with 85EnBECsa, only results from the experiment 85EnBECsa are presented. These values where selected considering previous studies with RAP and GFS and current study using HAFS. As mentioned in Subsection 4.3.2, the method proposed by Azevedo et al. (2020) should be explored in order to provide a more objective and appropriate hybrid weights for the system and study area.

Previous studies (HAMILL; SNYDER, 2000; WHITAKER et al., 2004) have shown that the localization of the covariances can bring relevant improvements in the analyses and forecasts in areas of low data density. Therefore, in this study both the vertical and horizontal localization of the covariances are explored. Three experiments are conducted testing horizontal localization values of 110 km and 330 km, and vertical localization values of 3 and 9 layers as in in Hu et al. (2017) for RAP. The experiment HL330sa is performed changing the horizontal localization radius to 330 km and keeping a vertical localization radius of 3 layers. The experiment VL9sa is then conducted increasing the vertical localization radius to 9 layers and maintaining the original horizontal localization radius of 110 km. Finally, a third experiment is performed in which both parameters are modified adopting a horizontal localization radius of 330 km and a vertical localization radius of 9 layers. This experiment is called VL9HL330sa. A horizontal localization radius of 110 km and a vertical localization radius of 3 layers is used in the rest of the experiments, following the results obtained in Chapter 4.

The supersaturation removal function in GSI showed great improvements in the forecasts of the case over central US, and then is also tested for this case study with the experiment CLIPSATsa. In CLIPSATsa, a combination of 85 % and 15 % static background error covariance is used.

Other experiments were performed, such as using an updated GSI code in which the PBL pseudo-observations function has been adjusted to be used with an FV3-based model. This experiment, called PSEUDOsa, showed similar results to 85EnBECsa in all forecasts and statistics analyzed, therefore the results are only shown in the analysis of the quantitative precipitation in Section 5.3.6. In addition, observation

system experiments (OSE) were conducted in order to examine the impact of the different data types used. Better results were found when all observations are assimilated, in terms of the precipitation representation and the ETS and FBIAS results, but the impacts of adding a data type each time is very small and are not shown.

The same baseline configuration in the analyses of the previous study is adopted in the simulations of this case over the tropics. This is in terms of the analysis grid ratio, ensemble grid ratio, and outer and inner loops for the minimization of the 3DVar cost function.

Table 5.4 - List of experiments conducted testing different options in GSI in this study.

Experiments	**BEC weights**	**Supersat. removal**	**PBL pseudo-obs.**	**Localization scales**
NoDAsa	**No data assimilation**			
3DVarsa	**0 % ensemble** 100 % static	false	false	hloc=110 km vloc=3 layers
100EnBECsa	**100 % ensemble** 0 % static	false	false	hloc=110 km vloc=3 layers
85EnBECsa	**85 % ensemble** 15 % static	false	false	hloc=110 km vloc=3 layers
VL9sa	**85 % ensemble** 15 % static	false	false	hloc=110 km **vloc=9 layers**
HL330sa	**85 % ensemble** 15 % static	false	false	**hloc=330 km** vloc=3 layers
VL9HL330sa	**85 % ensemble** 15 % static	false	false	**hloc=330 km vloc=9 layers**
CLIPSATsa	**85 % ensemble** 15 % static	**true**	false	hloc=110 km vloc=3 layers
PSEUDOsa	**85 % ensemble** 15 % static	false	**true**	hloc=110 km vloc=3 layers

SOURCE: Author's production.

5.3.3 Forecast verification

The lack of observations is not only an issue for the generation of the analyses but also for the verification of forecasts. In this case, satellite data are invaluable since they are available worldwide covering the Amazon region and have been extensively used in many researches (BUARQUE et al., 2011). Satellite-derived precipitation estimates is therefore used for the model verification along with surface observations

from GDAS prepBUFR for the 2 m temperature and dew point examination.

The CMORPH satellite precipitation estimates (XIE et al., 2017) are used for the verification of precipitation forecasts. CMORPH precipitation estimates are derived from geostationary satellite infrared data combined with passive microwave (PMW) retrievals from LEO satellites. A bias correction is applied using the CPC daily gauge analysis over land and the Global Precipitation Climatology Project (GPCP) pentad merged analysis of precipitation over ocean (XIE et al., 2017). In an assessment of the precipitation diurnal cycle over Brazil using various precipitation estimate products, Afonso et al. (2020) found that for northern South America including the coastal region and continental Amazon, CMORPH produces the best performance when compared to rain gauges. Nevertheless, it is worth mentioning that Palharini et al. (2020) showed that this product tends to overestimate the precipitation over this region. This product has a temporal frequency of 1 hour. The hourly MERGE has also great potential for being used for convective scales, however, an extensive evaluation and calibration of the product is needed for that temporal scale.

MET tools are used for the forecast verification. The PB2NC tool is used to convert the GDAS observations in BURF to the format used by MET. Since GDAS includes observations in a 6 hours time window, individual files were extracted to facilitate the verification at hours in between the synoptic times. The time window used for these data ranges from 1 hour and 30 minutes before to 1 hour and 30 minutes. Using the Point-Stat tool, the mean, RMSE, bias, and standard deviation of the difference between the point observations and forecasts are computed. The Grid-Stat tool is used for the verification of precipitation using the same thresholds as in Section 4.2.5. The ETS and FBIAS statistics are used for the statistical analysis.

5.3.4 Results and discussions

In this section, the results and subsequent discussions are presented. It follows the main sections of the results in the previous chapter in order to provide similar analyses for both cases study.

5.3.4.1 Examination of analyses

As shown in results from the case study over central US, the data availability and coverage are the backbone of rapid updated analyses. Figure 5.15 presents the spatial distribution of assimilated temperature (Figure 5.15a), wind (Figure 5.15b and c), and radiance observations (Figure 5.15d) at the 15:00 UTC cycle on 5 July 2020

for experiment 3DVarsa. The data availability and coverage is similar in other experiments and are not shown here. The analysis residuals are shown at each point. Temperature observations in Figure 5.15a are from conventional sources including radiosondes, surface marine observations such as buoys, synoptic observations over land, and METAR reports. At most of the same locations, humidity and surface pressure observations are also available. The conventional data is sparse and scattered throughout the domain but with the lowest analysis residuals. In Figure 5.15b, the winds are from the same conventional sources and from scatterometers over the ocean (ASCATW). Satellite-derived winds are shown in Figure 5.15c. Radiance observations from the MHS sensor from the MetOp B satellite covering the western side of the domain are presented in Figure 5.15d. The mean of the RMS(OmA) value in the bottom of each figure indicates that radiances present the larger values. At upper levels the coverage is improved by nonconventional sources. All these data combined have great potential to positively impact the analyses and forecasts.

Figure 5.15 - Spatial distribution of temperature (a), winds (b and c), and radiance (d) observations and analysis residuals (OmA) for the analysis at 15:00 UTC on 5 July 2020 from the experiment 3DVarsa. As in Figure 4.10, the color scale to the right indicates the magnitude of analysis residuals. The legend of observation type markers is shown at the top along with brackets listing associated counts and RMS error for the OmA. In the bottom of each panel is presented the total and averaged RMS of the OmA of all observations.

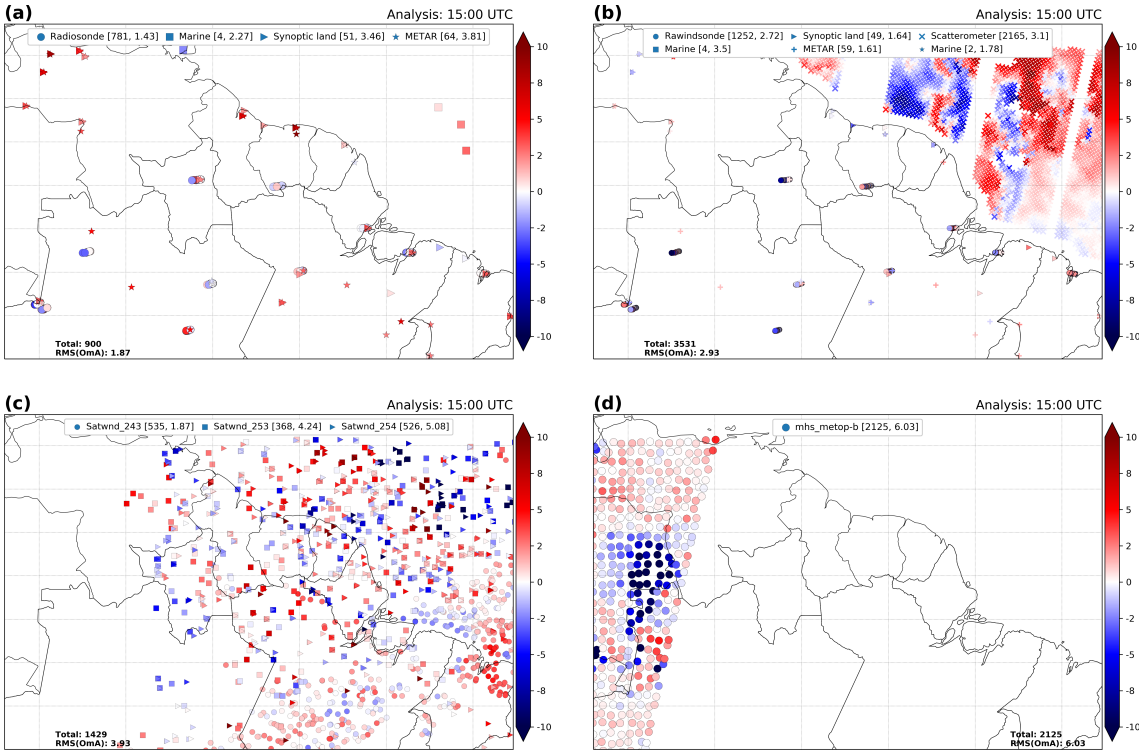

SOURCE: Author's production.

The RMS error and bias of the OmA and OmB of the temperature from all observation types for analyses in all cycles performed for experiments 85EnBECsa and 3DVarsa are shown in Figure 5.16. These results allow a further examination of the RRFS analysis on this region and confirm the good performance of the analysis system. The analyses created at each cycle are closer to the observations with lower RMS and bias of the OmA values. Especially, the hybrid 3DEnVar with 85 % of the ensemble error covariance shows less biased analyses when compared to 3DVarsa. However, there is an evident diurnal cycle with an increase of the errors during the afternoon hours and a decrease during the night and early morning. As observed in the case over central US, the RMS of the OmB shows an increase in the first cycle

after the model is cold started which may be related to the need of an spin-up in the cycling configuration. This occurs at cycles initialized at 03:00 UTC and 15:00 UTC followed by a noticeable increase in the RMS of OmB values at 18:00 UTC. These results corroborate the difficulty of predicting convection during the afternoon hours, which is more evident in these experiments because of the lower coverage of surface data, as shown in previous figure. This problem could be related to the fact that numerical models tend to produce rainfall earlier in the day than in the observations. Therefore, it would be interesting to evaluate the model diurnal cycle compared to CMORPH products in future studies. This issue could also be alleviated by using a different cycling configuration, which is a work already underway for RRFS.

Figure 5.16 - RMS and bias of the temperature background (OmB) and analysis (OmA) against all observation types for analyses in all cycles performed for experiments (a) 85EnBECsa and (b) 3DVarsa.

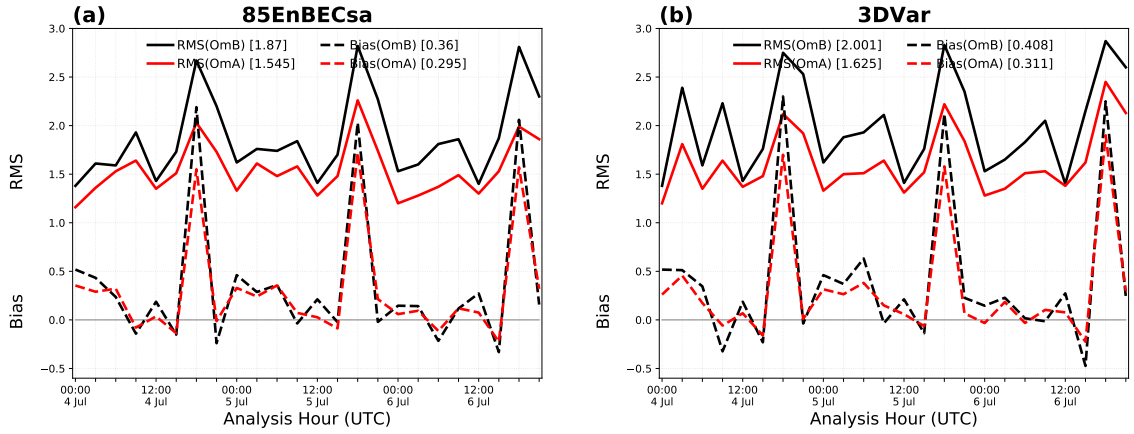

SOURCE: Author's production.

5.3.4.2 The impact of hybrid ensemble weights and ensemble localization radius

5.3.4.3 The impact of hybrid ensemble weights

The benefits of using hybrid analysis through a 3DEnVar analysis is investigated for this case study. Figure 5.17 presents the temperature and specific humidity analysis increments for the 15:00 UTC cycle on 5 July 2020 for experiments 100EnBECsa, 85EnBECsa, and 3DVarsa. The selection of this analysis hour follows the criteria

used in the previous case study; it is closer to the convection initiation and is created using warm start. The increments have lower magnitude than, for example, those shown for the case study over US. This is expected due to the lower data coverage and the temperature horizontal gradients in the tropics is much smaller than at higher latitudes (where the geostrophic adjustment induces a strong temperature response). The increments are more concentrated over certain points and some spread is observed in the surrounding areas. In 3DVarsa, the increments are smoother than in 85EnBECsa and 100EnBECsa. Meanwhile, the increments in 100EnBECsa are slightly more noisy than those in 85EnBECsa. This indicates the effects of using the contribution from an ensemble background error covariance in producing analyses with more flow-dependent characteristics. Although not shown here, the results of the OmA and OmB statistics for these experiments show lower RMS of the OmA in 85EnBECsa and 100EnBECsa when compared to 3DVar, with 85EnBECsa slightly better than 100EnBECsa.

Figure 5.17 - Analysis increment for temperature (K) (a, b, and c) and specific humidity (g kg^{-1}) (d, e, and f) at the first level above the surface for 15:00 UTC on 5 July 2020, for experiments 100EnBECsa (a and d) 85EnBECsa (b and e), and 3DVarsa (c and f).

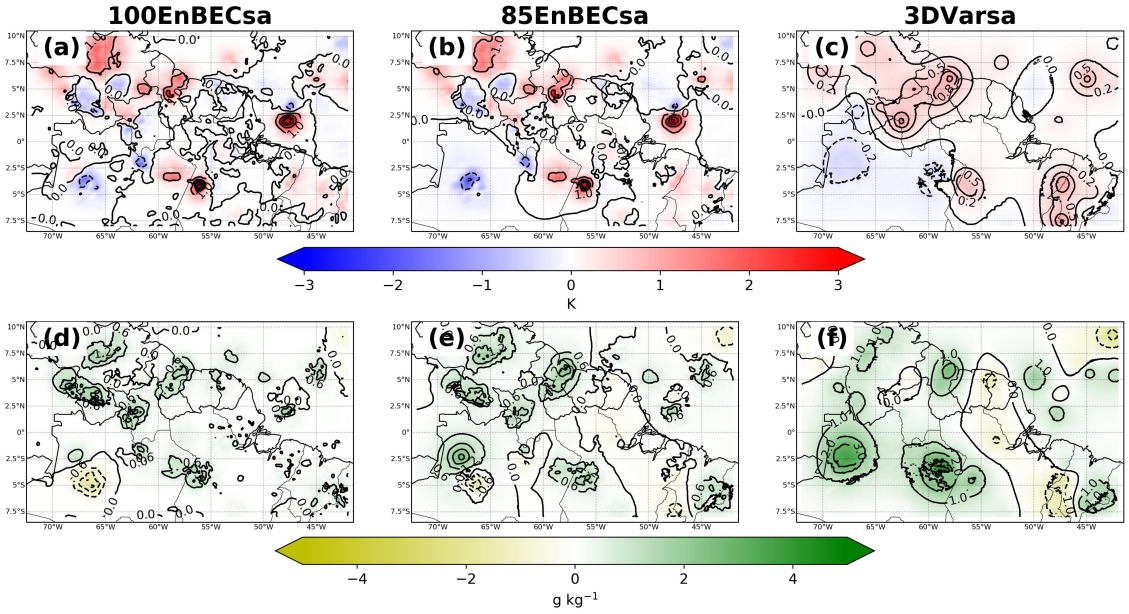

SOURCE: Author's production.

The 2, 4, and 6 h forecasts of 1 h accumulated precipitation from the 15:00 UTC cycle on 5 July 2020 are examined in Figure 5.18 for experiments 100EnBECsa, 85EnBECsa, 3DVarsa, and NoDAsa along with the precipitation estimates from CMORPH at valid hours 17:00, 19:00, and 21:00 UTC, respectively. The experiments using RRFS correctly capture the the precipitation along the coast from northern Para, Brazil until eastern Venezuela and the convection occurring over northern Amazonas and Roraima, Brazil, and southeastern Venezuela. This indicates the ability of the system in representing the large scale conditions, which are better represented in the experiments using data assimilation. The data assimilation has a greater impact in the first 2 and 4 h forecast where experiments with data assimilation show positive impacts over the experiment NoDAsa. Between the experiments with data assimilation, 3DVarsa shows an overestimate of the intensity and coverage of the precipitation at all forecasts lengths. Meanwhile, the experiment 85EnBECsa shows a better agreement with the precipitation estimates than 100EnBECsa and 3DVarsa. At 4 h and 6 h forecast, the experiment 100EnBECsa shows improvements in the precipitation coverage along the coast as in other parts of the domain, but 85EnBECsa shows slightly better results. All experiments overproduce the precipitation over the ocean, especially in 3DVarsa.

Figure 5.18 - As in Figure 5.14, but for experiments 100EnBECsa (d, e, and f), 85EnBECsa (g, h, and i), 3DVarsa (j, k, and l), and NoDAsa (m, n, and o).

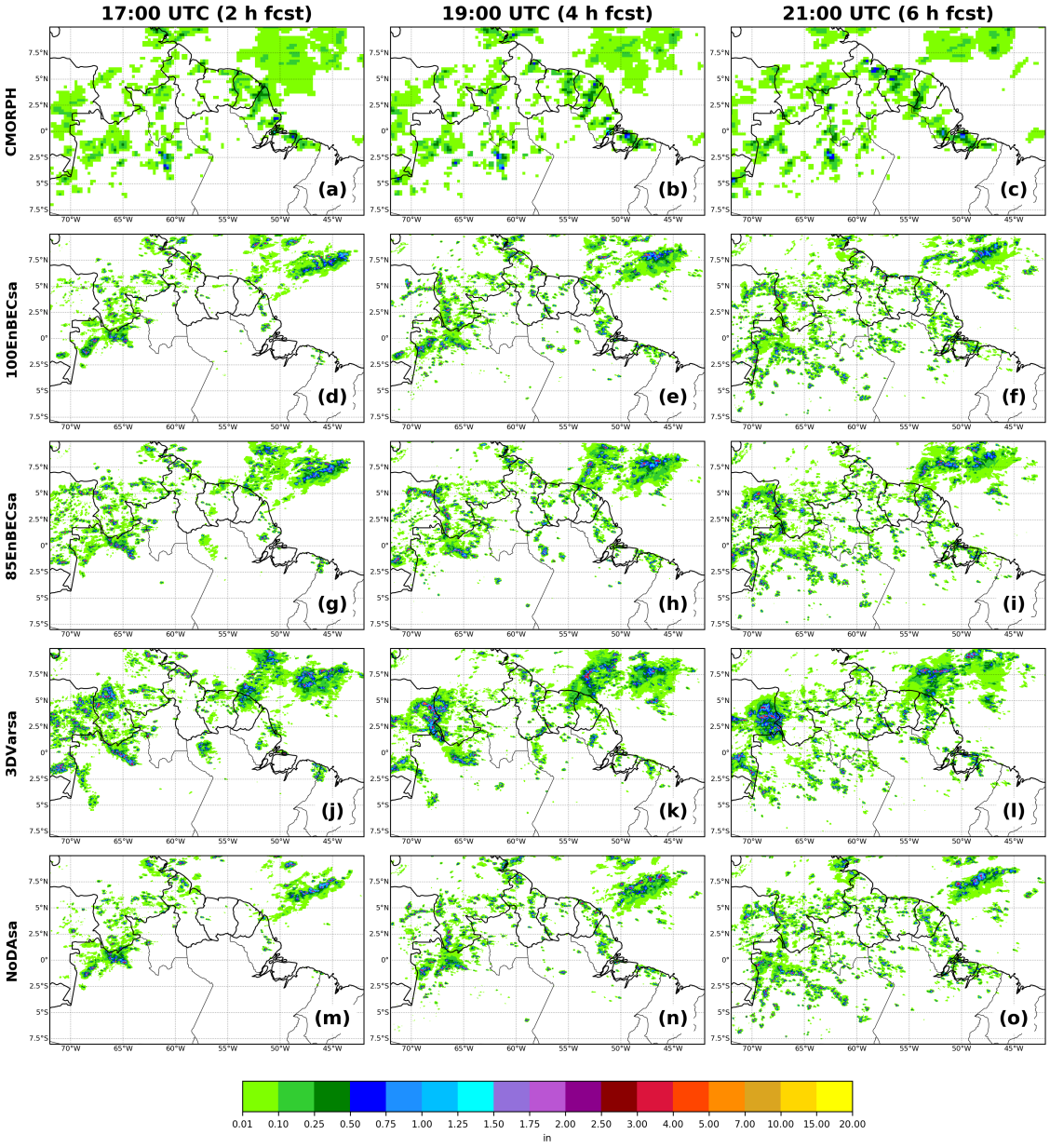

SOURCE: Author's production.

Figure 5.19 presents the RMSE and bias for the 3 h forecast of 2 m temperature (Figure 5.19a and c) and 2 m dew point temperature (Figure 5.19b and d) for experiments 100EnBECsa, 85EnBECsa, 3DVarsa and NoDAsa. First of all, it is noticeable that 2 m temperature and 2 m dew point RMSE and bias values follow the diurnal

cycle, with lower RMSE and bias values during the night and larger values during the afternoon, which is similar to results in Figure 5.16. The larger negative temperature bias during the afternoon may be a consequence of the fact that the observed temperature is "biased" towards the river margin temperature and not the temperature away from rivers since most of the conventional data sources are located along the Amazon River. 2 m temperature RMSE values show a positive impact from the data assimilation at cycles initialized between 00:00 UTC to 09:00 UTC (03:00 UTC to 12:00 UTC), with the lower RMSE values in the experiment 85EnBECsa (Figure 5.19a–b). However, between cycles initialized at 15:00 UTC and 21:00 UTC, the lower RMSE and bias are in the experiment NoDAsa. This indicates that although the analyses are closer to the observation at these hours, as shown in Figure 5.16, the forecasts are still dominated by the large scale boundary conditions due to less data availability for the surface. 2 m dew point temperature RMSE and bias values show improvements in experiments 85EnBECsa and 100EnBECsa over NoDAsa at the same hours as in 2 m temperature, while more neutral impact during the afternoon cycles. Overall, results between experiments with data assimilation show that 3DVarsa has the lowest performance in both variables.

Figure 5.19 - RMSE and bias for the 3 h forecast of 2 m temperature (a and c) and 2 m dew point temperature (b and d) against synoptic station and METAR observations for experiments 100EnBECsa, 85EnBECsa, 3DVarsa, and NoDAsa. The legend for each experiment is shown at the bottom of panel (c). The RMSE averaged over all cycles is shown in panels (a) and (b) for each experiment.

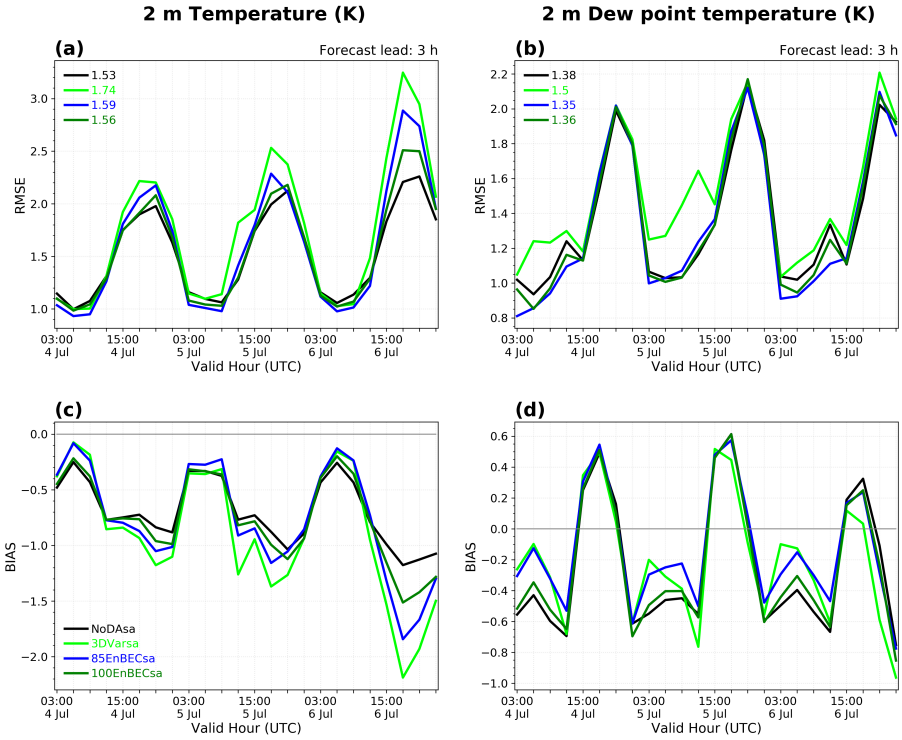

SOURCE: Author's production.

5.3.4.4 The impact of covariance localization

In order to increase the correlations between variables at larger distances in both vertical and horizontal scales, experiments VL9sa, HL330sa, and VL9HL330sa were conducted and results are explored in this subsection. Similar to Figure 5.17, Figure 5.20 presents the analysis increments of temperature and specific humidity for the 15:00 UTC cycle on 5 July 2020 but for experiment VL9sa, HL330sa, and VL9HL330sa. For this case study, the increase of the vertical localization radius from 3 to 9 layers shows almost neutral impact in the analysis when compared to 85EnBECsa. However, increasing the horizontal localization from 110 to 330 km shows a clear impact in the temperature and specific humidity analysis increments (Figure 5.20b and e). Larger analysis increments, in coverage and magnitude, are ob-

served in many parts of the domain. Increments are also more detailed (less smooth) than increments in VL9sa. In the experiment VL9HL330sa (Figure 5.20c and f), in which both length scales are modified, the analysis increments are similar to HL330sa but slightly less intense because of the change in the vertical localization. These results corroborate the importance of the covariance localization.

Figure 5.20 - As in Figure 5.17, but for experiments VL9sa (a and d), HL330sa (b and e), and VL9HL330sa (c and f) for 15:00 UTC on 5 July 2020.

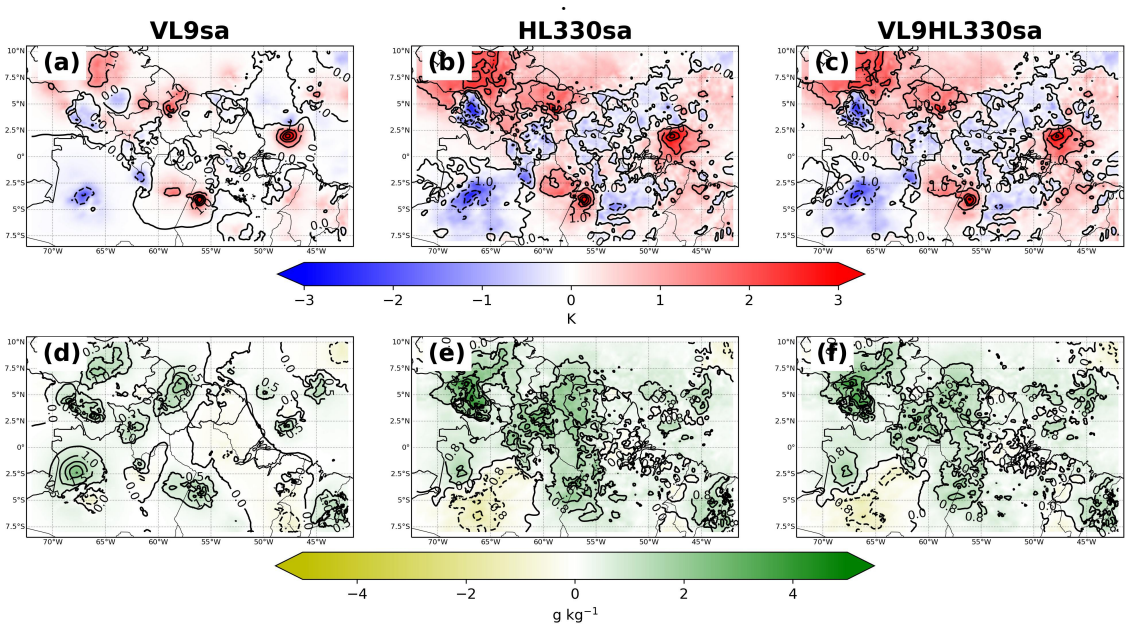

SOURCE: Author's production.

An analysis of the RMS and bias of the OmA and OmB gives another view of the impact of the localization scale modifications in this study. Figure 5.21 presents these results for experiments 85EnBECsa and VL9HL330sa. The results from VL9HL330sa are very similar to 85EnBECsa. However, the spikes in the RMS of the OmB values observed in 85EnBECsa are improved in VL9HL330sa, in particular in the cycles initialized at 18:00 UTC. The bias in VL9HL330sa is also slightly lower than in 85EnBECsa. However, an increase of the same magnitude is observed in the averaged RMS of the OmA in VL9HL330sa when compared to 85EnBECsa.

Figure 5.21 - As in Figure 5.16, but for experiments 85EnBECsa (a) and VL9HL330sa (b).

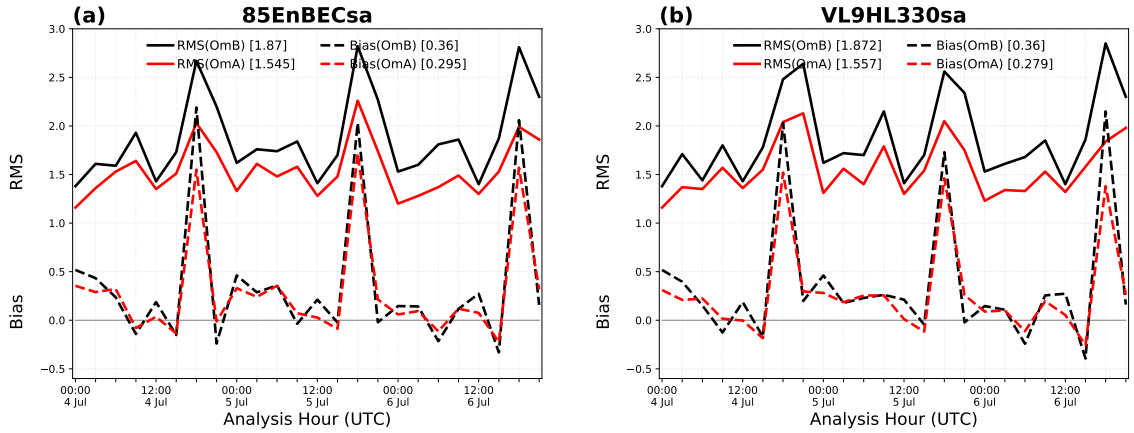

SOURCE: Author's production.

In order to investigate whether or not the adjustments in the temperature and specific humidity analysis increments have also improved the forecasts, the precipitation forecasts are analyzed. Figure 5.22 presents the 2, 4, and 6 h forecast of 1 h accumulated precipitation and the estimates from CMORPH. Overall, the results are slightly similar, but improvements in the precipitation along the coast are observed in the experiments with the increase of the horizontal localization at all forecast lengths. A slightly better coverage of the precipitation is shown in HL330sa and VL9HL330sa at 2 h forecast when compared to 85EnBECsa. At 4 and 6 h forecasts, the experiment VL9HL330sa show results that match better the precipitation estimates.

Figure 5.22 - As in Figure 5.18, but for experiments 85EnBECsa (d, e, and f), VL9HL330sa (g, h, and i), HL330sa (j, k, and l), and VL9sa (m, n, and o).

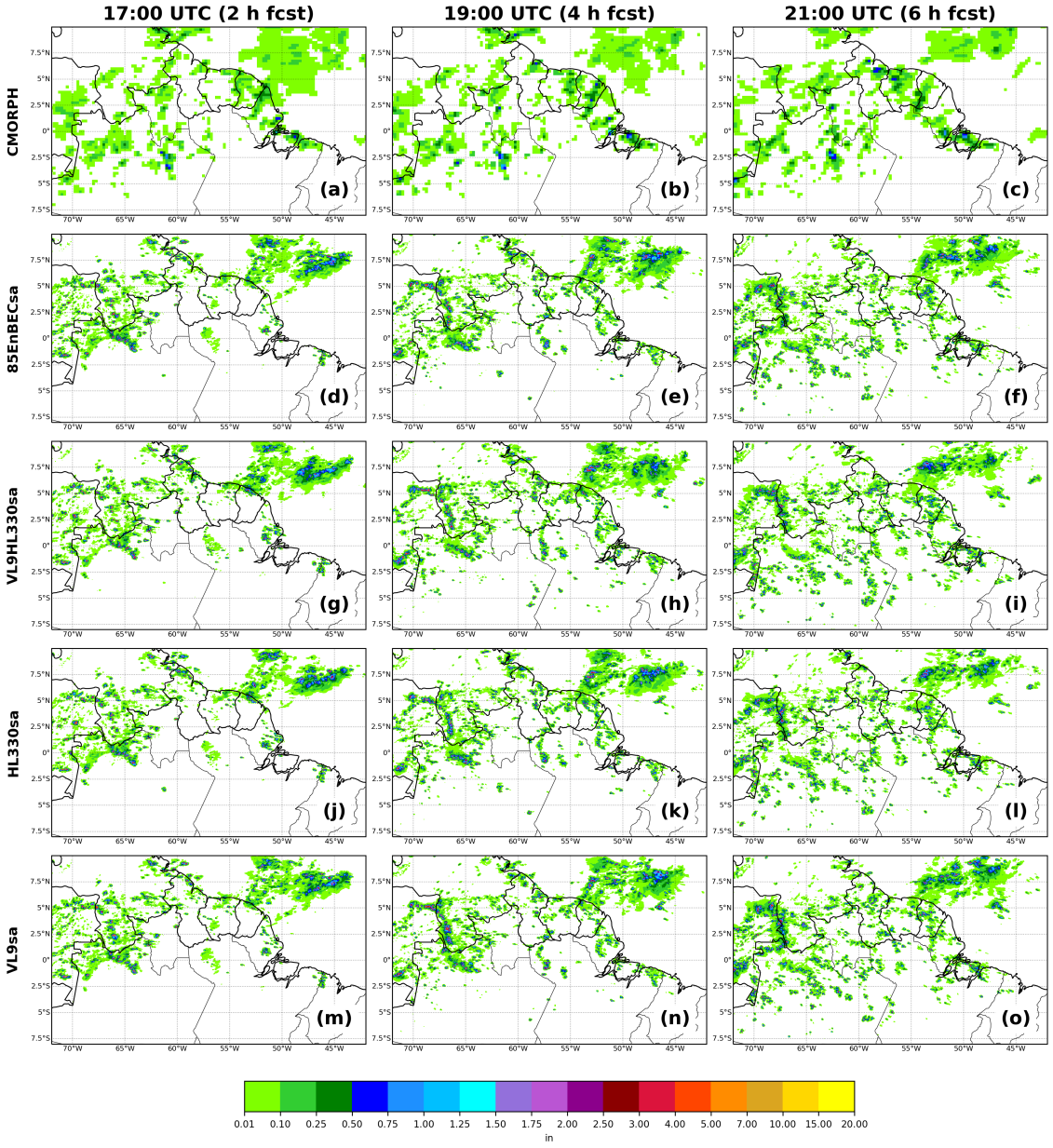

SOURCE: Author's production.

The RMSE and bias for the 3 h forecast of 2 m temperature (Figure 5.23a and c) and 2 m dew point temperature (Figure 5.23b and d) for experiments 85EnBECsa, VL9HL330sa, HL330sa, VL9sa, and NoDAsa are presented in Figure 5.23. The RMSE and bias show the same diurnal pattern as in Figure 5.19. However,

the differences between experiments with data assimilation and without it are more marked. The impact of the variation in the horizontal and vertical localization radius is almost neutral to negative in most of the cycles and for both variables when compared to 85EnBECsa. The experiment VL9HL330sa shows the worst performance at cycles initialized between 15:00 UTC and 21:00 UTC, when the NoDAsa performs best.

Figure 5.23 - As in Figure 5.19, but for experiments 85EnBECsa, VL9HL330sa, HL330sa, VL9sa, and NoDAsa.

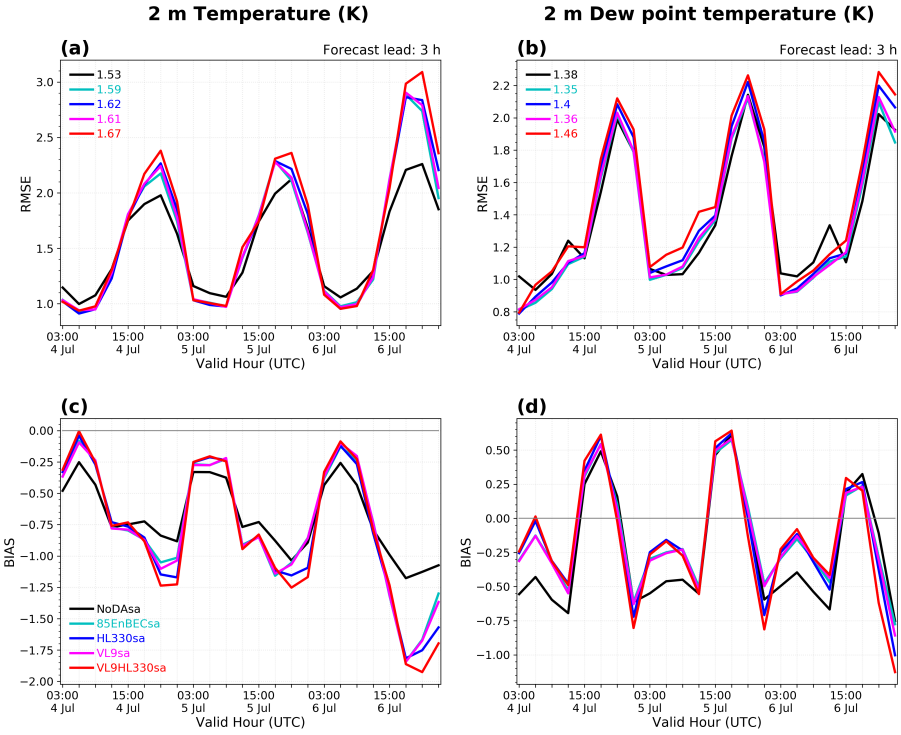

SOURCE: Author's production.

5.3.5 The impact of supersaturation removal and PBL pseudo observations

The function to remove supersaturation in the background, during the analysis process in GSI, was activated in the experiment CLIPSATsa. As in Section 4.3.4, the difference in the specific humidity (g kg^{-1}) analyses between experiments with and without activating this option is analyzed. Figure 5.24 shows the difference between the 85EnBECsa analysis and the CLIPSATsa analysis with the supersaturation clip-

ping function activated (85EnBECsa vs. CLIPSATsa) at model hybrid level 50, for the 15:00 UTC cycle on 5 July 2020. More positive and negative differences with a larger magnitude are observed in the southwestern part of the domain over state of Amazonas and northwestern Para in Brazil, and also over Guyana which corresponds with the area where precipitation is occurring according to the CMORPH estimates.

Figure 5.24 - Difference in specific humidity (g kg^{-1}) fields for the 15:00 UTC cycle on 5 July 2020 between analyses without and with supersaturation clipping activated (85EnBECsa vs. CLIPSATsa), at model hybrid level 50.

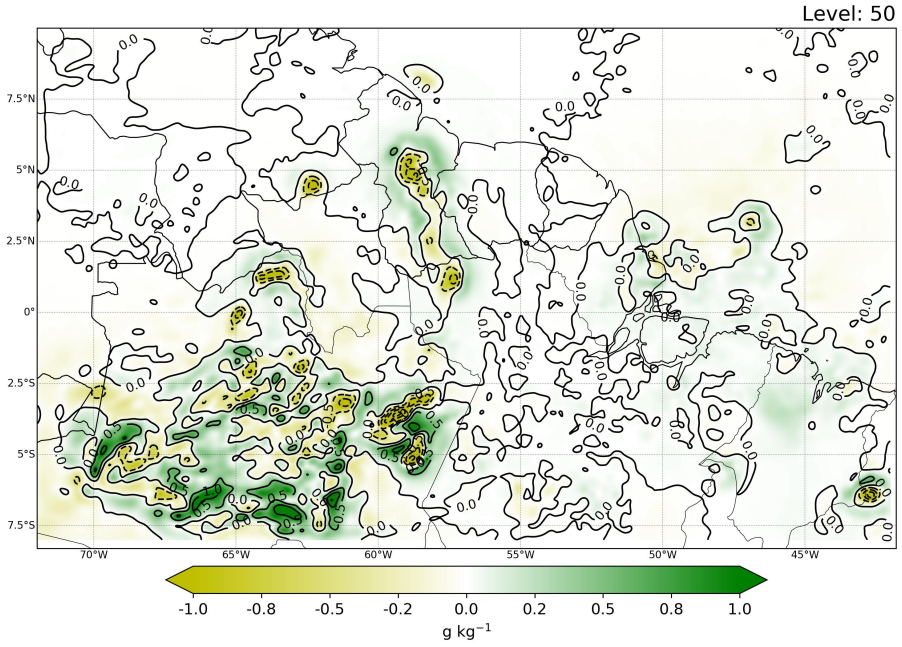

SOURCE: Author's production.

The 2, 4, and 6 h forecasts of 1 h accumulated precipitation from the 15:00 UTC cycle on 5 July 2020 for experiments CLIPSATsa and 85EnBECsa are shown in Figure 5.25 along with the precipitation estimates from CMORPH at valid hours 17:00, 19:00, and 21:00 UTC, respectively. CLIPSATsa shows improvements when compared with 85EnBECsa, especially over the ocean at all forecast lengths. However, over land, the improvements are mainly at 4 and 6 h forecasts with a slightly better coverage of the precipitation along the coast.

Figure 5.25 - As in Figure 5.18, but for experiments 85EnBECsa (d, e, and f), CLIPSATsa (g, h, and i).

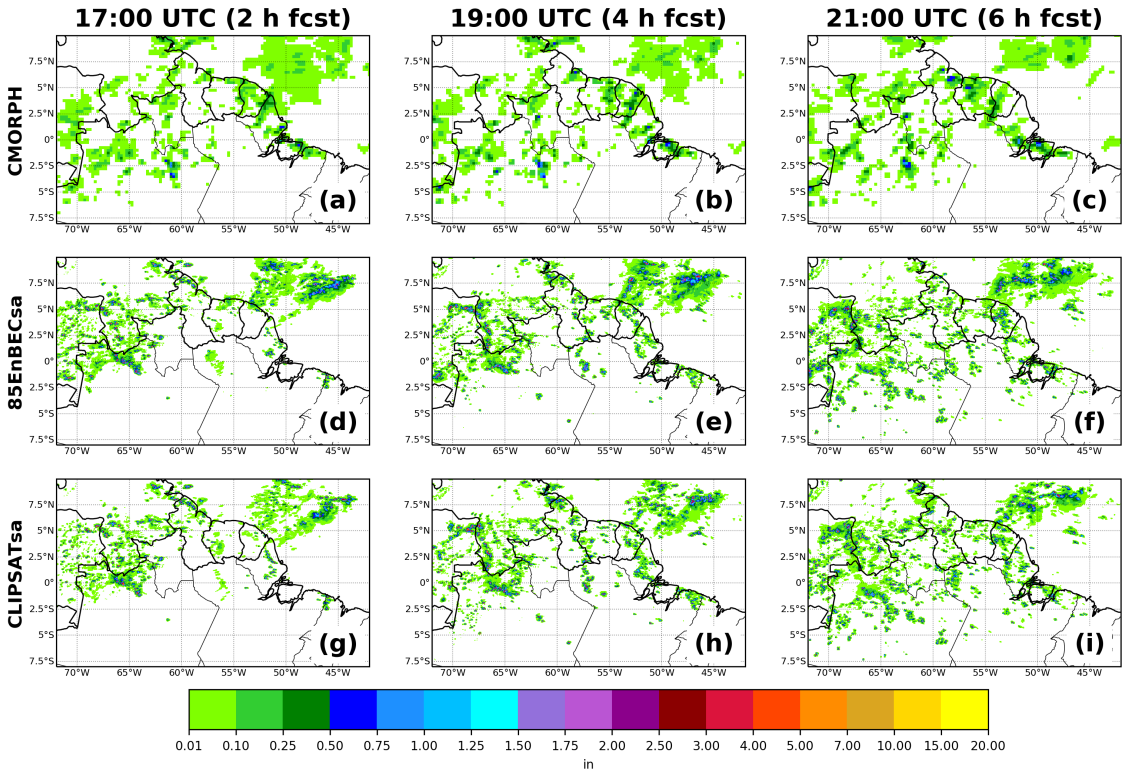

SOURCE: Author's production.

5.3.6 Quantitative precipitation forecast verification

A further evaluation of the precipitation forecasts was performed in terms of the ETS and FBIAS for the same thresholds analyzed in the case over central US (i.e., 0.01 inches h^{-1} and 0.25 inches h^{-1}). Figure 5.26 shows the ETS and FBIAS for 1 h accumulated precipitation greater than 0.01 inches h^{-1} (Figure 5.26a and c) and 0.25 inches h^{-1} (Figure 5.26b and d) for experiments CLIPSATsa, PSEUDOsa, VL9H330sa, 100EnBECsa, 85EnBECsa, 3DVarsa, and NoDAsa aggregated at each forecast lead hour. Overall, the ETS and FBIAS results for both thresholds indicate that 3DVar performs better than the other experiments especially in the first 2 h forecast. For the next forecast lengths, a better performance of the 1 h accumulated precipitation greater than 0.01 inches h^{-1} is achieved in 85EnBECsa followed by PSEUDOsa, VL9H330sa, and CLIPSATsa until 9 h forecast. In the following forecast hours, the impact from the data assimilation starts to decay, although the

experiment CLIPSATsa shows the slightly best performance from the 9 h to the 24 h forecast. The experiment 100EnBECsa shows better performance than NoDAsa, but worse than the other experiments with data assimilation. The FBIAS results for this threshold shows that 3DVar performs better followed by the experiments 85EnBECsa, PSEUDOsa, VL9H330sa, and CLIPSATsa which show better results than 100EnBECsa and NoDAsa. The values of the FBIAS indicate that all experiments underperfom the frequency with which observed events were observed. For 1 h accumulated precipitation greater than 0.25 inches h^{-1}, the performance of the system is overall low, with the ETS and FBIAS results from all experiments concentrating at lower ranges and 3DVar showing the best results at shorter lead times. However, these results should be carefully interpreted since a grid-to-grid approach is being used for the computation of the ETS and FBIAS, which may not be ideal for this case. A grid-to-grid verification may benefit the experiment that overestimates precipitation (3DVar) given that the estimated precipitation shows scattered areas of accumulated precipitation throughout the domain, which is more difficult for the model to accurately predict. A more appropriate approach for convective scales such as the neighborhood approach may be considered in future studies as indicated in Schwartz and Sobash (2017).

Figure 5.26 - ETS (a and b) and FBIAS (c and d) for 1 h accumulated precipitation forecasts greater than 0.01 inches (a and c) and 0.25 inches (b and d) from experiments CLIPSATsa, PSEUDOsa, VL9H330sa, 100EnBECsa, 85EnBECsa, 3DVarsa, and NoDAsa for 24 hour forecasts.

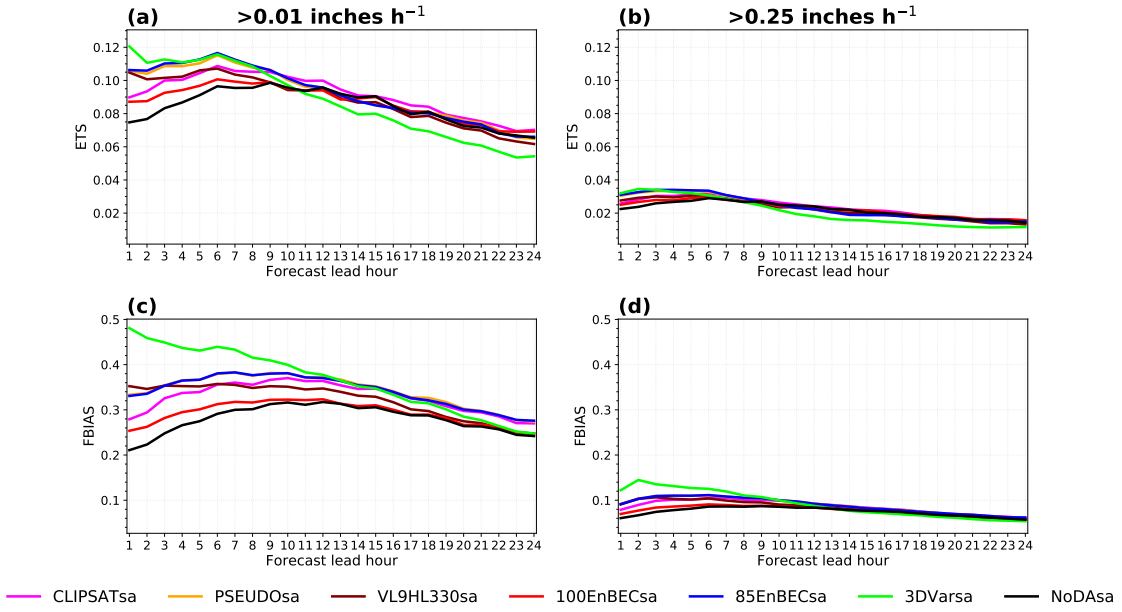

SOURCE: Author's production.

6 CONCLUSIONS, FINAL REMARKS, AND FUTURE WORK

The NOAA next generation rapidly-updated, convection-allowing forecast system, or RRFS, is under development and aims to replace the current operational suite of convection-allowing models at NCEP in the next operational upgrade. RRFS is built upon the SRW and the current prototype RRFS uses GSI as the analysis component, providing a suitable research framework to assess the ability of this forecast system to represent convection. In this study, the data assimilation framework for the prototype RRFS is investigated through the simulation of frequent weather systems over mid- and tropical latitudes, such as a case of a typical spring squall line over central US and an Amazon coastal squall line case during the 2020 Amazon dry season. Over both regions, sensitivities to various configurations and algorithms available in GSI are analyzed in order to find the best configuration to produce more realistic convection forecasts and provide guidance on the convective scale data assimilation over regions of the globe with low data density, as in the Amazon region.

6.1 Conclusions

The case study over central US is an squall line that occurred over Oklahoma during the afternoon of 4 May 2020. Overall, the configurations tested are able to capture the main characteristics of the major convective systems during the execution period. The main findings from this case study are listed below:

a) FV3LAM with the RRFSv1a physics suite has good potential for storm forecasts, giving a reasonably good simulation of the convective initiation and evolution of the squall line;

b) The convection in the current prototype RRFS tends to be overestimated in intensity and underestimated in its extent, as found in previous studies on FV3-based convection-allowing models;

c) The data assimilation makes the analyses fit the observations more closely in all cycles. However, the RMS errors of the OmB show distinguishable spikes in cycles where FV3LAM 1 h forecasts are initialized from an external model as background for the analyses, which indicates the FV3LAM is still under spin-up in this situation;

d) Experiments with data assimilation show an overall positive impact compared with the experiment without data assimilation. The data assimilation using pure ensemble background error covariance (100EnBEC) per-

forms better at 2 h forecasts for the storms, but 75 % ensemble background error covariance (75EnBEC) produces better forecasts in all forecast lengths with a better positioning of the squall line evolution, especially at 4 h forecast. Lower RMSE and bias are also found in experiment 75EnBEC for the analyzed surface variables and most vertical profiles;

e) Reducing the vertical localization from 3 layers to 1 layer in the lowest 10 layers of the analysis grid leads to, in general, a less skillful forecast. This suggests that the vertical localization configuration used in RAP is already a good choice and should be used in RRFS;

f) Convection is greatly improved when using PBL pseudo-observations from surface 2 m temperature and 2 m moisture observations based on RAP configurations, especially at 4 h forecast with a better coverage and positioning of the convection. The promising results found in this study for the storm forecast indicates the potential of the PBL pseudo-observations function in future versions of RRFS;

g) Supersaturation clipping in GSI can improve specific humidity fields in the analyses, allowing for more realistic storm and precipitation forecasts at longer forecast lengths. At shorter forecast lead hours, it produces more spurious convection but precipitation forecasts are as skillful as in experiments 75EnBEC and 100EnBEC;

h) FV3LAM hourly accumulated precipitation forecasts for different thresholds indicate that heavier precipitation (>0.25 inches (6.35 mm)) is more difficult to predict than light precipitation (>0.01 inches (0.254 mm)). The data assimilation clearly improved precipitation forecasts up to 13 h for both thresholds analyzed;

i) The experiment using 100 % ensemble background error covariance showed the best 1 h accumulated precipitation forecast quality in the first 4 hours forecast for lighter precipitation, while experiment 75EnBEC performed better for 1 h accumulated precipitation greater than 0.25 inches.

The second case study is investigated in Chapter 5. The initial challenge for this study is the case selection. A methodology, based on different references, is developed and applied. The following steps are followed, firstly determining the onset and end of the dry season for the Amazon during 2020 following the work of Marengo et al. (2001), then executing the ForTraCC to identify and track convective systems

in satellite infrared imagery for the period previously determined, and finally, following Cohen et al. (1995) and Oliveira and Oyama (2015) search for clusters in the convective system that meet certain criteria, in terms of their size, tilting, and eccentricity. The last step is more subjective since it was not possible to establish the whole life cycle of the squall line case with this objective methodology. From this methodology, it is found that:

a) The dry season of 2020 near the mouth of the Amazon was between 21 June and 29 October 2020, approximately. This is between the earliest climatological limits suggested in the literature, although the end was earlier than the climatological range;

b) The results from the ForTraCC execution indicate that northwestern Amazon is the preferred region of formation of convective system during this period. It extends through the west and central west Amazon;

c) The source region for the Amazon coastal squall lines is clearly identified over northern Amazon and occur mostly in July, as shown in previous studies. In this month is also observed a slightly larger amount of long-lived systems. The largest amount of systems that lasted between 3 and 6 hours are initiated in October;

d) Most of the convective systems in all categories have genesis in July, followed by August, October, and September and the average maximum duration of all systems is around 12 hours;

e) The objective methodology applied in this study is able to adequately identify the main convective system associated with an Amazon coastal squall line, as a linear band along the coast. During the occurrence of this system there was the presence of a low level jet parallel to the coast in the vertical level from 900 to 600 hPa, as suggested in the literature.

The Amazon coastal squall line case that initiated during the afternoon of 5 July 2020 is studied through the execution of various numerical experiments. Overall, results suggest that RRFS provide reasonably good guidance for the tropical region. From this results can be concluded that:

a) RRFS is able to capture the main large scale patterns with a correct positioning of the precipitating systems as analyzed using the CMORPH precipitation estimates.;

b) A CCPP physics suite based on HRRR physical parameterizations shows a better representation of the precipitation, while the GFS-based physics suite shows larger coverage and intensity than the precipitation estimates;

c) Despite the low coverage of the available data for experiments with data assimilation, the data assimilation system performs adequately over this region, with RRFS analyses closer to the observations in all cycles;

d) The precipitation coverage along the coast and other parts of the domain are improved when using data assimilation. Experiments 85EnBECsa and 100EnBECsa show a closer agreement with the precipitation estimates of the domain at 4 and 6 h forecast, with 85EnBECsa showing better results at all forecast lengths;

e) There is a notable diurnal cycle in the RMSE and bias values, with the NoDAsa outperforming the experiments with data assimilation during the afternoon hours. Errors associated with the convection occurrence and the less coverage of surface observation in the domain may have contributed to these results;

f) The experiment 3DVarsa shows the large RMSE and bias for when comparing against observations of 2 m temperature and 2 m dew point temperature in all cycles, while the experiment 85EnBECsa performs better than the others during the night and early morning hours;

g) Increasing the localization radius in the ensemble-based error covariance, analysis increments show more flow-dependent characteristics, particularly when increasing the horizontal localization radius from 110 km to 330 km which also allows for improvements in the RMS of the OmA values and to represent slightly better the satellite-derived precipitation estimates. Nevertheless, when comparing against surface observations, the impact is neutral to negative;

h) When activating the supersaturation removal in GSI for this case study, the results show positive impacts against 85EnBECsa with a slightly better representation of the precipitation along the coast. However, the improvements are small and mainly concentrated at larger forecast lengths;

i) The 1 h accumulated precipitation forecasts for different thresholds corroborates the results found for the case over central US, that heavier precipitation (>0.25 inches (6.35 mm)) is more difficult to predict than light

precipitation (>0.01 inches (0.254 mm)), which has also been found in many other studies using different forecasting systems;

j) The 1 h accumulated precipitation forecasts skill in terms of ETS and FBIAS using a gridpoint-based verification does not seem appropriate for the precipitation verification of this case study.

6.2 Final remarks

Since RRFS is under development and an official release is still not available, not many studies are found in the literature covering the different components of the system. Therefore, aside from the study of Tong et al. (2020), this thesis is the first study investigating convective scale data assimilation developments with the FV3LAM modeling system within the RRFS framework. Furthermore, the results found in this study contribute to fill a major gap in the literature on the current capabilities of RRFS, over regions with high and low data density. Additionally, it is the first study over the Amazon region using a convective data assimilation system to represent the convection associated with Amazon coastal squall lines and all the challenges that represents are highlighted. At the same time, taking into account that RRFS is under active development, results shown here are linked to the specific version used which may differ from the latest developments of each of RRFS components.

Though a single case of squall line is analyzed over each region and RRFS components are under development, this study provides valuable insights into the performance of prototype RRFS with diverse configurations. More extensive testing of RRFS, covering a wider variety of cases, larger domain, and longer period of time, is needed to demonstrate whether results found here are robust or may be case dependent. Through the case study over northern South America it is shown that ForTraCC outputs can serve as a starting point for modeling studies over the Amazon region. The results from Chapter 5 show that RRFS has potential for the tropical areas, especially when using a HRRR-based CCPP suite. Even though the amount of data available for the simulations was sparse over the domain configured, results show that using hybrid data assimilation forecasts outperform results from 3DVarsa. Other verification approaches should be considered for the forecast verification when comparing against satellite-derived products, such as neighborhood and object-based methods. This work give indication of the performance of a convection-allowing system using 3-hourly cycles and data already available in the GTS. Although further testing and evaluation are warranted in addition to the

options tested here, data assimilation proves to be crucial to improve short term forecasts of storms and precipitation in RRFS.

Finally, it is important to mention that the activities developed in this work and the results reported in this thesis are connected with a current Memorandum of Understanding between CPTEC-INPE and NCEP-NOAA, which is in conclusion process. This doctorate thesis is an example of collaboration between these institutions, contributes with the internationalization of the Graduate Program, and give indications of the potential of the RRFS for future convective data assimilation applications at CPTEC-INPE inside this collaboration process.

Preliminary results of Chapter 4 are already published in the DTC Newsletter (BANOS, 2020) and as a final report in the DTC Visitor Project website (BANOS et al., 2021a), and a seminar was presented at the Developmental Testbed Center (the recorded video can be found at `https://www.youtube.com/watch?v=0KbZHyRe4IQ`). Additionally, an article is under revision and posted as preprint on Geoscientific Model Development (BANOS et al., 2021c). Results from Chapter 5 are under preparation for submission to the journal Monthly Weather Review.

6.3 Future work

CPTEC has a new PNT development strategy based on community efforts involving universities and other Brazilian Institutes. The goal is to provide Brazilian society with a community-based Unified Earth System Model, in which the data assimilation in all components has been taken into account from the initial conception of the project. Continuing research along the same lines as this thesis will contribute significantly to this community model in different aspects, such as the evaluation process, data assimilation activities, etc.

Despite all the options tested in this study, it is clear that there is still much to investigate regarding the capabilities of RRFS over the CONUS and the tropics. As many topics were covered, several paths for the continuation of this work in the future are being considered. A few suggestions are listed below:

- Future studies may be focused on defining a more complete methodology to objectively identify squall lines using ForTraCC. This is particularly important for modeling studies over the Amazon region where the radar coverage and availability is limited;
- Explore other cycling strategies in which the large scale atmosphere is

efficiently updated in order to reduce the spikes showed in the OmB and OmA statistics. This can lead to analysis closer to the observations and model forecasts. At present, work is underway at NOAA's Global Systems Laboratory (GSL) and EMC to determine the best cycling strategy for this system.

- Investigate the assimilation of radar data over the CONUS and the Amazon, which can help to improve the information on the convective scale related to hydrometeors;

- Explore ensemble methods for the analysis and model forecasts. Although this approach is more computationally expensive, the use of ensemble may help to create analyses closer to the observations through the use of adequate perturbation methodologies for the analysis and forecast ensemble;

- Investigate the use of GOES-16 GLM data as proxy for reflectivity in the data assimilation system. This approach would be particularly important for the convective scale data assimilation over regions that relies on satellite data, such as the Amazon;

- Extend the satellite radiance data assimilation to all sky situations in which cloud and precipitation-affected pixels are also included. This has proved to improve the forecasts in NWP centers in recent years and with the high temporal and spatial resolution of sensors on geostationary satellites such as the Advanced Baseline Imager (ABI) on GOES16, more realistic analyses and forecasts can be achieved for convective scales.

- In this study, GSI is the analysis system used for prototype RRFS, however, it needs to be pointed out that for UFS applications, the Joint Effort for Data assimilation Integration (JEDI) is being developed, which will replace GSI as the operational data assimilation system of the NCEP in the future (TREMOLET; AULIGNE, 2018). Two public releases of JEDI are already available (`https://www.jcsda.org/jedi-fv3-release`), fostering community contributions since early stages of development. Therefore, future studies may be focused on the use of JEDI for RRFS instead of GSI.

REFERENCES

AFONSO, J. M. d. S.; VILA, D. A.; GAN, M. A.; QUISPE, D. P.; BARRETO, N. d. J. d. C.; CHINCHAY, J. H. H.; PALHARINI, R. S. A. Precipitation diurnal cycle assessment of satellite-based estimates over Brazil. **Remote Sensing**, v. 12, n. 14, p. 2339, 2020. 104

ALCÂNTARA, C. R.; SILVA-DIAS, M. A. F.; SOUZA, E. P.; COHEN, J. C. P. Verification of the role of the low level jets in Amazon squall lines. **Atmospheric Research**, v. 100, n. 1, p. 36–44, 2011. 4, 27, 30, 87

ALEXANDER, C.; CARLEY, J. Short-range weather in operations. **Bulletin of the UFS Community**, p. 9, 2020. Available from: <https://www.ufscommunity.org/wp-content/uploads/2021/03/Bulletin_UFS_Community_Winter_2020_Full.pdf>. 1, 3

ALPERT, J. C.; YUDIN, V. A.; STROBACH, E. Atmospheric gravity wave sources correlated with resolved-scale gravity wave activity and sub-grid scale parameterization in the FV3GFS model. In: AGU FALL MEETING, 2019. **Proceedings...** [S.l.]: AGU, 2019. 32

ARAGÃO, L. E. O. C.; POULTER, B.; BARLOW, J. B.; ANDERSON, L. O.; MALHI, Y.; SAATCHI, S.; PHILLIPS, O. L.; GLOOR, E. Environmental change and the carbon balance of Amazonian forests. **Biological Reviews**, v. 89, n. 4, p. 913–931, 2014. Available from: <https://onlinelibrary.wiley.com/doi/abs/10.1111/brv.12088>. 4

AZEVEDO, H. B. d.; GONÇALVES, L. G. G. d.; BASTARZ, C. F.; SILVEIRA, B. B. Observing system experiments in a 3DVAR data assimilation system at CPTEC/INPE. **Weather and Forecasting**, v. 32, n. 3, p. 873–880, 2017. ISSN 0882-8156. Available from: <http://journals.ametsoc.org/doi/10.1175/WAF-D-15-0168.1>. 24

AZEVEDO, H. B. D.; GONÇALVES, L. G. G. D.; KALNAY, E.; WESPETAL, M. Dynamically weighted hybrid gain data assimilation: perfect model testing. **Tellus A: Dynamic Meteorology and Oceanography**, v. 72, n. 1, p. 1–11, 2020. Available from: <https://doi.org/10.1080/16000870.2020.1835310>. 17, 65, 102

BALLARD, S. P. et al. Convective scale data assimilation and nowcasting. In: SEMINAR ON DATA ASSIMILATION FOR ATMOSPHERE AND OCEAN, 2012. **Proceedings...** [S.l.]: ECMWF, 2012. p. 265–300. 19

BANNISTER, R. N. A review of operational methods of variational and ensemble-variational data assimilation. **Quarterly Journal of the Royal Meteorological Society**, v. 143, n. 703, p. 607–633, 2017. ISSN 0035-9009. Available from: <https://rmets.onlinelibrary.wiley.com/doi/abs/10.1002/qj.2982>. 18, 23

BANNISTER, R. N.; CHIPILSKI, H. G.; MARTINEZ-ALVARADO, O. Techniques and challenges in the assimilation of atmospheric water observations for numerical weather prediction towards convective scales. **Quarterly Journal of the Royal Meteorological Society**, v. 146, n. 726, p. 1–48, 2019. Available from: <https://rmets.onlinelibrary.wiley.com/doi/abs/10.1002/qj.3652>. 1, 23

BANOS, I. H. Assessing the FV3-LAM Data Assimilation Capability to Represent Convection. **DTC Newsletter**, n. 23, 2020. Available from: <https://dtcenter.org/news/2020/04#2115>. 126

BANOS, I. H.; DTC DA team; SAPUCCI, L. F. **Test and evaluation of CCPP physics suites and data assimilation capabilities to improve the Rapid Refresh Forecast System for convection forecasts**. [S.l.], 2021. 15 p. Available from: <https://dtcenter.org/sites/default/files/visitor-projects/Ivette-DTC_SUMMARY_REPORT2021.pdf>. 48, 126

BANOS, I. H.; MAYFIELD, W. D.; GE, G.; SAPUCCI, L. F.; CARLEY, J. R.; NANCE, L. **Assessment of the data assimilation framework for the prototype Rapid Refresh Forecast System and impacts on forecasts of convective storms**. Zenodo, aug. 2021. Available from: <https://doi.org/10.5281/zenodo.5226389>. 161

_____. Assessment of the data assimilation framework for the Rapid Refresh Forecast System v0.1 and impacts on forecasts of convective storms. **Geoscientific Model Development Discussions**, p. 1–36, 2021. 126

_____. **Rapid Refresh Forecast System (RRFS) v0.1**. Zenodo, oct. 2021. Available from: <https://doi.org/10.5281/zenodo.5546592>. 161

BANOS, I. H.; SAPUCCI, L. F.; AVANÇO, L. A.; DINIZ, F. L. R. Impacto da assimilação de perfis de refratividade do satélite Metop-B nas previsões de tempo do CPTEC/INPE durante os meses de janeiro e agosto de 2014. **Revista Brasileira de Meteorologia**, v. 33, p. 65–81, 2018. 24

BANOS, I. H.; SAPUCCI, L. F.; CUCURULL, L.; BASTARZ, C. F.; SILVEIRA, B. B. Assimilation of GPSRO bending angle profiles into the Brazilian global atmospheric model. **Remote Sensing**, v. 11, n. 3, p. 256, 2019. 24

BARNES, S. L. A technique for maximizing details in numerical weather map analysis. **Journal of Applied Meteorology and Climatology**, v. 3, n. 4, p. 396 – 409, 1964. Available from: <https://journals.ametsoc.org/view/journals/apme/3/4/1520-0450_1964_003_0396_atfmdi_2_0_co_2.xml>. 8

BASTARZ, C. F. **Global Hybrid Ensemble Variational Data Assimilation at CPTEC**. 275 p. Tese (Doutorado em Meteorologia) — Instituto Nacional de Pesquisas Espaciais (INPE), São José dos Campos, 2017. 24

BATHMANN, K. **The GSI minimization code structure**. 2021. Available from: <https://github.com/NOAA-EMC/GSI/wiki/GSI_Minimization_Code_Explained.pdf>. 33

BAUER, P.; THORPE, A.; BRUNET, G. The quiet revolution of numerical weather prediction. **Nature**, v. 525, n. 7567, p. 47–55, Sep 2015. ISSN 1476-4687. Available from: <https://doi.org/10.1038/nature14956>. 1, 12

BENJAMIN, S. G.; JAMES, E. P.; BROWN, J. M.; SZOKE, E. J.; KENYON, J. S.; AHMADOV, R. Diagnostic fields developed for hourly updated NOAA weather models. **NOAA Technical Memorandum OAR GSL-66**, 2020. Available from: <https://repository.library.noaa.gov/view/noaa/24212>. 35

BENJAMIN, S. G.; JAMISON, B. D.; MONINGER, W. R.; SAHM, S. R.; SCHWARTZ, B. E.; SCHLATTER, T. W. Relative short-range forecast impact from aircraft, profiler, radiosonde, VAD, GPS-PW, METAR, and mesonet observations via the RUC hourly assimilation cycle. **Monthly Weather Review**, v. 138, n. 4, p. 1319 – 1343, 2010. Available from: <https://journals.ametsoc.org/view/journals/mwre/138/4/2009mwr3097.1.xml>. 20

BENJAMIN, S. G. et al. A North American hourly assimilation and model forecast cycle: the Rapid Refresh. **Monthly Weather Review**, v. 144, n. 4, p. 1669–1694, 2016. Available from: <https://journals.ametsoc.org/view/journals/mwre/144/4/mwr-d-15-0242.1.xml>. 3, 20, 35, 47, 50, 51

_____. Stratiform cloud-hydrometeor assimilation for HRRR and RAP model short-range weather prediction. **Monthly Weather Review**, 2021. 20

BENJAMIN, S. G.; WEYGANDT, S. S.; DEVENYI, D.; MANIKIN, J. B. G.; SMITH, T.; SMIRNOVA, T. Improved moisture and PBL initialization in the RUC using METAR data. In: CONFERENCE SEVERE LOCAL STORMS, 22., 2004. **Preprints...** [S.l.]: SPC, 2004. 20

BERGTHöRSSON, P.; DööS, B. R. Numerical weather map analysis. **Tellus**, v. 7, n. 3, p. 329–340, 1955. Available from: <https://doi.org/10.3402/tellusa.v7i3.8902>. 8

BERNARDET, L.; FIRL, G.; HEINZELLER, D.; CARSON, L.; SUN, X.; PAN, L.; ZHANG, M. Engaging the community in the development of physics for NWP models. In: EGU GENERAL ASSEMBLY CONFERENCE, 2020. **Abstracts...** 2020. Available from: <https://ui.adsabs.harvard.edu/abs/2020{EGU}GA..2222093B>. 32

BETTS, A. K.; JAKOB, C. Evaluation of the diurnal cycle of precipitation, surface thermodynamics, and surface fluxes in the ECMWF model using LBA data. **Journal of Geophysical Research: Atmospheres**, v. 107, n. D20, p. LBA 12–1–LBA 12–8, 2002. Available from: <https://agupubs.onlinelibrary.wiley.com/doi/abs/10.1029/2001JD000427>. 4

BIAZETO, B.; DIAS, M. A. S. Analysis of the impact of rainfall assimilation during lba atmospheric mesoscale missions in southwest amazon. **Atmospheric research**, v. 107, p. 126–144, 2012. 4

BJERKNES, V. The problem of weather prediction, as seen from the standpoints of mechanics and physics. **Meteorologische Zeitschrift**, 1904. 7

BLACK, T. et al. A limited area modeling capability for the finite-volume cubed-sphere (FV3) dynamical core and comparison with a global two-way nest. **Journal of Advances in Modeling Earth Systems**, p. e2021MS002483, 2021. 2, 31, 32

BLUESTEIN, H. B.; JAIN, M. H. Formation of mesoscale lines of precipitation: severe squall lines in Oklahoma during the spring. **Journal of the Atmospheric Sciences**, v. 42, n. 16, p. 1711–1732, 1985. 26, 27

BOUTTIER, F.; COURTIER, P. Data assimilation concepts and methods March 1999. **Meteorological Training Course Lecture Series. ECMWF**, v. 718, p. 59, 2002. 9, 10, 13

BROUSSEAU, P.; BERRE, L.; BOUTTIER, F.; DESROZIERS, G. Background-error covariances for a convective-scale data-assimilation system: AROME–France 3D-Var. **Quarterly Journal of the Royal Meteorological Society**, v. 137, n. 655, p. 409–422, 2011. ISSN 1477-870X. Available from: <http://dx.doi.org/10.1002/qj.750>. 19

_____. Flow-dependent background-error covariances for a convective-scale data assimilation system. **Quarterly Journal of the Royal Meteorological Society**, v. 138, n. 663, p. 310–322, 2012. Available from: <https://rmets.onlinelibrary.wiley.com/doi/abs/10.1002/qj.920>. 3, 19

BROWN, B.; JENSEN, T.; GOTWAY, J. H.; BULLOCK, R.; GILLELAND, E.; FOWLER, T.; NEWMAN, K.; ADRIAANSEN, D.; BLANK, L.; BUREK, T.; HARROLD, M.; HERTNEKY, T.; KALB, C.; KUCERA, P.; NANCE, L.; OPATZ, J.; VIGH, J.; WOLFF, J. The Model Evaluation Tools (MET): more than a decade of community-supported forecast verification. **Bulletin of the American Meteorological Society**, v. 102, n. 4, p. E782 – E807, 2021. Available from: <https://journals.ametsoc.org/view/journals/bams/102/4/BAMS-D-19-0093.1.xml>. 5, 37

BUARQUE, D. C.; PAIVA, R. C. D. de; CLARKE, R. T.; MENDES, C. A. B. A comparison of Amazon rainfall characteristics derived from TRMM, CMORPH and the Brazilian national rain gauge network. **Journal of Geophysical Research: Atmospheres**, v. 116, n. D19, 2011. Available from: <https://agupubs.onlinelibrary.wiley.com/doi/abs/10.1029/2011JD016060>. 103

BUEHNER, M. Ensemble-derived stationary and flow-dependent background-error covariances: evaluation in a quasi-operational NWP setting. **Quarterly Journal of the Royal Meteorological Society**, v. 131, p. 1013–1043, 2005. Available from: <https://doi.org/10.1256/qj.04.15>. 17

CAMPOS, T. L. d. O. B. **O potencial do PWV-GPS em predizer tempestades: estudo de caso de linhas de instabilidade**. 125 p. Tese

(Doutorado em Meteorologia) — Instituto Nacional de Pesquisas Espaciais (INPE), São José dos Campos, 2018. Available from: <http://urlib.net/rep/8JMKD3MGP3W34R/3RDBFNH>. 4, 25

CARLEY, J. R.; MATTHEWS, M.; MORRIS, M. T.; PONDECA, M. S. F. V. D.; COLAVITO, J.; YANG, R. Variational assimilation of web camera-derived estimates of visibility for Alaska aviation. **Experimental Results**, v. 2, p. e14, 2021. 34

CAVALCANTI, I. F. A.; KOUSKY, V. E. Influencias da circulacao de escala sinotica na circulacao da brisa maritima na costa N-NE da America do Sul. In: CONGRESSO BRASILEIRO DE METEOROLOGIA, 2., 1982, Pelotas, RS. **Anais...** [S.l.]: SBM, 1982. p. 409–425. 27

CHANG, C.-C.; PENNY, S. G.; YANG, S.-C. Hybrid gain data assimilation using variational corrections in the subspace orthogonal to the ensemble. **Monthly Weather Review**, v. 148, n. 6, p. 2331–2350, 2020. 17

CIMSS. **CIMSS cooperative agreement annual report**. [S.l.], 2014. 302 p. Available from: <https://cimss.ssec.wisc.edu/reports/CIMSS-CA-Report_2014_Final.pdf>. 73

CLARK, P.; ROBERTS, N.; LEAN, H.; BALLARD, S. P.; CHARLTON-PEREZ, C. Convection-permitting models: a step-change in rainfall forecasting. **Meteorological Applications**, v. 23, n. 2, p. 165–181, 2016. 18, 19

COHEN, J. C. P.; SILVA-DIAS, M. A. F.; NOBRE, C. A. Environmental conditions associated with Amazonian squall lines: a case study. **Monthly Weather Review**, v. 123, n. 11, p. 3163–3174, 1995. 4, 27, 29, 30, 79, 87, 88, 89, 93, 95, 123

COHEN, J. C. P.; SILVA-DIAS, M. A. F. d.; NOBRE, C. A. Aspectos climatologicos das linhas de instabilidade na Amazonia. **Climanálise - Boletim de Monitoramento e Análise Climática**, v. 4, n. 11, p. 34–40, nov. 1989. ISSN 0103-0019. Access in: 12 nov. 2021. 29

COLEMAN, J.; LAW, K. Meteorology. In: **Reference module in earth systems and environmental sciences**. [s.n.], 2015. ISBN 978-0-12-409548-9. Available from: <https://www.sciencedirect.com/science/article/pii/B9780124095489094926>. 18, 26

CRESSMAN, G. P. An operational objective analysis system. **Monthly Weather Review**, v. 87, n. 10, p. 367 – 374, 1959. Available from: <https://journals.ametsoc.org/view/journals/mwre/87/10/1520-0493_1959_087_0367_aooas_2_0_co_2.xml>. 8

CUCURULL, L.; DERBER, J. C.; PURSER, R. J. A bending angle forward operator for global positioning system radio occultation measurements. **Journal of Geophysical Research-Atmospheres**, v. 118, n. 1, p. 14–28, 2013. ISSN 2169897X. Available from: <<GotoISI>://WOS:000317834900002>. 25

DALEY, R. **Atmospheric data analysis**. [S.l.: s.n.], 1991. ISBN 0-521-38215-7. 9, 13

DAVIS, C. A.; BROWN, B. G.; BULLOCK, R.; HALLEY-GOTWAY, J. The Method for Object-Based Diagnostic Evaluation (MODE) applied to numerical forecasts from the 2005 NSSL/SPC Spring Program. **Weather and Forecasting**, v. 24, n. 5, p. 1252 – 1267, 2009. Available from: <https://journals.ametsoc.org/view/journals/wefo/24/5/2009waf2222241_1.xml>. 37

DERBER, J.; ROSATI, A. A global oceanic data assimilation system. **Journal of Physical Oceanography**, v. 19, n. 9, p. 1333–1347, 1989. 11

DIXON, M.; LI, Z.; LEAN, H.; ROBERTS, N.; BALLARD, S. Impact of data assimilation on forecasting convection over the United Kingdom using a high-resolution version of the Met Office Unified Model. **Monthly Weather Review**, v. 137, n. 5, p. 1562–1584, 2009. Available from: <https://journals.ametsoc.org/view/journals/mwre/137/5/2008mwr2561.1.xml>. 3

DONG, J.; LIU, B.; ZHANG, Z.; WANG, W.; MEHRA, A.; HAZELTON, A. T.; WINTERBOTTOM, H. R.; ZHU, L.; WU, K.; ZHANG, C.; TALLAPRAGADA, V.; ZHANG, X.; GOPALAKRISHNAN, S.; MARKS, F. The evaluation of real-time hurricane analysis and forecast system (HAFS) stand-alone regional (SAR) model performance for the 2019 Atlantic hurricane season. **Atmosphere**, v. 11, n. 6, 2020. ISSN 2073-4433. Available from: <https://www.mdpi.com/2073-4433/11/6/617>. 2

DONG, L.; LEUNG, L. R.; LU, J.; SONG, F. Double-ITCZ as an emergent constraint for future precipitation over Mediterranean climate regions in the North Hemisphere. **Geophysical Research Letters**, v. 48, n. 3, p. e2020GL091569,

2021. E2020GL091569 2020GL091569. Available from: <https://agupubs.onlinelibrary.wiley.com/doi/abs/10.1029/2020GL091569>. 4

DURáN-QUESADA, A.; REBOITA, M.; GIMENO, L. Precipitation in tropical America and the associated sources of moisture: a short review. **Hydrological Sciences Journal**, v. 57, n. 4, p. 612–624, 2012. Available from: <https://doi.org/10.1080/02626667.2012.673723>. 4

EMC. **Strategic implementation plan for evolution of NGGPS to a national Unified Modeling System (First Annual Update)**. [S.l.], 2018. 171 p. Available from: <https://www.weather.gov/media/sti/nggps/UFS%20SIP%20FY19-21_20181129.pdf>. 39

ETHERTON, B. J.; BISHOP, C. H. Resilience of hybrid ensemble/3DVAR analysis schemes to model error and ensemble covariance error. **Monthly Weather Review**, v. 132, n. 5, p. 1065–1080, 2004. 16

EUROPEAN CENTRE FOR MEDIUM-RANGE WEATHER FORECASTS. **ERA5 Reanalysis (0.25 Degree Latitude-Longitude Grid)**. Boulder CO: Research Data Archive at the National Center for Atmospheric Research, Computational and Information Systems Laboratory, 2019. Available from: <https://doi.org/10.5065/BH6N-5N20>. 95

EVENSEN, G. Sequential data assimilation with a nonlinear quasi-geostrophic model using Monte Carlo methods to forecast error statistics. **Journal of Geophysical Research: Oceans**, v. 99, n. C5, p. 10143–10162, 1994. 13

FERREIRA, R. C.; HERDIES, D. L.; VENDRASCO, É. P.; BENETI, C. A. A.; BISCARO, T. S. Impacto da assimilação de dados de radar em sistemas convectivos de mesoescala: um estudo de caso. **Revista Brasileira de Meteorologia**, v. 32, p. 447–458, 2017. 25

FERTIG, E.; BAEK, S.-J.; HUNT, B.; OTT, E.; SZUNYOGH, I.; ARAVéQUIA, J.; KALNAY, E.; LI, H.; LIU, J. Observation bias correction with an ensemble Kalman filter. **Tellus A: Dynamic Meteorology and Oceanography**, v. 61, n. 2, p. 210–226, 2009. Available from: <https://doi.org/10.1111/j.1600-0870.2008.00378.x>. 23

FIGUEROA, S. N.; BONATTI, J. P.; KUBOTA, P. Y.; GRELL, G. A.; MORRISON, H.; BARROS, S. R. M.; FERNANDEZ, J. P. R.; RAMIREZ, E.;

SIQUEIRA, L.; LUZIA, G.; SILVA, J.; SILVA, J. R.; PENDHARKAR, J.; CAPISTRANO, V. B.; ALVIM, D. S.; ENORé, D. P.; DINIZ, F. L. R.; SATYAMURTI, P.; CAVALCANTI, I. F. A.; NOBRE, P.; BARBOSA, H. M. J.; MENDES, C. L.; PANETTA, J. The Brazilian Global Atmospheric Model (BAM): Performance for tropical rainfall forecasting and sensitivity to convective scheme and horizontal resolution. **Weather and Forecasting**, v. 31, n. 5, p. 1547 – 1572, 2016. Available from: <https://journals.ametsoc.org/view/journals/wefo/31/5/waf-d-16-0062_1.xml>. 24

GALLO, B. T. et al. Exploring convection-allowing model evaluation strategies for severe local storms using the finite-volume cubed-sphere (FV3) model core. **Weather and Forecasting**, v. 36, n. 1, p. 3–19, 2021. 2

GAMACHE, J. F.; JR, R. A. H. Mesoscale air motions associated with a tropical squall line. **Monthly Weather Review**, v. 110, n. 2, p. 118–135, 1982. 29

GANDIN, L. Objective Analysis of Meteorological Fields; Translated from the Russian. Jerusalem (Israel Program for Scientific Translations). **Quarterly Journal of the Royal Meteorological Society**, v. 92, p. 242p, 1965. 8

GAO, S.; DU, N.; MIN, J.; YU, H. Impact of assimilating radar data using a hybrid 4DEnVar approach on prediction of convective events. **Tellus A: Dynamic Meteorology and Oceanography**, v. 73, n. 1, p. 1–19, 2021. 3, 21

GARSTANG, M.; JR, H. L. M.; HALVERSON, J.; GRECO, S.; SCALA, J. Amazon coastal squall lines. Part I: structure and kinematics. **Monthly Weather Review**, v. 122, n. 4, p. 608–622, 1994. 4, 28, 79, 91

GARSTANG, M.; ULANSKI, S.; GRECO, S.; SCALA, J.; SWAP, R.; FITZJARRALD, D.; MARTIN, D.; BROWELL, E.; SHIPMAN, M.; CONNORS, V.; HARRISS, R.; TALBOT, R. The Amazon Boundary-Layer Experiment (ABLE 2B): a meteorological perspective. **Bulletin of the American Meteorological Society**, v. 71, n. 1, p. 19 – 32, 1990. Available from: <https://journals.ametsoc.org/view/journals/bams/71/1/1520-0477_1990_071_0019_tablea_2_0_co_2.xml>. 27, 79

GASPARI, G.; COHN, S. E. Construction of correlation functions in two and three dimensions. **Quarterly Journal of the Royal Meteorological Society**, v. 125, n. 554, p. 723–757, 1999. 14, 15

GEER, A.; BAORDO, F.; BORMANN, N.; CHAMBON, P.; ENGLISH, S.; KAZUMORI, M.; LAWRENCE, H.; LEAN, P.; LONITZ, K.; LUPU, C. The growing impact of satellite observations sensitive to humidity, cloud and precipitation. **Quarterly Journal of the Royal Meteorological Society**, v. 143, n. 709, p. 3189–3206, 2017. 22

GEER, A. J. et al. All-sky satellite data assimilation at operational weather forecasting centres. **Quarterly Journal of the Royal Meteorological Society**, v. 144, n. 713, p. 1191–1217, 2018. 22

GERMANO, M. F.; OYAMA, M. D. Local circulation features in the eastern Amazon: high-resolution simulation. **Journal of Aerospace Technology and Management**, v. 12, 2020. Available from: <https://www.scielo.br/j/jatm/a/rLfppf3KcvcmkCzWrSSdCcy/?format=pdf&lang=en>. 4, 18

GHATE, V. P.; KOLLIAS, P. On the controls of daytime precipitation in the Amazonian dry season. **Journal of Hydrometeorology**, v. 17, n. 12, p. 3079 – 3097, 2016. Available from: <https://journals.ametsoc.org/view/journals/hydr/17/12/jhm-d-16-0101_1.xml>. 30

GHIL, M.; MALANOTTE-RIZZOLI, P. Data assimilation in meteorology and oceanography. **Advances in Geophysics**, v. 33, p. 141–266, 1991. 12

GILCHRIST, B.; CRESSMAN, G. P. An experiment in objective analysis. **Tellus**, v. 6, n. 4, p. 309–318, 1954. Available from: <https://onlinelibrary.wiley.com/doi/abs/10.1111/j.2153-3490.1954.tb01126.x>. 8

GRECO, S.; SCALA, J.; HALVERSON, J.; JR, H. L. M.; TAO, W.-K.; GARSTANG, M. Amazon coastal squall lines. Part II: heat and moisture transports. **Monthly Weather Review**, v. 122, n. 4, p. 623–635, 1994. 27, 29

GRECO, S.; SWAP, R.; GARSTANG, M.; ULANSKI, S.; SHIPHAM, M.; HARRISS, R.; TALBOT, R.; ANDREAE, M.; ARTAXO, P. Rainfall and surface kinematic conditions over central Amazonia during ABLE 2B. **Journal of Geophysical Research: Atmospheres**, v. 95, n. D10, p. 17001–17014, 1990. 4, 27, 28

GRIMM, A. M.; DIAS, P. L. S. Analysis of tropical–extratropical interactions with influence functions of a barotropic model. **Journal of Atmospheric Sciences**, v. 52, n. 20, p. 3538 – 3555, 1995. Available from: <https://journals.ametsoc.org/view/journals/atsc/52/20/1520-0469_1995_052_3538_aotiwi_2_0_co_2.xml>. 4

GUSTAFSSON, N.; HUANG, X.-Y.; YANG, X.; MOGENSEN, K.; LINDSKOG, M.; VIGNES, O.; WILHELMSSON, T.; THORSTEINSSON, S. Four-dimensional variational data assimilation for a limited area model. **Tellus A: Dynamic Meteorology and Oceanography**, v. 64, n. 1, p. 14985, 2012. 19

GUSTAFSSON, N.; JANJI, T.; SCHRAFF, C.; LEUENBERGER, D.; WEISSMAN, M.; REICH, H.; BROUSSEAU, P.; MONTMERLE, T.; WATTRELOT, E.; BUČÁNEK, A.; MILE, M.; HAMDI, R.; LINDSKOG, M.; BARKMEIJER, J.; DAHLBOM, M.; MACPHERSON, B.; BALLARD, S.; INVERARITY, G.; CARLEY, J.; ALEXANDER, C.; DOWELL, D.; LIU, S.; IKUTA, Y.; FUJITA, T. Survey of data assimilation methods for convective-scale numerical weather prediction at operational centres. **Quarterly Journal of the Royal Meteorological Society**, v. 144, p. 1218–1256, 2018. Available from: <https://doi.org/10.1002/qj.3179>. 2, 12, 18, 23, 51, 68

HA, J. H.; LIM, G. H.; CHOI, S. J. Assimilation of GPS radio occultation refractivity data with WRF 3DVAR and its impact on the prediction of a heavy rainfall event. **Journal of Applied Meteorology and Climatology**, v. 53, n. 6, p. 1381–1398, 2014. 23

HAAN, S. D.; STOFFELEN, A. Assimilation of high-resolution Mode-S wind and temperature observations in a regional NWP model for nowcasting applications. **Weather and Forecasting**, v. 27, n. 4, p. 918–937, 2012. 21

HAMILL, T. M.; SNYDER, C. A hybrid ensemble Kalman filter–3D variational analysis scheme. **Monthly Weather Review**, v. 128, n. 8, p. 2905–2919, 2000. 13, 14, 15, 16, 102

HAMILL, T. M.; WHITAKER, J. S. Accounting for the error due to unresolved scales in ensemble data assimilation: a comparison of different approaches. **Monthly Weather Review**, v. 133, n. 11, p. 3132–3147, 2005. 14

HAMILL, T. M.; WHITAKER, J. S.; SNYDER, C. Distance-dependent filtering of background error covariance estimates in an ensemble Kalman filter. **Monthly Weather Review**, v. 129, n. 11, p. 2776–2790, 2001. ISSN 1520-0493. Available from: <https://journals.ametsoc.org/view/journals/mwre/129/11/1520-0493_2001_129_2776_ddfobe_2.0.co_2.xml>. 13, 14, 51

HARRIS, L.; CHEN, X.; ZHOU, L.; CHEN, J.-H. The nonhydrostatic solver of the GFDL finite-volume cubed-sphere dynamical core. **NOAA Technical**

Memorandum OAR GFDL, v. 2020-003, 2020. Available from: <https://repository.library.noaa.gov/view/noaa/27489>. 31

HARRIS, L. et al. GFDL SHiELD: a unified system for weather-to-seasonal prediction. **Journal of Advances in Modeling Earth Systems**, v. 12, n. 10, p. e2020MS002223, 2020. 1

HARRIS, L. M.; LIN, S.-J. A two-way nested global-regional dynamical core on the cubed-sphere grid. **Monthly Weather Review**, v. 141, n. 1, p. 283–306, 2013. Available from: <https://journals.ametsoc.org/view/journals/mwre/141/1/mwr-d-11-00201.1.xml>. 1, 31

HARRIS, L. M.; LIN, S.-J.; TU, C. High-resolution climate simulations using GFDL HiRAM with a stretched global grid. **Journal of Climate**, v. 29, n. 11, p. 4293–4314, 2016. ISSN 0894-8755. Available from: <https://doi.org/10.1175/JCLI-D-15-0389.1>. 31

HARROLD, M.; HERTNEKY, T.; KALINA, E.; NEWMAN, K.; KETEFIAN, G.; GRELL, E. D.; LYBARGER, N. D.; NELSON, B. Investigating the scalability of convective and microphysics parameterizations in the Unified Forecast System Short-Range Weather (UFS-SRW) application. In: AMERICAN METEOROLOGICAL SOCIETY ANNUAL MEETING, 101., 2021. **Proceedings...** [S.l.]: AMS, 2021. 3, 40

HAZELEGER, W. et al. EC-Earth: a seamless earth-system prediction approach in action. **Bulletin of the American Meteorological Society**, v. 91, n. 10, p. 1357–1364, 2010. Available from: <https://journals.ametsoc.org/view/journals/bams/91/10/2010bams2877_1.xml>. 1

HEINZELLER, D.; BERNARDET, L.; FIRL, G.; CARSON, L.; SCHRAMM, J.; ZHANG, M.; DUDHIA, J.; GILL, D.; DUDA, M.; GOLDHABER, S.; CRAIG, C.; VITT, F.; VERTENSTEIN, M. The Common Community Physics Package CCPP: unifying physics across NOAA and NCAR models using a common software framework. In: EGU GENERAL ASSEMBLY CONFERENCE, 2019. **Abstracts...** EGU, 2019. Available from: <https://ui.adsabs.harvard.edu/abs/2019{EGU}GA..21..223H>. 32

HERDIES, D. L.; ARAVéQUIA, J. A.; FERREIRA, S. H. S.; ANDREOLI, R. V.; SAPUCCI, L. F. A assimilação de dados no CPTEC/INPE. **Boletim da Sociedade Brasileira de Meteorologia**, v. 32, n. 1, p. 57–64, 2008. Abril. 23

HOCKER, J. E.; BASARA, J. B. A 10-year spatial climatology of squall line storms across Oklahoma. **International Journal of Climatology: A Journal of the Royal Meteorological Society**, v. 28, n. 6, p. 765–775, 2008. 26

HOFFMAN, R. N. The effect of thinning and superobservations in a simple one-dimensional data analysis with mischaracterized error. **Monthly Weather Review**, v. 146, n. 4, p. 1181–1195, 2018. 22

HOLM, E.; ANDERSSON, E.; BELJAARS, A.; LOPEZ, P.; MAHFOUF, J.-F.; SIMMONS, A.; THEPAUT, J.-N. Assimilation and modelling of the hydrologic cycle: ECMWF's status and plans. **ECMWF Technical Memoranda**, v. 383, p. 55, 2002. 33

HOUTEKAMER, P. L.; MITCHELL, H. L. Data assimilation using an ensemble Kalman filter technique. **Monthly Weather Review**, v. 126, n. 3, p. 796–811, 1998. 15

_____. A sequential ensemble Kalman filter for atmospheric data assimilation. **Monthly Weather Review**, v. 129, n. 1, p. 123–137, 2001. ISSN 1520-0493. 14, 51

HU, M.; BENJAMIN, S. G.; LADWIG, T. T.; DOWELL, D. C.; WEYGANDT, S. S.; ALEXANDER, C. R.; WHITAKER, J. S. GSI three-dimensional ensemble–variational hybrid data assimilation using a global ensemble for the regional Rapid Refresh model. **Monthly Weather Review**, v. 145, n. 10, p. 4205–4225, 2017. Available from: <https://journals.ametsoc.org/view/journals/mwre/145/10/mwr-d-16-0418.1.xml>. 3, 34, 43, 46, 47, 48, 51, 52, 68, 102

HU, M.; GE, G.; CHUNHUA, Z.; STARK, D.; SHAO, H.; NEWMAN, K.; BECK, J.; ZHANG, X. **Grid-point Statistical Interpolation (GSI) user's guide version 3.7**. [S.l.], 2018. 149 p. Available from: <https://dtcenter.org/sites/default/files/GSIUserGuide_v3.7_0.pdf>. 54

HU, M.; LI, R.; TRAHAN, S.; HOLT, C.; WEYGANDT, S.; ALEXANDER, C. R. Initial development testing and evaluation of the RAP/HRRR similar data assimilation functions for FV3 LAM-based RRFS. In: AMERICAN METEOROLOGICAL SOCIETY ANNUAL MEETING, 101., 2021. **Proceedings...** [S.l.]: AMS, 2021. 34

HU, M.; XUE, M.; BREWSTER, K. 3DVAR and cloud analysis with WSR-88D level-ii data for the prediction of the Fort Worth, Texas, tornadic thunderstorms. Part I: cloud analysis and its impact. **Monthly Weather Review**, v. 134, n. 2, p. 675–698, 2006. ISSN 0027-0644. Available from: <https://journals.ametsoc.org/view/journals/mwre/134/2/mwr3092.1.xml>. 20

HU, M.; XUE, M.; GAO, J.; BREWSTER, K. 3DVAR and cloud analysis with WSR-88D level-ii data for the prediction of the Fort Worth, texas, tornadic thunderstorms. Part II: impact of radial velocity analysis via 3dvar. **Monthly Weather Review**, v. 134, n. 2, p. 699–721, 2006. ISSN 0027-0644. Available from: <https://journals.ametsoc.org/view/journals/mwre/134/2/mwr3093.1.xml>. 20

HUANG, B.; WANG, X.; KLEIST, D. T.; LEI, T. A simultaneous multiscale data assimilation using scale-dependent localization in GSI-based hybrid 4DEnVar for NCEP FV3-based GFS. **Monthly Weather Review**, v. 149, n. 2, p. 479 – 501, 2021. Available from: <https://journals.ametsoc.org/view/journals/mwre/149/2/MWR-D-20-0166.1.xml>. 34

HUANG, C. Y.; KUO, Y. H.; CHEN, S. Y.; TERNG, C. T.; CHIEN, F. C.; LIN, P. L.; KUEH, M. T.; CHEN, S. H.; YANG, M. J.; WANG, C. J.; RAO, A. S. P. Impact of GPS radio occultation data assimilation on regional weather predictions. **GPS Solutions**, v. 14, n. 1, p. 35–49, 2009. ISSN 10805370. 23

HUBERT, L. F.; KRUEGER, A. F.; WINSTON, J. S. The double Intertropical Convergence Zone–Fact or fiction? **Journal of Atmospheric Sciences**, v. 26, n. 4, p. 771 – 773, 1969. Available from: <https://journals.ametsoc.org/view/journals/atsc/26/4/1520-0469_1969_026_0771_tdiczf_2_0_co_2.xml>. 4

HUFFMAN, G. J.; BOLVIN, D. T.; BRAITHWAITE, D.; HSU, K.; JOYCE, R.; KIDD, C.; NELKIN, E. J.; XIE, P. **NASA Global Precipitation Measurement (GPM) Integrated Multi-satellitE Retrievals for GPM (IMERG). Algorithm theoretical basis doc., version 4.5**. [S.l.], 2015a. 26 p. Available from: <http://pmm.nasa.gov/sites/default/files/document_files/IMERG_ATBD_V4.5.pdf>. 81

HUFFMAN, G. J.; BOLVIN, D. T.; NELKIN, E. J. **Day 1 IMERG final run release notes. NASA Doc.** [S.l.], 2015b. 9 p. Available from: <http://pmm.nasa.gov/sites/default/files/document_files/IMERG_FinalRun_Day1_release_notes.pdf>. 81

_____. **Integrated Multi-satellitE Retrievals for GPM (IMERG) technical documentation. NASA Doc.** [S.l.], 2015b. 47 p. Available from: <http://pmm.nasa.gov/sites/default/files/document_files/IMERG_doc.pdf>. 81

HUNT, B. R.; KOSTELICH, E. J.; SZUNYOGH, I. Efficient data assimilation for spatiotemporal chaos: a local ensemble transform Kalman filter. **Physica D: Nonlinear Phenomena**, v. 230, n. 1-2, p. 112–126, 2007. 17

HWANG, Y.-T.; FRIERSON, D. M. Link between the double-Intertropical Convergence Zone problem and cloud biases over the Southern Ocean. **Proceedings of the National Academy of Sciences**, v. 110, n. 13, p. 4935–4940, 2013. 4

IACONO, M. J.; DELAMERE, J. S.; MLAWER, E. J.; SHEPHARD, M. W.; CLOUGH, S. A.; COLLINS, W. D. Radiative forcing by long-lived greenhouse gases: calculations with the AER radiative transfer models. **Journal of Geophysical Research: Atmospheres**, v. 113, n. D13, 2008. Available from: <https://agupubs.onlinelibrary.wiley.com/doi/full/10.1029/2008JD009944>. 32

ITTERLY, K. F.; TAYLOR, P. C.; DODSON, J. B. Sensitivity of the Amazonian convective diurnal cycle to its environment in observations and reanalysis. **Journal of Geophysical Research: Atmospheres**, v. 123, n. 22, p. 12,621–12,646, 2018. Available from: <https://agupubs.onlinelibrary.wiley.com/doi/abs/10.1029/2018JD029251>. 4

JANJIć, Z. I.; GERRITY, J. P.; NICKOVIC, S. An alternative approach to nonhydrostatic modeling. **Monthly Weather Review**, v. 129, p. 1164–1178, 2001. Available from: <https://doi.org/10.1175/1520-0493(2001)129%3C1164:Aaatnm%3E2.0.Co;2>. 31, 39

JANJIĆ, T.; MCLAUGHLIN, D.; COHN, S. E.; VERLAAN, M. Conservation of mass and preservation of positivity with ensemble-type Kalman filter algorithms. **Monthly Weather Review**, v. 142, n. 2, p. 755–773, 2014. Available from: <https://journals.ametsoc.org/view/journals/mwre/142/2/mwr-d-13-00056.1.xml>. 52, 76

JANJIĆ, T.; RUCKSTUHL, Y.; TOINT, P. L. A data assimilation algorithm for predicting rain. **Quarterly Journal of the Royal Meteorological Society**, v. 147, n. 736, p. 1949–1963, 2021. 76

JENSEN, T.; BROWN, B.; BULLOCK, R.; FOWLER, T.; GOTWAY, J. H.; NEWMAN, K. **The Model Evaluation Tools v9.0 (METv9.0) user's guide.** [S.l.], 2020. Available from: <https://dtcenter.org/sites/default/les/community-code/met/docs/user-guide/MET_Users_Guide_v9.0.pdf>. 37, 77

JI, M.; TOEPFER, F. **Dynamical core evaluation test report for NOAA's Next Generation Global Prediction System (NGGPS)**. [S.l.], 2016. 93 p. Available from: <https://repository.library.noaa.gov/view/noaa/18653>. 1

KALINA, E.; GRELL, E. D.; HARROLD, M.; HERTNEKY, T.; NEWMAN, K. Evaluating hydrometeor type and amount in the Unified Forecast System. In: AMERICAN METEOROLOGICAL SOCIETY ANNUAL MEETING, 101., 2021. **Proceedings...** [S.l.], 2021. 3, 40

KALMAN, R. E. A new approach to linear filtering and prediction problems. **Journal of Basic Engineering**, n. March, p. 35–45, 1960. 12

Kalman, R. E.; BUCY, R. S. New results in linear filtering and prediction theory. **Journal of Basic Engineering**, v. 83, p. 95–108, 1961. 12

KALNAY, E. **Atmospheric modeling, data assimilation and predictability**. [S.l.]: Cambridge University Press, 2003. 2, 9, 11, 12

KELLER, M.; SILVA-DIAS, M. A.; NEPSTAD, D. C.; ANDREAE, M. O. The Large-Scale Biosphere-Atmosphere Experiment in Amazonia: analyzing regional land use change effects. In: **Ecosystems and Land Use Change**. American Geophysical Union, 2004. p. 321–334. Geophysical Monograph Series 153. Available from: <https://www.fs.usda.gov/treesearch/pubs/30201>. 20, 79

KHAIROUTDINOV, M.; RANDALL, D. High-resolution simulation of shallow-to-deep convection transition over land. **Journal of the Atmospheric Sciences**, v. 63, n. 12, p. 3421 – 3436, 2006. Available from: <https://journals.ametsoc.org/view/journals/atsc/63/12/jas3810.1.xml>. 4

KLEIST, D. T.; IDE, K. An OSSE-based evaluation of hybrid variational-ensemble data assimilation for the NCEP GFS. Part I: system description and 3D-hybrid results. **Monthly Weather Review**, v. 143, n. 2, p. 433–451, 2015. ISSN 15200493. Available from: <https://journals.ametsoc.org/view/journals/mwre/143/2/mwr-d-13-00351.1.xml>. 18, 33, 34

_____. An OSSE-based evaluation of hybrid variational–ensemble data assimilation for the NCEP GFS. Part II: 4DEnVar and hybrid variants. **Monthly Weather Review**, v. 143, n. 2, p. 452–470, 2015. ISSN 0027-0644. Available from: <https://doi.org/10.1175/MWR-D-13-00350.1>. 34

KLEIST, D. T.; PARRISH, D. F.; DERBER, J. C.; TREADON, R.; WU, W.-S.; LORD, S. Introduction of the GSI into the NCEP global data assimilation system. **Weather and Forecasting**, v. 24, n. 6, p. 1691–1705, 2009. Available from: <https://journals.ametsoc.org/view/journals/wefo/24/6/2009waf2222201_1.xml>. 3, 33, 35, 45, 46

KOTSUKI, S.; OTA, Y.; MIYOSHI, T. Adaptive covariance relaxation methods for ensemble data assimilation: experiments in the real atmosphere. **Quarterly Journal of the Royal Meteorological Society**, v. 143, n. 705, p. 2001–2015, 2017. Available from: <https://rmets.onlinelibrary.wiley.com/doi/abs/10.1002/qj.3060>. 14

KOUSKY, V. E. Diurnal rainfall variation in northeast Brazil. **Monthly Weather Review**, v. 108, n. 4, p. 488–498, 1980. 27

LADSTÄDTER, F.; STEINER, A. K.; SCHWÄRZ, M.; KIRCHENGAST, G. Climate intercomparison of GPS radio occultation, RS90/92 radiosondes and GRUAN from 2002 to 2013. **Atmospheric Measurement Techniques**, v. 8, n. 4, p. 1819–1834, 2015. ISSN 18678548. 23

LEAN, H. W.; CLARK, P. A.; DIXON, M.; ROBERTS, N. M.; FITCH, A.; FORBES, R.; HALLIWELL, C. Characteristics of high-resolution versions of the Met Office Unified Model for forecasting convection over the United Kingdom. **Monthly Weather Review**, v. 136, n. 9, p. 3408–3424, 2008. 1, 18

LI, X.; DERBER, J.; MOORTHI, S. An atmosphere-ocean partially coupled data assimilation and prediction system developed within the NCEP GFS/CFS. In: EGU GENERAL ASSEMBLY CONFERENCE, 2015. **Abstracts...** [S.l.]: EGU, 2015. 32

LIEBMANN, B.; SMITH, C. A. Description of a complete (interpolated) outgoing longwave radiation dataset. **Bulletin of the American Meteorological Society**, v. 77, p. 1275–1277, 1996. 81

LILLY, D. K. Numerical prediction of thunderstorms–has its time come? **Quarterly Journal of the Royal Meteorological Society**, v. 116, n. 494, p. 779–798, 1990. 18

LIN, S.-J. A finite-volume integration method for computing pressure gradient force in general vertical coordinates. **Quarterly Journal of the Royal Meteorological Society**, v. 123, n. 542, p. 1749–1762, 1997. ISSN 0035-9009. Available from: <https://doi.org/10.1002/qj.49712354214>. 31

_____. A "vertically lagrangian" finite-volume dynamical core for global models. **Monthly Weather Review**, v. 132, n. 10, p. 2293–2307, 2004. ISSN 0027-0644. Available from: <https://doi.org/10.1175/1520-0493(2004)132<2293:AVLFDC>2.0.CO;2>. 1, 31

LIN, S.-J.; ROOD, R. B. Multidimensional flux-form semi-lagrangian transport schemes. **Monthly Weather Review**, v. 124, n. 9, p. 2046–2070, 1996. ISSN 0027-0644. Available from: <https://doi.org/10.1175/1520-0493(1996)124<2046:MFFSLT>2.0.CO;2>. 31

_____. An explicit flux-form semi-lagrangian shallow-water model on the sphere. **Quarterly Journal of the Royal Meteorological Society**, v. 123, n. 544, p. 2477–2498, 1997. ISSN 0035-9009. Available from: <https://rmets.onlinelibrary.wiley.com/doi/abs/10.1002/qj.49712354416>. 31

LIN, Y.; MITCHELL, K. E. The NCEP stage II/IV hourly precipitation analyses: Development and applications. In: CONFERENCE ON HYDROLOGY, 19., 2005. **Proceedings...** AMS, 2005. Available from: <http://ams.confex.com/ams/pdfpapers/83847.pdf>. 55

LINK, J. S.; TOLMAN, H. L.; BAYLER, E.; HOLT, C.; BROWN, C. W.; BURKE, P. B.; CARMAN, J. C.; CROSS, S. L.; DUNNE, J. P.; LIPTON, D. W.; MARIOTTI, A.; METHOT, R. D.; MYERS, E. P.; SCHNEIDER, T. L.; GRASSO, M.; ROBINSON, K. **High-level NOAA unified modeling overview**. 2017. Available from: <https://repository.library.noaa.gov/view/noaa/14156>. 1, 39

LOEHRER, S. M.; JOHNSON, R. H. Surface pressure and precipitation life cycle characteristics of PRE-STORM mesoscale convective systems. **Monthly Weather Review**, v. 123, n. 3, p. 600–621, 1995. 26, 27

LONG, P. E. **An economical and compatible scheme for parameterizing the stable surface layer in the medium range forecast model**. 1986. Miscellaneous. Available from: <https://repository.library.noaa.gov/view/noaa/11489>. 32

LORENC, A. C. Analysis methods for numerical weather prediction. **Quarterly Journal of the Royal Meteorological Society**, v. 112, n. 474, p. 1177–1194, 1986. 9, 12

_____. Development of an operational variational assimilation scheme (data assimilation in meteorology and oceanography: Theory and practice). **Journal of the Meteorological Society of Japan. Serie II**, v. 75, n. 1B, p. 339–346, 1997. 11

_____. The potential of the ensemble Kalman filter for NWP—A comparison with 4D-Var. **Quarterly Journal of the Royal Meteorological Society: A journal of the Atmospheric Sciences, Applied Meteorology and Physical Oceanography**, v. 129, n. 595, p. 3183–3203, 2003. ISSN 0035-9009. 17, 34

LORENC, A. C.; BALLARD, S. P.; BELL, R. S.; INGLEBY, N. B.; ANDREWS, P. L. F.; BARKER, D. M.; BRAY, J. R.; CLAYTON, A. M.; DALBY, T.; LI, D.; PAYNE, T. J.; SAUNDERS, F. W. The Met. Office global three-dimensional variational data assimilation scheme. **Quarterly Journal of the Royal Meteorological Society**, v. 126, n. 570, p. 2991–3012, 2000. Available from: <https://rmets.onlinelibrary.wiley.com/doi/abs/10.1002/qj.49712657002>. 12

LORENZ, E. N. Deterministic nonperiodic flow. **Journal of Atmospheric Sciences**, v. 20, n. 2, p. 130–141, 1963. 7

MACHADO, L. A. T.; SILVA-DIAS, M. A. F.; MORALES, C.; FISCH, G.; VILA, D.; ALBRECHT, R.; GOODMAN, S. J.; CALHEIROS, A. J. P.; BISCARO, T.; KUMMEROW, C.; COHEN, J.; FITZJARRALD, D.; NASCIMENTO, E. L.; SAKAMOTO, M. S.; CUNNINGHAM, C.; CHABOUREAU, J.-P.; PETERSEN, W. A.; ADAMS, D. K.; BALDINI, L.; ANGELIS, C. F.; SAPUCCI, L. F.; SALIO, P.; BARBOSA, H. M. J.; LANDULFO, E.; SOUZA, R. A. F.; BLAKESLEE, R. J.; BAILEY, J.; FREITAS, S.; LIMA, W. F. A.; TOKAY, A. The Chuva project: How does convection vary across Brazil? **Bulletin of the American Meteorological Society**, v. 95, n. 9, p. 1365 – 1380, 2014. Available from: <https://journals.ametsoc.org/view/journals/bams/95/9/bams-d-13-00084.1.xml>. 4

MARENGO, J. A.; LIEBMANN, B.; KOUSKY, V. E.; FILIZOLA-JUNIOR, N. P.; WAINER, I. C. Onset and end of the rainy season in the brazilian Amazon Basin. **Journal of Climate**, v. 14, n. 5, 2001. 81, 82, 83, 122

MARTIN, S. T.; ARTAXO, P.; MACHADO, L. A.; MANZI, A. O.; SOUZA, R. A.; SCHUMACHER, C.; WANG, J.; ANDREAE, M. O.; BARBOSA, H. M.; FAN, J.; FISCH, G.; GOLDSTEIN, A. H.; GUENTHER, A.; JIMENEZ, J. L.; PÖSCHL, U.; SILVA-DIAS, M. A.; SMITH, J. N.; WENDISCH, M. Introduction: bservations and modeling of the Green Ocean Amazon (GoAmazon2014/5). **Atmospheric Chemistry and Physics**, v. 16, n. 8, p. 4785–4797, 2016. ISSN 16807324. 26, 79

MCCAUL, E. W.; WEISMAN, M. L. The sensitivity of simulated supercell structure and intensity to variations in the shapes of environmental buoyancy and shear profiles. **Monthly Weather Review**, v. 129, n. 4, p. 664 – 687, 2001. Available from: <https://journals.ametsoc.org/view/journals/mwre/129/4/1520-0493_2001_129_0664_tsosss_2.0.co_2.xml>. 41

MCCORMACK, J.; HOPPEL, K.; SISKIND, D. Parameterization of middle atmospheric water vapor photochemistry for high-altitude NWP and data assimilation. **Atmospheric Chemistry and Physics**, v. 8, n. 24, p. 7519–7532, 2008. Available from: <https://acp.copernicus.org/articles/8/7519/2008/>. 33

MLAWER, E. J.; TAUBMAN, S. J.; BROWN, P. D.; IACONO, M. J.; CLOUGH, S. A. Radiative transfer for inhomogeneous atmospheres: RRTM, a validated correlated-k model for the longwave. **Journal of Geophysical Research: Atmospheres**, v. 102, n. D14, p. 16663–16682, 1997. Available from: <https://agupubs.onlinelibrary.wiley.com/doi/abs/10.1029/97JD00237>. 32

MORRIS, M. T.; CARLEY, J. R.; COLóN, E.; GIBBS, A.; PONDECA, M. S. F. V. D.; LEVINE, S. A quality assessment of the Real-Time Mesoscale Analysis (RTMA) for aviation. **Weather and Forecasting**, v. 35, n. 3, p. 977 – 996, 2020. Available from: <https://journals.ametsoc.org/view/journals/wefo/35/3/waf-d-19-0201.1.xml>. 56

NAKANISHI, M.; NIINO, H. Development of an improved turbulence closure model for the atmospheric boundary layer. **Journal of the Meteorological Society of Japan. Serie II**, v. 87, n. 5, p. 895–912, 2009. 32

NATIONAL RESEARCH COUNCIL. Synergies between weather and climate modeling. In: WADA, K.; COMBES, F. (Ed.). **A National Strategy for Advancing Climate Modeling**. Washington, DC: The National Academies Pres, 2012. 1, 39

NEWMAN, K.; GRELL, E. D.; KALINA, E.; HARROLD, M.; KETEFIAN, G.; HERTNEKY, T.; LYBARGER, N. D. Investigation of land–atmosphere interactions in the Unified Forecast System Short-Range Weather (UFS-SRW) application. In: AMERICAN METEOROLOGICAL SOCIETY ANNUAL MEETING, 101., 2021. **Proceedings...** [S.l.]: AMS, 2021. 40

NIU, G.-Y. et al. The community Noah land surface model with multiparameterization options (Noah-MP): 1. Model description and evaluation with local-scale measurements. **Journal of Geophysical Research: Atmospheres**, v. 116, n. D12, 2011. Available from: <https://agupubs.onlinelibrary.wiley.com/doi/full/10.1029/2010JD015139>. 32

NOBRE, J. P. G.; VENDRASCO, É. P.; BASTARZ, C. F. Impact of ensemble-variational data assimilation in heavy rain forecast over Brazilian Northeast. **Atmosphere**, v. 12, n. 9, 2021. ISSN 2073-4433. Available from: <https://www.mdpi.com/2073-4433/12/9/1201>. 26

NWS. **Service Change Notice 21-20 Updated: Upgrade NCEP Global Forecast Systems (GFS) to v16: effective March 22, 2021**. 2021. Available from: <https://www.weather.gov/media/notification/scn_21-20_gfsv16.0_aaa_update.pdf>. 39

OLIVEIRA, F. P. de; OYAMA, M. D. Antecedent atmospheric conditions related to squall-line initiation over the northern coast of Brazil in July. **Weather and Forecasting**, v. 30, n. 5, p. 1254 – 1264, 2015. Available from: <https://journals.ametsoc.org/view/journals/wefo/30/5/waf-d-14-00120_1.xml>. 4, 30, 80, 81, 91, 123

OLSON, J. B.; KENYON, J. S.; ANGEVINE, W. A.; BROWN, J. M.; PAGOWSKI, M.; SUŠELJ, K. **A description of the MYNN-EDMF scheme and the coupling to other components in WRF–ARW**. 2019. Technical Memorandum. Available from: <https://repository.library.noaa.gov/view/noaa/19837>. 32

OPPENHEIM, A. V.; SCHAFER, R. W. **Discrete-time signal processing**. [S.l.: s.n.], 1989. 15

PALHARINI, R. S. A.; VILA, D. A.; RODRIGUES, D. T.; QUISPE, D. P.; PALHARINI, R. C.; SIQUEIRA, R. A. de; AFONSO, J. M. de S. Assessment of the extreme precipitation by satellite estimates over South America. **Remote Sensing**, v. 12, n. 13, p. 2085, 2020. 104

PALMER, T.; HAGEDORN, R. **Predictability of Weather and Climate**. [s.n.], 2006. 702 p. ISBN 9780511225017. Available from: <https://books.google.com.br/books?id=vobtjwEACAAJ>. 8, 13

PANOFSKY, R. A. Objective weather-map analysis. **Journal of Atmospheric Sciences**, v. 6, n. 6, p. 386 – 392, 1949. Available from: <https://journals.ametsoc.org/view/journals/atsc/6/6/1520-0469_1949_006_0386_owma_2_0_co_2.xml>. 8

PARKER, M. D.; JOHNSON, R. H. Organizational modes of midlatitude mesoscale convective systems. **Monthly Weather Review**, v. 128, n. 10, p. 3413 – 3436, 2000. Available from: <https://journals.ametsoc.org/view/journals/mwre/128/10/1520-0493_2001_129_3413_omommc_2.0.co_2.xml>. 26, 27

PARRISH, D. F.; DERBER, J. C. The National Meteorological Center's spectral statistical-interpolation analysis system. **Monthly Weather Review**, v. 120, n. 8, p. 1747–1763, 1992. ISSN 0027-0644. Available from: <https://journals.ametsoc.org/view/journals/mwre/120/8/1520-0493_1992_120_1747_tnmcss_2_0_co_2.xml>. 11, 12, 33

PENNA, B. R.; SILVEIRA, B. B.; GONÇALVES, L. G. G. d.; SOUZA, S. S. d. Avaliação da temperatura de brilho nos canais sensíveis à superfície terrestre no sistema G3DVAR do CPTEC/INPE: série NOAA. **Revista Brasileira de Meteorologia**, v. 30, n. 3, p. 340–350, Sept. 2015. ISSN 0102-7786. Available from: <http://dx.doi.org/10.1590/0102-778620140030>. Access in: 09 nov. 2021. 24

PENNY, S. G. The hybrid local ensemble transform Kalman filter. **Monthly Weather Review**, v. 142, n. 6, p. 2139–2149, 2014. 17

POINCARÉ, H.; MAITLAND, F. **Science and method**. [S.l.]: London; Edinburgh; Dublin; New York, 1914. 7

POTERJOY, J.; SOBASH, R. A.; ANDERSON, J. L. Convective-scale data assimilation for the weather research and forecasting model using the local particle filter. **Monthly Weather Review**, v. 145, n. 5, p. 1897–1918, 2017. ISSN

0027-0644. Available from:
<http://journals.ametsoc.org/doi/10.1175/MWR-D-16-0298.1>. 2, 20

PURSER, R. J.; JOVIC, D.; KETEFIAN, G.; BLACK, T.; BECK, J.; DONG, J.; CARLEY, J. The extended Schmidt gnomonic grid for regional applications. In: UNIFIED FORECAST SYSTEM (UFS) USERS' WORKSHOP, 2020. **Proceedings...** DTC, 2020. Available from: <https://dtcenter.org/sites/default/files/events/2020/2-purser-james.pdf>. 42, 97

PURSER, R. J.; WU, W.-S.; PARRISH, D. F.; ROBERTS, N. M. Numerical aspects of the application of recursive filters to variational statistical analysis. Part I: spatially homogeneous and isotropic gaussian covariances. **Monthly Weather Review**, v. 131, n. 8, p. 1524–1535, 2003. ISSN 1520-0493. 33, 34, 51

PUTMAN, W. M.; LIN, S.-J. Finite-volume transport on various cubed-sphere grids. **Journal of Computational Physics**, v. 227, n. 1, p. 55–78, 2007. Available from: <https://doi.org/10.1016/j.jcp.2007.07.022>. 31

REHBEIN, A.; AMBRIZZI, T.; MECHOSO, C. R. Mesoscale convective systems over the Amazon basin. Part I: climatological aspects. **International Journal of Climatology**, v. 38, n. 1, p. 215–229, 2018. 86, 87, 88, 90, 93

REHBEIN, A.; AMBRIZZI, T.; MECHOSO, C. R.; ESPINOSA, S. A.; MYERS, T. A. Mesoscale convective systems over the Amazon basin: the GoAmazon2014/5 program. **International Journal of Climatology**, v. 39, n. 15, p. 5599–5618, 2019. 26

RIBEIRO, B. Z.; SELUCHI, M. E. A climatology of quasi-linear convective systems and associated synoptic-scale environments in southern Brazil. **International Journal of Climatology**, v. 39, n. 2, p. 857–877, 2019. 27

ROBERTS, B.; GALLO, B. T.; JIRAK, I. L.; CLARK, A. J.; DOWELL, D. C.; WANG, X.; WANG, Y. What does a convection-allowing ensemble of opportunity buy us in forecasting thunderstorms? **Weather and Forecasting**, v. 35, n. 6, p. 2293–2316, 2020. ISSN 0882-8156. Available from:
<https://journals.ametsoc.org/waf/article-abstract/35/6/2293/354717/What-Does-a-Convection-Allowing-Ensemble-of?redirectedFrom=fulltext>. 39

ROTUNNO, R.; KLEMP, J. B.; WEISMAN, M. L. A theory for strong, long-lived squall lines. **Journal of Atmospheric Sciences**, v. 45, n. 3, p. 463–485, 1988. 26, 27

ROZANTE, J. R. **Produto de precipitação MERGE**. [S.l.], 2017. Available from: <http://ftp.cptec.inpe.br/modelos/io/produtos/MERGE/read_me_MERGE.pdf>. 81

ROZANTE, J. R.; GUTIERREZ, E. R.; FERNANDES, A. de A.; VILA, D. A. Performance of precipitation products obtained from combinations of satellite and surface observations. **International Journal of Remote Sensing**, v. 41, n. 19, p. 7585–7604, 2020. Available from: <https://doi.org/10.1080/01431161.2020.1763504>. 81

ROZANTE, J. R.; MOREIRA, D. S.; GONCALVES, L. G. G. de; VILA, D. A. Combining TRMM and surface observations of precipitation: technique and validation over South America. **Weather and Forecasting**, v. 25, n. 3, p. 885–894, 2010. 81

SAPUCCI, L. F.; DINIZ, F. L. R.; BASTARZ, C. F.; AVANÇO, L. A. Inclusion of Global Navigation Satellite System radio occultation data into Center for Weather Forecast and Climate Studies Local Ensemble Transform Kalman Filter (LETKF) using the Radio Occultation Processing Package as an observation operator. **Meteorological Applications**, v. 23, n. 2, p. 328–338, April 2016. ISSN 1350-4827. 24

SCHUMACHER, R. S.; DAVIS, C. A. Ensemble-based forecast uncertainty analysis of diverse heavy rainfall events. **Weather and Forecasting**, v. 25, n. 4, p. 1103 – 1122, 2010. Available from: <https://journals.ametsoc.org/view/journals/wefo/25/4/2010waf2222378_1.xml>. 13

SCHUMACHER, R. S.; RASMUSSEN, K. L. The formation, character and changing nature of mesoscale convective systems. **Nature Reviews Earth & Environment**, v. 1, n. 6, p. 300–314, 2020. 26

SCHWARTZ, C. S.; POTERJOY, J.; CARLEY, J. R.; DOWELL, D. C.; ROMINE, G. S.; IDE, K. Comparing partial and continuously cycling ensemble Kalman filter data assimilation systems for convection-allowing ensemble forecast initialization. **Weather and Forecasting**, v. 37, n. 1, p. 85 – 112, 2022. Available from: <https:

//journals.ametsoc.org/view/journals/wefo/37/1/WAF-D-21-0069.1.xml>. 47

SCHWARTZ, C. S.; SOBASH, R. A. Generating probabilistic forecasts from convection-allowing ensembles using neighborhood approaches: a review and recommendations. **Monthly Weather Review**, v. 145, n. 9, p. 3397 – 3418, 2017. Available from: <https://journals.ametsoc.org/view/journals/mwre/145/9/mwr-d-16-0400.1.xml>. 119

_____. Revisiting sensitivity to horizontal grid spacing in convection-allowing models over the central and eastern United States. **Monthly Weather Review**, v. 147, n. 12, p. 4411–4435, 2019. Available from: <https://journals.ametsoc.org/view/journals/mwre/147/12/mwr-d-19-0115.1.xml>. 1, 18

SHAO, H. et al. Bridging research to operations transitions: status and plans of community GSI. **Bulletin of the American Meteorological Society**, v. 97, n. 8, p. 1427–1440, 2016. Available from: <https://journals.ametsoc.org/view/journals/bams/97/8/bams-d-13-00245.1.xml>. 34

SHEN, F.; XUE, M.; MIN, J. A comparison of limited-area 3DVAR and ETKF-En3DVAR data assimilation using radar observations at convective scale for the prediction of Typhoon Saomai (2006). **Meteorological Applications**, v. 24, n. 4, p. 628–641, 2017. Available from: <https://rmets.onlinelibrary.wiley.com/doi/abs/10.1002/met.1663>. 3, 21

SILVA-DIAS, M. A. F.; FERREIRA, R. N. Application of a linear spectral model to the study of Amazonian squall lines during GTE/ABLE 2B. **Journal of Geophysical Research: Atmospheres**, v. 97, n. D18, p. 20405–20419, 1992. Available from: <https://agupubs.onlinelibrary.wiley.com/doi/abs/10.1029/92JD01333>. 4

_____. _____. **Journal of Geophysical Research: Atmospheres**, v. 97, n. D18, p. 20405–20419, 1992. Available from: <https://agupubs.onlinelibrary.wiley.com/doi/abs/10.1029/92JD01333>. 27, 29

SILVEIRA, B. B. **A emissividade da superfície continental em micro-ondas e suas implicações na assimilação de radiâncias**. 239 p. Tese (Doutorado em Meteorologia) — Instituto Nacional de Pesquisas Espaciais

(INPE), São José dos Campos, 2017. Available from: <http://urlib.net/ibi/8JMKD3MGP3W34P/3PH9BTE>. 24

SKAMAROCK, W. C.; KLEMP, J. B.; DUDHIA, J.; GILL, D. O.; BARKER, D. M.; WANG, W.; POWERS, J. G. **A description of the advanced research WRF version 3. NCAR technical note-475+ STR**. [S.l.], 2008. Available from: <http://dx.doi.org/10.5065/D68S4MVH>. 31, 39

SMITH, T. L.; BENJAMIN, S. G.; BROWN, J. M.; WEYGANDT, S.; SMIRNOVA, T.; SCHWARTZ, B. 11.1 convection forecasts from the hourly updated, 3-km high resolution rapid refresh (HRRR) model. In: CONFERENCE ON SEVERE LOCAL STORMS, 24., 2008. **Proceedings...** AMS, 2008. Available from: <https://ams.confex.com/ams/pdfpapers/142055.pdf>. 3

SMITH, T. L.; BENJAMIN, S. G.; GUTMAN, S. I.; SAHM, S. Short-range forecast impact from assimilation of GPS-IPW observations into the Rapid Update Cycle. **Monthly Weather Review**, v. 135, n. 8, p. 2914–2930, 2007. Available from: <https://journals.ametsoc.org/view/journals/mwre/135/8/mwr3436.1.xml>. 20

SNYDER, C.; ZHANG, F. Assimilation of simulated doppler radar observations with an Ensemble Kalman filter. **Monthly Weather Review**, v. 131, n. 8, p. 1663 – 1677, 2003. Available from: <https://journals.ametsoc.org/view/journals/mwre/131/8/_2555.1.xml>. 21

SUN, J.; TRIER, S. B.; XIAO, Q.; WEISMAN, M. L.; WANG, H.; YING, Z.; XU, M.; ZHANG, Y. Sensitivity of 0–12-h warm-season precipitation forecasts over the central United States to model initialization. **Weather Forecasting**, v. 27, p. 832–855, 2012. 21

SUN, W.-Y.; ORLANSKI, I. Large mesoscale convection and sea breeze circulation. Part I: linear stability analysis. **Journal of Atmospheric Sciences**, v. 38, n. 8, p. 1675 – 1693, 1981. Available from: <https://journals.ametsoc.org/view/journals/atsc/38/8/1520-0469_1981_038_1675_lmcasb_2_0_co_2.xml>. 27

TAO, W. K.; SIMPSON, J.; SUI, C. H.; FERRIER, B.; LANG, S.; SCALA, J.; CHOU, M. D.; PICKERING, K. Heating, moisture, and water budgets of tropical and midlatitude squall lines: comparisons and sensitivity to longwave radiation. **Journal of Atmospheric Sciences**, v. 50, n. 5, p. 673 – 690, 1993. Available

from: <https://journals.ametsoc.org/view/journals/atsc/50/5/1520-0469_1993_050_0673_hmawbo_2_0_co_2.xml>. 26

THOMPSON, G.; EIDHAMMER, T. A study of aerosol impacts on clouds and precipitation development in a large winter cyclone. **Journal of the Atmospheric Sciences**, v. 71, n. 10, p. 3636–3658, 2014. Available from: <https://journals.ametsoc.org/view/journals/atsc/71/10/jas-d-13-0305.1.xml>. 32, 100

TONG, C.-C.; JUNG, Y.; XUE, M.; LIU, C. Direct assimilation of radar data with ensemble Kalman filter and hybrid ensemble-variational method in the National Weather Service operational data assimilation system GSI for the stand-alone regional FV3 model at a convection-allowing resolution. **Geophysical Research Letters**, v. 47, n. 19, p. e2020GL090179, 2020. 3, 21, 40, 51, 125

TONG, W.; LI, G.; SUN, J.; TANG, X.; ZHANG, Y. Design strategies of an hourly update 3DVAR data assimilation system for improved convective forecasting. **Weather and Forecasting**, v. 31, n. 5, p. 1673–1695, 2016. Available from: <https://journals.ametsoc.org/view/journals/wefo/31/5/waf-d-16-0041_1.xml>. 52, 76

TRAPP, R. J.; TESSENDORF, S. A.; GODFREY, E. S.; BROOKS, H. E. Tornadoes from squall lines and bow echoes. Part I: climatological distribution. **Weather and Forecasting**, v. 20, n. 1, p. 23 – 34, 2005. Available from: <https://journals.ametsoc.org/view/journals/wefo/20/1/waf-835_1.xml>. 26

TREMOLET, Y.; AULIGNE, T. The Joint Effort for Data assimilation Integration (JEDI). In: JOINT CENTER FOR SATELLITE DATA ASSIMILATION (JCSDA) NOAA TESTBED AND PROVING GROUND WORKSHOP. **Proceedings...** Kansas City, MO: JCSDA, 2018. Available from: <https://www.testbeds.noaa.gov/events/2018/workshop/presentations/>. 127

UFS. **About UFS applications**. 2019. Available from: <https://ufscommunity.org/science/aboutapps/>. 39

UFS DEVELOPMENT TEAM. **Unified Forecast System (UFS) Short-Range Weather (SRW) application**. Zenodo, mar. 2021. Available from: <https://doi.org/10.5281/zenodo.4534994>. 3

UPP. **UPP users guide V4**. [S.l.], 2021. 24 p. Available from: <https://dtcenter.org/sites/default/files/community-code/upp-users-guide-v4.pdf>. 35

VENDRASCO, E. P.; MACHADO, L. A.; ARAUJO, C. S.; RIBAUD, J.-F.; FERREIRA, R. C. Potential use of the GLM for nowcasting and data assimilation. **Atmospheric Research**, v. 242, p. 105019, 2020. 25

VENDRASCO, E. P.; SUN, J.; HERDIES, D. L.; ANGELIS, C. F. de. Constraining a 3DVAR radar data assimilation system with large-scale analysis to improve short-range precipitation forecasts. **Journal of Applied Meteorology and Climatology**, v. 55, n. 3, p. 673 – 690, 2016. Available from: <https://journals.ametsoc.org/view/journals/apme/55/3/jamc-d-15-0010.1.xml>. 5, 25, 76

VILA, D. A.; GONCALVES, L. G. G. de; TOLL, D. L.; ROZANTE, J. R. Statistical evaluation of combined daily gauge observations and rainfall satellite estimates over continental South America. **Journal of Hydrometeorology**, v. 10, n. 2, p. 533 – 543, 2009. Available from: <https://journals.ametsoc.org/view/journals/hydr/10/2/2008jhm1048_1.xml>. 81

VILA, D. A.; MACHADO, L. A. T.; LAURENT, H.; VELASCO, I. Forecast and tracking the evolution of cloud clusters (ForTraCC) using satellite infrared imagery: methodology and validation. **Weather Forecasting**, v. 23, p. 233–245, 2008. Available from: <https://doi.org/10.1175/2007WAF2006121.1>. 30, 80, 84

VILLANUEA-BIRREL, C. M.; SCHREINER, B.; KUO, B. Using radio occultation soundings to study mesoscale convective systems. In: ANNUAL AMS STUDENT CONFERENCE – 88TH AMERICAN METEOROLOGICAL SOCIETY ANNUAL MEETING, 7., 2008. **Proceedings...** New Orleans, LA: AMS, 2008. 23

WANG, H.; SUN, J.; FAN, S.; HUANG, X.-Y. Indirect assimilation of radar reflectivity with WRF 3D-Var and its impact on prediction of four summertime convective events. **Journal of Applied Meteorology and Climatology**, v. 52, n. 4, p. 889 – 902, 2013. Available from: <https://journals.ametsoc.org/view/journals/apme/52/4/jamc-d-12-0120.1.xml>. 21

WANG, H.; SUN, J.; ZHANG, X.; HUANG, X.-Y.; AULIGNé, T. Radar data assimilation with WRF 4D-Var. Part I: system development and preliminary testing. **Monthly Weather Review**, v. 141, n. 7, p. 2224 – 2244, 2013. Available

from: <https://journals.ametsoc.org/view/journals/mwre/141/7/mwr-d-12-00168.1.xml>. 21

WANG, X. Incorporating ensemble covariance in the Gridpoint Statistical Interpolation variational minimization: a mathematical framework. **Monthly Weather Review**, v. 138, n. 7, p. 2990–2995, 2010. ISSN 0027-0644. Available from: <https://doi.org/10.1175/2010MWR3245.1>. 33, 34

WANG, X.; HAMILL, T. M.; WHITAKER, J. S.; BISHOP, C. H. A comparison of hybrid ensemble transform Kalman filter–optimum interpolation and ensemble square root filter analysis schemes. **Monthly Weather Review**, v. 135, n. 3, p. 1055–1076, 2007. 16

_____. A comparison of the hybrid and EnSRF analysis schemes in the presence of model errors due to unresolved scales. **Monthly Weather Review**, v. 137, n. 10, p. 3219–3232, 2009. 17

WANG, X.; PARRISH, D.; KLEIST, D.; WHITAKER, J. GSI 3DVar-based ensemble-variational hybrid data assimilation for NCEP Global Forecast System: single-resolution experiments. **Monthly Weather Review**, v. 141, n. 11, p. 4098–4117, 2013. ISSN 0027-0644. Available from: <https://doi.org/10.1175/MWR-D-12-00141.1>. 33

WANG, Y.; WANG, X. Direct assimilation of radar reflectivity without tangent linear and adjoint of the nonlinear observation operator in the GSI-Based EnVar system: methodology and experiment with the 8 may 2003 Oklahoma city tornadic supercell. **Monthly Weather Review**, v. 145, n. 4, p. 1447–1471, 2017. ISSN 0027-0644. Available from: <https://doi.org/10.1175/MWR-D-16-0231.1>. 33

WEISMAN, M. L.; KLEMP, J. B. The dependence of numerically simulated convective storms on vertical wind shear and buoyancy. **Monthly Weather Review**, v. 110, n. 6, p. 504 – 520, 1982. Available from: <https://journals.ametsoc.org/view/journals/mwre/110/6/1520-0493_1982_110_0504_tdonsc_2_0_co_2.xml>. 41

WEISMAN, M. L.; KLEMP, J. B.; ROTUNNO, R. Structure and evolution of numerically simulated squall lines. **Journal of Atmospheric Sciences**, v. 45, n. 14, p. 1990–2013, 1988. 26

WEISSMANN, M.; GEISS, S.; NECKER, T.; SOMMER, M. What observations do we need for convective-scale data assimilation? In: RIKEN INTERNATIONAL

SYMPOSIUM ON DATA ASSIMILATION, 2017. **Proceedings...** Kobe, Japan, 2017. p. 1–24. Available from: <http://www.data-assimilation.riken.jp/risda2017/>. 22

WHITAKER, J.; HAMILL, T.; WEI, X.; SONG, Y.; TOTH, Z. Ensemble data assimilation with the NCEP Global Forecast System. **Monthly Weather Review**, v. 136, p. 463–482, 2008. Available from: <https://doi.org/10.1175/2007MWR2018.1>. 14

WHITAKER, J. S.; COMPO, G. P.; WEI, X.; HAMILL, T. M. Reanalysis without radiosondes using ensemble data assimilation. **Monthly Weather Review**, v. 132, n. 5, p. 1190–1200, 2004. 14, 102

WHITAKER, J. S.; HAMILL, T. M. Ensemble data assimilation without perturbed observations. **Monthly Weather Review**, v. 130, n. 7, p. 1913–1924, 2002. 13

WILKS, D. S. **Statistical methods in the atmospheric sciences**. 2.ed. ed. [S.l.]: Elsevier, 2006. ISBN 9780127519661. 55, 77

WMO. **Guide to WMO table driven code forms: FM 94 BUFR and FM 95 CREX**. [S.l.], 2002. Available from: <https://www.wmo.int/pages/prog/www/WDM/Guides/BUFRCREXGuide-English.html>. 37, 53

WOHL, E.; BARROS, A.; BRUNSELL, N.; CHAPPELL, N. A.; COE, M.; GIAMBELLUCA, T.; GOLDSMITH, S.; HARMON, R.; HENDRICKX, J. M. H.; JUVIK, J.; MCDONNELL, J.; OGDEN, F. The hydrology of the humid tropics. **Nature Climate Change**, v. 2, n. 9, p. 655–662, Sep 2012. ISSN 1758-6798. Available from: <https://doi.org/10.1038/nclimate1556>. 97

WONG, M.; ROMINE, G.; SNYDER, C. Model improvement via systematic investigation of physics tendencies. **Monthly Weather Review**, v. 148, n. 2, p. 671 – 688, 2020. Available from: <https://journals.ametsoc.org/view/journals/mwre/148/2/mwr-d-19-0255.1.xml>. 75

WU, W.; PURSER, R. J.; PARRISH, D. Three-dimensional variational analysis with spatially inhomogeneous covariances. **Monthly Weather Review**, v. 130, p. 2905–2916, 2002. Available from: <https://doi.org/10.1175/1520-0493(2002)130<2905:TDVAWS>2.0.CO;2>. 3, 33, 34

WU, W.-S.; PARRISH, D. F.; ROGERS, E.; LIN, Y. Regional ensemble–variational data assimilation using global ensemble forecasts. **Weather and Forecasting**, v. 32, n. 1, p. 83–96, 2017. ISSN 0882-8156. Available from: <https://doi.org/10.1175/WAF-D-16-0045.1>. 33, 34, 46

XIE, P.; JOYCE, R.; WU, S.; YOO, S.-H.; YAROSH, Y.; SUN, F.; LIN, R. Reprocessed, bias-corrected CMORPH global high-resolution precipitation estimates from 1998. **Journal of Hydrometeorology**, v. 18, n. 6, p. 1617–1641, 2017. 104

XU, K.-M.; RANDALL, D. A. A semiempirical cloudiness parameterization for use in climate models. **Journal of the Atmospheric Sciences**, v. 53, n. 21, p. 3084–3102, 1996. 32

YANO, J.-I.; ZIEMIAŃSKI, M. Z.; CULLEN, M.; TERMONIA, P.; ONVLEE, J.; BENGTSSON, L.; CARRASSI, A.; DAVY, R.; DELUCA, A.; GRAY, S. L.; HOMAR, V.; KOHLER, M.; KRICHAK, S.; MICHAELIDES, S.; PHILLIPS, V. T. J.; SOARES, P. M. M.; WYSZOGRODZKI, A. A. Scientific challenges of convective-scale numerical weather prediction. **Bulletin of the American Meteorological Society**, v. 99, n. 4, p. 699–710, 2018. Available from: <https://journals.ametsoc.org/view/journals/bams/99/4/bams-d-17-0125.1.xml>. 1, 23

ZENG, N. Seasonal cycle and interannual variability in the Amazon hydrologic cycle. **Journal of Geophysical Research: Atmospheres**, v. 104, n. D8, p. 9097–9106, 1999. 81

ZHANG, J.; HOWARD, K.; LANGSTON, C.; KANEY, B.; QI, Y.; TANG, L.; GRAMS, H.; WANG, Y.; COCKS, S.; MARTINAITIS, S.; ARTHUR, A.; COOPER, K.; BROGDEN, J.; KITZMILLER, D. Multi-Radar Multi-Sensor (MRMS) quantitative precipitation estimation: initial operating capabilities. **Bulletin of the American Meteorological Society**, v. 97(4), p. 621–638, 2016. Available from: <https://doi.org/10.1175/BAMS-D-14-00174.1>. 55

ZHOU, L.; LIN, S.-J.; CHEN, J.-H.; HARRIS, L. M.; CHEN, X.; REES, S. L. Toward convective-scale prediction within the next generation global prediction system. **Bulletin of the American Meteorological Society**, v. 100, n. 7, p. 1225–1243, 2019. Available from: <https://journals.ametsoc.org/view/journals/bams/100/7/bams-d-17-0246.1.xml>. 2

APPENDIX A - CODE AND DATA AVAILABILITY

The source code repository of the SRW version 1.0.0 is available at https://github.com/ufs-community/ufs-srweather-app (last access: 22 January 2021). The source code of the GSI analysis system used can be found at https://github.com/NOAA-EMC/GSI, branch feature/rrfs (last access: 4 February 2021). The frozen version of the prototype RRFS used in this study (RRFS v0.1) can be found in Banos et al. (2021d). The MET v9.0.0 source code can be found at https://github.com/dtcenter/MET/tree/main_v9.0. ICs, LBCs, and RAP observations used to perform the experiments and verify the forecasts were obtained from NOAA's High Performance Storage System (HPSS) archives. Stage IV precipitation observations were downloaded from the NCAR Earth Observing Laboratory data server at https://data.eol.ucar.edu/cgi-bin/codiac/fgr_form/id=21.093 (last access: 2 December 2020). Hourly MRMS composite reflectivity mosaic (optimal method) observations are available on the Iowa Environmental Mesonet archives at https://mesonet.agron.iastate.edu/archive/ (last access: 27 February 2021). Storm reports were obtained from the SPC archives available at https://www.spc.noaa.gov/climo/reports/200504_rpts.html (last access: 14 July 2021). All data used for the case study over northern South America are publicly available at the Research Data Archive (RDA[1]) of NCAR. The namelist files used for cold or warm start the model, for the analyses in each experiment, and for the generation of the model grid, topography and surface climatology are provided online along with the model configuration file, the file used in the analyses to read the horizontal and vertical scales from an external file, all scripts used to execute every task of the workflow, all scripts used to process model outputs with MET, as well as all scripts and data used to create all figures of the paper, via Zenodo (BANOS et al., 2021b).

[1] https://rda.ucar.edu/